In situ Bragg coherent X-ray diffraction imaging of nanoscale strain evolution



David Yang

Keble College

University of Oxford

A thesis submitted for the degree of

Doctor of Philosophy

Trinity 2022

Declaration

I declare that this thesis is entirely my own work, and except where otherwise stated, describes my own research.

D. Yang,

Keble College

Dedication

This thesis is dedicated to my parents. Without their love and personal sacrifices, I would not be where I am today.

Acknowledgements

This thesis would not be possible without the guidance of my supervisor, Felix. Your enthusiasm for science has been inspiring–it has been a very rewarding experience working with you during my DPhil. Thank you for your optimism, advice, and encouragement–I could not have asked for a better supervisor and mentor for this DPhil journey.

Particular thanks to Nick. You've been a great mentor and have massively helped me navigate through the intricacies of BCDI. I would like to gratefully acknowledge the other members of the Hofmann Group, past and present: Hongbing, Rima, Abdallah, Kay, Seb, Minyi, Tom, and Guanze for being great colleagues and friends who enabled my scientific pursuits. Thanks to all those in office 40.35 for fostering a supportive environment, and particularly to Dan and Nils, who began their DPhils at the same time, for being great friends.

My work would not have been possible without all the amazing beamline scientists at the APS. Thank you Ross and Wonsuk at beamline 34-ID-C for your patience with me and my ambitious experiments throughout the years. Also, thank you Wenjun, Ruqing and Dina at beamline 34-ID-E. Every interaction has been a valuable learning experience and I'm eager to see the new science after the APS upgrade.

I am grateful for all those at Keble College who have made my time very memorable, and especially for my friends who have been with me since matriculation: Sydney, Jack, Sabrina, Ani, Jasper, and Chloe. Thank you for providing me with laughs, comfort, food, and sanity during my DPhil. I would like to thank my coaches and teammates at OULRC and KCBC for giving me something to do besides work.

Finally, thanks to all my friends back at home and around the world, and especially to my parents, for their unwavering support. Equally important are my siblings, Jacky and Michelle, who have grown up alongside me and continued to provide laughter and encouragement thousands of kilometres from home.

I would like to gratefully acknowledge funding from the European Research Council under the European Union's Horizon 2020 research and innovation programme (grant agreement No 714697) and Keble Association Travel Grants (TT 2019, HT 2020). X-ray diffraction experiments were performed at the Advanced Photon Source, a US Department of Energy (DOE) Office of Science User Facility operated for the DOE Office of Science by Argonne National Laboratory under Contract No. DE-AC02-06CH11357. I acknowledge the use of characterisation facilities at the David Cockayne Centre for Electron Microscopy, Department of Materials, University of Oxford and the Advanced Research Computing (ARC) facility at the University of Oxford.

Abstract

The properties of crystalline materials are dictated by their lattice structure. The periodic arrangement of a perfect lattice is often impossible to achieve. Lattice defects such as dislocations induce lattice strains that can alter the behaviour of materials in certain environments. These defects could potentially be engineered to optimise desirable material properties if the relationship between these defects and material properties is well understood.

The study of how defects influence material properties requires the ability to image them during dynamic processes. A promising technique is Bragg coherent X-ray diffraction imaging (BCDI), which allows for the high resolution probing of 3D lattice strain in sub-micron volumes, making it an ideal technique to study crystal defects. BCDI leverages the coherence properties of X-rays to produce a 3D coherent X-ray diffraction pattern (CXDP) in the Fraunhofer regime for a specific Bragg reflection. This pattern can be inverted using phase retrieval algorithms to reconstruct the crystal morphology and phase, which provides direct information about internal atomic displacements along the scattering vector. Importantly, BCDI can be performed under ambient conditions, allowing for a variety of sample environments to be explored to study lattice strain evolution.

This thesis reports the study of defects and their evolution in annealing and corrosion using *in situ* BCDI. Prior to the *in situ* work, some challenges in the BCDI measurements are addressed. The first is to correctly transform data from the detector coordinate frame in which data is acquired to an orthogonal sample frame. This allows for the correct interpretation of the result in the sample frame for multi-reflection BCDI measurements.

While this was done for one BCDI instrument, the framework is completely general and coordinate transformations for any other instrument can be easily carried out. To measure CXDPs of multiple reflections from the same crystal, detailed knowledge of the crystal orientation is essential. This is not generally known *a priori*. Here, EBSD is used to produce an accurate orientation matrix for BCDI alignment, allowing the orientation to be determined without the use of dedicated synchrotron time or beamlines. Finally, a refined strain computation approach for multi-reflection BCDI is also presented. By using a complex exponential to calculate the strain, a more faithful reconstruction is obtained by interpolating and finding phase derivatives in data with phase jumps.

Using these refinements, *in situ* BCDI studies are carried out. *In situ* BCDI annealing of focused-ion beam (FIB) damaged Au microcrystals was performed to study the annihilation of defects through thermal diffusion. A change in morphology, average lattice strain, displacement field, and facet areas is observed throughout the annealing cycle, and suggest that self-diffusion of Au is the primary cause for the evolution of lattice structure, rather than Ga impurities caused by FIB milling. Furthermore, the study of separate reflections shows quite different behaviour depending on which reflection is analysed. These new insights open up opportunities for managing and removing FIB and more generally irradiation damage at the nanoscale.

In situ BCDI corrosion of a Co-Fe microcrystal shows how corrosion can affect the lattice strain inside a crystal. Here, the more strained surface layers of the crystal corrode first, and an increase in average tensile strain accumulates during corrosion. It also enabled the computation of the local, 3D-resolved dissolution rate. It is revealed that the preferential dissolution of facets is not necessarily dictated by localised strain, but by the geometry associated with the measurement. This opens the door to more detailed studies to identify the most critical corrosion sites and mechanisms, which is important for designing next generation materials for harsh environments.

Contents

1 Introduction **1**

2 Survey of literature **8**

2.1 Introduction to X-rays 8

2.1.1 X-ray sources 9

2.1.1.1 Cathode-ray tubes 9

2.1.1.2 Synchrotron radiation 10

2.2 X-ray interaction with matter 12

2.2.1 Scattering from an electron 13

2.2.2 Scattering from an atom 16

2.2.3 Scattering from crystals 18

2.2.3.1 Bragg's Law 20

2.2.3.2 An infinite crystal 21

2.2.3.3 A finite crystal 23

2.2.3.4 A strained crystal 25

2.3 Bragg coherent X-ray diffraction imaging measurement 27

2.3.1 Coherence 27

2.3.1.1 Spatial coherence 28

2.3.1.2 Temporal coherence 29

2.3.1.3 Partial coherence 29

2.3.2 Measurement Geometry 32

2.3.2.1 Ewald's sphere 32
2.4 Phase retrieval 34
2.4.1 Oversampling 34
2.4.2 Uniqueness 37
2.4.3 Gerchberg-Saxton 38
2.4.4 Error-reduction 39
2.4.4.1 Shrinkwrap 40
2.4.5 Hybrid input-output 40
2.4.6 Guided algorithms 41
2.4.7 Error metrics 43
2.4.7.1 Sharpness 43
2.4.7.2 Maximum volume 44
2.4.7.3 Normalised mean difference 45
2.4.7.4 Free log-likelihood 45
2.4.8 Spatial resolution 46
2.4.8.1 Rayleigh resolution 47
2.4.8.2 Phase retrieval transfer function 47
2.4.8.3 Line spread function 48
2.4.8.4 Fourier shell correlation 48
2.4.9 Phase retrieval development 48
2.4.9.1 Gerchberg-Saxton based phasing algorithms 49
2.4.9.2 Partial coherence phase retrieval 49
2.4.9.3 Simultaneous multi-Bragg peak phase retrieval 51
2.4.9.4 Absence of measured data 54
2.4.9.5 Machine learning-based phase retrieval 56
2.4.10 Strain calculation 58
2.5 Experimental developments 59
2.5.1 2D coherent X-ray diffraction imaging 60

2.5.2 3D coherent X-ray diffraction imaging 60
2.5.3 Bragg coherent X-ray diffraction imaging 61
2.5.4 Multi-reflection Bragg coherent X-ray diffraction imaging 63
2.5.5 Micro-beam Laue microcrystal alignment 63
2.5.6 FIB sample manufacture 65
2.5.7 3D Bragg ptychography 66
2.5.8 *In situ* and *in operando* BCDI studies 69
2.5.9 X-ray free electron lasers 73
2.6 Summary of literature review 73

3 Mapping data between sample and detector conjugated spaces in Bragg coherent diffraction imaging 77

3.1 Abstract 78
3.2 Introduction 78
3.3 Simulation geometry 79
3.4 Computer codes 81
3.4.1 Bragg coherent X-ray diffraction imaging simulation 81
3.4.2 Space transformation scripts 82
3.5 Space transformations 83
3.5.1 Sample space to lab space 84
3.5.2 Lab space to reciprocal lab space 86
3.5.3 Reciprocal lab space to detector reciprocal space 86
3.5.4 Detector reciprocal space to detector conjugated space 88
3.5.5 Detector conjugated space to lab space 89
3.6 Application of mapping scripts 89
3.6.1 Transfer from detector conjugated space to sample space 90
3.6.2 Transfer from sample space to detector conjugated space 90
3.6.3 Transfer from detector conjugated space to detector conjugated space 92

3.7 Conclusion . . . 93
3.8 Data availability . . . 94

4 Refinements for Bragg coherent X-ray diffraction imaging: Electron backscatter diffraction alignment and strain field computation 95

4.1 Abstract . . . 96
4.2 Introduction . . . 97
4.3 Experimental methodology . . . 98
4.3.1 Microcrystal fabrication . . . 98
4.3.2 Electron backscatter diffraction . . . 99
4.3.3 Micro-beam Laue X-ray diffraction . . . 104
4.3.4 Bragg coherent X-ray diffraction imaging . . . 107
4.3.5 Sample mounting . . . 109
4.4 Results and Discussion . . . 110
4.4.1 Orientation matrix comparison . . . 110
4.4.2 Determination of strain . . . 114
4.5 Conclusion . . . 118
4.6 Data availability . . . 118

5 Annealing of focused ion beam damage in gold microcrystals: An *in situ* Bragg coherent X-ray diffraction imaging study 119

5.1 Abstract . . . 120
5.2 Introduction . . . 121
5.3 Experimental methodology . . . 123
5.3.1 Sample preparation . . . 123
5.3.2 Bragg coherent X-ray diffraction . . . 125
5.3.2.1 *In situ* annealing . . . 126
5.3.3 Phasing of the diffraction data . . . 129
5.4 Results and discussion . . . 130

5.4.1 Crystal strain and morphology 130
5.4.2 Facet area 132
5.4.3 Normalised displacement field cross-correlation matrix 133
5.4.4 Normalised morphology cross-correlation matrix 136
5.4.5 Average lattice strain in regions of interest 138
5.4.6 Analysis technique comparisons 140
5.4.7 Diffusion considerations 141
5.5 Conclusion 143
5.6 Data availability 144

6 *In situ* Bragg coherent X-ray diffraction imaging of corrosion in a Co-Fe alloy microcrystal 145

6.1 Abstract 146
6.2 Introduction 146
6.3 Methods 149
6.3.1 Sample manufacture 149
6.3.2 Experimental measurements 150
6.3.3 Corrosion 151
6.4 Results 152
6.5 Discussion 154
6.5.1 Crystal morphology 154
6.5.2 Dissolution 156
6.5.3 Crystal strain 159
6.6 Conclusion 161
6.7 Data availability 162

7 Conclusions 163

A Chapter 3 Appendix 167

A.1 34-ID-C beamline to right-handed conversion 167

A.2 Laboratory example additional images 167
A.2.1 Electron micrograph comparison 168
A.2.2 Laboratory SS shape comparison 168
A.2.3 DCS shape reconstruction 168

B Chapter 4 Appendix **171**

B.1 Phase retrieval 171
B.2 EDX results 172
B.3 Supplementary video descriptions 172

C Chapter 5 Appendix **174**

C.1 34-ID-C heater cell 174
C.2 Effect of seeding on the retrieved electron density 174
C.3 Phase retrieval 177
C.4 Spatial resolution 178
C.5 Dislocations in crystal B, (200) reflection 178
C.6 Standard deviation of average strain 178
C.7 CXDP comparison 179
C.8 Supplementary video descriptions 179

D Chapter 6 Appendix **185**

D.1 Phase retrieval 185
D.2 Facet evolution 186
D.3 EDX results 187
D.4 Supplementary video descriptions 189

E List of abbreviations **190**

References **193**

Chapter 1

Introduction

Lattice defects control the properties of crystalline materials in a wide range of fields such as electronics, catalysis, computing, energy, and transportation. These defects control the charge carrier mobility in semiconductor nanostructures [1], selectivity of catalysts for chemical reactions [2], photon emission in next-generation quantum devices [3], degradation of battery electrodes for energy storage [4], and structural performance of alloys, e.g. for aerospace [5] and nuclear industries [6]. Selecting and designing appropriate materials for future applications requires an understanding of how these defects can be engineered to induce specific material properties.

Lattice defects interact through the strain fields they produce. These strain fields, which extend through the bulk material, originate from the displacement of atoms from their ideal lattice position. Defects interact with each other as well as other microstructural features to dictate the material's chemical [2], electronic [4] and mechanical properties [5]. Remarkably, material properties can also be affected by seemingly subtle environmental changes, e.g. the presence of trace amounts of hydrogen can cause steel embrittlement [7]. Such slight perturbations, which may lead to material failure, necessitate the study of how defects and their associated strain fields are influenced by their environment.

To monitor single crystal defect behaviour, defects can be isolated in sub-micron 3D

volumes. However, studies in this regime are complicated by the use of smaller sample volumes, which can generate results that deviate from the sample's bulk properties [8–10]. For example, studies show that crystalline materials can have a "smaller-is-stronger" effect [8,11], as their strength becomes more dependent on the length scale imposed by the sample, rather than the intrinsic material length scales. Nonetheless, the study of isolated, individual defects during dynamic processes remains important to elucidate their role in determining material properties.

In situ strain measurements with nanometre spatial resolution have become increasingly valuable over the past few decades because they can explore how defects interact with their environment [12–14]. Specifically, transmission electron microscopy (TEM) techniques such as high-resolution TEM (HRTEM) and scanning TEM (STEM), allow dislocation strain fields to be measured with atomic resolution [15], shown in Fig. 1.1, and can enable the study of dynamic systems *in situ* [16–18].

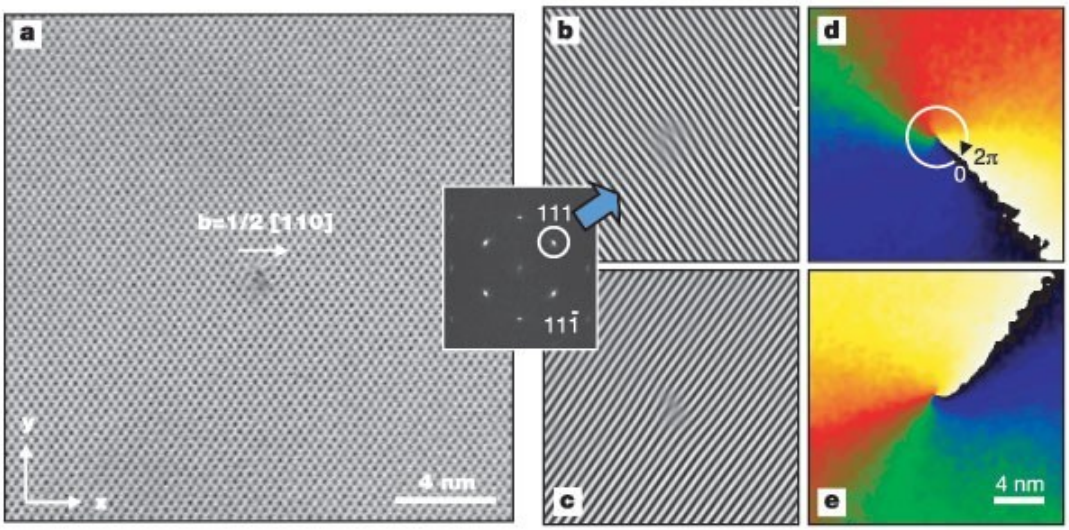

Figure 1.1: An edge dislocation in silicon was imaged using a combination of high-resolution electron microscopy and geometric phase analysis. A high-resolution electron microscope image in the $[1\bar{1}0]$ orientation with a Burgers vector $\mathbf{b} = 1/2[110]$ is shown in (a). Lattice fringes obtained by Fourier space filtering are magnified and shown in (b) for (111) and (c) for $(11\bar{1})$. Phase images are shown in (d) for (111) and (e) for $(11\bar{1})$. The colour range is 0 to 2π rad. Image obtained with permission from Hytch *et al.* [15].

These *in situ* TEM studies have been crucial in confirming various calculations and models, e.g. density functional theory, molecular dynamics, and kinetic Monte Carlo [19], but these experiments can be prone to issues such as electron beam stability, electron beam

induced heating, radiation damage, undesired liquid reactions and unwanted byproducts [18]. While TEM techniques benefit from the short de Broglie wavelength of electrons, allowing for high spatial resolution imaging, they are generally limited by the weak penetration depth of electrons and dynamical scattering effects. This typically restricts the sample to dimensions of less than 100 nm thick [20]. Thus, most of the material is very close to the free surface, which acts as a defect sink and significantly modifies the defect population [21–23]. The fabrication of TEM samples can require the use of focused ion beam (FIB) milling, but it can induce undesired sample modifications [24–29]. Additionally, 3D strain analysis is challenging with TEM, as only displacement components perpendicular to the dislocation line or a 2D projection of the dislocation can be measured [15]. This severely limits the observation of strains created by 3D dislocation structures and junctions that control material properties [30].

To overcome some of these limitations, synchrotron X-ray techniques can be used as a complementary imaging method. X-rays allow us to observe crystals with a greater penetration depth compared to that of electrons, enabling the study of larger volumes of material without the use of a vacuum or potentially less damage to the sample [20]. However, the small numerical aperture and poorer efficiency of X-ray optics limit the spatial resolution for many X-ray based techniques [31]. Typically, sub-micron spatial resolution can be obtained using techniques such as scanning X-ray diffraction mapping [32], dark-field X-ray microscopy [33], and micro-beam Laue diffraction [34]. To bring the spatial resolution down to tens of nanometres [35], the X-ray focusing optics can be removed, thereby improving the signal-to-noise ratio [36]. The removal of lenses is the basis for a lensless imaging technique known as coherent X-ray diffraction imaging (CDI).

In CDI, the scattered light is collected from a sample that has been fully illuminated by a coherent, monochromatic X-ray beam. The light is captured directly on a pixelated detector positioned in the far-field (Fraunhofer) transmission geometry. In the Fraunhofer regime, the collected signal is a diffraction pattern, which is proportional to the

squared Fourier transform, $|\mathscr{F}|^2$, of the sample. Thus, when measuring the diffraction pattern intensity, the phase, ψ, is lost. The phase encodes the structural information of the image–without it, the real space image cannot be obtained. Fortunately, the phase of an oversampled diffraction pattern can be recovered [37] using an iterative phase retrieval or phasing algorithm [38–40]. The phasing algorithm essentially becomes the "lens" for CDI techniques, making the image resolution, in theory, limited by the wavelength of X-rays ($\sim$ 1 Å), numerical aperture, number of photons, and the stability of the sample and system. Once the phase is recovered, it can be combined with the known amplitude, or the square root of the measured intensity, to reconstruct the real space image using an inverse Fourier transform, $\mathscr{F}^{-1}$ [41].

CDI becomes sensitive to lattice displacements if the detector is placed in the Bragg geometry for a specific *hkl* reflection, known as Bragg CDI (BCDI). At the Bragg condition, the sample is often rotated in small increments ($\sim 0.005°$), $\delta\theta$, about an axis to sample 2D slices of the 3D diffraction pattern or Bragg peak. A schematic of a typical BCDI setup is shown in Fig 1.2.

After phase retrieval and taking the $\mathscr{F}^{-1}$ of the complex wavefield, coordinate transforms are applied to generate an orthonormalised, real space reconstruction of the crystal [43–45]. Here, the retrieved phase can be used to identify structural defects inside the crystal lattice by noting characteristic phase variations [46]. The phase is related to the internal atomic displacement field of the object projected along the scattering vector for a particular *hkl* reflection. Characteristic variations of the phase can also be used to identify defects. These displacements correspond to atomic deviations from their ideal lattice positions and thus, information such as the strain field can also be determined from the displacement field for a particular *hkl* reflection. Although BCDI can achieve a strain resolution of $\sim 2\times10^{-4}$ [22, 29, 30, 47], the interpretation of the atomic displacements from their ideal positions can be ambiguous for a single reflection [48], as only displacement along the direction of the scattering vector is measured. For a clearer analysis of the state of a crystal exposed to a particular environment, multiple reflections can be measured for

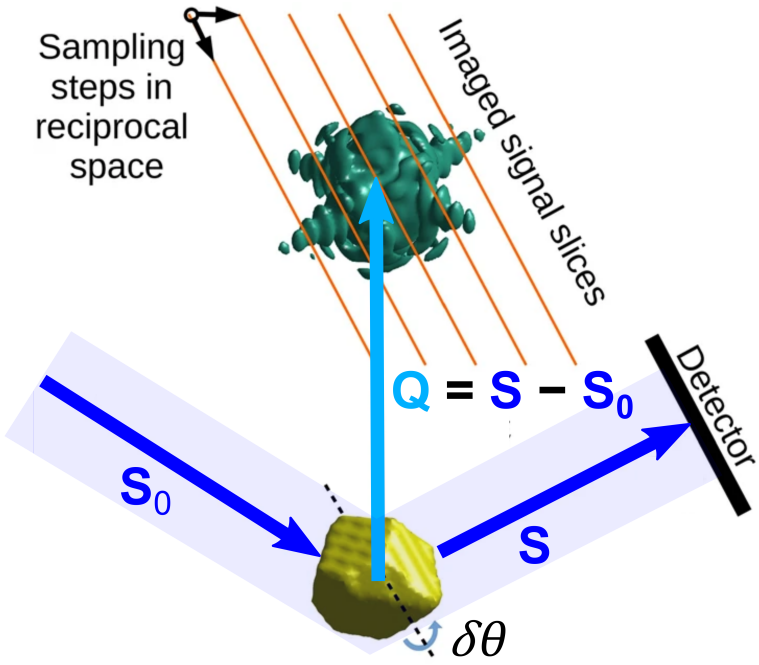

Figure 1.2: A crystal is illuminated by an incident coherent X-ray beam, $\mathbf{S_0}$ in the BCDI geometry. The reflected beam, $\mathbf{S}$, is captured by the detector in the Fraunhofer regime. The crystal is rotated about an axis by small increments, $\delta\theta$, to sample the Bragg peak centred about the scattering vector, $\mathbf{Q}$, in reciprocal space. Image adapted from Maddali *et al.* under the Creative Commons CC BY license [42].

a single crystal, known as multi-reflection BCDI (MBCDI), to calculate the 3D lattice strain and rotation tensor [22, 29, 30, 47, 49, 50].

BCDI combines high spatial resolution, excellent strain sensitivity and the ability to probe 3D volumes into an imaging tool that has been used to study crystal strain fields for nearly two decades [14,51,52]. Many have applied BCDI to various sample environments for *in situ* studies of crystal defects [52–56]. One limiting factor of *in situ* BCDI experiments is that only one reflection is often measured. Although it is theoretically possible to measure multiple reflections to obtain the 3D strain and rotation tensors, MBCDI experiments are generally challenging as they require knowledge of the sample orientation, stable measurement environments, and many days of beamtime [57].

Prior to the work presented in this thesis, only two experiments, Choi *et al.* [58] and Assefa *et al.* [59] used *in situ* BCDI to measure more than one reflection. The lack of complete strain and rotation information in single-reflection *in situ* BCDI studies limits our understanding of how defects interact with their environment. Acquiring a thorough

understanding of how defects evolve enables us to develop more accurate material models and engineer high performance materials with tailored properties and functionality. This thesis will contribute to the understanding of lattice defects by expanding the use of *in situ* BCDI to study annealing and corrosion. Specifically, I aim to address the following key questions.

1. How can BCDI become an everyday microscopy tool?
2. How are strain fields and their corresponding defects removed during a dynamic process?
3. How do localised strain fields and different morphological features interact with the sample environment?
4. To what extent can *in situ* BCDI be used as a tool to probe defect evolution?

This thesis addresses the above questions in the form of a department-approved integrated thesis. This thesis contains four scholarly articles fully published in peer-reviewed, major journals (*J. Synchrotron Radiat., J. Appl. Crystallogr., CrystEngComm*) [43,48,49, 60] . Due to the collaborative nature of science, I have recognised individuals who have contributed to the work at the beginning of each Chapter (3-6).

I begin by reviewing the core BCDI theory and relevant literature in Chapter 2. This review covers the fundamental physics for BCDI measurements. I begin with a discussion of X-rays and how they interact with crystalline matter. From there I discuss the importance of X-ray coherence and the measurement geometry required for BCDI. A review of phase retrieval methods, as well as a discussion of BCDI developments, will follow. This chapter also contains an overview of *in situ* BCDI studies on defect-containing structures and concludes with an overall summary and some limitations of *in situ* BCDI.

Chapter 3 examines the correct coordinate transformations required following phase retrieval. The issue is that the reconstructed objects are sheared due to the detector geometry, and need to be transformed to an orthogonal coordinate frame for accurate interpretation. This lays the groundwork for MBCDI analysis presented later in the thesis,

whereby different reflections for a single crystal need to be transformed to a common real space sample frame for further analysis.

Chapter 4 addresses the first key question of my thesis and explores how BCDI can become accessible. Here I outline a reliable procedure for using EBSD to orient the crystal for BCDI, enabling users to find Bragg peaks from specific crystals more easily at the beamline. BCDI measurements of specific crystals can now be made at beamlines that do not have a co-located Laue instrument. I also highlight a more efficient and accurate method to calculate the strain fields for each reflection. These new methods are used to recover the 3D strain and rotation tensor for a Fe-Ni microcrystal.

Chapter 5 addresses the second key question of my thesis and explores how defects induced by FIB milling can be annealed. Two reflections from two crystals each were measured to explore the evolution of average lattice strain, facet sizes, lattice displacements and crystal morphologies. I find that annealing can be used as a pathway to remove FIB-induced strain. Here, dislocation escape happens prior to more macroscopic rearrangement, i.e. the formation of new facets at higher temperatures. Finally, Ga-Au diffusion does not seem to play a major role in the structural changes during annealing. Rather, the dynamics observed seem to be primarily linked to Au self-diffusion and resulting defect mobility.

Chapter 6 addresses the third key question of my thesis and explores how localised crystal structure is influenced by corrosion. Here, I perform MBCDI at ambient conditions, determining the full strain and rotation tensors of the crystal prior to corrosion. Single-reflection *in situ* BCDI measurements provide critical information about the crystal strain field and morphology evolution and can help determine the defect mechanisms responsible for the creation and elimination of preferential corrosion sites.

The conclusions from this thesis are presented in Chapter 7. Important findings from each chapter are presented in the context of the advances made to *in situ* BCDI for probing microcrystal evolution.

Chapter 2

Survey of literature

The chapter starts with a discussion of how X-rays interact with crystalline matter, which can lead to the formation of diffraction patterns. Phase retrieval, the primary method for processing these diffraction patterns is then presented, followed by how strain can be interpreted from the resulting reconstructions. Historical developments in the BCDI technique will then be discussed, before moving on to a discussion of modern updates in the experimental and computational work.

2.1 Introduction to X-rays

X-rays are a form of electromagnetic radiation first discovered by Wilhelm Röntgen in 1895 [61]. Upon its discovery, X-rays were used as a revolutionary form of medical imaging as they allowed people to observe their bone structure. This is because X-ray absorption is proportional to Z^4 [62], where Z is the atomic number, thus allowing X-rays to pass more readily through light elements in tissue than the heavier elements within bone. Similar to other forms of light, X-rays are a combination of synchronised electric and magnetic field waves that oscillate perpendicular to each other and to the direction of propagation (Fig. 2.1).

Their higher energy enables X-rays to penetrate through materials:

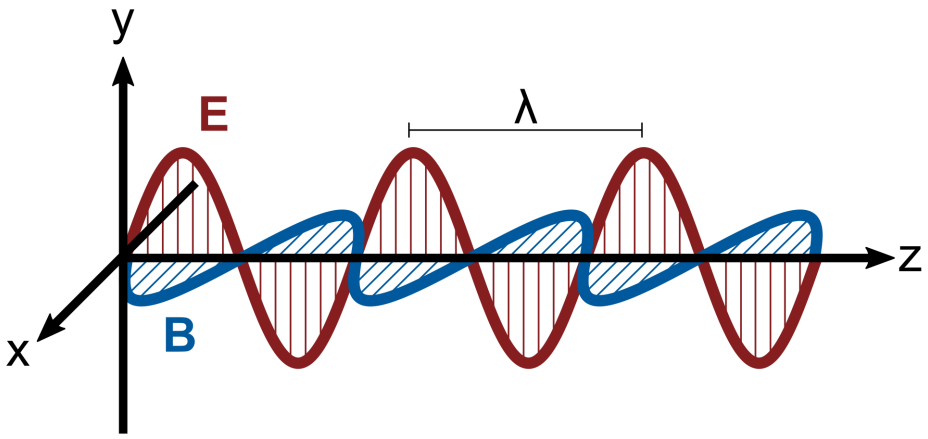

Figure 2.1: A plane-polarised electromagnetic wave. Synchronised perpendicular electric (**E**, parallel to y-axis) and magnetic (**B**, parallel to x-axis) fields are shown normal to the direction of propagation. The z-axis describes the direction of propagation and the wavelength is described by λ.

$$E = \frac{hc}{\lambda}, \tag{2.1}$$

where h is Planck's constant, c is the speed of light, and λ is the wavelength. Typically, X-rays have a wavelength of 10 nm to 0.01 nm (about 124 eV to 124 keV), allowing for imaging spatial resolutions to be far greater than that achievable with visible light. This is because the spatial resolution, Δx_s, defined as the distance on the sample for two features to be optically resolved, is directly proportional to λ through the Rayleigh criterion [62],

$$\Delta x_s = 1.22\frac{\lambda f}{D_l} = 0.61\frac{\lambda}{\mathrm{NA}}, \tag{2.2}$$

where D_l is the diameter of the lens, f is the focal length, and NA is the numerical aperture.

2.1.1 X-ray sources

2.1.1.1 Cathode-ray tubes

In the early 1900s, the main source of X-rays were cathode-ray tubes developed by William Coolidge [62]. A cathode-ray tube involves heating a tungsten filament and applying a voltage to accelerate electrons towards a cooled anode. The rapid deceleration

upon hitting the anode, known as "bremsstrahlung," or "breaking radiation," produces X-rays with a broad energy spectrum and a maximum X-ray energy dependent on the applied voltage. Furthermore, this method can cause electrons found in the inner orbitals to be ejected. The vacancy is replaced by an electron from an outer orbital, producing a characteristic X-ray. Overall, cathode-ray tubes are relatively inefficient at producing X-rays because much of the kinetic energy from the electrons is converted to heat. Developments such as implementing a rotating anode increased the cooling rate, which enabled improvements in X-ray intensity, but overall, this type of X-ray source lacked the energy, precision, and intensity compared to synchrotron sources which emerged in the 1970s.

2.1.1.2 Synchrotron radiation

The X-rays pertaining to this thesis are from a third-generation synchrotron source, the Advanced Photon Source (APS) at Argonne National Laboratory (ANL), IL, USA. Synchrotron radiation is characterised by its high brilliance compared to other X-ray sources. Brilliance combines different aspects that characterise the quality of an X-ray beam through the following expression [62],

$$\text{Brilliance} = \frac{(\text{Photons/second})}{(\text{Beam divergence [mrad]})^2(\text{source area [mm]})^2(0.1\%\ \text{Energy bandwidth})}, \tag{2.3}$$

which measures the flux per area corrected for divergence and monochromaticity. In these facilities, electrons are accelerated from a linear accelerator to relativistic speeds within a storage ring. The ring is not perfectly circular, as it consists of curved and straight sections. As the electrons pass through a curved bending magnet, the Lorentz force pushes the electron in a circular orbit, but the change in acceleration causes the emittance of X-ray radiation. The electrons replenish this energy loss as they travel through straight sections. The straight sections contain focusing magnets and radiofrequency cavities that provide a speed boost via electromagnetic fields that oscillate at radio frequencies.

The straight sections also often contain insertion devices (IDs) such as undulators or wigglers, which are arrays of alternating permanent magnetic dipoles in the direction of the travelling electron. The electrons oscillate within the magnetic field of the ID to produce X-rays. The oscillation path can be described by a deflection parameter, K [62],

$$K = \frac{e^- B_0 \lambda_u}{2\pi m_e c} = 0.934 \lambda_u[\text{cm}] B_0[\text{T}], \tag{2.4}$$

where $e^- = -1.6 \times 10^{-19}$ C is the election charge, B_0 is the average magnetic field and λ_u is the period of the magnetic structure. The difference lies in the degree of coherence of X-rays produced. Undulators ($K << 1$) create a small amplitudes of electron oscillation and produce more intense and coherent X-rays whereas wigglers ($K >> 1$) produce a broader X-ray energy spectrum.

The X-rays from the ID then enter a beamline (Fig. 2.2). Normally for a CDI experiment, the X-rays pass through a monochromator, which selects the appropriate wavelength for the experiment and the energy resolution, $\Delta\lambda/\lambda$. At BCDI beamline 34-ID-C at the APS, a Si(111) double crystal monochromator is used to fine tune the X-ray bandwidth ($\Delta\lambda/\lambda \approx 10^{-4}$). The first crystal is oriented such that a (111) reflection of Si is satisfied from the incoming X-ray beam. The X-ray is reflected and travels to the second crystal which is oriented to satisfy the same Bragg condition. After selecting an appropriate wavelength, the size of the beam is cut using horizontal and vertical slits.

A focusing device such as a zone plate or Kirkpatrick-Baez (KB) mirrors is then used to adjust the X-ray spot size at the sample plane. At beamline 34-ID-C, KB mirrors are used to focus the X-ray to a $\sim 1\ \mu\text{m} \times 1\ \mu\text{m}$ spot size. KB mirrors consist of two curved reflective silicon crystals that focus the X-ray beam in the horizontal and vertical directions [64]. This enables the flux to be concentrated at the focus.

The focused X-rays then interact with the sample, described in Chapter 2.2, and the scattered X-rays are collected on a hybrid-pixel detector. As X-rays hit the detector, they trigger an electron cascade and the number of electrons collected at each pixel will be proportional to the intensity. At BCDI beamline 34-ID-C, a 256 × 256 pixel module on a

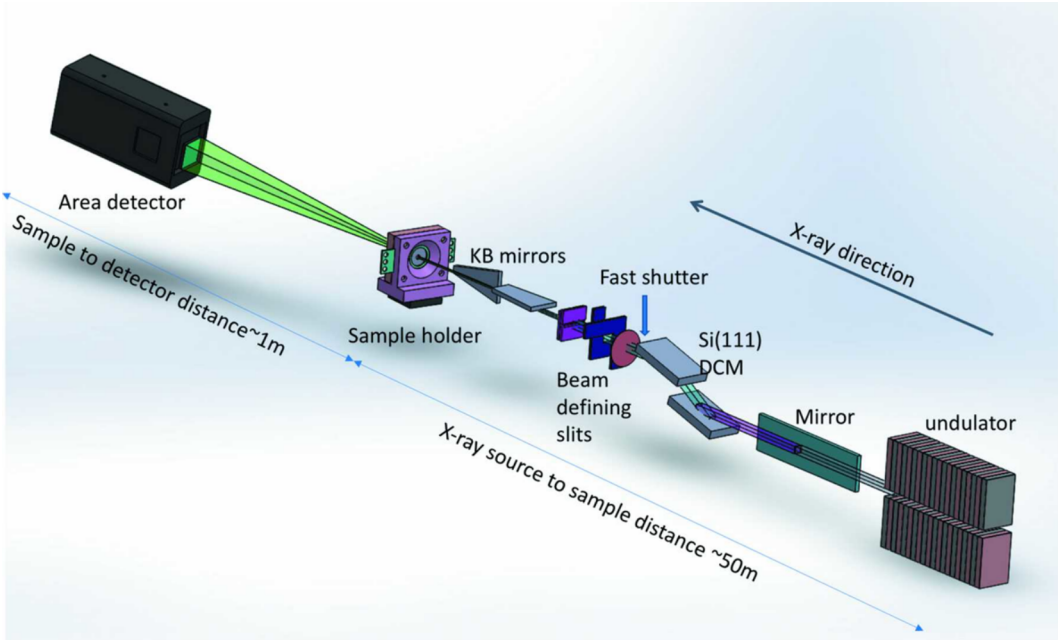

Figure 2.2: An outline of BCDI beamline 34-ID-C at the APS. The higher frequency X-rays from the undulator are filtered by a deflective mirror to produce a pink beam. The X-ray energy is then tuned by the Si(111) double crystal monochromator and collimated using beam defining slits. The beam is focused using KB mirrors onto the sample. A reflected X-ray beam is captured on a pixelated area detector for a specific Bragg reflection. Image obtained with permission from Li *et al.* [63].

512×512 pixel Timepix area detector (Amsterdam Scientific Instruments) with a GaAs sensor and pixel size, p, of $55\ \mu\text{m} \times 55$ is used for all experiments in this thesis. The detector is placed $\sim 1-2$ m away from the sample to ensure diffraction is observed in the far-field (Fraunhofer) regime for CDI.

2.2 X-ray interaction with matter

There are three outcomes when X-rays interact with matter, listed below.

1. The photoelectric effect can occur, where the X-ray knocks an electron from an orbital. If the electron was from an inner orbital, another electron from a higher orbital drops down to fill the void, emitting a characteristic X-ray or Auger electron.

2. The X-ray is inelastically scattered (e.g. Compton scattering). A photon is emitted with lower energy than the incident photon. The kinetic energy of the incident X-ray is not conserved.

3. The X-ray is elastically scattered. The X-ray excites an electron, which emits a photon with the same energy as the incident photon. The kinetic energy of the incident X-ray is conserved.

The elastically scattered scenario is relevant for BCDI. Only the electric interaction between the light and the electrons in the crystal is considered since the magnetic interaction is much smaller. The kinematical approximation, where the scattering occurs only once in the sample for each photon, is assumed. This holds well for samples with dimensions that are significantly smaller than the attenuation length, which for BCDI the sample dimensions are less than 1 μm. The incident X-ray wavefront is assumed to be planar, rather than spherical, as the sample is far away from the source and typically at the focal plane of an X-ray optic at the beamline. The detector is placed in the far-field Fraunhofer regime at a particular angle where the scattered wavefronts form a diffraction pattern.

2.2.1 Scattering from an electron

As X-rays interact with matter, they excite electrons that oscillate and behave as dipoles. The oscillation causes a change in acceleration of the electrons and causes the spherical emission of X-rays with the same energy as the incident wave, known as Thomson scattering. The electric and magnetic fields found in X-rays (Fig. 2.1) obey Maxwell's equations. Assuming that an X-ray travels through a vacuum in free space, Maxwell's equations simplify to: [65]

$$\begin{aligned} \nabla \times \mathbf{B} &= \varepsilon_0 \frac{\partial \mathbf{E}}{\partial t}, \\ \nabla \times \mathbf{E} &= -\mu_0 \frac{\partial \mathbf{B}}{\partial t}, \\ \nabla \cdot \mathbf{E} &= 0, \\ \nabla \cdot \mathbf{B} &= 0, \end{aligned} \tag{2.5}$$

where $\mathbf{E}$ and $\mathbf{B}$ are the electric and magnetic fields respectively, and ε_0 and μ_0 are

the electrical permittivity and magnetic permeability of free space respectively. Using elimination, one can find the partial differential relationships for **E** and **B** [65]:

$$\begin{aligned} \Delta \mathbf{E} &= \mu_0 \varepsilon_0 \frac{\partial^2 \mathbf{E}}{\partial t^2}, \\ \Delta \mathbf{B} &= \mu_0 \varepsilon_0 \frac{\partial^2 \mathbf{B}}{\partial t^2}, \end{aligned} \tag{2.6}$$

The simplest solution for the electric and magnetic field is a plane wave, which can be written in the following form [62] based on the X-ray shown in Fig. 2.1,

$$\begin{aligned} \mathbf{E}(z,t) &= E_0 e^{i(\omega t - kz)} \hat{y}, \\ \mathbf{B}(z,t) &= B_0 e^{i(\omega t - kz)} \hat{x}, \end{aligned} \tag{2.7}$$

where E_0 is the electric field magnitude, B_0 is the magnetic field magnitude, $k = 2\pi/\lambda$ is the wave number and $\omega = kc$ is the angular frequency.

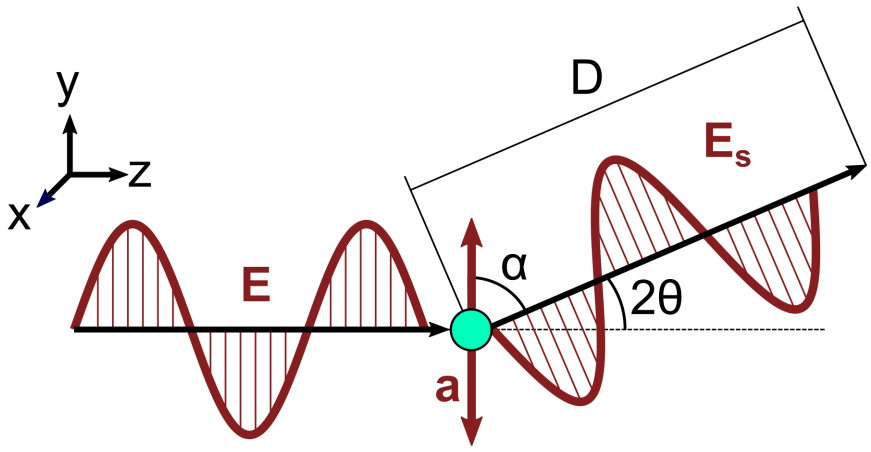

Figure 2.3: X-ray scattering from an electron. The electric field from the incident X-ray, **E** is radially scattered by an electron (green circle) at an angle α. Here, one of the scattered electric fields, $\mathbf{E_s}$, is shown. **a** is the acceleration of the electron in the same plane as the incident electric field. 2θ is the angle between the incident and scattered beams. D is the distance to the observer. The magnetic field perpendicular to both the electric field and the direction of propagation is not shown here for clarity.

As the electromagnetic plane waves interact with an electron, only the electric interaction is considered, as the magnetic interaction is small by comparison. If an electron is being scattered by the X-ray shown in Fig. 2.3, an acceleration, **a**, will be produced by an oscillating driving force, **F**, through Newton's second law [62],

$$\begin{aligned}\mathbf{a} &= \frac{F}{m_e} \\ &= \frac{e^{-}\mathbf{E}}{m_e} \\ &= \frac{e^{-}}{m_e} E_0 e^{i(\omega t - kz)} \hat{y},\end{aligned} \tag{2.8}$$

where e^{-} is the charge for one electron and m_e is the mass of an electron. For a given time, t, at a distance, D, from the electron, the scattered electric field E_s produced by an oscillating dipole in the far-field is [62]

$$E_s(D,t) = -\frac{e^{-}}{4\pi\varepsilon_0 c^2 D} |\mathbf{a}(t')| \sin(\alpha) \tag{2.9}$$

Note the factor of -1 refers to the 180° phase shift between the incident and scattered waves [62]. Here, t' is defined as a time before the observed time, t, because the scattered electric field amplitude requires travelling time before being observed, thus $t' = t - D/c$. The angle between the scattered electric field and the acceleration is α (Fig. 2.3) and is later used to determine the polarisation in Eq. 2.12, which affects the observed intensity. Evaluating $|\mathbf{a}(t')|\sin(\alpha)$ gives

$$\begin{aligned}|\mathbf{a}(t')|\sin(\alpha) &= \frac{e^{-}}{m_e} E(0,t')\sin(\alpha) \\ &= \frac{e^{-}}{m_e} E_0 e^{i[\omega(t-D/c)]} \sin(\alpha) \\ &= \frac{e^{-}}{m_e} E_0 e^{i(\omega t - kD)} \sin(\alpha),\end{aligned} \tag{2.10}$$

which can be substituted into Eq. 2.9,

$$\begin{aligned}E_s &= -\frac{(e^{-})^2}{4\pi\varepsilon_0 m_e c^2 D} E_0 e^{i(\omega t - kD)} \sin(\alpha) \\ &= -\frac{r_e}{D} E_0 e^{i(\omega t - kD)} \sin(\alpha),\end{aligned} \tag{2.11}$$

where r_e is the classical radius of the electron, $r_e = \frac{(e^{-})^2}{4\pi\varepsilon_0 m_e c^2}$ [62].

Here, the $\sin(\alpha)$ term determines the polarisation of the scattered X-ray. Since the intensity of the X-ray, I, is proportional to the squared modulus of the scattered electric

field for an electron, $|E_s|^2$, thus $I \propto \sin^2(\alpha)$. The expression $\sin^2(\alpha)$ is related to the types of polarisation by [65]:

$$\sin^2(\alpha) = \begin{cases} 1 & \sigma - \text{polarisation, } E_\sigma \\ \cos^2(2\theta) & \pi - \text{polarisation, } E_\pi \end{cases}, \tag{2.12}$$

The intensity of the X-ray is reduced by $\cos^2(2\theta)$ (π-polarisation) except when the direction of polarisation is perpendicular to the scattering plane (σ-polarisation).

2.2.2 Scattering from an atom

Next, consider the scattering from a group of electrons around an atom. In the simplest representation, atoms can be thought of as consisting of a nucleus and an electron cloud. The electron cloud is represented by the continuous electron density, $\rho(\mathbf{r})$, which describes the probability of finding an electron at a position vector $\mathbf{r}$. Accordingly, the total electronic charge, Z, for an atom is given by,

$$\int \rho(\mathbf{r}) d\mathbf{r} = Z. \tag{2.13}$$

As an incident X-ray wavevector $\mathbf{S}_0$ with modulus $|\mathbf{S}_0| = 2\pi/\lambda$ is elastically scattered by an atom, there is a phase difference when it interacts with a volume element at the centre compared to a volume element at position $\mathbf{r}$ (Fig. 2.4). The difference is the projection of $\mathbf{r}$ onto $\mathbf{S}_0$, i.e. the dot product $\mathbf{S}_0 \cdot \mathbf{r}$. Similarly, the outgoing wavevector $\mathbf{S}$ with modulus $|\mathbf{S}| = 2\pi/\lambda$ has a phase difference given by $\mathbf{S} \cdot \mathbf{r}$. The difference in phase, $\Delta\psi$, given by

$$\Delta\psi = \mathbf{S} \cdot \mathbf{r} - \mathbf{S}_0 \cdot \mathbf{r} = (\mathbf{S} - \mathbf{S}_0) \cdot \mathbf{r} = \mathbf{Q} \cdot \mathbf{r}, \tag{2.14}$$

where $\mathbf{Q}$ is the scattering vector that describes the change in direction of the incident wavevector,

$$\mathbf{Q} = \mathbf{S} - \mathbf{S}_0. \tag{2.15}$$

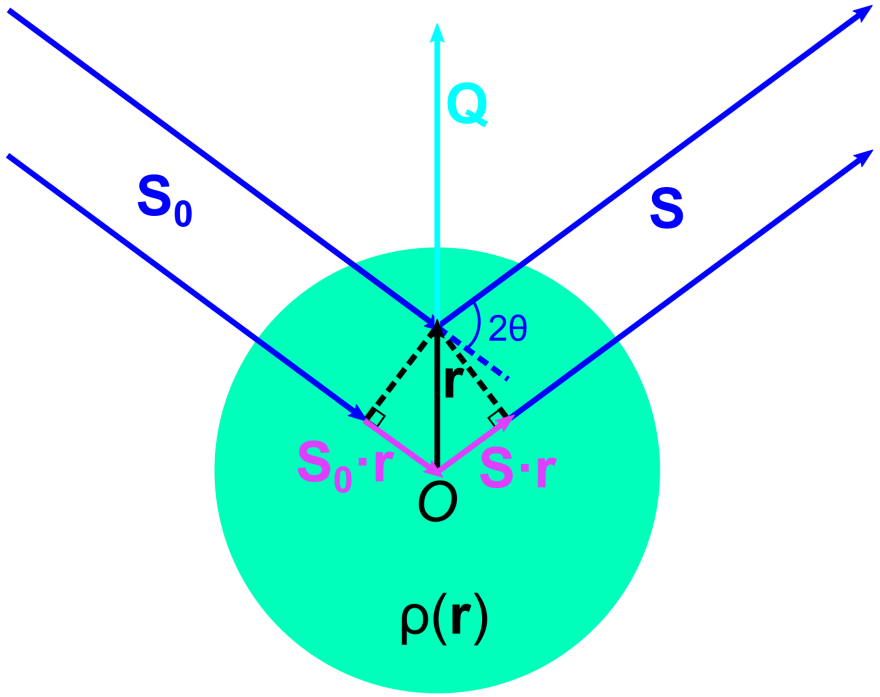

Figure 2.4: The X-ray scattering associated with an atom. Electron cloud, $\rho(\mathbf{r})$, is represented by a green circle. The blue arrows represent the X-ray beam. $\mathbf{S_0}$ describes the incident X-ray beam and $\mathbf{S}$ describes the outgoing X-ray beam. $\mathbf{Q} = \mathbf{S} - \mathbf{S_0}$ is the scattering vector shown in cyan. The wavelength difference between the origin, O and position $\mathbf{r}$, is shown in purple.

Every position can contribute to X-ray scattering, where the amplitude scattered at a specific position is $\rho(\mathbf{r})d\mathbf{r}$ weighted by the phase factor, $e^{i\mathbf{Q}\cdot\mathbf{r}}$. According to the Huygens principle, only the sum of the superimposed waves emitted from electrons can be measured [66], thus the scattering amplitude from the entire atom is obtained from,

$$f(\mathbf{Q}) = \int \rho(\mathbf{r}) e^{i\mathbf{Q}\cdot\mathbf{r}} d\mathbf{r} = \begin{cases} \mathbf{Q} \to 0 & f \to Z \\ \mathbf{Q} \to \infty & f \to 0 \end{cases}, \tag{2.16}$$

where $f(\mathbf{Q})$ is the atomic form factor. If $\mathbf{Q} \to 0$ then the phase factor $e^{i\mathbf{Q}\cdot\mathbf{r}} \to 1$ and Eq. 2.16 becomes Eq. 2.13 as all the electrons in the atom scatter. As $\mathbf{Q} \to \infty$, the phase factor becomes oscillating. This causes destructive interference and Eq. 2.16 becomes 0. Note that the distribution of the electron density in the sample is connected to its scattering

amplitude through a Fourier transform,

$$\mathscr{F}[f(\mathbf{r})] = F(\mathbf{Q}) = \int f(\mathbf{r}) e^{i\mathbf{Q}\cdot\mathbf{r}} d\mathbf{r}, \tag{2.17}$$

in this thesis. The resulting scattering amplitude, $A(\mathbf{Q})$, is the form factor (Eq. 2.16) multiplied by the scattering from one electron, E_s (Eq. 2.11) [62],

$$A(\mathbf{Q}) = E_s \int \rho(\mathbf{r}) e^{i\mathbf{Q}\cdot\mathbf{r}} d\mathbf{r}. \tag{2.18}$$

2.2.3 Scattering from crystals

Crystalline materials are highly ordered structures that are created by repeating a group of atoms called a unit cell. Crystals can be defined by a lattice, an ordered arrangement of identical points, where at each point exists a motif, which can be an atom or molecule. In 3D, there are 14 unique lattices known as Bravais lattices that can be repeated to fill an infinite space without any overlaps or voids. A particular lattice, ρ_{L}, can be described as an array of Dirac delta functions, $\delta(\mathbf{r})$, whose value is zero except at zero, where the value is one [62],

$$\rho_{\mathrm{L}}(\mathbf{r}) = \sum_p \delta(\mathbf{r} - \mathbf{R}_p), \tag{2.19}$$

where $\mathbf{r}$ is the position vector and $\mathbf{R}_p$ is the lattice vector describing the location of each point in 3D and also the set of discrete translations applicable for the unit cell. $\mathbf{R}_p$ is defined as [62],

$$\mathbf{R}_p = u\mathbf{a} + v\mathbf{b} + w\mathbf{c}, \tag{2.20}$$

where u, v, w, are integers and $\mathbf{a}$, $\mathbf{b}$, $\mathbf{c}$ are real space basis vectors. These basis vectors form the unit cell (Fig. 2.5), which is also described by angles α (the angle between the b and c axes), β (the angle between the c and a axes), and γ (the angle between the a and

b axes). In this thesis, only face-centred cubic (fcc) materials are studied, thus **a**, **b**, and **c** form an orthonormal basis. For every k^{th} atom in the unit cell, the electron density can be described as [62]

$$\rho_{\text{unit cell}}(\mathbf{r}) = \sum_k \rho_k(\mathbf{r} - \mathbf{r}_k). \tag{2.21}$$

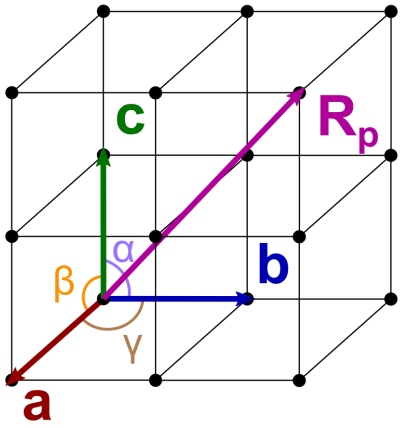

Figure 2.5: Illustration of a cubic crystal lattice structure. Here the motif is represented by the black points. The unit cell is defined by real space orthonormal basis vectors **a**, **b** and **c**. Angles α (the angle between the b and c axes), β (the angle between the c and a axes), and γ (the angle between the a and b axes) here are 90°. $\mathbf{R}_p$ is an example of a reciprocal lattice point shown as a vector from the origin (Eq. 2.20).

Now that a unit cell and lattice are defined, the electron density of an infinite crystal, $\rho_{\text{crystal}}(\mathbf{r})$ is the convolution, denoted by $\circledast$, of the electron density of the $\rho_{\text{unit cell}}(\mathbf{r})$ with a lattice [62],

$$\rho_{\text{crystal}}(\mathbf{r}) = \rho_{\text{unit cell}}(\mathbf{r}) \circledast \rho_{\text{L}}(\mathbf{r}). \tag{2.22}$$

Next, lattice planes are described, which periodically intersect the crystal lattice. They are described by integer Miller indices hkl, where each Miller index describes reciprocal intercepts a/h, b/k, and c/l along the **a**, **b**, **c** axes respectively. Conveniently, the (hkl) normal vector is $[hkl]$ for cubic systems, and for each plane, there exists a set of planes that are equivalent by lattice symmetry. This set of planes is described using the notation $\{hkl\}$. For a cubic system, the inter-planar spacing is given by,

$$d_{hkl} = \frac{a_0}{\sqrt{h^2 + k^2 + l^2}}, \tag{2.23}$$

where a_0 is the lattice parameter.

Miller indices are particularly convenient in lattice reciprocal space. Lattice reciprocal space can be obtained by the Fourier transform of any real space lattice. For every real space lattice, there is a reciprocal lattice given by,

$$\rho_{\mathrm{RL}}(\mathbf{Q}) = \frac{(2\pi)^3}{V_{\text{unit cell}}} \sum_{hkl} \delta(\mathbf{Q} - \mathbf{H}_{hkl}), \tag{2.24}$$

where $V_{\text{unit cell}}$ is the volume of the unit cell, and $\mathbf{H}_{hkl}$ is the reciprocal lattice vector,

$$\mathbf{H}_{hkl} = h\mathbf{a}^* + k\mathbf{b}^* + l\mathbf{c}^*, \tag{2.25}$$

where $|\mathbf{H}_{hkl}| = \frac{2\pi}{d_{hkl}}$. The reciprocal lattice basis vectors, $\mathbf{a}^*$, $\mathbf{b}^*$, and $\mathbf{c}^*$ are related to the real space basis vectors by:

$$\mathbf{a}^* = 2\pi \frac{\mathbf{b} \times \mathbf{c}}{\mathbf{a} \cdot (\mathbf{b} \times \mathbf{c})}, \qquad \mathbf{b}^* = 2\pi \frac{\mathbf{c} \times \mathbf{a}}{\mathbf{b} \cdot (\mathbf{c} \times \mathbf{a})} \qquad \text{and} \qquad \mathbf{c}^* = 2\pi \frac{\mathbf{a} \times \mathbf{b}}{\mathbf{c} \cdot (\mathbf{a} \times \mathbf{b})}. \tag{2.26}$$

Now that the crystal lattice in real and reciprocal space is defined, the conditions necessary for constructive interference that lead to diffraction patterns can be discussed.

2.2.3.1 Bragg's Law

X-ray wavelengths are comparable to interatomic spacing, allowing diffraction to occur. This was first discovered by Max von Laue [67] who used copper sulphate crystals as a diffraction grating for X-rays. The continuing work of William Henry Bragg and William Lawrence Bragg [68, 69] has led to the development of crystallography. Most notably, Bragg described the geometric conditions required for the constructive inference of elastically scattered X-rays (Fig. 2.6).

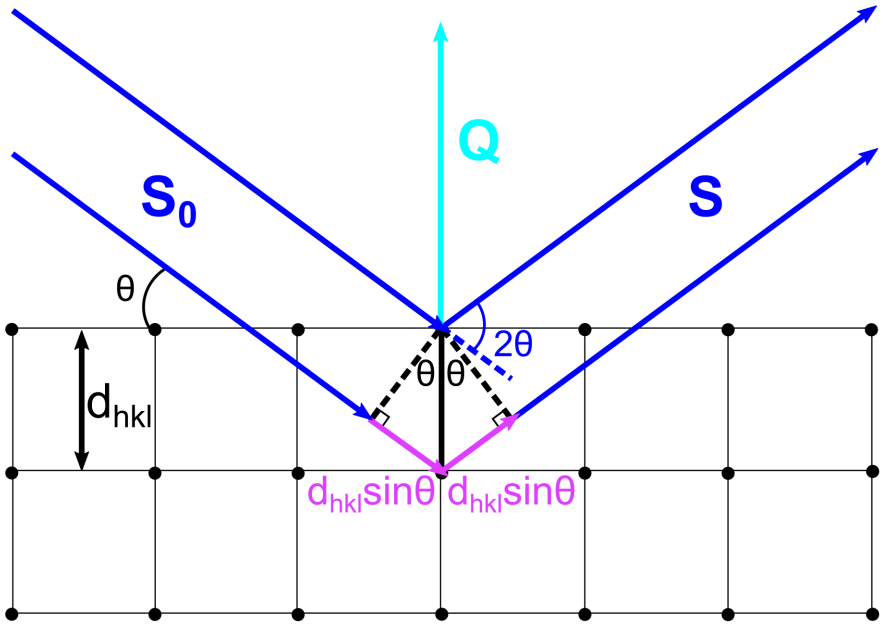

Figure 2.6: The geometry associated with Bragg's law. Here the blue arrows represent the X-ray beam. $\mathbf{S_0}$ describes the incident X-ray beam and $\mathbf{S}$ describes the outgoing X-ray beam. $\mathbf{Q} = \mathbf{S} - \mathbf{S_0}$ is the scattering vector shown in cyan. θ is the incident angle to the crystallographic plane. 2θ is the angle between the incident and reflected beams. The path length difference is shown in purple.

Similar to Fig. 2.4 and Eq. 2.14, Bragg's law highlights that there is a phase difference as X-rays reflect off a crystal plane. For the constructive interference of scattered X-rays, the phase difference between the scattered waves from each plane within the crystal should be an integer multiple of the wavelength of the incident x-ray beam. This relationship is known as Bragg's law,

$$2d_{hkl}\sin(\theta) = n\lambda, \tag{2.27}$$

where d_{hkl} is the interplanar spacing (Eq. 2.23) and n is an integer. This powerful relationship allows one to determine the orientation of the crystal to observe diffraction, which is the foundation for BCDI.

2.2.3.2 An infinite crystal

The scattering amplitude from an infinite crystal comes from the superposition of the scattered amplitudes from each individual atom. Here, each atom, p, occupies a lattice

site at position $\mathbf{R}_p$, and from $\mathbf{R}_p$ there is a position vector, $\mathbf{r}_p$, which describes a point in the electron density of the atom whose centre is at $\mathbf{R}_p$. Similar to the phase shifts within the electron density of a single atom, here there are phase shifts with respect to each lattice position, given by $e^{i\mathbf{Q}\cdot\mathbf{R}_p}$. The scattering amplitude of the crystal is given by the summation of the scattering amplitudes of all atoms in the crystal weighted by their phase shift [62],

$$\begin{aligned} A(\mathbf{Q}) &= \sum_p A_i(\mathbf{Q}) e^{i\mathbf{Q}\cdot\mathbf{R}_p} \\ &= E_s \sum_p f_i(\mathbf{Q}) e^{i\mathbf{Q}\cdot\mathbf{R}_p}, \end{aligned} \tag{2.28}$$

where $A_i(\mathbf{Q})$ is the scattering amplitude for one atom in the crystal, E_s is the scattered electric field for one electron (Eq. 2.11), and $f_i(\mathbf{Q})$ is the atomic form factor for one atom (Eq. 2.16). Since crystals are atoms arranged inside repeating unit cells, the scattering amplitude for the crystal can also be described by the scattering amplitude for each unit cell multiplied by the lattice. To formulate this mathematically, $\mathbf{R}_p$ can be decomposed as $\mathbf{R}_p = \mathbf{R}_j + \mathbf{r}_k$, where $\mathbf{R}_j$ corresponds to a lattice point and $\mathbf{r}_k$ is a local point for an atom in the unit cell at $\mathbf{R}_j$. Eq. 2.28 then becomes [62]

$$\begin{aligned} A(\mathbf{Q}) &= E_s \sum_p f_i(\mathbf{Q}) e^{i\mathbf{Q}\cdot\mathbf{R}_p} \\ &= E_s \sum_j \sum_k f_i(\mathbf{Q}) e^{i\mathbf{Q}\cdot(\mathbf{R}_j+\mathbf{r}_k)} \\ &= E_s \underbrace{\sum_k f_i(\mathbf{Q}) e^{i\mathbf{Q}\cdot\mathbf{r}_k}}_{\text{unit cell structure factor}} \underbrace{\sum_j e^{i\mathbf{Q}\cdot\mathbf{R}_j}}_{\text{lattice}}, \end{aligned} \tag{2.29}$$

where it is simply the lattice summation is multiplied by $F(\mathbf{Q})$ the unit cell structure factor [62],

$$F(\mathbf{Q}) = \sum_k f_i(\mathbf{Q}) e^{i\mathbf{Q}\cdot\mathbf{r}_k}, \tag{2.30}$$

and $f_i(\mathbf{Q})$ is the atomic form factor for atom i defined previously (Eq. 2.16). Here,

based on Eq. 2.28, note that the scattering amplitude of the crystal is the Fourier transform of its electron density,

$$A(\mathbf{Q}) = E_s \int \rho_{\text{crystal}}(\mathbf{r}) e^{i\mathbf{Q}\cdot\mathbf{r}} d\mathbf{r} \tag{2.31}$$

This is because a crystal structure is a convolution of a lattice function (Eq. 2.19) and a unit cell (Eq. 2.21) and the convolution of two functions, $f(\mathbf{r})$ and $g(\mathbf{r})$, has the property

$$\begin{aligned} \mathscr{F}\left[f(\mathbf{r}) \circledast g(\mathbf{r})\right] &= \mathscr{F}\left[f(\mathbf{r})\right]\mathscr{F}\left[g(\mathbf{r})\right] \\ \mathscr{F}\left[f(\mathbf{r})g(\mathbf{r})\right] &= \mathscr{F}\left[f(\mathbf{r})\right] \circledast \mathscr{F}\left[g(\mathbf{r})\right]. \end{aligned} \tag{2.32}$$

2.2.3.3 A finite crystal

Crystals studied using CDI have finite size, which must be factored into the scattering amplitude. A finite crystal can be defined by a binary shape function, $s(\mathbf{r})$ [70],

$$s(\mathbf{r}) = \begin{cases} 1 & \text{if } \mathbf{r} \in V_{\text{crystal}} \\ 0 & \text{if } \mathbf{r} \notin V_{\text{crystal}} \end{cases}, \tag{2.33}$$

where V_{crystal} is the volume of the crystal. The shape function is factored into the electron density of an infinite crystal, previously defined in Eq. 2.22, to give [70]

$$\rho_{\text{crystal}}(\mathbf{r}) = \rho_{\text{unit cell}}(\mathbf{r}) \circledast [\rho_{\text{L}}(\mathbf{r}) \cdot s(\mathbf{r})]. \tag{2.34}$$

Combining this with the previous note that the scattering amplitude of the crystal is the Fourier transform of its structure, the scattering amplitude for a finite crystal can be determined by the convolution theorem (Eq 2.32) [70],

$$A(\mathbf{Q}) = E_s F(\mathbf{Q}) \cdot [\rho_{\text{RL}}(\mathbf{Q}) \circledast S(\mathbf{Q})], \tag{2.35}$$

where $F(\mathbf{Q})$ is the unit cell structure factor defined in Eq. 2.30, ρ_{RL} is the reciprocal lattice defined in Eq. 2.24, and $S(\mathbf{Q})$ is the Fourier transform of the crystal shape function,

$S(\mathbf{Q}) = \int s(\mathbf{r}) e^{i\mathbf{Q}\cdot\mathbf{r}} d\mathbf{r}$. Substituting these two equations into Eq. 2.35 yields [62]

$$A(\mathbf{Q}) = E_s \underbrace{\sum_k f_i(\mathbf{Q}) e^{i\mathbf{Q}\cdot\mathbf{r}_k}}_{\text{unit cell}} \cdot \left[\underbrace{\frac{(2\pi)^3}{V_{\text{unit cell}}} \sum_{hkl} \delta(\mathbf{Q} - \mathbf{H}_{hkl})}_{\text{reciprocal lattice}} \circledast S(\mathbf{Q}) \right]. \tag{2.36}$$

In Eq. 2.36 the scattering condition is satisfied when

$$\mathbf{Q} = \mathbf{H}_{hkl}, \tag{2.37}$$

known as the Laue condition. This indicates that the scattering intensity is located only at discrete points of the reciprocal lattice, which also satisfies the geometric requirements in real space to obtain constructive interference. In CDI, the measurable quantity is the intensity, I, recorded on the detector. The intensity is related to the amplitude by

$$\begin{aligned} I(\mathbf{Q}) &= A(\mathbf{Q}) A^*(\mathbf{Q}) \\ &= |A(\mathbf{Q})|^2 \\ &= E_s^2 \frac{|F(\mathbf{Q})|^2}{V_{\text{unit cell}}^2} \sum_{hkl} |S(\mathbf{Q} - \mathbf{H}_{hkl})|^2, \end{aligned} \tag{2.38}$$

where * denotes complex conjugation. This intensity is known as a Bragg peak, which contains the X-ray scattering from all illuminated unit cells in the finite crystal. Eq. 2.38 also shows that each Bragg peak contains the Fourier transform of the crystal shape. The unit cell structure factor is weakly dependent on $\mathbf{Q}$ and is thus considered a constant at the Bragg condition. For a perfect crystal, since the intensity depends only on the Fourier transform of the non-complex shape, the pattern will be locally symmetric about each Bragg point, since the Fourier transform of a real object is centrosymmetric. In the next section, the intensity change in the presence of lattice displacements will be discussed.

2.2.3.4 A strained crystal

Atoms can be perturbed from their ideal lattice positions resulting in crystal defects. These defects deform the lattice, creating a lattice displacement field, $\mathbf{u}(\mathbf{r})$. Atoms displaced from their perfect lattice positions will experience a displacement, $\mathbf{u}(\mathbf{R}_p)$. The electron density of the crystal in the presence of a displacement field is,

$$\rho_{\text{strained crystal}}(\mathbf{r}) = \sum_{j}^{J}\sum_{k}^{K}\rho_{jk}(\mathbf{r}-\mathbf{R}_{jk}-\mathbf{u}(\mathbf{R}_{jk})), \tag{2.39}$$

Where J is the number of unit cells and K is the number of atoms in the unit cell. It is assumed that all atoms are displaced uniformly such that $\mathbf{u}(\mathbf{R}_p) = \mathbf{u}(\mathbf{R}_j)$ [70], in other words, a strained, infinite crystal can be modelled as unit cells being displaced from the rest of the material (Fig 2.7).

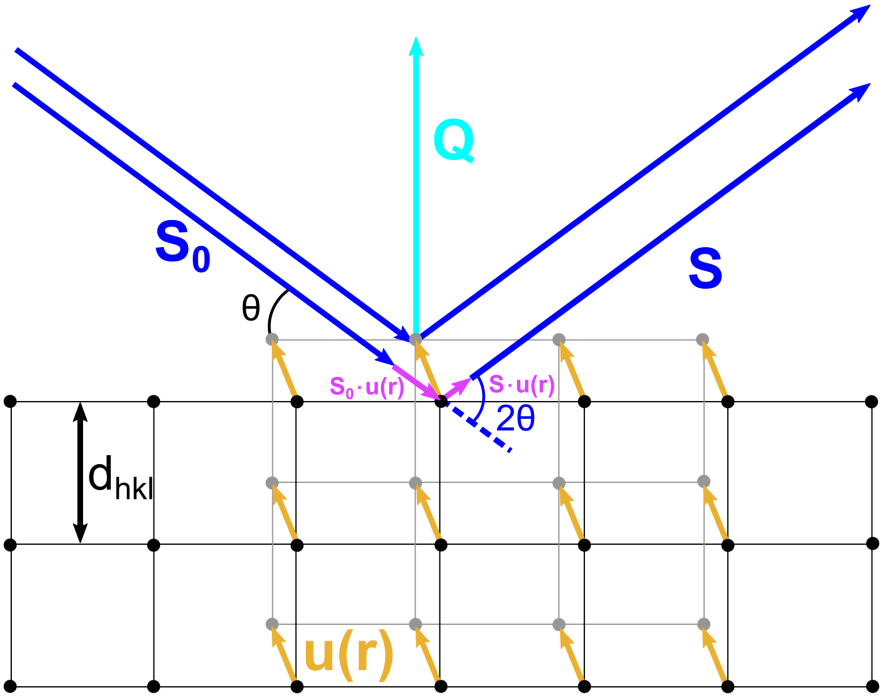

Figure 2.7: The phase shift associated with a lattice displacement field. The black circles represent the ideal lattice positions, while the grey circles represent displaced lattice positions according to $\mathbf{u}(\mathbf{r})$. Here the blue arrows represent the X-ray beam. $\mathbf{S_0}$ describes the incident X-ray beam and $\mathbf{S}$ describes the outgoing X-ray beam. $\mathbf{Q} = \mathbf{S} - \mathbf{S_0}$ is the scattering vector shown in cyan. The path length difference is shown in pink, and is represented by a projection of the X-ray wavefront on the displacement field in orange. The phase difference is $\psi_{hkl}(\mathbf{r}) = \mathbf{S}\cdot\mathbf{u}(\mathbf{r}) - \mathbf{S}_0\cdot\mathbf{u}(\mathbf{r}) = \mathbf{Q}\cdot\mathbf{u}(\mathbf{r})$.

The scattered amplitude in a disordered crystal can be derived by substituting Eq. 2.39

into Eq. 2.31 [70]:

$$A(\mathbf{Q}) = E_s \sum_j^J F_j(\mathbf{Q}) e^{i\mathbf{Q}\cdot\mathbf{u}(\mathbf{R}_j)} e^{i\mathbf{Q}\cdot\mathbf{R}_j} \tag{2.40}$$

where $F_j(\mathbf{Q})$ is the structure factor for a particular unit cell. Similar to the arguments presented in chapters 2.2.2 and 2.2.3.3 the phase shift caused by the displacement field is accounted for by an exponential term, $e^{i\mathbf{Q}\cdot\mathbf{u}(\mathbf{R}_j)}$, hence why it is included in Eq. 2.40 and not for an unstrained crystal in Eq. 2.31. Factoring in the shape of a finite crystal, $s(\mathbf{r})$ (Eq. 2.33) into Eq. 2.40,

$$A(\mathbf{Q}) = E_s F(\mathbf{Q}) \int \rho_L(\mathbf{r}) s(\mathbf{r}) e^{i\mathbf{Q}\cdot\mathbf{u}(\mathbf{r})} e^{i\mathbf{Q}\cdot\mathbf{r}} d\mathbf{r}, \tag{2.41}$$

and assume that the structure factor for the different cells is the same, $F_j(\mathbf{Q}) = F(\mathbf{Q})$. Here note that the shape function is now complex as it contains the information about the displacement field. The complex shape function, $S_{\text{strained crystal}}(\mathbf{r})$, is defined as [70]

$$S_{\text{strained crystal}}(\mathbf{r}) = s(\mathbf{r}) e^{i\mathbf{Q}\cdot\mathbf{u}(\mathbf{r})}, \tag{2.42}$$

and the Fourier transform, $S_{\text{strained crystal}}(\mathbf{Q}) = \int s(\mathbf{r}) e^{i\mathbf{Q}\cdot\mathbf{u}(\mathbf{r})} e^{i\mathbf{Q}\cdot\mathbf{r}} d\mathbf{r}$. For a strained crystal, the intensity is very similar to that of an unstrained finite crystal (Eq. 2.38) and is given by,

$$\begin{aligned} I(\mathbf{Q}) &= A(\mathbf{Q}) A^*(\mathbf{Q}) \\ &= |A(\mathbf{Q})|^2 \\ &= E_s^2 \frac{|F(\mathbf{Q})|^2}{V_{\text{unit cell}}^2} \sum_{hkl} |S_{\text{strained crystal}}(\mathbf{Q} - \mathbf{H}_{hkl})|^2. \end{aligned} \tag{2.43}$$

For strained crystals, the complex phase factor encoded in the complex shape function (Eq. 2.42) breaks the Bragg peak symmetry. This excludes the 0th order forward scattering Bragg peak where $\mathbf{Q} = 0$ because it only contains the shape information. Fig. 2.7 highlights that the phase for a particular reflection is related to the scattering vector and

displacement field by

$$\psi_{hkl}(\mathbf{r}) = \mathbf{Q}_{hkl} \cdot \mathbf{u}(\mathbf{r}). \tag{2.44}$$

From this equation, a phase shift of 2π corresponds to a displacement of d_{hkl} from the ideal lattice position. The dependence of the phase on specific reflections means that each Bragg peak will be unique. Furthermore, there will no longer be centrosymmetry for Bragg peaks from strained crystals. Here note that the phase information that describes a projection of the displacement field onto the scattering vector is lost in the intensity measurement (Eq. 2.43), but it can be recovered if the Bragg peak is sampled properly, as discussed later in Chapter 2.4.1. Phase retrieval algorithms can be used to recover the phase, which are discussed in Chapter 2.4.

2.3 Bragg coherent X-ray diffraction imaging measurement

For BCDI, one must collect a 3D coherent X-ray diffraction pattern (CXDP) for an illuminated crystal at a particular Bragg condition. Here I discuss the necessary requirements in the laboratory pertaining to the coherence of the X-ray source as well as the measurement geometry to collect a CXDP for a specific *hkl* reflection. The CXDP is the intensity of the scattered wavefield (Eq. 2.43) and contains the complex electron density of the crystal, which will be recovered later in Chapter 2.4.

2.3.1 Coherence

The previous derivations assume perfect coherence, where the X-rays have a single wavelength and are perfectly in-phase. Coherence is a measure of the spatial and temporal correlation of points on a wavefield, and having high coherence is critical for constructive interference to produce sharp diffraction patterns. Here, a wavefield will be characterised by

its spatial (transverse) coherence length and a temporal (longitudinal) coherence length.

2.3.1.1 Spatial coherence

The transverse coherence length, ξ_t, considers the beam's cross-sectional coherence. Fig. 2.8 shows two X-rays with the same wavelength coming from a source with a width of w_t. They travel in slightly different angular directions ($\Delta\theta$) and will coincide at some distance, L, away from the source. The transverse coherence length is where the two waves (solid and dashed red lines) are phase-shifted by half a cycle at distance L [62]. From Fig. 2.8, ξ_t can be derived by equating two expressions for $\tan(\Delta\theta)$,

$$\begin{aligned} \frac{\lambda}{2\xi_t} &= \frac{w_t}{L}, \\ \xi_t &= \frac{\lambda L}{2w_t}, \end{aligned} \tag{2.45}$$

where subscript t can be horizontal, h, or vertical, v. In the context of synchrotron radiation, the transverse coherence length is defined by the distance from the source and the collimation of the beam using beamline optics. For a third generation synchrotron, $\xi_h \approx 50\ \mu$m and $\xi_w \approx 10\ \mu$m [71].

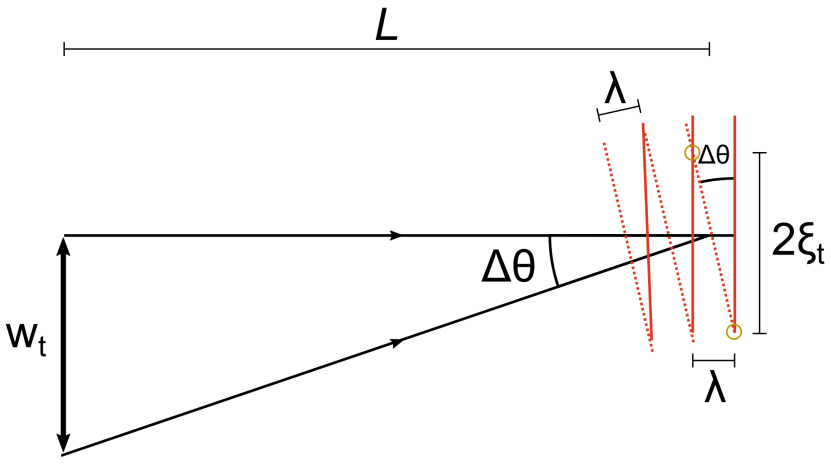

Figure 2.8: A spatial or transverse coherence length, ξ_t, is defined as the length by which two waves (solid and dashed red lines) are phase-shifted by half a cycle at distance L. The path difference is designated by $\Delta\theta$. The yellow circles highlight points where the two waves are shifted by a cycle and are used to determine the length $2\xi_t$. Both waves originate from the same source, have the same wavelength, λ, but propagate in different directions.

2.3.1.2 Temporal coherence

The temporal coherence length, ξ_l, pertains to the beam's propagation in the longitudinal direction. Due to any difference in wavelength, $\Delta\lambda$, X-rays that are initially in-phase become out-of-phase when they travel a distance of N wavelengths. The temporal coherence length measures the distance for two wavefronts (with wavelengths λ and $\lambda - \Delta\lambda$) to be phase-shifted by half a cycle [62]. From Fig. 2.9, ξ_l can be derived by first equating the distance travelled by each wave [62],

$$\begin{aligned} N\lambda &= (N+1)(\lambda - \Delta\lambda), \\ N+1 &= \frac{\lambda}{\Delta\lambda}. \end{aligned} \tag{2.46}$$

This result implies that $N \approx \frac{\lambda}{\Delta\lambda}$. Now from Fig. 2.9 we can see that

$$\begin{aligned} 2\xi_l &= N\lambda, \\ \xi_l &\approx \frac{\lambda^2}{2\Delta\lambda}. \end{aligned} \tag{2.47}$$

The temporal coherence is therefore defined by the bandwidth of the X-ray beam, which is determined by the monochromator ($\approx 10^{-4}$ for a Si(111) double crystal monochromator). At beamline 34-ID-C at the APS, $\xi_l = 0.66 \pm 0.02\mu$m [71], which is the main limiting coherence volume dimension for BCDI samples.

2.3.1.3 Partial coherence

Synchrotron X-ray sources are partially coherent [72, 73], meaning that only a small coherence volume can be used for BCDI. Ideally, the X-ray will be focused to maximise flux on the sample. The sample should fit inside the coherence volume of the beam, $V_{\text{coh}} = \xi_h \xi_v \xi_l$, and the optical path length difference (OPLD) must be smaller than the shortest coherence length, which is in the longitudinal direction, otherwise, the visibility of fringes will be affected [71]. The OPLD corresponds to the distance travelled by the X-ray in the crystal before exiting, which depends on the crystal size, incident angle, and

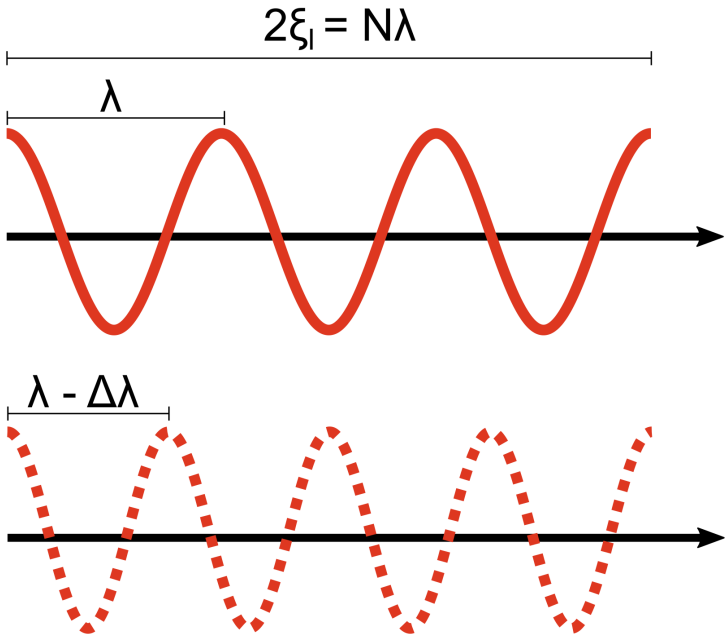

Figure 2.9: A temporal or longitudinal coherence length, ξ_l, is defined as the length by which two waves (solid and dashed red lines) are phase-shifted by half a cycle. Both waves originate from the same source and propagate in the same direction, but have different wavelengths, λ and $\lambda - \Delta\lambda$.

exit angle, making it reflection-dependent. If the OPLD exceeds the temporal coherence length, partial coherence effects will become important. Some degree of partial coherence can be tolerated using partial coherence correction during phase retrieval (Chapter 2.4.9.2).

Partial coherence results in a blurring of diffraction pattern fringes. If these effects are ignored within a phase retrieval algorithm, resulting reconstructions could contain artefacts, non-unique solutions or fail to reach convergence [71, 74]. The intensity scattered from a partially coherent X-ray beam can be written as [75]

$$I(\mathbf{Q}) = \iint J(\mathbf{r}_1,\mathbf{r}_2)\gamma_{\|}(\mathbf{r}_2-\mathbf{r}_1)\rho(\mathbf{r}_1)\rho(\mathbf{r}_2)e^{i\mathbf{Q}\cdot(\mathbf{r}_1-\mathbf{r}_2)}d\mathbf{r}_1 d\mathbf{r}_2, \tag{2.48}$$

where $\mathbf{r}$ is a point on the wave function, $\gamma_{\|}$ characterises the temporal coherence properties, and $J(\mathbf{r}_1,\mathbf{r}_2)$ is the mutual optical intensity (MOI), described by the Schell model [76],

$$J(\mathbf{r}_1,\mathbf{r}_2) = A(\mathbf{r}_1)A^*(\mathbf{r}_2)\gamma_{\perp}(\mathbf{r}_2-\mathbf{r}_1), \tag{2.49}$$

where A is a complex illuminating wavefield and $\gamma_\perp$ characterises the spatial coherence properties. Note that the coherence properties can simplify to one term known as the normalised MCF, $\gamma = \gamma_\perp \gamma_\parallel$. The recorded partially coherent intensity, $I_{\mathrm{pc}}(\mathbf{Q})$, is the coherent intensity, $I_{\mathrm{c}}(\mathbf{Q})$, convolved with the Fourier transform of the normalised MCF, $\hat{\gamma}(\mathbf{Q})$ [75, 77],

$$I_{\mathrm{pc}}(\mathbf{Q}) = I_{\mathrm{c}}(\mathbf{Q}) \circledast \hat{\gamma}(\mathbf{Q}). \tag{2.50}$$

The normalised MCF describes the change in coherence for an initially coherent wavefield as it propagates. Given any two points on the wavefield, $\mathbf{r}_1$ and $\mathbf{r}_2$, separated by a time offset of τ, the MCF can be interpreted as the time-averaged cross-correlation of the two points for a measurement time, T. The MCF, $\Gamma(\mathbf{r}_1, \mathbf{r}_2, \tau)$, is represented by [78]

$$\begin{aligned} \Gamma(\mathbf{r}_1, \mathbf{r}_2, \tau) &= \langle A(\mathbf{r}_1, t) A^*(\mathbf{r}_2, t+\tau) \rangle_T \\ &= \lim_{T\to\infty} \frac{1}{2T} \int_{-T}^{T} A(\mathbf{r}_1, t) A^*(\mathbf{r}_2, t+\tau) dt \end{aligned} \tag{2.51}$$

Note that the MCF is assumed to be ergodic since X-rays are created stochastically by atomic scattering or the acceleration of electrons. The MCF also assumes that T is much longer than the time of oscillation for an X-ray. Therefore, the time average is equal to the ensemble average.

In Eq. 2.51, if $\mathbf{r} = \mathbf{r}_1 = \mathbf{r}_2$ and $\tau = 0$ then the averaged intensity of the wavefield over the measurement time at $\mathbf{r}$ is [79],

$$\Gamma(\mathbf{r}, \mathbf{r}, 0) = \langle A(\mathbf{r}, t) A^*(\mathbf{r}, t) \rangle = \langle I(\mathbf{r}, t) \rangle \tag{2.52}$$

This equation makes it convenient to normalise the MCF,

$$\begin{aligned} \gamma(\mathbf{r}, \mathbf{r}, \tau) &= \frac{\Gamma(\mathbf{r}_1, \mathbf{r}_2, \tau)}{\sqrt{\Gamma(\mathbf{r}_1, \mathbf{r}_1, 0)\Gamma(\mathbf{r}_2, \mathbf{r}_2, 0)}} \\ &= \frac{\Gamma(\mathbf{r}_1, \mathbf{r}_2, \tau)}{\sqrt{\langle I(\mathbf{r}_1, t) \rangle \langle I(\mathbf{r}_2, t) \rangle}}, \end{aligned} \tag{2.53}$$

which is equal to 0 for a completely incoherent wavefield and equal to 1 for a fully coherent wavefield. A normalised MCF between 0 and 1 describes a partially coherent wavefield.

2.3.2 Measurement Geometry

For BCDI, a monochromatic X-ray illuminates a sample placed in a diffractometer. The geometry of the sample position and the diffractometer must satisfy Bragg's law (Eq. 2.27 and Fig. 2.6). The sample is positioned using stage motors to record a scattered X-ray reflection on a detector positioned in the far field and satisfies the oversampling condition (Chapter 2.4.1). The sample and detector positioning can easily be achieved if the orientation of the sample is known, which will be further discussed in Chapter 4.

At the aligned Bragg condition for a particular *hkl* reflection, the centre of mass of the 3D Bragg peak or CXDP appears in the centre of the detector. The aim is to record the 3D CXDP such that an image can be reconstructed using phase retrieval algorithms presented in Chapter 2.4. The CXDP can be collected by taking sequential 2D slices of it in reciprocal space using a pixelated area detector. This can be achieved by rotating the illuminated sample at small increments (Eq. 2.59 or $\sim 0.005°$), known as rocking, resulting in the reciprocal lattice point moving through the Ewald sphere. For a 2D visualisation, see Fig. 2.10, which describes the collection of a 03 Bragg peak on a simple 2D cubic system using an Ewald sphere construction [80].

2.3.2.1 Ewald's sphere

The Ewald sphere is a visualisation of the relationship between the reciprocal lattice and scattering geometry [80]. At each reciprocal lattice point, there exists a 3D Bragg peak defined by its Miller indices. The incident wavevector points towards the reciprocal space origin, 000, and creates a sphere with a radius of $|\mathbf{S}_0| = |\mathbf{S}| = \frac{2\pi}{\lambda}$. The outgoing wavevector also points to the surface of the sphere where another Bragg peak is present. Therefore, the scattering vector points from the reciprocal space origin to the intersection of the

outgoing vector and the Ewald sphere, which is also the location of the specular Bragg peak. Since the origin of reciprocal space can connect to any other lattice point by $\mathbf{H}_{hkl}$, any Bragg peak that lies on the circumference of the Ewald sphere satisfies the Laue condition as $\mathbf{Q} = \mathbf{H}_{hkl}$. Therefore, when the detector is placed on the Ewald sphere normal to the outgoing wavevector, the detector captures a 2D slice through the Bragg peak. The rocking of the crystal about a fixed central axis then moves the entire reciprocal space lattice about its origin such that the Bragg peak moves through the detector and can be measured (Fig. 2.10). Since λ is small, the radius of the Ewald sphere is large and the 2D slice through the Bragg peak is approximately flat.

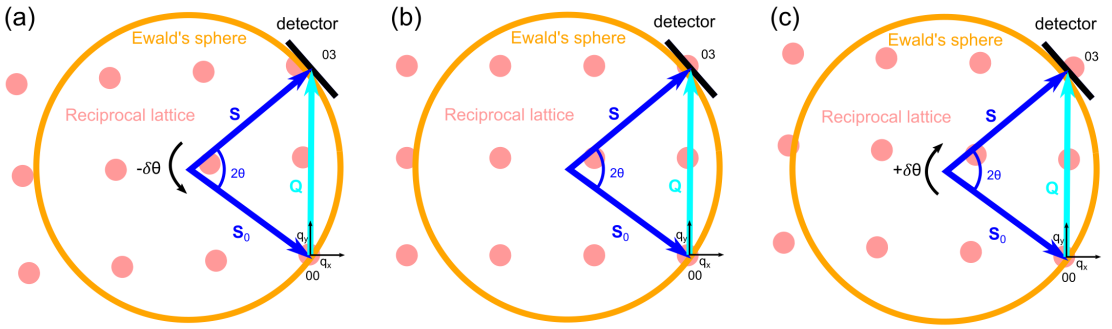

Figure 2.10: Ewald's sphere (orange circle) projected on a 2D reciprocal space lattice (pink circles) for a cubic system to show the collection of a diffraction pattern on a detector (black line) as a consequence of rotating the crystal from $-\delta\theta$ to $+\delta\theta$. $\mathbf{Q}$ is the momentum transfer vector, $\mathbf{S}_0$ is the incident wavevector and $\mathbf{S}$ is the outgoing wavevector. The radius of Ewald's sphere is $|\mathbf{S}_0| = |\mathbf{S}| = \frac{2\pi}{\lambda}$. The detector surface is normal to $\mathbf{S}$. By geometry, $\mathbf{Q} = 4\pi\sin(\theta)/\lambda$. (a) shows that rotating the sample to $-\delta\theta$ rotates reciprocal space lattice in the same direction so that the detector moves away from the 03 Bragg peak. (b) shows the detector is at the centre of the 03 Bragg peak. (c) shows that rotating the sample to $+\delta\theta$ rotates reciprocal space lattice in the same direction such that the detector moves through to the opposite side of the 03 Bragg peak.

After the 2D slices are collected by rotating through the Bragg condition, they can be stacked to form the 3D CXDP. However, due to the angular rotation through the Bragg condition at a specific detector radial position, the 3D CXDP will be sheared due to its non-orthonormalised basis which describes detector reciprocal space. Reconstructions of the CXDP will produce an image in detector conjugated space which is also a non-orthonormalised basis. These reconstructions will need to be corrected for the shear associated with their measurement geometry, which is discussed in Chapter 3.

Another way to collect the 3D CXDP is to vary the X-ray energy [81], which will be

discussed in Chapter 2.5.8.

2.4 Phase retrieval

From Chapter 2.2.3.4, the intensity of the CXDP from the scattered wavefield of a strained, finite crystal contains the Fourier transform of the complex crystal electron density. However, the phase of the complex amplitude (Eq. 2.44), which provides information about the displacement field projected onto the scattering vector, cannot be directly recovered in the intensity measurement. This is because the pixelated area detectors count photons. However, the intensity of the diffraction pattern contains the phase information encoded in the pattern's fringes, provided that the pattern is sampled by at least twice the Nyquist frequency, according to Sayre's response to Shannon's theorem [37]. The phase can be recovered using a variety of iterative techniques [82] that apply constraints in real and reciprocal space, allowing the sample to be reconstructed. Thus, the physical lens in lens-based imaging methods, which is used to refocus scattered waves with their associated phases to produce an image of the sample, is replaced by a phase retrieval algorithm in CDI. This chapter presents a chronological review of the most commonly used phase retrieval algorithms in the field, as well as recent developments in those algorithms.

2.4.1 Oversampling

Before the discussion of phase retrieval techniques, I will first outline the conditions required to recover the phase. In 1949, Shannon [83] stated that the Fourier transform of a function that is non-zero over the interval a is completely specified if it is sampled with a spacing of $2\pi/a$, which is the Nyquist frequency. Note that in this thesis we will use angular wavevectors, hence the factor of 2π in the Nyquist frequency. However, this sampling rate only applies if both the amplitude and phase are known, which is not the case in CDI. Sayre's response to Shannon's theorem [37] stated that at least twice the Nyquist frequency (Fig. 2.11) or an interval of π/a is required to recover the original function if

only the amplitude is known.

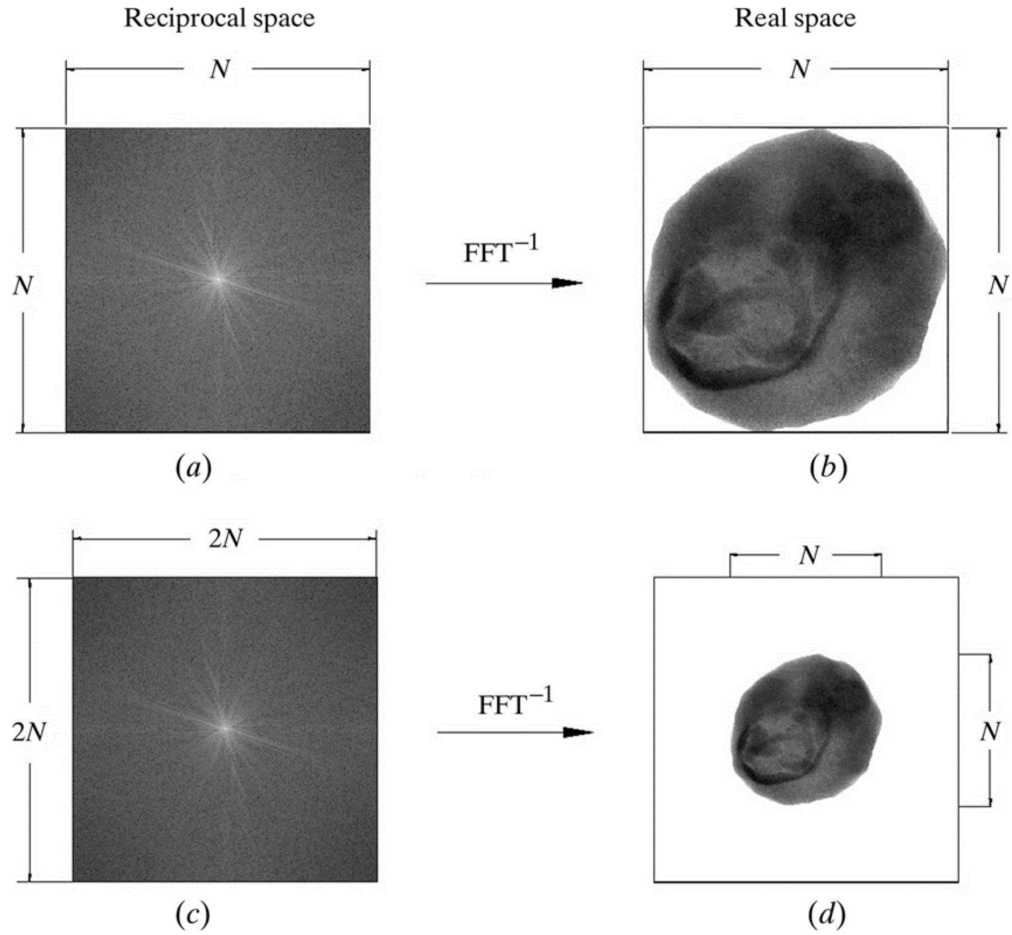

Figure 2.11: Comparison of sampling frequencies. (a) Shows the intensity of a noncrystalline object (b). The pattern is sampled at the Nyquist frequency and the inverse Fourier transform will fill the $N \times N$ array. (c) Shows the intensity of (d), the noncrystalline object now surrounded by an empty region. The pattern is sampled at twice the Nyquist frequency, which can be used to recover the correct phase and shape. Image obtained with permission from Miao *et al.* [84].

For CDI, the diffraction pattern is collected on a pixelated area detector where the pixels serve as discrete sampling points, making the diffraction pattern a discrete measurement. Eq. 2.31 describes the amplitude of the diffracted wavefield from a crystal as a Fourier transform of the crystal's electron density. Here, that expression can be discretised as,

$$|A(\mathbf{Q})| = \left| E_s \sum_{n=0}^{N-1} \rho_{\text{crystal}}(\mathbf{r}_n) e^{\frac{i2\pi\mathbf{Q}\cdot\mathbf{r}_n}{N}} \right|, \tag{2.54}$$

where N is the number of pixels, $\mathbf{r}_n$ is a pixel coordinate in real space, and $\mathbf{Q}$ is a pixel

coordinate in reciprocal space. Eq. 2.54 describes a set of N equations used to solve for the complex electron density of the crystal at each pixel given the magnitude of its Fourier transform, $|A(\mathbf{Q})|$. Therefore, at each pixel, there are two unknown variables, the magnitude and the phase of $\rho_{\text{crystal}}(\mathbf{r})$. For a 1D scenario, the number of unknown variables is $2N$. This extends to 2D and 3D with $2N^2$ and $2N^3$ unknown variables respectively.

To solve Eq. 2.54, constraints will need to be introduced to decrease the number of unknown variables. Known values can be introduced for $\rho_{\text{crystal}}(\mathbf{r})$ that do not scatter, i.e. $\rho_{\text{crystal}}(\mathbf{r}) = 0$ if $\mathbf{r}$ is outside the crystal (Fig. 2.11), by decreasing the size of the crystal by half. Therefore, there are N unknown variables ($N/2$ pixels $\times$ 2 unknown variables per pixel) and N equations. The oversampling ratio of 2 for 1D, 2D, and 3D systems by surrounding the crystal with a non-scattering region was first introduced by Miao in 1998 [85], who demonstrated that the oversampling ratio of two per dimension proposed by Bates in 1982 [85] was not necessary. In real space, this is most easily interpreted as the ratio between the number of pixels in the computational array to the number of pixels in the crystal [85],

$$\sigma = \frac{\text{total number of pixels in array}}{\text{total number of pixels in crystal}} \geq 2 \tag{2.55}$$

To translate this oversampling ratio to reciprocal space, consider a crystal with a diameter, d. The smallest distance in reciprocal space related to the largest dimension of the sample is $\Delta Q_d = \frac{2\pi}{d}$. The fringe spacing, Δx_f, observed in a diffraction pattern on the detector has an inverse relationship with the size of the crystal,

$$\Delta x_f \approx \frac{\Delta Q_d D}{|\mathbf{S}|} = \frac{\lambda D}{d}, \tag{2.56}$$

where D is the distance from the sample to the detector. Note that this is only for strain-free crystals, which will be explained in Chapter 2.4.7.1. In real space, our sampling range is at least $2d$ for an oversampling ratio of at least 2. Therefore, the maximum sampling distance in reciprocal space is $\Delta Q \leq \frac{2\pi}{2d} = \frac{\pi}{d}$. This means that the pixel size, p,

must be

$$p \leq \frac{\lambda D}{2d}. \tag{2.57}$$

By comparing Eq. 2.57 to Eq. 2.56, the pixel size must be half the fringe spacing or smaller. This translates to having at least two pixels separating each fringe along one dimension on the detector,

$$\sigma = \frac{\text{fringe spacing}}{\text{detector pixel size}} = \frac{\lambda D}{dp} \geq 2. \tag{2.58}$$

Note that Eq. 2.58 can be used as an expression to determine the detector distance for a particular oversampling ratio. For angular sampling with twice the Nyquist frequency, based on the geometry shown in Fig 2.10, the step size is given by

$$\begin{aligned} \sin(\delta\theta) &\leq \frac{\Delta Q}{|\mathbf{Q}|} \\ \delta\theta &\lessapprox \frac{\Delta Q}{|\mathbf{Q}|} = \frac{\lambda}{4d\sin(\theta)}. \end{aligned} \tag{2.59}$$

2.4.2 Uniqueness

When reconstructing an object from its Fourier magnitude alone, the solution is not unique. The magnitude of the Fourier transform for an object function, $f(\mathbf{r})$, is indistinguishable in the following scenarios:

(i) Spatial shift: $|\mathscr{F}[f(\mathbf{r})]| = |\mathscr{F}[f(\mathbf{r}+\mathbf{r_0})]|$, where $\mathbf{r_0}$ is a translation vector

(ii) Phase shift: $|\mathscr{F}[f(\mathbf{r})]| = |\mathscr{F}[f(\mathbf{r})e^{i\psi}]|$

(iii) Conjugate: $|\mathscr{F}[f(\mathbf{r})]| = |\mathscr{F}[f^*(-\mathbf{r})]|$

Despite the issue of having non-unique solutions for a given Fourier magnitude, solutions have been proposed to circumvent each scenario. The spatial shift can be accounted for by shifting the iterates in real space such that their centre of mass lies in the centre of the array during phase retrieval. The phase shift does not present a concern in this

thesis as the strain is determined from the gradient of the phase (Chapter 2.4.10). The complex conjugate or "twin" of an object is related to the original by mirroring. During phase retrieval, the ambiguity of having a non-unique, twinned solution can cause stagnation, especially in the presence of noise, where the algorithm becomes trapped in a higher local minimum compared to that of the twinned or normal object. To force the algorithm towards one of the solutions, a tight, asymmetric support (Chapter 2.4.4.1) can be implemented during the phase retrieval process. The final result can be confirmed, and converted to the conjugate solution if necessary, with prior knowledge of the object, e.g. SEM images. If multiple reconstructions are averaged, then the twinned reconstructions need to be converted for proper analysis.

The twin image problem can be resolved using curved wavefronts, e.g. Fresnel-regime CDI [86, 87] and ptychography [88]. The curved wavefront will break the symmetry of incident and outgoing planar wavefronts, allowing for the reconstruction of a unique solution [86]. This can reduce the stagnation that is often found in the phase retrieval process for CDI data.

2.4.3 Gerchberg-Saxton

The first iterative phase retrieval algorithm was proposed by Gerchberg and Saxton in 1972 [38] for electron diffraction. To obtain the missing phases, one would first need to obtain an image of the sample in the Fourier plane using electron diffraction and in the real plane using electron microscopy. The algorithm proposed iterative switching between real and reciprocal space using a fast Fourier transform (FFT) and its inverse (IFFT):

(i) apply random phases between $-\pi$ and π to the real image,

(ii) take the fast Fourier transform of the result obtained in (i),

(iii) replace the diffraction amplitude from (ii) with the measured diffraction pattern,

(iv) perform an inverse fast Fourier transform on (iii) to yield a real image,

(v) replace the magnitude from (iv) with the measured real image

(vi) repeat (ii) - (v) until convergence is obtained.

There are limitations to this early method. The first is the need for a real image, which can require electron microscopy. The second is that the error does not necessarily decrease with every iteration. Occasionally, the error would plateau or be trapped in a local minimum due to the presence of non-unique solutions as discussed in Chapter 2.4.2. This local minimum occurs because the same intensity signal can be produced by $A(\mathbf{Q})$ or $A^*(-\mathbf{Q})$ and a combination of these twins can cause stagnation in the algorithm.

2.4.4 Error-reduction

In 1978, Fienup proposed the error-reduction (ER) algorithm, a generalisation of the Gerchberg-Saxton (GS) algorithm [39] with a relaxed physical constraint. One no longer requires *a priori* knowledge of the sample in real space. The real space boundary condition in the GS algorithm is replaced by a finite "support" region, $\Omega(\mathbf{r})$. The support is a binary mask that describes where the electron density is allowed to exist, by allowing non-zero magnitude in the support and forcing the magnitude to be zero everywhere else. A starting guess for the support can be determined from the auto-correlation function [89], which is equal to an inverse Fourier transform of the measured intensity. The reciprocal space constraint remains the same, where the amplitude of the diffraction pattern replaces the magnitude of the iterate in the Fourier domain. A forward-calculated iterate in the ER algorithm, $g_{n+1}(\mathbf{r})$, can be defined by:

$$g_{n+1}(\mathbf{r}) = \begin{cases} g'_n(\mathbf{r}) & \text{if } \mathbf{r} \in \Omega(\mathbf{r}) \\ 0 & \text{if } \mathbf{r} \notin \Omega(\mathbf{r}) \end{cases} \tag{2.60}$$

where $g'_n(\mathbf{r})$ is the calculated real space iterate. A flowchart of the algorithm is shown in Fig. 2.12.

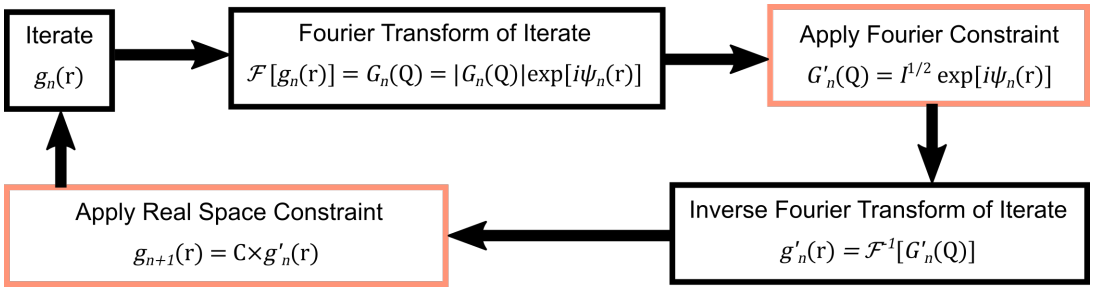

Figure 2.12: An overview of a general phasing algorithm. $g_n(\mathbf{r})$ is the real space iterate at iteration n, $\psi_n(\mathbf{r})$ is the iterate's phase, I is the measured diffraction intensity, $g'_n(\mathbf{r})$ is the calculated real space iterate, $G'_n(\mathbf{Q})$ is the calculated reciprocal space iterate and C is an algorithm-specific parameter, corresponding to Eq. 2.60 or Eq. 2.61.

2.4.4.1 Shrinkwrap

To obtain the best BCDI reconstruction, the real space constraint should be as close as possible to the morphology of the sample. Since the support begins with an initial estimate, it should be updated to drive the solution to a local minimum error. The support can be updated after every few iterations using a "shrinkwrap" method [89], which effectively converges the shape of the support to the shape of the final object. After every $\sim 5-100$ iterations, the support is updated by convolving the current reconstructed object with a Gaussian and binarising the result according to a threshold $\sim 10\%$ of its maximum value. By changing the standard deviation of the Gaussian, a different support "tightness" can be used. As the solution converges, it can be useful to decrease the standard deviation to produce a tighter support and potentially a better reconstruction of the object.

2.4.5 Hybrid input-output

Similar to the GS algorithm, the ER algorithm suffers from stagnation because it always minimises the error between the calculated iterate and measurement data, leaving no opportunity to escape local minima. To explore solutions outside the local minimum, with the aim of reaching the global minimum, Fienup proposed a hybrid input-output (HIO) algorithm [40]:

$$g_{n+1}(\mathbf{r}) = \begin{cases} g'_n(\mathbf{r}) & \text{if } \mathbf{r} \in \Omega(\mathbf{r}) \\ g_n(\mathbf{r}) - \beta g'_n(\mathbf{r}) & \text{if } \mathbf{r} \notin \Omega(\mathbf{r}) \end{cases} \tag{2.61}$$

where $g_n(\mathbf{r})$ is the current iterate and β is a feedback constant, where $0 < \beta < 1$. In practice, $\beta \approx 0.9$, and if $\beta = 1$ the HIO algorithm becomes the ER algorithm. Here the reciprocal space constraint is applied the same as in the ER algorithm, but the real space constraint differs when outside the support. Rather than setting the value to 0 outside the support, the HIO algorithm takes the current iterate and combines it with part of the calculated iterate. After each iteration of HIO, the current iterates in both real in reciprocal space are not necessarily the best guesses of the final solution, making the HIO algorithm less susceptible to stagnation compared to the ER algorithm. The HIO algorithm can also be combined with shrinkwrapping the support to achieve convergence. Having a tight support is crucial for HIO because otherwise the algorithm can fail to converge [90], but an overly tight support will also cause the convergence to fail [91].

In this thesis, a combination of ER and HIO algorithms are used to produce faithful reconstructions. The HIO algorithm is less constrained in real space, allowing for flexibility in finding a localised minimum as close as possible to the global minima. The ER algorithm is appropriate for finding a precise convergence around a localised minimum. Both approaches can be combined with shrinkwrapping for faster convergence.

2.4.6 Guided algorithms

The CXDP data is tampered by Poisson noise created by the particle nature of light, thus the convergence of a solution to the ground truth using iterative phase retrieval algorithms is never guaranteed. If different starting guesses are used for the reconstruction of a CXDP, different solutions may be produced using the same algorithm and number of iterations. Therefore, it becomes very difficult to tell which of these solutions provides the best reconstructed image.

In this thesis, a guided ER and HIO algorithm combined with shrinkwrapping and

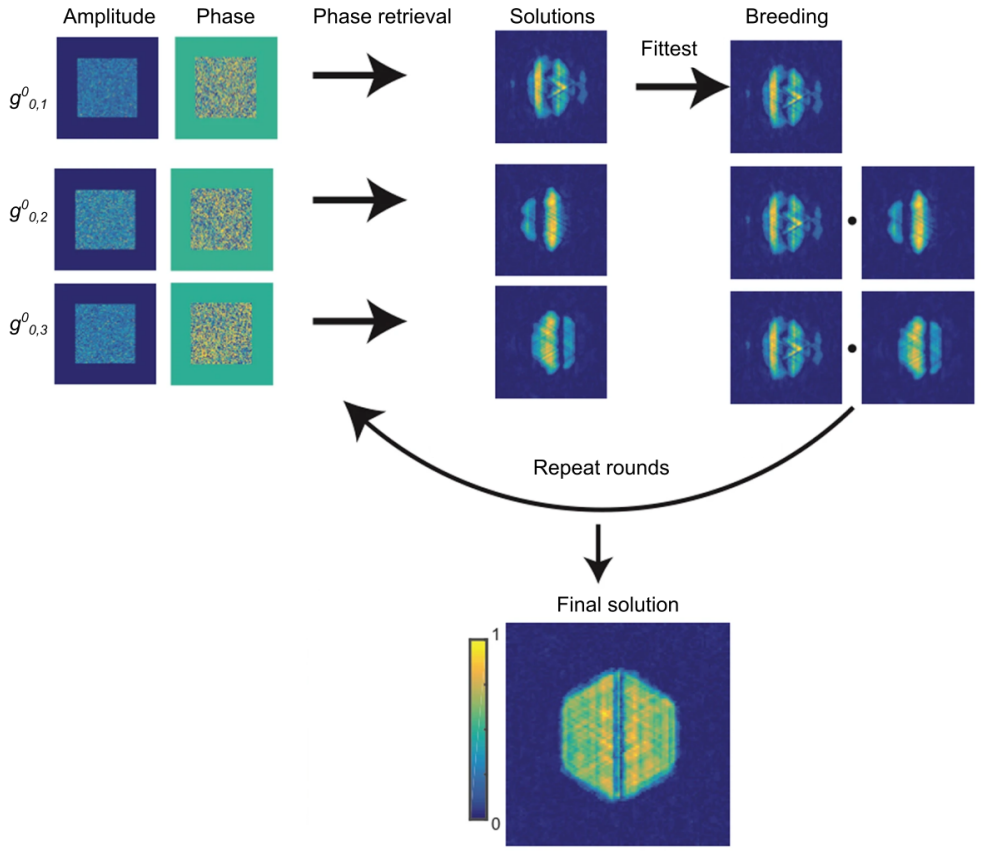

Figure 2.13: Flow chart for a 2D guided phase retrieval algorithm that can be extended to 3D. Three random starts, $g^0_{n,\,1}$, $g^0_{n,\,2}$, $g^0_{n,\,3}$, are inputs to independent phase retrieval algorithms. The solutions are ranked based on a fitness metric and the fittest solution is bred with the remaining solutions to become inputs for the next round of phase retrieval. This process is repeated for a number of rounds to produce the final reconstruction. Image adapted from Ulvestad *et al.* under the Creative Commons CC BY license [92].

occasionally, partial coherence correction (Chapter 2.4.9.2), is used to produce faithful reconstructions. This guided approach is based on the work of Chen *et al.* in 2007, who created a guided HIO algorithm for X-ray diffraction microscopy that begins with a number of different starting guesses [93] (Fig. 2.13). Each initial guess, $g^0_{n,\,o}$, where o is a guess, is fed to a defined phase retrieval algorithm consisting of a number of iterations. The algorithm then selects the best solution according to an error function, e.g. Eq. 2.66. Once the fittest solution has been selected for a given round, r, it is "bred" with the other solutions using a geometric average,

$$g^{r+1}_{0,\,o}(\mathbf{r}) = \sqrt{g^r_{n,\,\text{best}}(\mathbf{r}) g^r_{n,\,o}(\mathbf{r})} \tag{2.62}$$

to produce initial guesses for the next round of independent phase retrieval. This process of breeding initial guesses into successive rounds of independent phase retrieval is repeated to drive the solution towards the global minimum. At the end of the phase retrieval algorithm at a local minimum, hundreds of ER iterations are performed with shrink wrap to reduce the error. The final few iterations for the fittest solution are then averaged to maximise the consistent features in the reconstruction. Depending on the fitness metric, solutions can be biased towards *a priori* knowledge. Metrics to evaluate the quality of a BCDI reconstruction will be discussed next.

2.4.7 Error metrics

The goal of an iterative phase retrieval algorithm is to minimise the error between a particular solution and the ground truth. However, it is impossible to know the full ground truth in real space for laboratory-based BCDI measurements. Conceptually, one can image a BCDI sample using a SEM to find the morphology, but the strain distribution of the sample cannot be truly known. However, real space metrics based on *a priori* knowledge of the sample, such as sharpness and maximum volume, can be used. More commonly, error metrics used for BCDI are in reciprocal space, as only the measured and calculated intensities are known. Two common error metrics, χ^2 and more recently, the free log-likelihood, are also described in this section.

2.4.7.1 Sharpness

Metrics based on the reconstruction of the objects are useful when the measured diffraction intensity is low. The sharpness metric is a measurement of anti-sparsity through the recovered amplitude uniformity. It is calculated by the sum of the absolute value of the reconstruction over all voxels raised to the fourth power,

$$E_s = \sum_{\mathbf{r}} |\rho(\mathbf{r})|^4. \tag{2.63}$$

A lower sharpness metric corresponds to a better reconstruction. Equivalently, the sharpness metric can be normalised to preserve units [94],

$$E_{s,\,norm} = \left(\sum_{\mathbf{r}} |\rho(\mathbf{r})|^{\frac{1}{4}} \right)^4. \tag{2.64}$$

This metric was previously used to yield the best reconstructions for strained samples [95]. Strain causes the broadening of Bragg peaks [96] since the crystal amplitude will contain an additional complex factor (Eq. 2.41). The addition of the complex component will lead to a narrower auto-correlation function, which could be used as an initial support, resulting in a smaller crystal than is actually to be reconstructed [95]. However, a similar broad Bragg peak could arise if the crystal were smaller but unstrained. If the Fourier space-based χ^2 error metric (Chapter 2.4.7.3) were used to compare a reconstruction of a large strained crystal and a small unstrained crystal, the error would have indiscriminate values. Hence, the sharpness metric typically favours more uniform, larger electron densities for strained crystals.

2.4.7.2 Maximum volume

The maximum volume error metric is similar to the sharpness metric in that it favours large volumes after thresholding, but disregards amplitude uniformity. The maximum volume error metric can be written as [92]

$$E_{\text{vol}} = \frac{\sum_{\mathbf{r}} |\rho(\mathbf{r})|}{\max(|\rho(\mathbf{r})|)},\ |\rho(\mathbf{r})| = \begin{cases} 1 & \rho(\mathbf{r}) \geq 0.2 \\ 0 & \rho(\mathbf{r}) < 0.2 \end{cases}, \tag{2.65}$$

where the maximum value corresponds to a more converged reconstruction. The maximum volume metric performs best at low signal-to-noise ratios when trying to recover dislocations in simulated data [92]. Since the recovered crystal amplitude is naturally low for low photon counts, selecting the solution with the largest thresholded volume would correspond to a more converged solution.

2.4.7.3 Normalised mean difference

The most popular error metric, χ^2, has been implemented in most BCDI experiments and simulations. It is determined by calculating the summed square of the difference between calculated and measured amplitudes, normalised by the square of the measured amplitude at each pixel, n:

$$\chi^2 = \frac{\sum_n |A_n^{\text{calc}} - A_n^{\text{meas}}|^2}{\sum_n |A_n^{\text{meas}}|^2}. \tag{2.66}$$

For good convergence, $\chi^2 \lessapprox 10^{-3}$ [97]. The issue with this metric is that it completely relies on the diffraction pattern measured, which can be heavily influenced by noise, partial coherence effects, and missing data [98–100]. Furthermore, the size of the crystal cannot be uniquely determined from an oversampled diffraction pattern alone, as a CXDP from a large strained crystal could have a similar Bragg peak width as a CXDP from a small unstrained crystal (Chapter 2.4.7.1) [95]. This can make it difficult to find the true size of the crystal and potentially results in solutions with incorrect crystal sizes [101]. The absence of a reliable error metric has motivated the implementation of an unbiased free log-likelihood figure of merit discussed next.

2.4.7.4 Free log-likelihood

In 2020, Favre-Nicolin *et al.* [101] introduced an unbiased metric to determine the error from a phased solution. The issue is that having larger supports than the actual sample can lead to indiscriminate χ^2 errors. This is because a larger support equates to more free parameters the algorithm can use to better fit the diffraction data, making it difficult for a phase retrieval algorithm to select the solution with a tighter support. The ideal solution would be the one with a tight support refined by shrinkwrapping (Chapter 2.4.4.1) and a strong correlation with the measured diffraction pattern. They propose using a free log-likelihood, where $\sim 5\%$ of measured CXDP voxels are isolated from the reconstruction algorithm. These are labelled as a "free" set of voxels and are defined by 3 voxel radius

clusters randomly placed away from the maximum intensity. During the Fourier update step of a phase retrieval algorithm, the free set is masked so the calculated values are kept. The error metric, LLK_{free}, is based on the Poisson log-likelihood [102], and computed only over the free set of pixels. The metric is given by,

$$LLK_{free} = -\frac{1}{N}\sum_{n} \log \frac{(I_n^{\text{calc}})^{I_n^{\text{meas}}}}{I_n^{\text{meas}}!} e^{-I_n^{\text{calc}}}, \tag{2.67}$$

where n is the number of pixels in the free set, I^{calc} is the calculated intensity, and I^{meas} is the measured intensity. LLK_{free} is limited by counting statistics, where a CXDP with many zero values will have a low LLK_{free}. Furthermore, having a low LLK_{free} only means that it is probabilistically a better solution. LLK_{free} is only a relative metric that allows for the comparison within a population of solutions with the same set of free pixels. As a result, this metric works best with a guided algorithm (Chapter 2.4.6).

Other metrics can be used to select the best solution, for example, enforcing the phase using simultaneous multi-Bragg peak phase retrieval [50, 103, 104], positivity of the real space electron density, uniformity of the amplitudes, and maximum volume [92]. However, application of these metrics requires strong *a priori* knowledge of the sample or the measurement of multiple Bragg peaks, making them less commonly implemented.

2.4.8 Spatial resolution

The spatial resolution of an image can be used as a metric to determine its quality. Unfortunately for BCDI, there is no universal measure for the spatial resolution calculation. It should depend on the reconstruction of the highest spatial frequency collected in the diffraction pattern, but this is not straightforward to determine. The scattered intensity surrounding a Bragg peak is anisotropic and dependent on the strain field and crystal morphology, which suggests that the resolution is also anisotropic [105]. Ideally, a metric should consider the spatial resolution from different directions.

2.4.8.1 Rayleigh resolution

Based on the Rayleigh criterion (Eq. 2.2) for lens-based imaging systems, the resolution is determined from the wavelength and numerical aperture [62]. The numerical aperture for lensless imaging is defined by the largest angle, θ_{max}, scattered by the sample from the optical axis where the intensity can be obtained and phased [75]. For BCDI, that angle is based on the detector size using the small-angle approximation $\theta_{max} = Np/D$, where N is the number of pixels on a square detector along one dimension. The spatial resolution of the reconstructed sample based on the Rayleigh criterion is [62]

$$\Delta x_s = \frac{\lambda D}{Np}. \tag{2.68}$$

However, a limitation is that diffraction patterns exhibit a strong radial decay and detectors do not have sufficient dynamic range to capture both high intensities at the centre of the diffraction peak and low intensities scattered to the edge of the detector. Therefore, not all the information can be phased in the region spanned by the numerical aperture and the actual spatial resolution should be higher.

2.4.8.2 Phase retrieval transfer function

The most common method to define the resolution for a solution is using the phase retrieval transfer function (PRTF) [106]. It consists of calculating the intensity of the averaged reconstructions and dividing it by the measured intensity over the entire range of measured $\mathbf{Q}$,

$$\mathrm{PRTF}(\mathbf{Q}) = \frac{|\mathscr{F}[\rho_{\mathrm{avg}}(\mathbf{r})]|^2}{I^{\mathrm{meas}}(\mathbf{Q})}. \tag{2.69}$$

The average solution reduces the intensity of the incompatible regions of the solutions. The ratio is 1 when the iterative algorithm converges perfectly and 0 where the algorithm fails to converge. By plotting the PRTF over shells of constant Q and where I^{meas} is nonzero, a conservative estimate of the spatial resolution can be obtained when the PRTF

reaches 0.5 [106].

2.4.8.3 Line spread function

Due to the asymmetry in the CXDP caused by strain and crystal morphology, the spatial resolution is also dependent on the direction. In this thesis, the resolution is determined from amplitude line profiles across a crystal/environment interface. The amplitude profile would ideally be a step function, with its derivative being a Dirac delta function. A real, non-binary, amplitude line profile can provide the spatial resolution by taking its derivative, known as a line spread function [107], and fitting it to a Gaussian curve. The full width at half maximum (FWHM) of the fitted Gaussian determines the resolution for that particular line profile direction [107]. By averaging the result from line profiles in different directions, the average spatial resolution of the crystal can be obtained.

2.4.8.4 Fourier shell correlation

Another measure of spatial resolution is using Fourier shell correlation (FSC) [108]. This method involves computing the normalised cross-correlation between two independent reconstructions, $G_1(Q)$ and $G_2(Q)$, over concentric shells in Fourier space,

$$\mathrm{FSC}(Q_i) = \frac{\sum_{Q\in Q_i} G_1(Q)\cdot G_2^*(Q)}{\sqrt{\sum_{Q\in Q_i}|G_1(Q)|^2\cdot\sum_{Q\in Q_i}|G_2(Q)|^2}}, \tag{2.70}$$

where Q_i is the set of points in the ith shell. It measures the consistency of the image spectra as a function of the spatial frequency or resolution. The resolution is determined by a FSC threshold, such as σ-factor or bit-based curves [109].

2.4.9 Phase retrieval development

CDI relies on the ability of a phase retrieval algorithm to reconstruct a faithful representation of the sample. However, it often becomes difficult to reconstruct highly strained crystals. These objects have highly distorted parts that scatter beyond the area of the de-

tector and can have complicated phase features surrounding defects. Other contributors to a failed reconstruction include partial coherence, increased noise, background, and missing data. This section will cover developments that have improved the ability of phase retrieval algorithms to minimise the error metric and recover an accurate representation of the object.

2.4.9.1 Gerchberg-Saxton based phasing algorithms

To resolve some of these phase retrieval challenges, others have developed the GS algorithm further. These algorithms include saddle point optimisation [82], difference map (DM) [110], matrix completion [111] and charge flipping [112], relaxed averaged alternating reflections (RAAR) [113] and others [114]. Generally, these methods enable tuneable real space and reciprocal space parameters that can be optimised for a particular dataset. Algorithms have been modified for highly strained crystals. Newton *et al.* have created the normalized density HIO algorithm to impose a uniform electron density in the reconstruction [115]. Huang *et al.* used phase constraint in the HIO algorithm [116] as an initialisation step to generate a support, followed by normal HIO to refine the object. None of these methods was implemented in this thesis as they required the optimisation of different parameters. In practice, the standard for many key experiments [47, 54, 95, 97, 117] has been alternating between tens of ER iterations and hundreds of HIO iterations [90], combined with shrinkwrap (Chapter 2.4.4.1) and implemented into a guided algorithm (Chapter 2.4.6).

2.4.9.2 Partial coherence phase retrieval

As discussed in Chapter 2.3.1.3, partial coherence effects could be considered if the reconstruction fails to converge (Fig. 2.14). A CXDP created by a partially coherent X-ray is related to the CXDP created by a perfectly coherent X-ray convolved with the Fourier transform of the normalised MCF (Eq. 2.50). Thus, the coherent intensity can be calculated from the partially coherent intensity if the Fourier transform of the normalised MCF

is known. The coherent intensity can then be used to recover the object. In 2012 Clark *et al.* [99] proposed a phasing algorithm to solve the Fourier transform of the X-ray's normalised MCF, $\hat{\gamma}(\mathbf{Q})$, simultaneously with phasing [99].

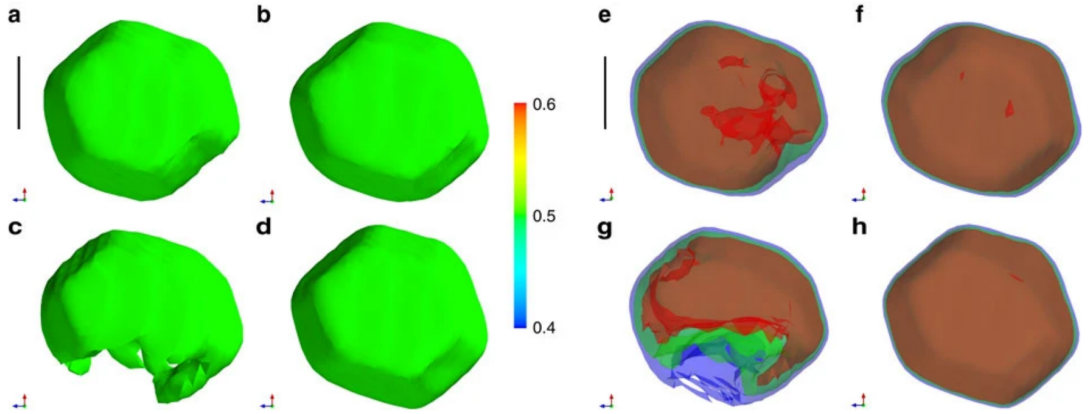

Figure 2.14: Reconstruction isosurfaces for a Au microcrystal using different coherence conditions. (a-–d) Reconstructed microcrystal from two coherence conditions viewed as opaque isosurfaces with an amplitude threshold of 50% maximum amplitude. (e-–h) Reconstructed microcrystal from two coherence conditions viewed as translucent isosurfaces with an amplitude threshold of 40-60% maximum amplitude. (a, e) Are imaged with a high coherence X-ray and phased assuming full coherence and (b, f) are phased assuming partial coherence. (c, g) Are imaged with a partially coherent X-ray and phased assuming full coherence and (d, h) are phased assuming partial coherence. The red and blue arrows correspond to the x-axis and z–axis respectively, and the green arrow is the y-axis pointing into the page. The black scale bar is 100 nm. Image is adapted with permission from Clark *et al.* [99].

To estimate the Fourier transform of the normalised MCF, 25 iterations of a Richardson—Lucy (RL) algorithm [118, 119] are used to update $\hat{\gamma}(\mathbf{Q})$ after every 15 iterations of phase retrieval [99]. The ith sub-iteration of $\hat{\gamma}^n(\mathbf{Q})$, where n is the iteration for the object, is [99]:

$$\hat{\gamma}^{n,i+1}(\mathbf{Q}) = \hat{\gamma}^{n,i}(\mathbf{Q}) \left(I^{\Delta n}(-\mathbf{Q}) \circledast \frac{I_{\text{pc}}^{\text{meas}}(\mathbf{Q})}{I^{\Delta n}(\mathbf{Q}) * \hat{\gamma}^{n,i}(\mathbf{Q})} \right), \tag{2.71}$$

where

$$I^{\Delta n}(\mathbf{Q}) = 2I^{n}(\mathbf{Q}) - I^{n-1}(\mathbf{Q}), \tag{2.72}$$

and $I^n(\mathbf{Q}) = |G_n(\mathbf{Q})|^2 = |\mathscr{F}[g_n(\mathbf{r})]|^2$ is the current guess of the fully coherent intensity based on the current recovered solution, $g_n(\mathbf{r})$. After the Fourier transform of the normalised MCF is updated using Eq. 2.71, the calculated partially coherent intensity, $I_{\text{pc}}^n(\mathbf{Q})$ [99],

$$I^n_{\mathrm{pc}}(\mathbf{Q}) = I^n(\mathbf{Q}) \circledast \hat{\gamma}^n(\mathbf{Q}). \tag{2.73}$$

is used to apply the reciprocal space constraint to calculated iterate, $G'_n(\mathbf{Q})$, [99],

$$G'_n(\mathbf{Q}) = G_n(\mathbf{Q}) \left(\frac{\sqrt{I^{\mathrm{meas}}_{\mathrm{pc}}(\mathbf{Q})}}{\sqrt{I^n_{\mathrm{pc}}(\mathbf{Q})}} \right). \tag{2.74}$$

Next, $G'_n(\mathbf{Q})$ is propagated to real space where a support is applied, shown previously in Fig. 2.12. The object and the Fourier transform of the X-ray's normalised MCF are updated in the phase retrieval algorithm until they both converge.

2.4.9.3 Simultaneous multi-Bragg peak phase retrieval

The increased popularity of MBCDI has enabled the collection of multiple Bragg peaks for a single crystal. Traditionally, phase retrieval of these CXDPs was performed independently, but a pathway for a simultaneous phase retrieval approach that shares information between the CXDPs could be conceived. These Bragg peaks originate from the same crystal and therefore should share the same orthogonalised support and phase determined from the displacement field (Eq. 2.44). A simultaneous, multi-Bragg peak phase retrieval process has the potential to achieve better convergence for strained objects and potentially reduce computation time.

In 2020, Newton [120] developed the first concurrent phase retrieval approach based on a simulated 3D nanocube with a displacement field. The workflow is similar to a GS approach, but with the addition of a phase constraint (Fig. 2.15) that collapses phasing artefacts for the reconstruction of each reflection. The phase constraint is determined using the calculated phases for each Bragg peak at every iterate to calculate the displacement field. Using the displacement field, the phase for each Bragg peak can be forward calculated and implemented into a HIO algorithm with 10 000 iterations. This was shown to produce sharper reconstructions and lower the error of the intensities compared to independent phase retrieval [120].

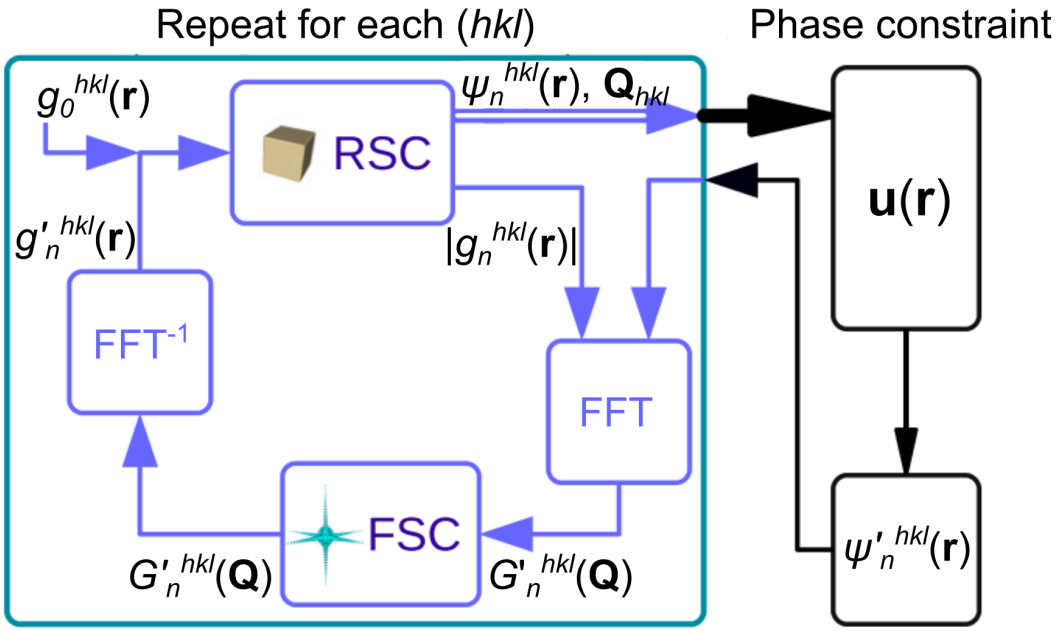

Figure 2.15: A flow chart of Newton's concurrent multi-Bragg reflection phasing method [120]. The chart enclosed in teal shows a general single reflection phase retrieval process (Fig. 2.12), which is repeated for concurrent phase retrieval. The black region shows a universal phase constraint that is applied to all reflections at every iteration. $\mathbf{Q}_{hkl}$ is the scattering vector, $g_n^{hkl}(\mathbf{r})$ is the real space iterate at iteration n, $\psi_n^{hkl}(\mathbf{r})$ is the iterate's phase, $g_n^{'hkl}(\mathbf{r})$ is the calculated real space iterate, $G_n^{'hkl}(\mathbf{Q})$ is the calculated reciprocal space iterate, $\psi_n^{'hkl}(\mathbf{r})$ is the iterate's phase calculated from the universal displacement field, $\mathbf{u}(\mathbf{r})$. RSC is the real space constraint and FSC is the Fourier space constraint. Image is adapted with permission from Newton [120].

Another idea is to share the support during simultaneous, multi-Bragg peak phase retrieval to reduce the real space constraint redundancy. Wang *et al.* implemented this in 2020 to reconstruct 3D battery cathode nanoparticles with 1% strain [121]. Their approach considered a simulated crystal undergoing structural phase transformation, and implemented a shared support multi-Bragg peak phase retrieval algorithm to reconstruct the crystal from noisy CXDPs at each time step. They used a combination of ER and RAAR algorithms with a total of 620 iterations to produce their solutions.

Wang *et al.* have implemented an approach where at each time step, 30 starting random guesses are initiated (similar to a guided algorithm in Chapter 2.4.6), producing multiple supports that are averaged to produce the final support for the time step. The final support across all time steps are then averaged, shrinkwrapped, binarised, and smoothed using a box filter to generate the most truthful shared support. This assumes that the crys-

tal's morphology is consistent during the phase transformation [121], but this may not be true for general cases.

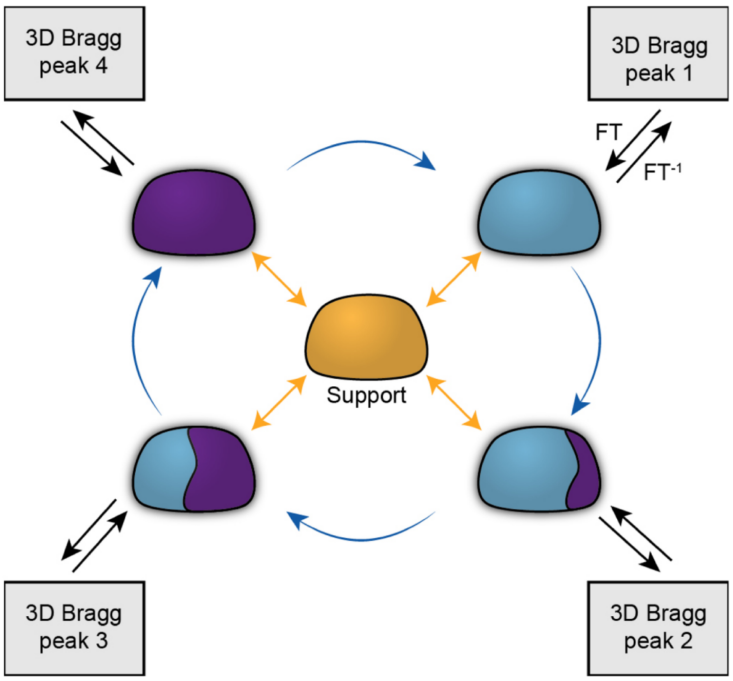

Figure 2.16: A flow chart of Wang's concurrent multi-Bragg reflection phasing method [121]. Here, each Bragg peak from different time points in the phase transformation is updated using a shared support. This assumes that the morphology of the crystal is constant throughout the transformation. Image is obtained from Wang *et al.* under the Creative Commons CC BY license [121]

A study by Gao *et al.* [104] furthered the ideas from Wang *et al.* [121] and Newton [120]. In 2021, Gao *et al.* produced a simultaneous MBCDI phase retrieval approach using 250 iterations from a combination of ER and HIO algorithms for simulated low strain and high strain Ag crystals. Every five iterations, the displacement field is calculated from the phase of each reflection in the sample frame and is used to predict the new phases in their respective detector conjugate spaces [104]. For highly strained crystals, a simultaneous, multi-Bragg peak phase retrieval algorithm has a generally higher success rate. The success of recovering all the peaks depends on whether dislocation-insensitive peaks are included to recover the displacement field, which will help solve the phase ambiguities for other reflections [104].

The first application of a simultaneous, multi-Bragg peak phase retrieval algorithm to laboratory-based data was performed by Wilkin *et al.* in 2021 [103]. They combined

universal support and displacement field constraints with a guided ER/HIO algorithm and compared the resulting reconstructions to those from independently phased Bragg peaks with the same guided algorithm. For a multi-peak reconstruction, the confidence metrics are the sum of all χ^2 (Eq. 2.66) values, χ^2_{sum}, and a loss function, L based on the recovery of the weighted displacement field error and normalised by the universal support volume [103],

$$L = \frac{\sum_{\mathbf{r}} |\bar{\rho}(\mathbf{r})| E(\mathbf{r})}{\sum_{\mathbf{r}} \bar{\Omega}(\mathbf{r})}, \tag{2.75}$$

where $E(\mathbf{r})$ is the error minimised in the calculation of the displacement field (Eq. 2.79), $\bar{\rho}(\mathbf{r})$ is the average amplitude over all reconstructed peaks and $\bar{\Omega}(\mathbf{r})$ is the universal support. The results show that the coupled guided ER/HIO algorithm produced lower χ^2_{sum} and L errors for both laboratory and simulated data. This is encouraging because even though guided algorithms produce the most faithful solutions, they can still benefit from a simultaneous phase retrieval framework.

2.4.9.4 Absence of measured data

Often, insufficient data can hinder reconstruction quality. Numerous factors can contribute to this, such as detector gaps, hot pixels, noise, undersampling, alien signals, or regions of missing intensity.

Many detectors consist of arrays of 256×256 pixels on a module that are combined together to make a larger detector array, e.g. Timepix area detectors (Amsterdam Scientific Instruments). The detector gaps between the modules are a few pixels wide, where no intensity measurement is made. Simulated results of CXDPs with different gap widths, when reconstructed, show the presence of striped artefacts which are determined by the width of the gap (Fig. 2.17) [98].

The detector gaps were not used during phase retrieval, i.e. when applying the reciprocal space constraint, the gap areas were not imposed [98]. The centre of mass should be as close as possible to the centre of the detector module to minimise low-frequency

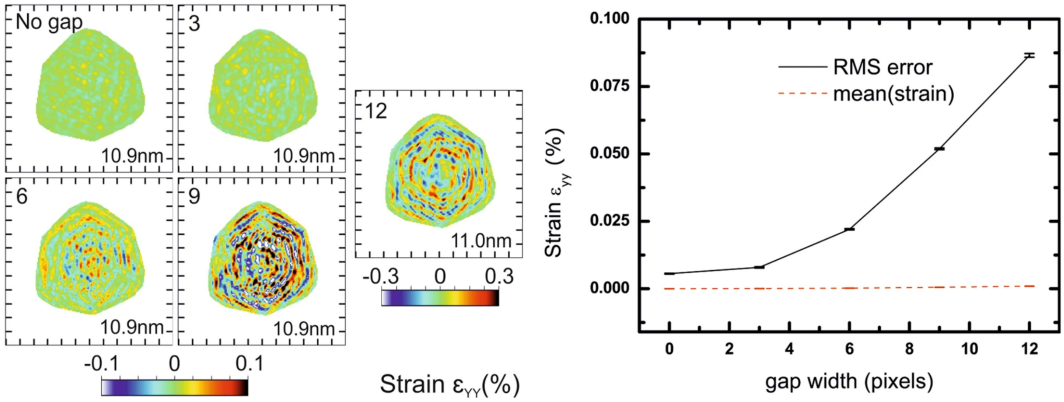

Figure 2.17: The effect of detector gaps on strain values for reconstructions from simulated data. Reconstruction slices of the XZ plane where the numbers in the top left corner correspond to the gap width in pixels (55 μm $\times$ 55 μm), and the resolution obtained from the PRTF are in the bottom right corner. The distance between two tick marks corresponds to 50 nm. The right shows that the RMS error for ε_{yy} has an exponential-like increase with gap width. Image is obtained from Carnis *et al.* under the Creative Commons CC BY license [98].

information loss in the detector gaps. Masking can also be used on hot or dead pixels, as well as alien signals, which are other crystals along the beam footprint that diffract at the same Bragg condition as the sample.

Shot noise in BCDI is due to accumulating photons on the detector. This noise is caused by the probability of a diffracted photon landing at a specific pixel and follows a Poisson distribution. The dynamic range on detectors is about $10^6 \frac{\text{photons}}{\text{second pixel}}$. Since the intensity of the CXDP decreases through a power-law radially outwards from its centre of mass (e.g. $I \propto \mathbf{Q}^{-4}$ for a spherical sample) [62], diffraction signals at high $\mathbf{Q}$ values are hard to measure without oversaturating the detector. Therefore, one must accumulate using low exposure times and sum the images together. Simulated results show that increasing the dynamic range will decrease the presence of reconstruction artefacts [98]. Some phase retrieval algorithms have been optimised for various noise models such as Gaussian (thermal) and Poisson (photon counting) to better perform data inversion for low signal-to-noise ratios [122].

The CXDPs must be at least twice oversampled, i.e. have at least two pixels separating each fringe along one dimension (Chapter 2.4.1). Occasionally, the CXDP might be less than twice oversampled to increase the signal-to-noise ratio or there are limitations with

moving the detector further away from the sample. To recover undersampled diffraction intensities below the Nyquist requirement, Fourier space compression can be considered to recover the object [123]. This would enable us to bin data to reduce computational resources without compromising reconstruction quality and perform BCDI at higher X-ray energies, which is currently being explored [124].

2.4.9.5 Machine learning-based phase retrieval

Reconstruction faithfulness and speed are primary areas of research. Highly strained crystals remain difficult for phase retrieval methods to reconstruct, and often require specialised methods [95, 99, 103] for successful phase retrieval. These methods also rely on fine sampling of CXDPs, which result in large arrays that are computationally intensive to invert. This needs to be addressed with the arrival of fourth-generation synchrotron light sources such as X-ray free electron lasers (Chapter 2.5.9), which can generate hundreds of 2D CXDPs per second. Furthermore, high coherence upgrades at third-generation synchrotron sources can provide two orders of magnitude in coherent flux [125], which will lead to similar increases in data volumes.

Moving away from the majority phase retrieval algorithms that rely on iterative, alternating projections, machine learning (ML) approaches have been applied to CDI data to reconstruct samples. ML consists of training a neural network (NN) to recognise patterns between input and output datasets to predict the output from foreign data. The first ML application to CDI was in 2018 when Cherukara *et al.* [126] trained two deep deconvolutional networks (DNNs) to learn the mapping of 2D CXDPs to their real space amplitude and phase. This allowed the prediction of the structure and phase of other simulated data in milliseconds, a remarkable improvement from GS-based phase retrieval algorithms that would take thousands of times longer. A limitation of this method is the simulated training dataset, which makes the DNNs perform less accurately when real data is input.

In 2021 Wu *et al.* used a 2D CNN solution as an initial guess for conventional iterative phasing methods. Their CNN model outputs an amplitude, phase, and support as a

starting guess and uses ER/HIO phasing algorithms to reconstruct finer details [127]. By using a more accurate starting guess, few iterations are required to approach the global minima, thereby reducing computational requirements. From the ML side, this avoids the inaccuracy of using the CNN to predict the solution directly, as the CNN is not trained using real data. The iterative phasing allows other local minima to be explored, allowing a more faithful reconstruction to be achieved.

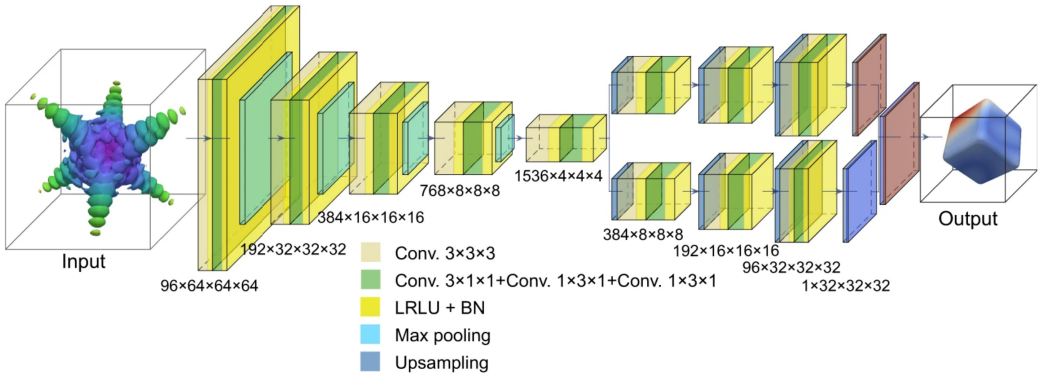

Figure 2.18: Architecture of a 3D deep neural network for CDI phase retrieval. The overall network consists of one encoder and two decoder networks. The encoder encodes the input 3D CXDP data through a progression of convolutional blocks. The encoded result passes through the two decoder networks to generate the complex electron density of the measured crystal. Image is obtained from Wu *et al.* under the Creative Commons CC BY license [128].

Various implementations of ML in CDI have been implemented recently in 3D. A more recent study by Wu *et al.* have created a ML model (Fig. 2.18) that combines conventional supervised learning followed by a refinement procedure based on unsupervised transfer learning [128]. An important finding was that this refinement process can recover phases directly without any pre-training, which comes at the cost of reconstruction time [128]. Another approach has been demonstrated by using a CNN to output spherical harmonics, which describe the surfaces and electron density of the 3D objects, which are then refined using an adaptive feedback algorithm. [129]. A defect classification CNN was created in 2021 by Lim *et al.* [130] using 3D training data from atomistic modelling. Here, the model was able to classify screw and edge dislocation on both simulated and experimental 3D CXDPs, without the need for refinement. Another CNN was created in 2021 by Chan *et al.* [131] that also used atomic simulations but also enforced X-ray

scattering physics in the training process.

2.4.10 Strain calculation

After retrieving the phase of the complex crystal electron density from a BCDI measurement, it can be used to calculate the atomic displacement or strain field. One component of the displacement field projected along the Bragg vector, $\mathbf{u}_{hkl}(\mathbf{r})$, can be determined by rearranging Eq. 2.44 to:

$$\mathbf{u}_{hkl}(\mathbf{r}) = \frac{\psi_{hkl}(\mathbf{r})}{|\mathbf{Q}_{hkl}|}, \tag{2.76}$$

Since the strain is the spatial derivative of the displacement field, one component of the strain tensor projected along the Bragg vector, $\varepsilon_{hkl}(\mathbf{r})$, can be determined via

$$\varepsilon_{hkl}(\mathbf{r}) = \nabla \mathbf{u}_{hkl}(\mathbf{r}) \cdot \left(\frac{\mathbf{Q}_{hkl}}{|\mathbf{Q}_{hkl}|} \right). \tag{2.77}$$

More conveniently, this can be expressed using the phase directly by taking the gradient of Eq. 2.44 and rearranging to:

$$\varepsilon_{hkl}(\mathbf{r}) = \nabla \psi_{hkl}(\mathbf{r}) \cdot \left(\frac{\mathbf{Q}_{hkl}}{|\mathbf{Q}_{hkl}|^2} \right). \tag{2.78}$$

For MBCDI, if at least three non-collinear reflections are measured, $\mathbf{u}(\mathbf{r})$ can be determined by minimising the least-squares error, $E(\mathbf{r})$ [50, 57]:

$$E(\mathbf{r}) = \sum_{hkl} [\mathbf{Q}_{hkl} \cdot \mathbf{u}(\mathbf{r}) - \psi_{hkl}(\mathbf{r})]^2 \tag{2.79}$$

where $\mathbf{Q}_{hkl} \cdot \mathbf{u}(\mathbf{r})$ is the forward calculated phase and $\psi_{hkl}(\mathbf{r})$ is the measured phase for a particular *hkl* reflection. From $\mathbf{u}(\mathbf{r})$, the full 3D lattice strain tensor, $\varepsilon(\mathbf{r})$, and rotation tensor, $\omega(\mathbf{r})$, for small displacements in rectilinear coordinates is [132]:

$$\begin{aligned}\varepsilon(\mathbf{r}) &= \frac{1}{2}\left\{\nabla\mathbf{u}(\mathbf{r}) + [\nabla\mathbf{u}(\mathbf{r})]^{\top}\right\} \\ &= \begin{bmatrix} \varepsilon_{xx} & \varepsilon_{xy} & \varepsilon_{xz} \\ \varepsilon_{yx} & \varepsilon_{yy} & \varepsilon_{yz} \\ \varepsilon_{zx} & \varepsilon_{zy} & \varepsilon_{zz} \end{bmatrix},\ \varepsilon_{ij} = \frac{1}{2}\left(\frac{\partial u_i}{\partial j} + \frac{\partial u_j}{\partial i}\right),\end{aligned} \tag{2.80}$$

$$\begin{aligned}\omega(\mathbf{r}) &= \frac{1}{2}\left\{\nabla\mathbf{u}(\mathbf{r}) - [\nabla\mathbf{u}(\mathbf{r})]^{\top}\right\} \\ &= \begin{bmatrix} 0 & \omega_z & -\omega_y \\ -\omega_z & 0 & \omega_x \\ \omega_y & -\omega_x & 0 \end{bmatrix},\ \omega_{ij} = \frac{1}{2}\left(\frac{\partial u_i}{\partial j} - \frac{\partial u_j}{\partial i}\right).\end{aligned} \tag{2.81}$$

An optimised approach to determine the spatial derivatives of the displacement field directly from the phase derivatives of multiple reflections is by minimising [30]:

$$E(\mathbf{r})_j = \sum_{hkl,j}\left[\mathbf{Q}_{hkl}\cdot\frac{\partial\mathbf{u}(\mathbf{r})}{\partial j} - \frac{\partial\psi_{hkl}(\mathbf{r})}{\partial j}\right]^2, \tag{2.82}$$

where j corresponds to the spatial x, y, or z coordinate.

2.5 Experimental developments

This chapter discusses the history of BCDI, originating from the first CDI experiment to contemporary *in situ* BCDI experiments. A review of experimental techniques and sample preparation methods will be discussed in roughly chronological order. Advanced experimental procedures, as well as novel sample preparation methods pertaining to this thesis, will also be considered.

2.5.1 2D coherent X-ray diffraction imaging

BCDI is the application of CDI in Bragg geometry. CDI is measured in the transmission regime, where the detector is placed behind the object perpendicular to the forward scattered beam. The concept of CDI came from Sayre in 1952 [37] after he noted that oversampled diffraction patterns contained phase information, as explained in Chapter 2.4. However, for X-rays this idea was not realised until 1999, when Miao *et al.* successfully executed the first CDI experiment at the National Synchrotron Light Source at Brookhaven National Laboratory, USA [41]. The sample was six letters formed from 100 nm diameter gold dots, each 80 nm thick, deposited on a silicon nitride membrane. The diffraction patterns were collected in the forward scattering regime by illuminating the sample with a coherent X-ray source ($\lambda = 1.7$ nm). The reconstruction, with a spatial resolution of 75 nm, successfully matched the electron microscopy image of the sample.

2.5.2 3D coherent X-ray diffraction imaging

The ability to recover an image successfully in 2D CDI has led to the implementation of CDI to image a 3D object using tomography. Tomography involves collecting 2D projections from rotating an object and can be applied in X-ray diffraction to obtain a 3D diffraction pattern. In 2002, Miao *et al.* performed the first 3D reconstruction at SPring-8 in Hyōgo Prefecture, Japan [133]. They used a noncrystalline Ni sample, made using electron beam lithography, consisting of two single-layered Ni patterns ($2.5 \times 2 \times 0.1$ μm) rotated in-plane relative to each other and separated by a distance of 1 μm. Using an x-ray source with $\lambda = 0.2$ nm, 2D diffraction patterns were collected as the sample was rotated from $-75°$ to $75°$ in $5°$ increments. These patterns were assembled into a 3D diffraction pattern and phased. Both layers of the sample were reconstructed successfully with a resolution of 50 nm.

2.5.3 Bragg coherent X-ray diffraction imaging

CDI experiments in transmission mode, even for crystalline samples, are insensitive to lattice strain. Mathematically, this is because the incident and outgoing X-rays are parallel, so the scattering vector is ~ 0 and thus the displacement field cannot be projected and embedded in the phase of the scattered wavefield (Eq. 2.41). To obtain information about the atomic displacements inside the sample, a CXDP at Bragg condition must be collected.

The first CDI experiment in the Bragg geometry was performed by Robinson *et al.* in 2001 on a single Au nanocrystal at the APS [134]. The faceted crystals were prepared by dewetting [135] Au thin films evaporated on silicon wafers at 950°C. Using an X-ray source with $\lambda = 0.165$ nm, a 2D diffraction pattern was collected on a detector from an individual crystal about 1 μm $\times$ 1 μm $\times$ 1 μm oriented according to the $11\bar{1}$ reflection. A 2D projection of the crystal was successfully reconstructed using a combination of ER and HIO algorithms [40]. It was the first experiment to show the inversion of 2D data to obtain a projection of the crystal shape for an off-specular reflection.

A 3D CXDP was first collected in 2003 by Williams *et al.* by rocking a gold crystal about an axis [136]. An Au crystal similar to the one used by Robinson *et al.* [134], was illuminated with a coherent X-ray ($\lambda = 0.131$ nm). A 3D $\{111\}$ Bragg peak was collected by rotating in 0.002° steps about the Bragg condition over a total angular range of 0.1°. The rocking rotates the entire reciprocal space lattice about its origin such that the 3D Bragg peak moves through the detector and can be measured (Fig. 2.10). 2D CXDPs were collected on the detector and stacked to form a 3D CXDP used as the reciprocal space constraint for the alternating ER/HIO phase retrieval process [40]. Following phase retrieval, the real electron density of the crystal was determined and remained truthful when compared to SEM images of a Au nanocrystal.

Following the work from Williams *et al.* [136], Pfeifer *et al.* performed the first BCDI experiment at the APS where they were able to map a deformation field inside a Pb nanocrystal in 2006 [137] (Fig. 2.19). Using an analogous evaporation sample fab-

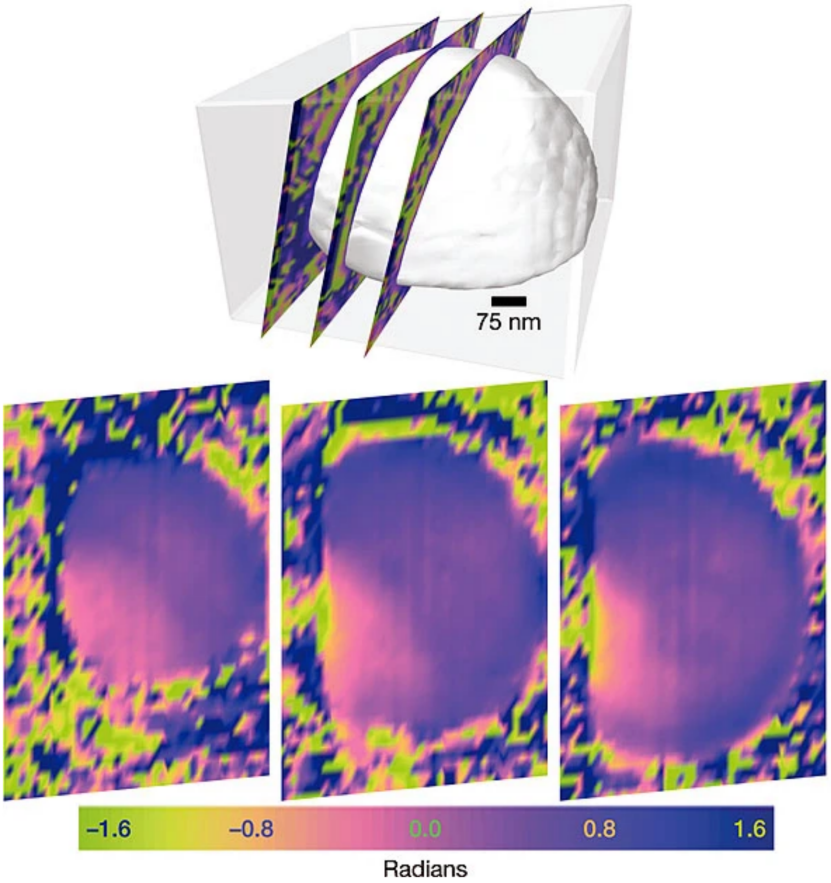

Figure 2.19: The first BCDI reconstruction with both amplitude and phase information. Parallel 2D phase slices through a dewetted Pb microcrystal are taken 138 nm apart. The translucent box is the real space constraint used in phase retrieval, shown here in an orthonormalised coordinate system. There is a change in the phase where the crystal makes contact with the substrate. Image is obtained with permission from Pfeifer *et al.* [137].

rication procedure as Robinson *et al.* [134], Pfeifer *et al.* synthesised Pb nanocrystals on a silicon substrate. With an X-ray source of $\lambda = 0.138$ nm, 50 diffraction patterns were collected with a rocking step size of $0.01°$ about the vertical axis. After phasing the data using a combination of ER and HIO algorithms the object was mapped back to the coordinate frame of the sample in real space, accounting for the sample and detector motor angles explained in Chapter 3. The final reconstruction had a resolution of 40 nm.

This was a groundbreaking moment as it demonstrated that BCDI could provide both morphology and strain information along the direction of the scattering vector. This provides one component of the strain tensor, which can be useful to probe changes in *in situ* or *in operando* experiments (Chapter 2.5.8). However, a single strain component

may be insufficient as some crystal defects, such as dislocations, are visible only when $\mathbf{Q}_{hkl} \cdot \mathbf{b} \neq 0$, where $\mathbf{b}$ is the Burgers vector, which characterises the magnitude and the direction of a dislocation [138]. In theory, it should be possible to recover the full 3D strain tensor if at least three linearly independent reflections are collected, which will allow an unambiguous interpretation of the lattice strain.

2.5.4 Multi-reflection Bragg coherent X-ray diffraction imaging

In 2010, Newton *et al.* measured six linearly independent reflections on ZnO nanorods at beamline 34-ID-C [50] (Fig. 2.20). They were the first to successfully perform MBCDI and calculate the full 3D lattice strain and rotation tensor. Previously, it was difficult to measure multiple reflections because one must know the sample orientation [57]. ZnO nanorods ($2-4$ μm in length, $1-2$ μm in width) were synthesised using chemical vapour deposition and placed onto a silicon substrate using micromanipulation. Since the alignment of these nanorods was known, MBCDI could be performed without the intensive search for Bragg peaks, which would be required for a randomly oriented crystal.

It is generally advantageous to have some knowledge of the orientation of the crystal to perform MBCDI. Otherwise, one might perform a time-intensive search in reciprocal space for two linearly independent Bragg peaks, from which the position of a third reflection can be found more easily. The small volume occupied by a BCDI Bragg peak in reciprocal space made it especially cumbersome to locate it on a small area detector. Thus, MBCDI had been extremely difficult. This served as motivation for a crystal alignment procedure for BCDI samples.

2.5.5 Micro-beam Laue microcrystal alignment

In 2017, Hofmann *et al.* developed an alignment procedure using micro-beam Laue at beamline 34-ID-E at the APS on gold micro-crystals [57]. For this experiment, Laue micro-diffraction measurements were used to determine the **UB** matrix, the orientation of the micro-crystal, which was then used to locate the positions of specific *hkl* reflections

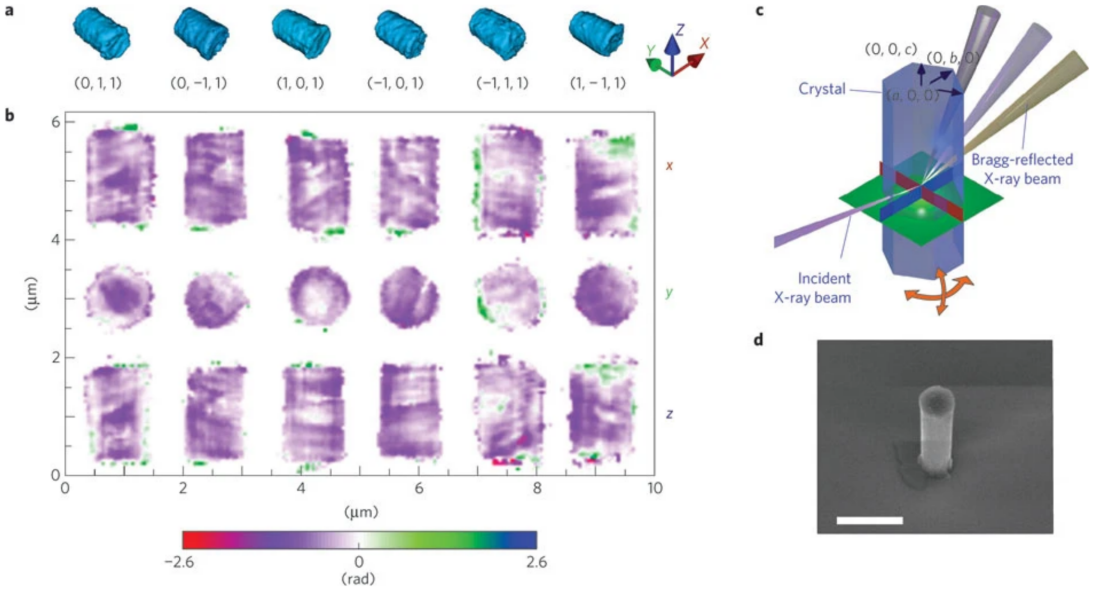

Figure 2.20: The first MBCDI experiment: the reconstruction of the 3D strain tensor of a ZnO nanorod on Si substrate. (a) Isosurfaces of each measured reconstruction with an 86% amplitude threshold. The crystallographic c-axis is parallel to the laboratory y-axis. (b) 2D slices of the reconstructed phases for each reflection, taken from the centre line normal to each axis. (c) Diagram showing the three slices of the phase map in (b) and the multiple Bragg reflections scattering from a single ZnO rod. (d) SEM image of the single ZnO nanorod used in the experiment. The white scale bar corresponds to 2μm. Image is obtained with permission from Newton *et al.* [50].

at beamline 34-ID-C for BCDI experiments. First, at 34-ID-E, the spatial position of the sample was identified using fluorescence, and then a polychromatic beam was used to collect a Laue diffraction pattern from specific microcrystals. Next, this pattern was indexed using *LaueGo* software (J. Z. Tischler, tischler@aps.anl.gov) and the orientation matrix was determined for 34-ID-C. This enabled subsequent MBCDI studies, such as analysing FIB-damaged gold nanocrystals [29, 47] and dislocation structures in tungsten [30], where knowing the 3D strain tensors is crucial for studying defect structures.

Another method to determine the orientation of a sample is by indexing pole figures, provided that a Bragg peak with a known reflection is already found [139]. By collecting a 3D Bragg peak with at least two visible, linearly independent truncation rods, the crystal orientation can be determined. The Bragg peak can be turned into a pole figure that can be indexed using texture analysis software to obtain the crystal orientation. Miller indices of the facets can then be determined from the orientation. This can further enable the study of facets and planar defects (e.g. stacking-faults, antiphase/twin-boundaries) that

also produce rods in reciprocal space [140].

These pre-alignment protocols have not only led to the increased popularity of MBCDI for determining the full strain tensor, [22, 29, 30, 47, 49], but also the integration of pink beam into BCDI beamline 34-ID-C by Pateras *et al.* [141]. In 2020, the commissioning of a double-bounce Si(111) monochromator allows Laue X-ray diffraction to be performed to determine the orientation of crystals. This enables MBCDI measurements of samples without any prior knowledge of lattice orientation. It eliminates the dependence on another X-ray instrument and offers the capability to study a wider range of samples.

2.5.6 FIB sample manufacture

BCDI requires a crystallographically isolated sample that is small enough to fit into the coherent dimensions of the X-ray beam. Most BCDI samples are naturally isolated microcrystals on a substrate. With the exception of studying grains in polycrystalline thin films [142–144], the majority of BCDI samples have been formed by dewetting [134], drop-casting [145], spin casting [146], chemical vapour deposition [14], or a sol-gel process [147]. Studying a macroscopic sample was therefore impossible unless it could exist as an isolated crystal. In 2020, Hofmann *et al.* proposed a new approach using FIB milling to manufacture a micron-sized strained tungsten sample from a macroscopic crystal [30] (Fig. 2.21).

Briefly, a region of interest was first identified using SEM. Next, a protective platinum layer was deposited onto the region of interest. A lamella containing the defect was milled out using FIB and lifted out using an *in situ* micromanipulator. With a second micromanipulator, the liftout lamella was flipped upside down and reattached to the original micromanipulator. The lamella was then welded to a silicon post with the defect centred above the top of the post. Finally, the lamella was shaped using FIB to a volume slightly less than 1 μm $\times$ 1 μm $\times$ 1 μm. MBCDI was performed on this sample, which extended the application of BCDI to any bulk crystalline material.

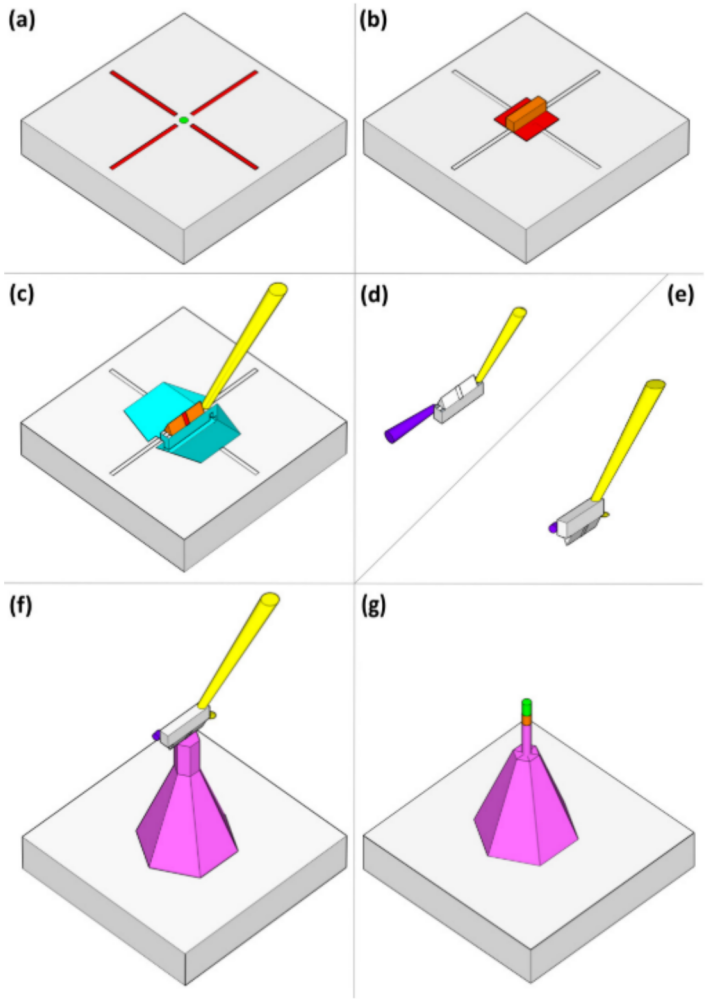

Figure 2.21: BCDI sample manufacture using FIB. (a) A feature of interest (green) is marked using Pt lines (red). (b) A patch of protective Pt (red) is deposited over the feature, then capped with a thick Pt block (orange). (c) A lamella containing the feature is milled out using FIB and lifted using an *in situ* micromanipulator (yellow). (d) The lamella is turned upside down using a second needle (purple) and then reattached to the micromanipulator (e). (f) The lamella is attached to a silicon post (magenta). (g) The lamella is then shaped using FIB to a microcrystal containing the feature of interest. Image is obtained with permission from Hofmann *et al.* [30].

2.5.7 3D Bragg ptychography

Ptychography extends the CDI field of view by rastering across a sample with overlapping illumination spots, recording partially redundant diffraction patterns [148] and was first demonstrated experimentally in 2007 by Rodenburg *et al.* [88]. These overlapping diffraction patterns are fed into a ptychographic iterative algorithm, e.g. PIE [148] and ePIE [149], to reconstruct the object.

Ptychography can be applied to Bragg geometry. BCDI requires a sample that can

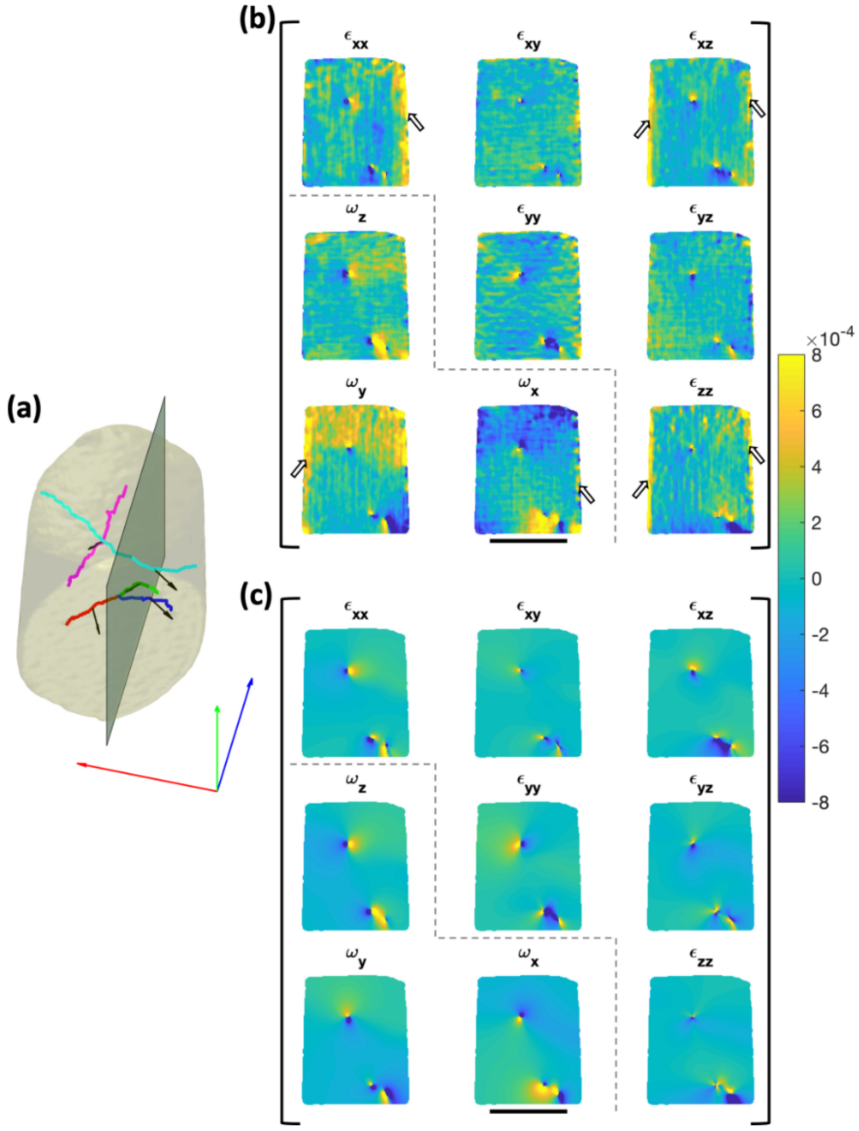

Figure 2.22: 3D strain and rotation tensor components from tungsten sampled extracted from FIB. (a) Rendering of the morphology showing dislocation lines and Burgers vectors (black arrows). Superimposed in green is the y-z plane on which strains in (b) and (c) are plotted. The red, green, and blue arrows, each with a length of 500 nm, correspond to x, y, and z axes respectively. (b) Lattice strains measured using MBCDI. The strain fields of dislocations that intersect the 2D slice can be easily identified. Hollow arrows point to the surface strain associated with residual FIB damage. (c) Lattice strains predicted using a 3D model of the dislocation structures in the sample plotted on the same plane as (b). The scale bar in (b) and (c) is 500 nm. Image is obtained with permission from Hofmann *et al.* [30].

fit inside the coherent dimensions of the beam, which is typically no larger than ~ 1 μm in any dimension. Bragg coherent X-ray ptychography (BP) can be used for samples with larger dimensions. BP was first demonstrated experimentally in 2011 by Godard *et al.* [150] and can be used for larger or weakly scattering samples [74, 150], such as a tungsten foil (Fig. 2.23). A key advantage of ptychography is that the probe overlap

constraint is stronger than the support constraint applied in CDI. This means that BP is potentially much better suited to the measurement of complex crystals with strong phase structure than conventional BCDI. Currently, BP can achieve a spatial resolution of ~ 10 nm and a strain resolution of $\sim 10^4$ [151]. Despite the attraction of measuring larger BCDI samples, BP suffers from positioning errors caused by the alignment of the centre of rotation with beam focus, uncertainty with piezo stage motors, and sample drifts [151].

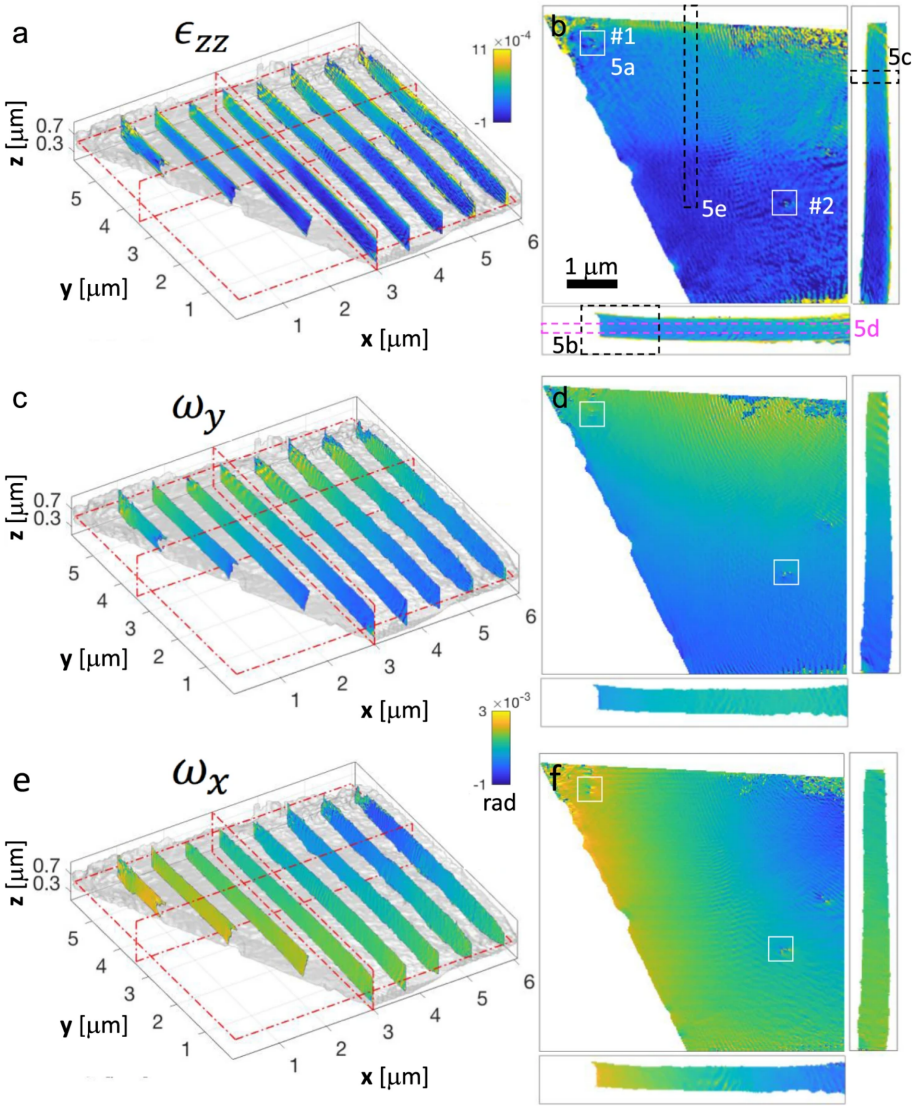

Figure 2.23: A Bragg ptychography reconstruction from an extended He-implanted polycrystalline tungsten foil. (a) A 3D isosurface rendering plot with an ε_{zz} strain map overlay. (b) Cross-section of the ε_{zz} map projected on the red rectangles indicated in (a). (c) 3D isosurface rendering plot with a ω_y lattice rotation overlay. (d) Cross-section of the ω_y map projected on the red rectangles indicated in (c). (e, f) are the same as (c, d) but with a ω_x lattice rotation overlay. Image is obtained from Li *et al.* under the Creative Commons CC BY license [152].

2.5.8 *In situ* and *in operando* BCDI studies

The ability for BCDI to be performed at ambient conditions makes it well-suited for *in situ* or *in operando* experiments. In the past 10 years, BCDI has proven to be a reliable tool for mechanical, electrical, thermal, and chemical experiments. In this section, some *in situ* and *in operando* experiments are listed and used to briefly describe how BCDI uniquely enables new information to be obtained.

The miniaturisation of structures has drawn considerable attention to the strength of nanomaterials. *In situ* mechanical experiments using BCDI enable localised strain fields to be observed as a function of the applied load. Recently, a Au microcrystal loaded with an AFM tip [153], a Au microcrystal pressed in a diamond-anvil cell [154] and a Au polycrystalline thin film subject to thermo-mechanical loading [144] have been studied. These sample environments are challenging to implement for TEM, but accessible with BCDI. Furthermore, BCDI allows for larger, sub-micron sample volumes compared to *in situ* TEM foil samples, enabling the visualisation of dislocation, morphology and strain field evolution during applied loads [153].

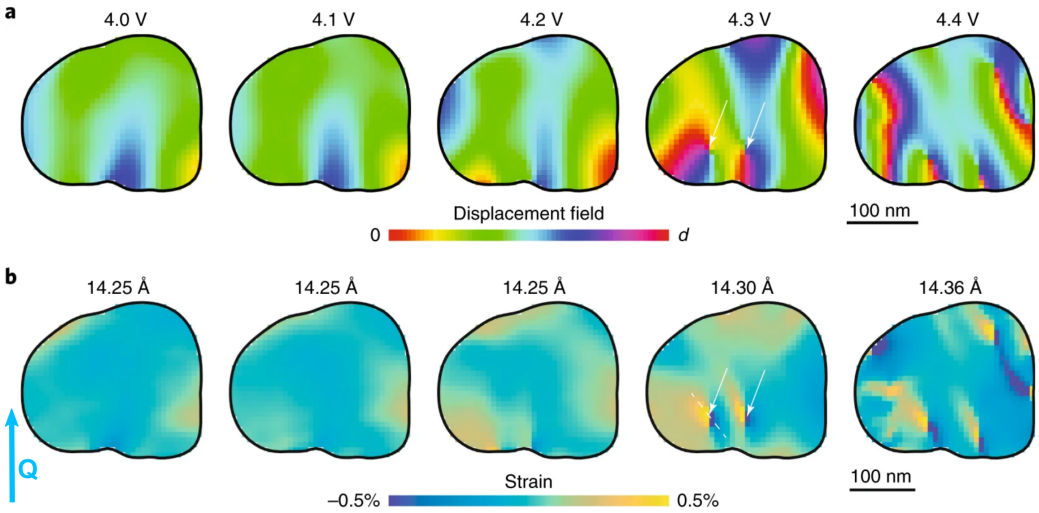

Figure 2.24: *In situ* evolution of a lithium-rich layered oxide nanoparticle during electrochemical charge. (a) 2D slices showing displacement field evolution along **Q** in a plane through the nanoparticle during charge. At 4.3 V, edge dislocations start to appear, indicated by white arrows. More dislocations appear at 4.4V. (b) 2D slices showing strain field evolution, perpendicular to the layered oxides, along the [001] direction. Voltage shown is with respect to Li^+. Image is modified with permission from Singer *et al.* [155].

Energy storage technology is increasingly in demand due to growing energy needs. *In*

operando BCDI electrical experiments enable the study of how defects in battery materials interact with an applied voltage, as the defects become mobile during charge transport. Examples of such BCDI studies on battery cathode materials include investigating topological defect dynamics [156], charge-discharge cycles [157], battery charging [155] (Fig. 2.24), and disconnection events [158]. The 3D strain information allows for the interpretation of different phases and how they change in response to an electrical bias; information that is inaccessible with any other technique.

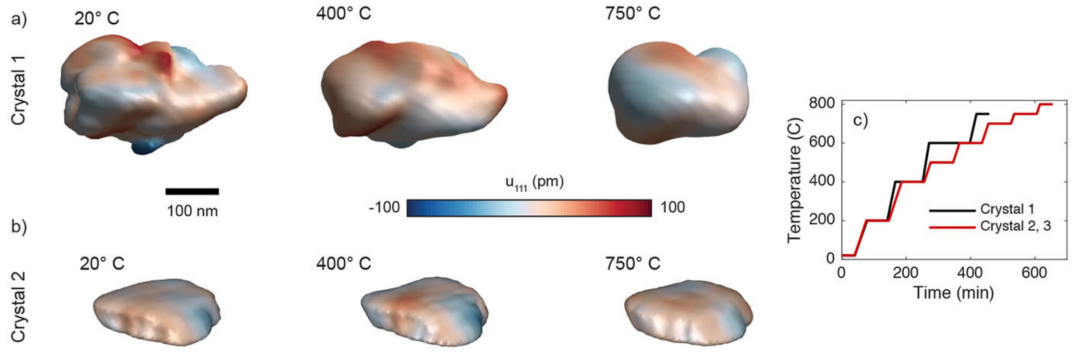

Figure 2.25: *In situ* BCDI annealing of nanodiamonds. (a) and (b) show crystals 1 and 2 respectively, at different stages during annealing. The morphology of reconstructions is coloured according to the near-surface displacement in the [111] direction. The temperature profile of the annealing is shown in (c). Image is obtained from Hruszkewycz *et al.* under the Creative Commons CC BY license [55].

Annealing is a process that allows for phase transitions as well as atomic diffusion within a crystal. *In situ* BCDI annealing experiments enable the study of how defects annihilate and interact with crystal surfaces. Furthermore, annealing allows for the diffusion of other elements to occur inside the crystal, enabling the study of diffusion mechanisms. Annealing in nanodiamonds [55] (Fig. 2.25), Fe diffusion into Au nanocrystals [56], and tetragonal-cubic phase transitions in $BaTiO_3$ nanocrystals [159] have been monitored using *in situ* BCDI. These results can lead to strain engineering in semiconductors [55] and the use of controlled diffusion to tailor specific material properties [56].

Chemical activity remains an important area for catalysis. *In situ* BCDI experiments enable the study of nanoparticle catalysts and interact with their environment. Furthermore, corrosion and oxidation remain key challenges in many industries. BCDI enables key information about 3D crystal morphology and strain evolution inaccessible to many

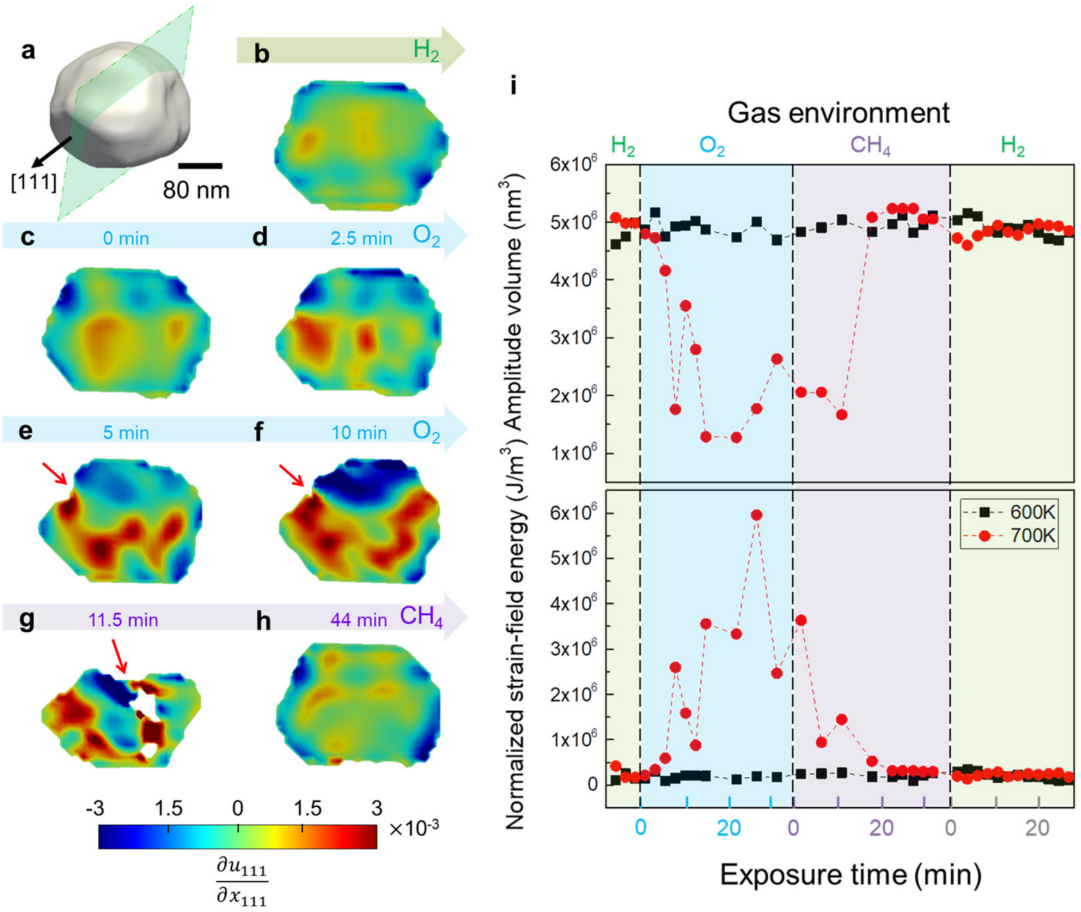

Figure 2.26: *In situ* BCDI oxidation of a Pt nanoparticle. (a) An isosurface rendering of the 111 reconstruction of a Pt nanoparticle in H_2. A green slice represents the position of the cross-sections. The strain evolution is based on gas environments. First in (b) H_2, followed by O_2 for (c) 0, (d) 2.5, (e) 5, and (f) 10 min. Next in CH_4 for (g) 11.5 and (h) 44 min. The red arrows indicate points that have compressive and tensile strains. (i) Shows the 111 amplitude volume (top) and normalised strain-field energy (bottom) as a function of time exposed to gas flows above (red circle) and below (black square) the activation temperature. Image is obtained with permission from Kim *et al.* [160].

EM techniques. Both aqueous and gas sample environments have been demonstrated, including catalytic oxidation on Pt nanocrystals [160] (Fig. 2.26), electrochemical strain evolution in Pt-Ni alloy nanoparticles [161] and dealloying in Au-Ag nanoparticles and thin film polycrystals [162]. These studies uniquely enable connections between chemical activity, lattice strain, and morphology.

While *in situ* or *in operando* BCDI enables samples in real operating environments to be measured, there remain several challenges. The first is sample stability. Conventional measurement of a Bragg peak requires rocking the crystal across an angular range of $\sim 1°$, which can pose issues in a sample environment with moving fluids. A way to circumvent

this issue is to use a variable-wavelength BCDI (vwBCDI) scan [81], where the sample is fixed at the Bragg condition but the X-ray energy is varied. This causes the length of the scattering vector to change. Compared to rocking, changing the energy is uncommon because it requires a monochromator that can be scanned in an automated fashion with minimal beam shift. The reconstruction is also more complicated as the pixel size and 3D Fourier transform must be modified to account for the changes in wavelength [81].

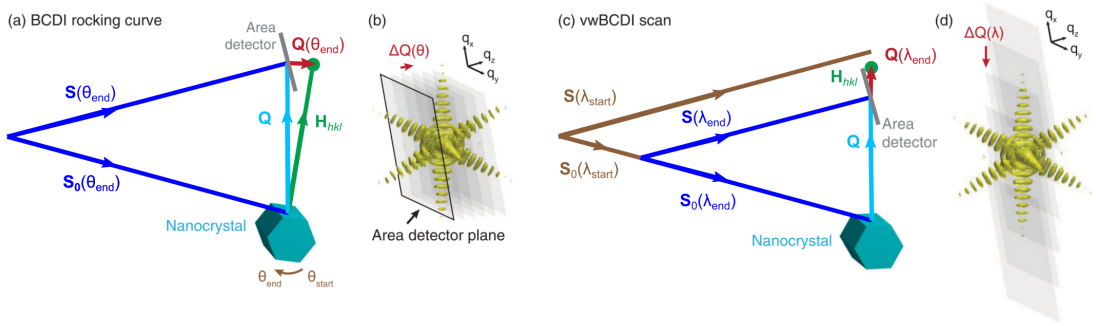

Figure 2.27: Comparing single energy BCDI to variable-wavelength BCDI (vwBCDI). A nanocrystal illuminated with a coherent X-ray and oriented such that the incident ($\mathbf{S}_0$) and exit ($\mathbf{S}$) beam wave vectors satisfy a Bragg condition, $\mathbf{Q} = \mathbf{H}_{hkl}$. To measure various components of the 3D Bragg peak intensity distribution, the scattering condition $\mathbf{Q} = \mathbf{S} - \mathbf{S}_0$ must be changed relative to $\mathbf{H}_{hkl}$. In a single energy BCDI rocking curve (a, b), this is done by changing the angle of the the Bragg peak. For vwBCDI (c, d), this is done by fixing the sample and changing the X-ray wavelength. Image is adapted with permission from Cha *et al.* [81].

Since it takes roughly 5-15 minutes to collect a CXDP with an acceptable signal-to-noise ratio, *in situ* and *in operando* BCDI studies can only resolve "slow" dynamics in a continuous process. Signal-to-noise ratio can be improved with longer exposure times and repeated measurements, but this comes at the expense of temporal resolution. Time-resolved BCDI reconstructions have been improved by reducing the oversampling requirement along the rocking curve dimension at each time step [94]. The rocking curves across the entire time series are reconstructed simultaneously to enforce a real space correlation between reconstructions at neighbouring time steps. This can increase the overall temporal resolution by a factor of 2-20 times [94]. Furthermore, continuous scanning has recently been developed for BCDI, which allows for up to 30% reduction in total scan time [163]. Continuous scanning refers to acquisitions where the sensor readings and actuator movements are concurrent, rather than sequential. This method removes the

overhead of step-settle-acquire scans while giving similar results [163]. This can be combined with time-resolved BCDI reconstructions to increase the temporal resolution for *in situ* and *in operando* BCDI studies

2.5.9 X-ray free electron lasers

Since 2009, newly developed X-ray free electron lasers (XFELs) have opened up the potential for ultrafast BCDI studies. In XFELs, the electrons are accelerated into a long undulator, causing the electrons to oscillate and emit bunches of highly coherent and brilliant X-rays with $\sim 10^{12}$ photons per pulse and ~ 100 fs pulse duration [164]. This has enabled ultrafast BCDI studies using an excitation laser followed by a coherent X-ray probe pulse. By varying the delay between the pump and probe, XFEL-based BCDI experiments have been performed to study acoustic phonon dynamics [165,166] and transient melting [167]. XFELs are capable of extending BCDI beyond steady-state experiments and are expected to increase in popularity due to the recent commissioning of the European XFEL (Germany, 2017), PAL-XFEL (South Korea, 2017), SwissFEL (Switzerland, 2019). The high intensity of XFELs brings its own challenges, for example, sample radiation damage, which would require several identical samples to be prepared for an experiment.

2.6 Summary of literature review

This literature review covered the fundamental theory behind BCDI and how it has evolved into an X-ray microscopy technique that uniquely allows the determination of 3D lattice strains in relatively large volumes. BCDI relies on high brilliance coherent X-rays that can be focused onto a crystal no larger than the X-ray's temporal coherence length. As the X-rays interact with a crystalline sample, they are elastically scattered to produce a diffraction pattern in the Fraunhofer regime. The collection of this diffraction pattern involves rocking the sample about a coordinate axis, which tilts the reciprocal space through

the Ewald's sphere. 2D slices through the CXDP are recorded and stacked to form the reciprocal space constraint for the phase retrieval algorithm. Proper oversampling of the diffraction pattern by at least twice the Nyquist frequency or 2 pixels per fringe along one dimension in the CXDP allows for the complex crystal electron density to be recovered using phase retrieval algorithms.

The most common phase retrieval algorithms for BCDI involve alternating between ER and HIO methods. They involve applying real space and reciprocal space constraints to converge the solution towards a local minimum. Incorporating these methods into a guided algorithm with partial coherence correction and support shrinkwrap produces faithful reconstructions, based on χ^2 and sharpness metrics, throughout this thesis. The result after phase retrieval is the complex crystal electron density. The magnitude corresponds to the real crystal electron density and the phase represents the projection of the crystal displacement field onto the scattering vector. If at least three Bragg peaks are measured, the strain and rotation tensors can be calculated.

The idea of recovering the phase from a diffraction pattern came from Sayre in 1952 [37]. However, due to the unavailability of a coherent X-ray source as well as computation limitations, this was not demonstrated until 1999 by Miao *et al.* [41] on a noncrystalline sample using synchrotron X-rays. This was the first demonstration of CDI, proving that early work on phase retrieval algorithms had been successful [38–40, 85, 168]. Following this 2D CDI experiment, in 2002 Miao demonstrated the first 3D CDI experiment using tomography and stacked the diffraction patterns together to form a 3D pattern to be phased, which successfully recovered the sample [133].

In 2001, Robinson *et al.* performed the first demonstration of CDI for a Bragg reflection of a Au microcrystal [134]. Although only a 2D image of the crystal was reconstructed, in 2003 Williams *et al.* demonstrated the collection of a 3D CXDP by rocking the crystal and were able to reconstruct the electron density. The first BCDI experiment where the phase was recovered was in 2006 by Pfeifer *et al.* [137]. This enabled BCDI to become an extremely powerful technique to probe lattice strains since the phase is directly

related to the displacement field (Eq. 2.44).

Since then, BCDI has been used to study a wide range of crystals, including noble metals [134, 142, 169], alloys [161, 162], geological compounds [95, 170, 171], semiconductors [50, 107, 172], and functional materials [117, 147]. Furthermore, it now enables any bulk material to be studied using FIB fabrication [30]. Crystals that far exceed the coherent dimensions of the X-ray can be compatible with Bragg ptychography [74,150,173].

An extension of the BCDI technique, MBCDI, was first performed in 2010 by Newton *et al.* to reconstruct the full strain and rotation tensors for a single ZnO rod [50]. MBCDI has been a very useful tool to study crystal defects [22, 29, 30, 47] but requires the crystal orientation to be known. A micro-beam Laue alignment procedure has been documented for the determination of the orientation for BCDI in 2017 [57], which allows for the rapid determination of accessible Bragg peaks.

BCDI has matured to enable plenty of *in situ* and *in operando* studies in the past decade. Notable applications include battery charging [155, 157], thermal diffusion [56, 174], dissolution [95], applied pressure [153,154] and catalytic oxidation [54,169]. XFEL-based BCDI studies are capable of studying transient processes [165–167] beyond conventional BCDI, and will increase in popularity as more XFELs are commissioned. To accompany the variety of crystals that need to be recovered, phase retrieval has matured to include partial coherence correction [99] as well as guided algorithms [93]. Particular focus is now on using machine learning to predict the amplitude and phase of the measured crystals [175]. The speed and accuracy of these advanced machine learning tools will enable greater data throughput from fourth-generation synchrotron sources.

In preparation for the next generation of synchrotron X-ray sources for BCDI, this thesis develops refinements for the BCDI technique and applies them to *in situ* studies. The next chapter will cover the correct coordinate transformations required to interpret the reconstruction in orthonormalised coordinates for any detector geometry. This will be followed by outlining a reliable procedure for using EBSD to orient samples for BCDI and highlighting a more efficient and accurate method to calculate the strain fields for

each reflection. These methods are applied to *in situ* BCDI experiments in annealing and corrosion to explore nanoscale lattice strain evolution.

Chapter 3

Mapping data between sample and detector conjugated spaces in Bragg coherent diffraction imaging

Here I cover the methodology behind the 3D space transformations, which are required in subsequent chapters to properly interpret the recovered amplitude and phase in orthonormalised sample coordinates. This is motivated by the need to interpret crystal reconstructions from different reflections in a common sample coordinate frame, which is now routinely performed in BCDI experiments. Prior to this, there have been published articles that show reconstructions with incorrect coordinate transformations, which led to the inaccurate analysis of the reconstruction's amplitude and phase. This chapter has been published as: D. Yang, N. W. Phillips, and F. Hofmann, "Mapping data between sample and detector conjugated spaces in Bragg coherent diffraction imaging," *Journal of Synchrotron Radiation*, vol. 26, no. 6, pp. 2055–2063, 2019 [43].

N.W. Phillips provided the tungsten laboratory BCDI data. The remainder of the work was carried out by the author under the supervision of F. Hofmann.

3.1 Abstract

Bragg coherent X-ray diffraction imaging (BCDI) is a non-destructive, lensless method for 3D-resolved, nanoscale strain imaging in microcrystals. A challenge, particularly for new users of the technique, is accurate mapping of experimental data, collected in the detector reciprocal space coordinate frame, to more convenient orthogonal coordinates, e.g. attached to the sample. This is particularly the case since different coordinate conventions are used at every BCDI beamline. The reconstruction algorithms and mapping scripts composed for individual beamlines are not readily interchangeable. To overcome this, a BCDI experiment simulation with a plugin script that converts all beamline angles to a universal, right-handed coordinate frame is introduced, making it possible to condense any beamline geometry into three rotation matrices. The simulation translates a user-specified 3D complex object to different BCDI-related coordinate frames. It also allows the generation of synthetic coherent diffraction data that can be inserted into any BCDI reconstruction algorithm to reconstruct the original user-specified object. Scripts are provided to map from sample space to detector conjugated space, detector conjugated space to sample space and detector conjugated space to detector conjugated space for a different reflection. This provides the reader with the basis for a flexible simulation tool kit that is easily adapted to different geometries. It is anticipated that this will find use in the generation of tailor-made supports for phasing of challenging data and exploration of novel geometries or data collection modalities.

3.2 Introduction

BCDI is an increasingly popular technique, but its disadvantage is the relatively high barrier to entry. It requires access to coherent diffraction beamlines at select synchrotrons, each with different geometry conventions. Here we introduce a BCDI simulation program with a beamline-specific plugin script that simplifies the geometry for a beamline by converting all motor rotation angles to a right-handed convention and generates three

fundamental matrices that fully describe the measurement (see Section 3.3). The simulation provides both the tools and the underlying theory required to move with ease between BCDI-related spaces. A challenge in the community is mapping between these spaces, particularly between detector conjugated space (DCS), where the measurement and phase retrieval are typically performed, and an orthogonal sample space (SS) attached to the object of study. We introduce three scripts that allow the reader to map from sample space to detector conjugated space, detector conjugated space to sample space, and detector conjugated space to detector conjugated space for a different crystal reflection. These scripts also incorporate the beamline-specific plugin, making them readily adaptable to any geometry.

3.3 Simulation geometry

This section covers the geometry that is used in the computer scripts and in Section 3.4. A schematic of the simulated geometry is shown in Fig. 3.1. The laboratory coordinates are oriented such that the incident X-ray beam is in the direction of the positive z-axis, the y-axis is vertically up and the x-axis is outboard to the left. Here the following coordinates are used to describe the various spaces:

$$\begin{aligned}
\text{Sample Space (SS)} &: \mathbf{x}_{\text{sam}},\ \mathbf{y}_{\text{sam}},\ \mathbf{z}_{\text{sam}},\\
\text{Lab Space (LS)} &: \mathbf{x},\ \mathbf{y},\ \mathbf{z},\\
\text{Reciprocal Lab Space (RLS)} &: \mathbf{q}_{\text{x}},\ \mathbf{q}_{\text{y}},\ \mathbf{q}_{\text{z}},\\
\text{Detector Reciprocal Space (DRS)} &: \mathbf{q}'_1,\ \mathbf{q}'_2,\ \mathbf{q}'_3,\\
\text{Detector Conjugated Space (DCS)} &: \mathbf{x}',\ \mathbf{y}',\ \mathbf{z}'.
\end{aligned} \tag{3.1}$$

The detector has two angles of rotation: δ and γ, which rotate about the y-axis and x-axis, respectively, when angles are set to zero as shown by [57], and all rotations adhere to a right-handed convention. The diffraction pattern is generated as if the detector were look-

ing down onto the sample (as opposed to a projection onto a film). Explicitly, this means that if there is a diffraction pattern on the detector screen, decreasing γ will move the detector up in the y or $\mathbf{q}_2'$ direction, and the peak will move down on the screen. Similarly, decreasing δ will move the detector to the right as $\mathbf{q}_1'$ increases and the peak will move left on the screen. The sample stage has three angles of rotation: χ, ϕ, and θ, which rotate about the z-axis, x-axis, and y-axis respectively, when angles are set to zero, also shown by [57]. If the sample is rocked about the y-axis by an increment of $\Delta\theta$ from negative to positive, this corresponds to collecting slices through the Bragg peak along the $\mathbf{q}_3'$ direction. In the case of the instrumentation at 34-ID-C, angular limits imposed by stage travel ranges need to be considered, as certain geometries are inaccessible (Appendix A.1).

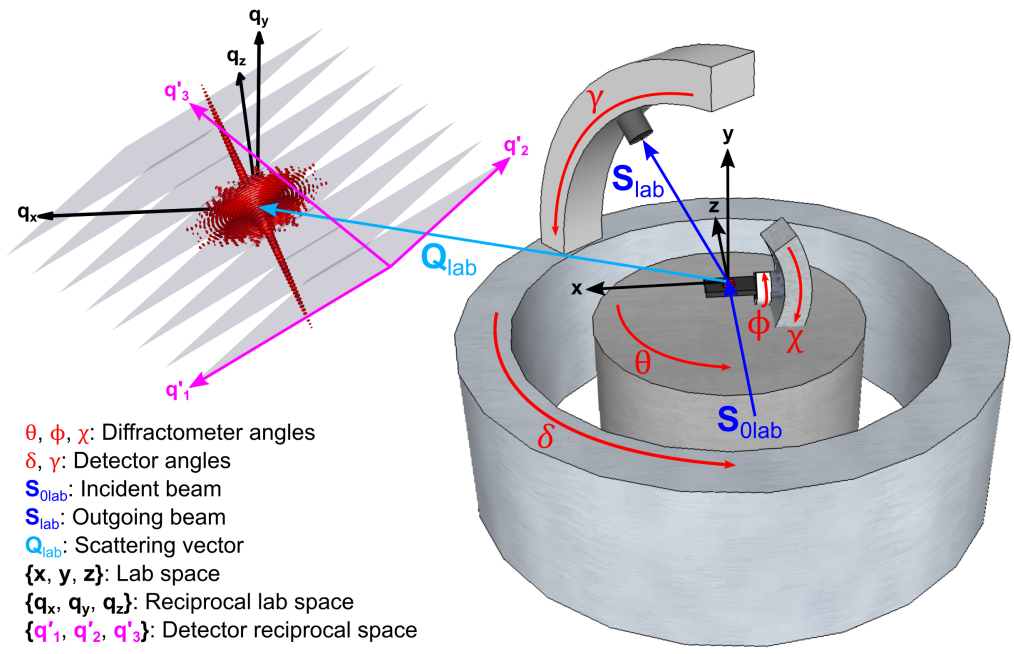

Figure 3.1: A schematic of the simulated experimental geometry showing 2D slices through the 3D Bragg peak as a consequence of rocking about the y-axis. Diffractometer angles, θ, ϕ, and χ, as well as detector angles δ and γ, are labelled with the red arrows pointing in the positive direction of rotation. $\mathbf{S}_{0\text{lab}}$ and $\mathbf{S}_{\text{lab}}$ represent the incident and reflected X-ray beams respectively. $\mathbf{Q}_{\text{lab}}$ is the scattering vector. Three coordinate frames are shown: lab space ($\mathbf{x}$, $\mathbf{y}$ and $\mathbf{z}$), reciprocal space ($\mathbf{q}_x$, $\mathbf{q}_y$ and $\mathbf{q}_z$) and detector reciprocal space ($\mathbf{q}_1'$, $\mathbf{q}_2'$ and $\mathbf{q}_3'$).

Overall, the geometry of a BCDI experiment requires three rotation matrices to fully describe the affine transformation between coordinate systems: $R_{\text{x,y,z}}$, $R_{\Delta q'_{1,2}}$, and $R_{\Delta q'_3}$, which correspond to the rotation matrices of the sample, detector and rocking axis re-

spectively. Once defined, the BCDI simulation and mapping can be carried out for any beamline.

3.4 Computer codes

A program, `BCDI_Simulation`, found at 10.5281/zenodo.3347113, and three scripts, `SS_to_DCS`, `DCS_to_DCS` and `DCS_to_SS`, available at 10.5281/zenodo.3347109, are published with this work. For the most updated version of the codes, the reader is asked to visit github.com/Hofmann-Group. The recommended machine requirements for these codes are: MATLAB version 2018b or later, 8GB RAM, an Intel or AMD x86-64 processor with four cores, and at least 2GB of free hard disk space. The use of an advanced research computing facility will greatly reduce computation time. For instance, the authors used the University of Oxford Advanced Research Computing (ARC) facility for this work [176]. The maximum recommended complex double array size for these settings is $256 \times 256 \times 256$, which can be saved as a separate `.mat` file. In this chapter, a script refers to a single MATLAB file, a program refers to a script that calls upon other scripts, and a code can refer to both scripts and programs.

3.4.1 Bragg coherent X-ray diffraction imaging simulation

The program, `BCDI_Simulation`, allows the simulation of a BCDI experiment starting with a user-defined shape (a 3D complex double array). Similar to a laboratory experiment, the reader is required to input the X-ray wavelength, pixel size, detector size, *hkl* reflection (or detector and sample position angles), rocking increment, rocking axis and detector distance. Alternatively, the **UB** matrix can be input if micro-beam Laue diffraction was used to pre-determine the lattice orientation of the sample [57]. Using the inputs, the program translates and plots the shape in five different spaces: sample space (SS), lab space (LS), reciprocal lab space (RLS), detector reciprocal space (DRS) and detector conjugated space (DCS); these spaces are described in detail in Section 3.5 and are shown

in Fig. 3.2. The simulation also produces a TIFF file containing 2D diffraction pattern slices through the simulated Bragg peak, which can be fed into a reconstruction algorithm, e.g. [99] to reconstruct the user-defined shape in LS and DCS. Accordingly, the simulated shapes can be compared with the reconstructed shapes. At the time of writing, the code's geometry is based on beamline 34-ID-C at the APS because it is a heavily used instrument in the history of BCDI. This beamline uses both left- and right-handed geometry while the simulation assumes only right-handed rotations. Embedded in the simulation is a script, `plugin_APS_34IDC` which converts these 34-ID-C conventions to the simulation's right-handed system for simplicity and generates the fundamental BCDI rotation matrices described in Section 3.3. The simulation can be easily adapted to any beamline.

3.4.2 Space transformation scripts

There are three MATLAB scripts that allow the transformation between various spaces involved in the BCDI reconstruction process. The inputs and outputs are all 3D complex MATLAB arrays. Two of the scripts have the option to create binary masks (based on a thresholded input amplitude) in DCS for a specific *hkl* of an object. The first, `SS_to_DCS`, will allow a reader to create a mask from a previously constructed SS shape, and the second, `DCS_to_DCS`, allows creation of a mask from a previously constructed DCS shape for a different *hkl* reflection. These phasing masks can be turned into "supports" by convolution with a Gaussian and thresholding to ensure that the support is about 10% larger than the mask. A support is often used as a starting guess in phase retrieval algorithms, where the phase of the diffraction pattern is obtained by mapping between DCS and DRS, applying real and reciprocal constraints, and updating the support every few iterations. These supports are used to set the outside amplitude to zero, since the object is assumed to be contained [50]. Having scripts to produce supports based on prior knowledge (e.g. a sample shape or measured reflection) is expected to aid in the convergence of solutions and produce more accurate reconstructions [89]. The third script, `DCS_to_SS` transforms a DCS shape to SS. Transformations to and from the SS is particularly useful for MBCDI,

which involves reconstructions from three or more different reflections to recover the full lattice strain tensor [29, 47]. By setting the sample motor angles to their zero positions, one can recover the LS shape instead of the SS shape, as explained in Section 3.5.1. Each of these scripts uses the beamline-dependent plugin as used in the simulation. We are working on creating plugins for other beamlines — contact the authors if you would like this code to be extended to your instrument.

3.5 Space transformations

This section pertains to the BCDI spaces in `BCDI_Simulation`, shown in Fig. 3.2. In the following, an outline is presented: Beginning from SS (i.e. the free standing object in its own reference frame), the goniometer rotates the specimen to LS, applying $R_{\mathrm{x,y,z}}$ on the SS basis vectors. The $\mathscr{F}$ is applied to LS, or equivalently, $\mathscr{F}[\mathrm{LS}]$, converting LS to RLS and taking the reciprocal of the LS basis vectors. The phase of the real space object is obtained as $\psi(\mathbf{r}) = \mathbf{Q}_{\mathrm{lab}} \cdot \mathbf{u}(\mathbf{r})$, which is stored in a variable rather than being recovered through an iterative algorithm. Next, the RLS is transformed to the DRS, where the measured Bragg peak lives, by applying detector and rocking matrices $R_{\Delta q'_{1,2}}$ and $R_{\Delta q'_3}$, in that order, to the RLS basis vectors. The inverse Fourier transform is applied, $\mathscr{F}^{-1}[\mathrm{DRS}]$, to get the DCS shape, turning the DRS basis vectors into detector conjugated real space vectors. Finally, the LS is recovered by applying the coordinate transform matrices, $R^{-1}_{\Delta q'_3}$ and $R^{-1}_{\Delta q'_{1,2}}$, in that order, to the DCS basis vectors.

To simplify, the simulation follows the following space transformation path: SS $\rightarrow$ LS $\rightarrow$ RLS $\rightarrow$ DRS $\rightarrow$ DCS $\rightarrow$ LS. For a laboratory BCDI experiment and reconstruction, the path is: DRS $\rightarrow$ DCS $\rightarrow$ LS. The SS and RLS steps are added in the simulation for clarity.

In each space the object, or its associated diffraction pattern, reside in a 3D pixel array. The basis vectors, calculated in the following subsections, capture how one moves from one pixel to the next along each axis in each space. If old basis vectors are given by $\mathbf{a}_1$,

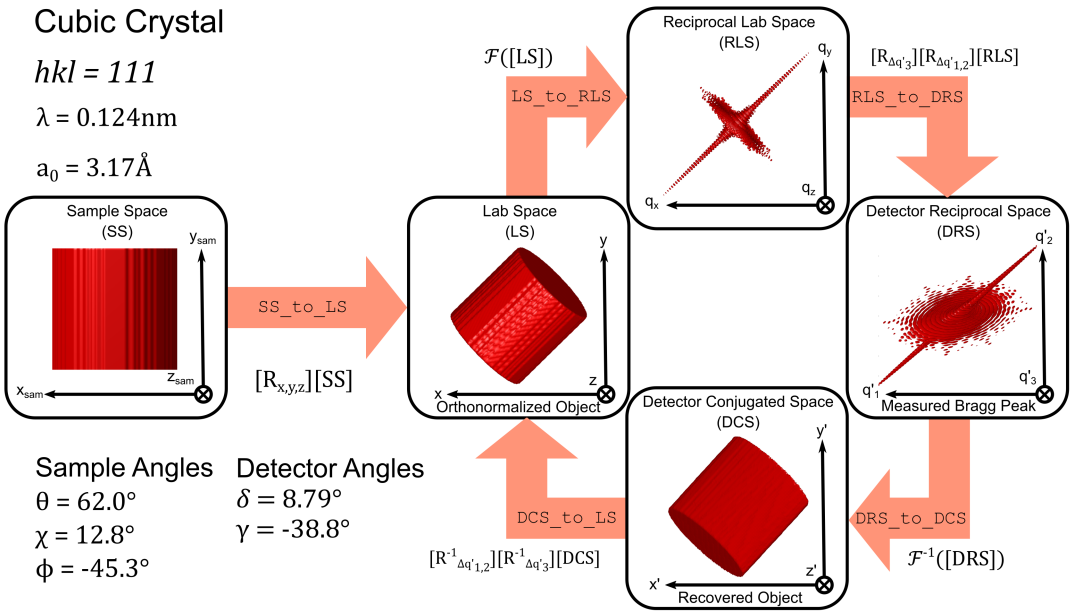

Figure 3.2: Coordinate reference spaces in the MATLAB simulation for a simulated cubic crystal cylinder at $hkl = (111)$, $a_0 = 3.17$ Å and $\lambda = 0.124$ nm based on the simulation geometry in Fig. 3.1. Mathematical operations that convert from one space to another are shown, along with their respective MATLAB script names inside the arrows.

$\mathbf{a}_2$ and $\mathbf{a}_3$ and new basis vectors are given by $\mathbf{b}_1$, $\mathbf{b}_2$ and $\mathbf{b}_3$, the transformation matrix, T, can be written as

$$T = \begin{bmatrix} | & | & | \\ \mathbf{a}_1 & \mathbf{a}_2 & \mathbf{a}_3 \\ | & | & | \end{bmatrix} \begin{bmatrix} | & | & | \\ \mathbf{b}_1 & \mathbf{b}_2 & \mathbf{b}_3 \\ | & | & | \end{bmatrix}^{-1}. \tag{3.2}$$

Once the basis vectors are known, the mapping of an array from one space to another can be achieved by linear interpolation in MATLAB: `new_array = interp3(a1grid, a2grid, a3grid, old_array, b1grid, b2grid, b3grid)`, where `a1grid`, `a2grid` and `a3grid` are the original meshgrid coordinates with pixel number along each axis. `b1grid`, `b2grid` and `b3grid` correspond to the new meshgrid coordinates transformed by T in equation (3.2). Here all basis vectors are defined in a global coordinate frame that is aligned with the lab coordinate frame.

3.5.1 Sample space to lab space

The SS frame is the reference frame attached to the sample. This is how the sample appears on the mount, before rotating to the required geometry for any given Bragg con-

dition. SS unit vectors are denoted by $\hat{\mathbf{x}}_{\text{sam}}$, $\hat{\mathbf{y}}_{\text{sam}}$, and $\hat{\mathbf{z}}_{\text{sam}}$. To convert these unit vectors to basis vectors, we multiply by a sample pixel size, $\text{p}_{\text{sam}_\text{x}}$, $\text{p}_{\text{sam}_\text{y}}$ or $\text{p}_{\text{sam}_\text{z}}$, [1]

$$\begin{aligned}
\mathbf{x}_{\text{sam}} &= \text{p}_{\text{sam}_\text{x}}\hat{\mathbf{x}}_{\text{sam}}, \\
\mathbf{y}_{\text{sam}} &= \text{p}_{\text{sam}_\text{y}}\hat{\mathbf{y}}_{\text{sam}}, \\
\mathbf{z}_{\text{sam}} &= \text{p}_{\text{sam}_\text{z}}\hat{\mathbf{z}}_{\text{sam}}.
\end{aligned} \tag{3.3}$$

When all sample angles, χ, ϕ, and θ, are zero, SS and LS are aligned. The sample is rotated by $R_{\text{x,y,z}}$ such that it is in the LS coordinate frame. The sample rotation matrix is

$$R_{\text{x,y,z}} = [R_{\text{y}}(\theta)][R_{\text{z}}(\chi)][R_{\text{x}}(\phi)], \tag{3.4}$$

where R_{y} is a right-handed rotation θ about the y-axis, R_{z} is a right-handed rotation χ about the z-axis, and R_{x} is a right-handed rotation ϕ about the x-axis. To map a position in the SS coordinate frame, $\mathbf{r}_{\text{SS}}$, to the LS coordinate frame, i.e. find $\mathbf{r}_{\text{LS}}$, we simply apply equation (3.4) to $\mathbf{r}_{\text{SS}}$, i.e. $\mathbf{r}_{\text{LS}} = [R_{\text{x,y,z}}][\mathbf{r}_{\text{SS}}]$. Thus, to obtain SS basis vectors in the global coordinate frame, we apply

$$\begin{aligned}
[\mathbf{x}_{\text{sam}}]_{\text{LS}} &= [R_{\text{x,y,z}}][\mathbf{x}_{\text{sam}}], \\
[\mathbf{y}_{\text{sam}}]_{\text{LS}} &= [R_{\text{x,y,z}}][\mathbf{y}_{\text{sam}}], \\
[\mathbf{z}_{\text{sam}}]_{\text{LS}} &= [R_{\text{x,y,z}}][\mathbf{z}_{\text{sam}}].
\end{aligned} \tag{3.5}$$

The LS basis vectors, $\mathbf{x}$, $\mathbf{y}$ and $\mathbf{z}$ are aligned with the axes of the lab frame (and the global reference frame), and their size, i.e. the pixel size, should be the same as in SS because both LS and SS coordinate frames are in orthogonal real space. We use T from equation (3.2) to then carry out the mapping.

[1] As a guide, $\text{p}_{\text{sam}_{\text{x,y,z}}} = \frac{\lambda D}{dN_{1,2}}$, where λ is the X-ray wavelength, D is the detector distance, d is the detector pixel size and N_1 and N_2 correspond to the number of steps or pixels in the data array in LS and RLS [56].

3.5.2 Lab space to reciprocal lab space

The LS is the reference space when a specific Bragg condition is being satisfied, in other words, as the sample sits when mounted on the goniometer at a beamline. To convert from LS to RLS, the $\mathscr{F}$ is applied to the array. For ease of simulation, prior to incorporating the position of the detector relative to the sample, we consider the complex wavefield plotted on an orthonormal reciprocal space coordinate grid. To convert from LS to RLS basis vectors, we apply the following operations,

$$\begin{aligned} V_{\mathrm{LS}} &= \mid (N_1\mathbf{x} \times N_2\mathbf{y}) \cdot N_3\mathbf{z} \mid \\ &= \mid \left(N_1 \mathrm{p}_{\mathrm{sam_x}}\hat{\mathbf{x}} \times N_2 \mathrm{p}_{\mathrm{sam_y}}\hat{\mathbf{y}}\right) \cdot N_3 \mathrm{p}_{\mathrm{sam_z}}\hat{\mathbf{z}} \mid \\ &= N_1N_2N_3 \mathrm{p}_{\mathrm{sam_x}} \mathrm{p}_{\mathrm{sam_y}} \mathrm{p}_{\mathrm{sam_z}} \quad \text{(Since } \hat{\mathbf{x}}\text{, } \hat{\mathbf{y}} \text{ and } \hat{\mathbf{z}} \text{ are orthogonal)}, \end{aligned} \tag{3.6}$$

$$\begin{aligned} \mathbf{q}_{\mathrm{x}} &= \frac{2\pi}{V_{\mathrm{LS}}}(N_2\mathbf{y} \times N_3\mathbf{z}) = \frac{2\pi}{N_1 \mathrm{p}_{\mathrm{sam_x}}}\hat{\mathbf{x}}, \\ \mathbf{q}_{\mathrm{y}} &= \frac{2\pi}{V_{\mathrm{LS}}}(N_3\mathbf{z} \times N_1\mathbf{x}) = \frac{2\pi}{N_2 \mathrm{p}_{\mathrm{sam_y}}}\hat{\mathbf{y}}, \\ \mathbf{q}_{\mathrm{z}} &= \frac{2\pi}{V_{\mathrm{LS}}}(N_1\mathbf{x} \times N_2\mathbf{y}) = \frac{2\pi}{N_3 \mathrm{p}_{\mathrm{sam_z}}}\hat{\mathbf{z}}, \end{aligned} \tag{3.7}$$

where V_{LS} is the volume created by $\mathbf{x}, \mathbf{y}$, and $\mathbf{z}$ and N_1, N_2, N_3, which corresponds to the number of steps or pixels in the data array [56]. Based on equation (3.7), normalizing $\mathbf{q}_{\mathrm{x}}$, $\mathbf{q}_{\mathrm{y}}$ and $\mathbf{q}_{\mathrm{z}}$ would give the LS unit vectors, $\hat{\mathbf{x}}$, $\hat{\mathbf{y}}$ and $\hat{\mathbf{z}}$, respectively.

3.5.3 Reciprocal lab space to detector reciprocal space

The detector will be placed at a position corresponding to the angle required to satisfy the Bragg condition for a specific *hkl*. In DRS, diffraction patterns without phase information are collected, which will occupy non-orthonormal reciprocal space. Here, we use the $'$ symbol to represent any set of non-orthogonal basis vectors. To translate from RLS to DRS basis vectors, a coordinate transform is applied to $\mathbf{q}_{\mathrm{x}}$, $\mathbf{q}_{\mathrm{y}}$, and $\mathbf{q}_{\mathrm{z}}$ based on the

detector position and rocking axis. For 34-ID-C, the detector is rotated by

$$R_{\Delta q'_{1,2}} = [R_y(\delta)][R_x(\gamma)], \tag{3.8}$$

where R_y is a right-handed rotation δ about the y-axis and R_x is a right-handed rotation γ about the x-axis. The rotation about the x-axis is performed before the rotation about the y-axis since the former is at the condition where $\delta = 0$ [177]. To collect diffraction patterns, we calculate $\mathbf{q}'_1$ and $\mathbf{q}'_2$ that describe in-plane reciprocal space pixel positions on the detector,

$$\begin{aligned} \mathbf{q}'_1 &= [R_{\Delta q'_{1,2}}] \begin{bmatrix} \frac{\lambda D}{pN_1} \\ 0 \\ 0 \end{bmatrix}, \\ \mathbf{q}'_2 &= [R_{\Delta q'_{1,2}}] \begin{bmatrix} 0 \\ \frac{\lambda D}{pN_2} \\ 0 \end{bmatrix}, \end{aligned} \tag{3.9}$$

where λ is the X-ray wavelength, D is the detector distance, p is the detector pixel size and N_1 and N_2 correspond to the number of detector pixels in the x and y directions respectively.

$\mathbf{q}'_3$ is determined by the rocking axis and requires the direction of the incident beam. For 34-ID-C, this is given by $\mathbf{S}_{0\text{lab}}$,

$$\mathbf{S}_{0\text{lab}} = \frac{2\pi}{\lambda} \begin{bmatrix} 0 \\ 0 \\ 1 \end{bmatrix}. \tag{3.10}$$

The diffracted beam, $\mathbf{S}_{\text{lab}}$, will be incident on the detector, thus $\mathbf{S}_{\text{lab}}$ is equal to $\mathbf{S}_{0\text{lab}}$ rotated by the detector matrix $R_{\Delta q'_{1,2}}$ in equation (3.8),

$$\mathbf{S}_{\text{lab}} = [R_{\Delta q'_{1,2}}][\mathbf{S}_{0\text{lab}}]. \tag{3.11}$$

Finally, the scattering vector, $\mathbf{Q}_{\text{lab}}$, is the centre of the diffraction peak in reciprocal space,

$$\mathbf{Q}_{\text{lab}} = \mathbf{S}_{\text{lab}} - \mathbf{S}_{0\text{lab}}. \tag{3.12}$$

For beamline 34-ID-C, rocking scans are performed about the y-axis with an increment of $\Delta\theta$ in lab coordinates. Note that we are interested in the momentum transfer in the frame of a particular crystal, so we must rotate $\mathbf{Q}_{\text{lab}}$ by $-\Delta\theta$ [177], so the rocking matrix, $R_{\Delta q'_3}$, is

$$R_{\Delta q'_3} = R_{\text{y}}(-\Delta\theta), \tag{3.13}$$

where R_{y} is a right-handed rotation by $-\Delta\theta$ about the y-axis. Accordingly, $\mathbf{q}'_3$ is

$$\mathbf{q}'_3 = [R_{\Delta q'_3}][\mathbf{Q}_{\text{lab}}] - \mathbf{Q}_{\text{lab}}. \tag{3.14}$$

Once $\mathbf{q}'_1$, $\mathbf{q}'_2$ and $\mathbf{q}'_3$ are known, the data from the RLS can be mapped into the DRS using the transformation approach of equation (3.2).

3.5.4 Detector reciprocal space to detector conjugated space

To convert from DRS to DCS, the $\mathscr{F}^{-1}$, is applied. In `BCDI_Simulation`, the phase calculated when $\mathscr{F}$ is applied to the LS shape in Section 3.5.1 is stored and used when

taking the $\mathscr{F}^{-1}$. However, in a laboratory-based experiment, the phase must be recovered using a phase retrieval algorithm [99] as it is lost during the detection process. Similar to DRS, DCS is a non-orthogonal space and will later need to be transformed back to LS to recover the object. The basis vectors for DCS are [173]:

$$V_{\mathrm{DRS}} = \mid \left(N_1\mathbf{q}_1' \times N_2\mathbf{q}_2'\right) \cdot N_3\mathbf{q}_3' \mid, \tag{3.15}$$

$$\begin{aligned}
\mathbf{x}' &= \frac{2\pi}{V_{\mathrm{DRS}}}\left(N_2\mathbf{q}_2' \times N_3\mathbf{q}_3'\right), \\
\mathbf{y}' &= \frac{2\pi}{V_{\mathrm{DRS}}}\left(N_3\mathbf{q}_3' \times N_1\mathbf{q}_1'\right), \\
\mathbf{z}' &= \frac{2\pi}{V_{\mathrm{DRS}}}\left(N_1\mathbf{q}_1' \times N_2\mathbf{q}_2'\right).
\end{aligned} \tag{3.16}$$

3.5.5 Detector conjugated space to lab space

Using the DCS basis vectors in equation (3.16) and the LS basis vectors in equation (3.5), a transformation matrix can be computed using equation (3.2) in order to map the object between these two spaces.

3.6 Application of mapping scripts

The following examples demonstrate the functionality of the scripts `SS_to_DCS`, `DCS_to_SS` and `DCS_to_DCS` through both the simulation of a cubic crystal cylinder and a laboratory-based strain microscopy sample composed of tungsten.

For the simulation, the original shape in SS is a $64 \times 64 \times 64$ pixel cylinder centred in a $256 \times 256 \times 256$ pixel array that has been oriented for the simulated measurement of a 111 reflection. This was performed at a detector distance of 1.77 m, a rocking increment

of 0.0027° and $\lambda = 0.124$ nm.

The laboratory-based measurement is from an experiment at 34-ID-C for the $\bar{1}10$ reflection from a tungsten microcrystal and is included to demonstrate the application of the scripts. It was performed at a detector distance of 1.75 m, a rocking increment of 0.005° and $\lambda = 0.124$ nm.

3.6.1 Transfer from detector conjugated space to sample space

Fig. 3.3 shows the transformation of simulated and laboratory-based DCS shapes to SS. It should be noted that the solution given by iterative phase retrieval possesses trivial non-uniqueness, where either the object or the twin of the object are valid solutions. Practically, it is normally possible to distinguish the true object from its twin by the orientation of the shape. In the case of the twin, one must take the conjugate of the $\mathscr{F}$ of the object. For the laboratory-based example in Fig. 3.3(b), the SS shape matches with the scanning electron microscope (SEM) images of the sample sitting on the mount shown in Appendix A.2.1, Fig. A.1, indicating that it is indeed the correct shape and orientation. Furthermore, SS shapes calculated from two different reflections, $\bar{1}\bar{1}0$ and $\bar{1}10$, shown in Appendix A.2.2, Fig. A.2, show a very high degree of overlap (99.84%), as they should when the phase retrieval has successfully converged and the re-mapping into SS frame has been carried out correctly.

Note that the overlap, even for the simulation, is not 100%. For the simulation, the primary source of discrepancy is interpolation, as the object is hard-edged and is thus limited by sampling resolution. For the laboratory-based experiment, sources of error include noise, motor angle accuracy and direction-dependent resolution [105].

3.6.2 Transfer from sample space to detector conjugated space

Fig. 3.4 shows the transformation of both SS shapes to DCS. The outputs of the script match the inputs of the `DCS_to_SS` in Fig. 3.3. For the laboratory-based example in Fig. 3.4(b), the calculated DCS shape matches the reconstructed DCS shape in Appendix

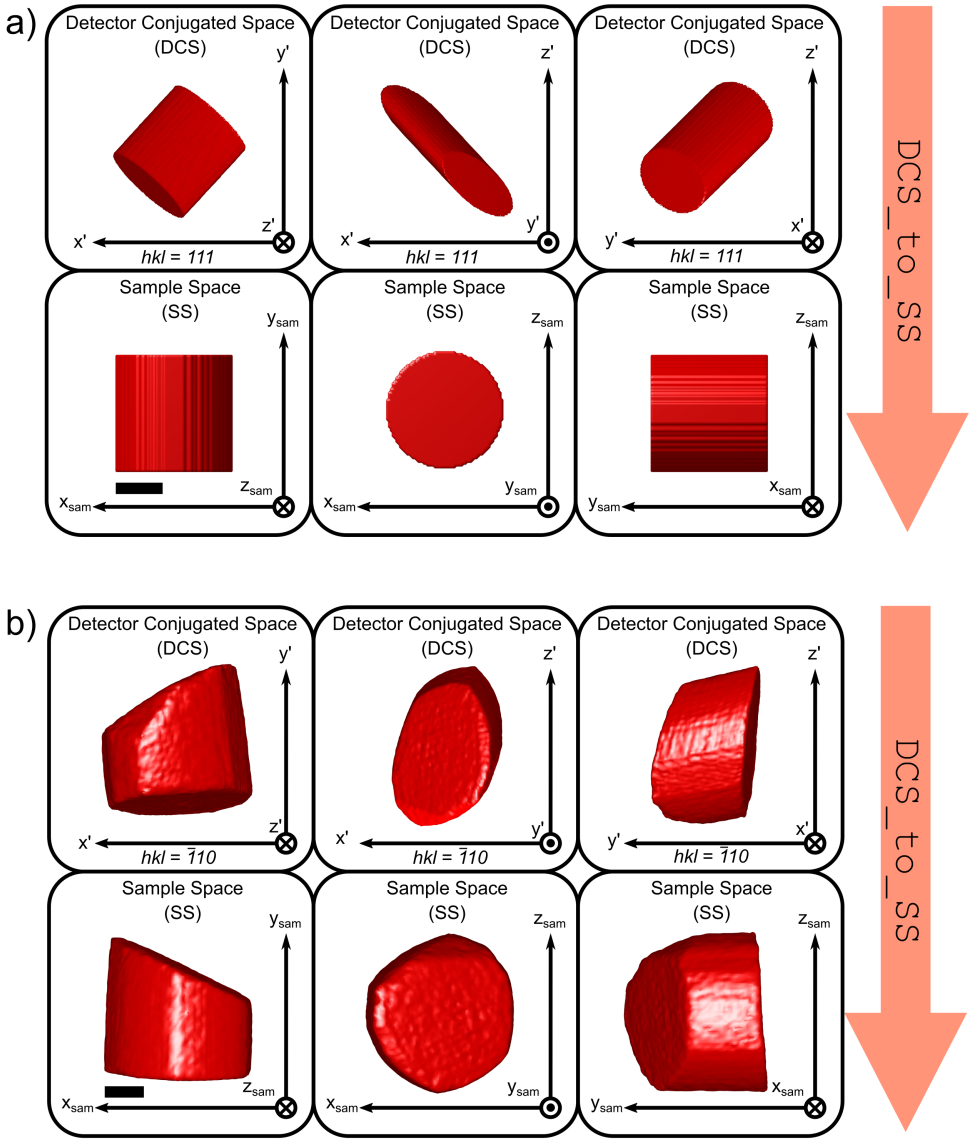

Figure 3.3: Demonstration of the script `DCS_to_SS` for both (a) simulation and (b) laboratory-based sample, displayed for the x-y, x-z and y-z planes from left to right. The DCS shape is a distorted version of the SS shape. After applying `DCS_to_SS`, the DCS shape has been correctly converted to the initial sample in SS, also shown in Appendix A.2.2 Fig. A.1. The scale bars in SS correspond to 200 nm.

A.2.3, Fig. A.3(b). The ability to map a shape from SS to DCS is important as it allows a support for reconstruction to be made, e.g. based on multiple-view SEM micrographs.

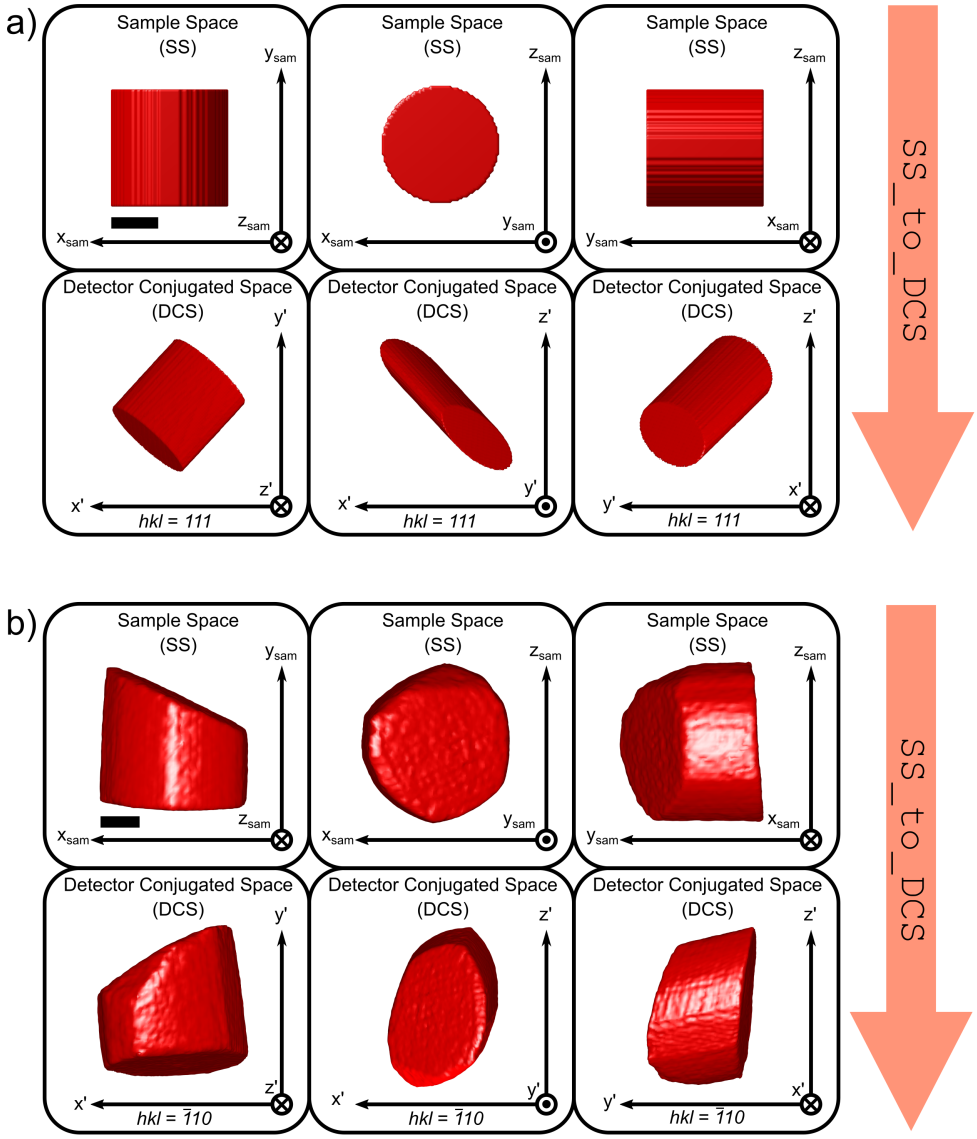

Figure 3.4: Demonstration of the script `SS_to_DCS` for both (a) simulation and (b) laboratory-based sample, displayed for the x-y, x-z and y-z planes. The SS shape is distorted to become the DCS shape after applying `SS_to_DCS`. The scale bars in SS correspond to 200 nm.

3.6.3 Transfer from detector conjugated space to detector conjugated space

Fig. 3.5 shows the transformation of both DCS shapes to the DCS for another reflection. In Fig. 3.5(a), the calculated output of the script matches the corresponding reconstructed DCS shape for the $\bar{1}20$ reflection in Appendix A.2.3, Fig. A.3(a). In Fig. 3.5(b), the calculated output of the script matches the corresponding reconstructed DCS shape for the $\bar{1}\bar{1}0$ reflection shown in Appendix A.2.3, Fig. A.3(b).

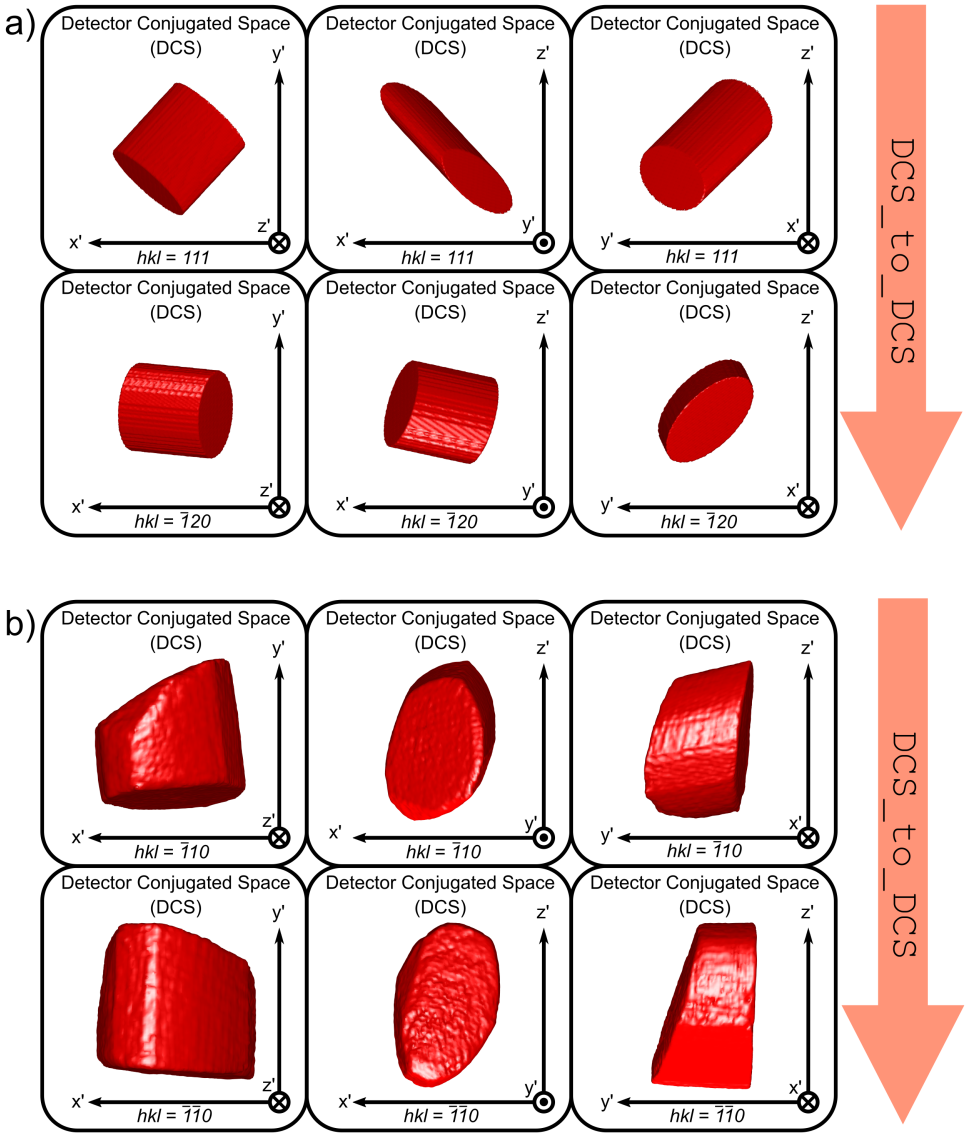

Figure 3.5: Demonstration of the script `DCS_to_DCS` for both (a) simulation and (b) laboratory-based sample, displayed for the x-y, x-z and y-z planes from left to right. The DCS shape for one reflection is transformed to SS (shown in Fig. 3.3) and then transformed to the DCS shape for another reflection.

3.7 Conclusion

The program, `BCDI_Simulation`, provides a flexible framework for mapping data between different coordinate frames in BCDI experiments. Importantly, it is easily adapted to the specific geometry used at different instruments. We generalize the inputs to three fundamental matrices: $R_{\mathrm{x,y,z}}$, $R_{\Delta \mathrm{q}'_{1,2}}$, and $R_{\Delta \mathrm{q}'_{3}}$, corresponding to the rotation of the sample, detector and rocking axis respectively.

As a lensless technique, BCDI's limiting factor is the maximum spatial frequency at

which the phase can be reliably recovered and the durability of the algorithm to reconstruct 3D objects [97]. Scripts `SS_to_DCS` and `DCS_to_DCS` provide a means to create more accurate DCS shapes, which could be turned into initial supports for phase retrieval. This will be particularly important for samples with complex geometry and/or strong phase variations where ab initio methods begin to stagnate. The final tool, `DCS_to_SS`, allows the reader to map the recovered sample shape into an orthogonal sample space. This is essential for MBCDI where multiple reflections from the same object are measured and must be projected into a common coordinate frame for analysis. We expect that these tools will be useful for the community in exploring data collection in different geometries, as well as new reconstruction approaches.

3.8 Data availability

The program, `BCDI_Simulation`, and space mapping scripts are publicly available at 10.5281/zenodo.3347113 and 10.5281/zenodo.3347109 respectively. For the most updated version of the codes, the reader is asked to visit github.com/Hofmann-Group.

Chapter 4

Refinements for Bragg coherent X-ray diffraction imaging: Electron backscatter diffraction alignment and strain field computation

In this chapter, two novel refinements for BCDI are presented: a new method to pre-align microcrystals for MBCDI, and an improved approach for computing the strain field with increased speed and accuracy. The pre-alignment method does not require synchrotron X-rays, but instead uses EBSD to find the orientation matrix of specific microcrystals. This permits the measurement of multiple BCDI reflections with ease for the recovery of the full 3D strain and rotation tensors. Furthermore, an efficient and more accurate approach to calculating strain is introduced, using the complex component of the phase, rather than the phase alone. This enables more subtle defect features to be visible, and can be computed faster than the previous computational methods. These tools are then used in subsequent chapters of this thesis. The chapter has been published as: D. Yang, M. T. Lapington, G. He, K. Song, M. Zhang, C. Barker, R. J. Harder, W. Cha, W. Liu, N. W. Phillips, and F. Hofmann, "Refinements for Bragg coherent X-ray diffraction imaging:

Electron backscatter diffraction alignment and strain field computation," *Journal of Applied Crystallography*, vol. 55, pp. 1184–1195, 2022 [60].

M.T. Lapington, G. He, K. Song, M. Zhang, and N.W. Phillips assisted with BCDI data collection. M.T. Lapington isolated microcrystals using FIB milling. G. He performed the EBSD measurements. C. Barker provided sputtered thin films for sample fabrication. BCDI experiments were performed remotely at 34-ID-C, with help from R.J. Harder and W. Cha. Micro-beam Laue X-ray diffraction experiments were performed remotely at 34-ID-E, with help from W. Liu. The remainder of the work was carried out by the author under the supervision of F. Hofmann.

4.1 Abstract

Bragg coherent X-ray diffraction imaging (BCDI) allows the three-dimensional (3D) measurement of lattice strain along the scattering vector for specific microcrystals. If at least three linearly independent reflections are measured, the 3D variation of the full lattice strain tensor within the microcrystal can be recovered. However, this requires knowledge of the crystal orientation, which is typically attained via estimates based on crystal geometry or synchrotron micro-beam Laue diffraction measurements. Here, we present an alternative method to determine the crystal orientation for BCDI measurements, by using electron backscatter diffraction (EBSD) to align Fe-Ni and Co-Fe alloy microcrystals on three different substrates. The orientation matrix is calculated from EBSD Euler angles and compared to the orientation determined using micro-beam Laue diffraction. The average angular mismatch between the orientation matrices is less than ~ 6 degrees, which is reasonable for the search for Bragg reflections. We demonstrate the use of an orientation matrix derived from EBSD to align and measure five reflections for a single Fe-Ni microcrystal using multi-reflection BCDI. Using this dataset, a refined strain field computation based on the gradient of the complex exponential of the phase is developed. This approach is shown to increase accuracy, especially in the presence of dislocations.

Our results demonstrate the feasibility of using EBSD to pre-align BCDI samples and the application of more efficient approaches to determine the full lattice strain tensor with greater accuracy.

4.2 Introduction

Since the development of BCDI in the early 2000s, most experiments feature the measurement of a single reflection, providing only one component of the strain tensor. However, the analysis of a single strain component can be ambiguous as different information is obtained for different reflections [48]. If at least three linearly independent reflections are measured, the full 3D strain tensor can be calculated. Before 2017, only three experiments [50, 178, 179] reported measuring more than one reflection on a single crystal. This is not surprising as multi-reflection BCDI (MBCDI) experiments require prior knowledge of the crystal orientation [50], or scanning extensive volumes of reciprocal space until two reflections are found, upon which further reflections can then be located.

The development of a micro-beam Laue X-ray diffraction pre-alignment procedure in 2017 [57] enabled the direct determination of the crystal orientation matrix, such that crystals could be reliably pre-aligned for MBCDI. Recently, a double-bounce Si(111) monochromator that allows Laue X-ray diffraction to be performed has been commissioned at BCDI beamline 34-ID-C at the APS [141]. Another method to determine the orientation of a sample is by indexing pole figures [139], however, this method requires a Bragg peak with known Miller indices to be found. The indexing is performed using texture analysis and relies on the samples to be well-faceted to produce truncation rods in reciprocal space that are perpendicular to facet surfaces. These pre-alignment protocols have not only led to the increased popularity of MBCDI for determination of the full strain tensor with respect to an arbitrary reference [22, 29, 30, 47, 49], but also enabled simultaneous, multi-Bragg peak phase retrieval procedures to increase reconstruction quality [103, 104, 120].

Here we present an alternative method of pre-determining crystal orientation for MBCDI alignment without relying on synchrotron X-rays. We use electron backscatter diffraction (EBSD) to determine the orientation [180] of randomly-oriented Fe-Ni and Co-Fe microcrystals on three different sapphire substrates. EBSD instruments are much more widespread and accessible than synchrotron instruments, and can be used as a valuable pre-screening tool for BCDI. EBSD measurements can produce 2D orientation maps with a high spatial resolution of $\sim$ 10 nm, thus enabling the selection of specific crystals with particular orientations or features such as twin domains. This allows the user to preserve synchrotron beamtime for BCDI measurements rather than performing pre-orientation measurements and analysis at the beamline. We compare orientation matrices found by EBSD to those measured by micro-beam Laue diffraction and the ultimately measured reflection positions in MBCDI. Using the pre-determined EBSD orientation matrix, we measured five crystal reflections for a Fe-Ni microcrystal (Fig. 4.6) and determined its full strain and rotation tensors with respect to the average lattice of the crystal. We also implement an alternative approach, by using use the complex component of the phase, rather than the phase alone, to efficiently calculate the phase derivatives required for the strain tensor determination and more accurately interpolate the recovered phase to sample coordinates.

4.3 Experimental methodology

4.3.1 Microcrystal fabrication

Samples were produced by sputter deposition of a thin film onto a single crystal sapphire wafer (C-plane orientation). One substrate with a film thickness of 375 nm was produced for the Fe-Ni microcrystals. It was dewetted in a vacuum furnace purged with a 5% hydrogen, balance Argon, gas mixture at 1250°C for 24 hours. The resulting crystals exhibit a faced-centred cubic (fcc) structure, range from 0.5 to 1.5 μm in size, (Fig. 4.1(a)) and adhere to the substrate surface. The substrate was cleaved to make substrates 1 and

2, both containing Fe-Ni microcrystals. Substrate 3 contained Co-Fe microcrystals that were produced in a similar way. The procedure and details for substrate 3 can be found elsewhere [49].

The samples were mounted on 12.5 mm diameter SEM specimen pin stubs using silver paint. Each substrate was coated with 10 nm of amorphous carbon via thermal evaporation using a Leica ACE600 coater to assist with scanning electron microscope (SEM) imaging. To facilitate reliable measurement of multiple reflections from a specific microcrystal, a ZEISS NVision 40 Ga ion FIB was used to remove the surrounding crystals within a 40 μm radius using currents from 6 nA to 150 pA, and acceleration voltage of 30 kV. Only SEM imaging was used to position the FIB milling scan to prevent large lattice strains caused by FIB imaging [47]. The isolated crystals on each substrate are shown in Fig. 4.2. Crystal 1B (Fig. 4.1(b)) was used for the computation of the strain and rotation tensors (Fig. 4.6).

Energy-dispersive X-ray spectroscopy (EDX) was used to determine the elemental composition of each crystal (Fig. 4.1(c)). EDX showed homogeneous distribution of all elements throughout the dewetted crystals (see Appendix B.2). EDX was performed on a ZEISS Merlin using an Xmax 150 detector (Oxford Instruments) using an elliptical region encapsulating crystal 2B on the substrate for 16 seconds with an accelerating voltage of 10 kV.

4.3.2 Electron backscatter diffraction

Crystal orientation was determined by EBSD using a ZEISS Merlin equipped with a Bruker Quantax EBSD system and a Bruker eFlash detector tilted at 4°. Electron backscatter patterns (EBSPs) were recorded with the sample tilted at 70° (Fig. 4.3) using an accelerating voltage of 30 kV and a current of 15 nA. EBSPs were 800×600 pixels and a step size of 19.8 nm was used between consecutive points on the sample. The diffraction patterns were indexed and the Euler angles were extracted for each pattern using the Bruker ESPRIT 2.1 EBSD software. The Euler data was exported and analysed using

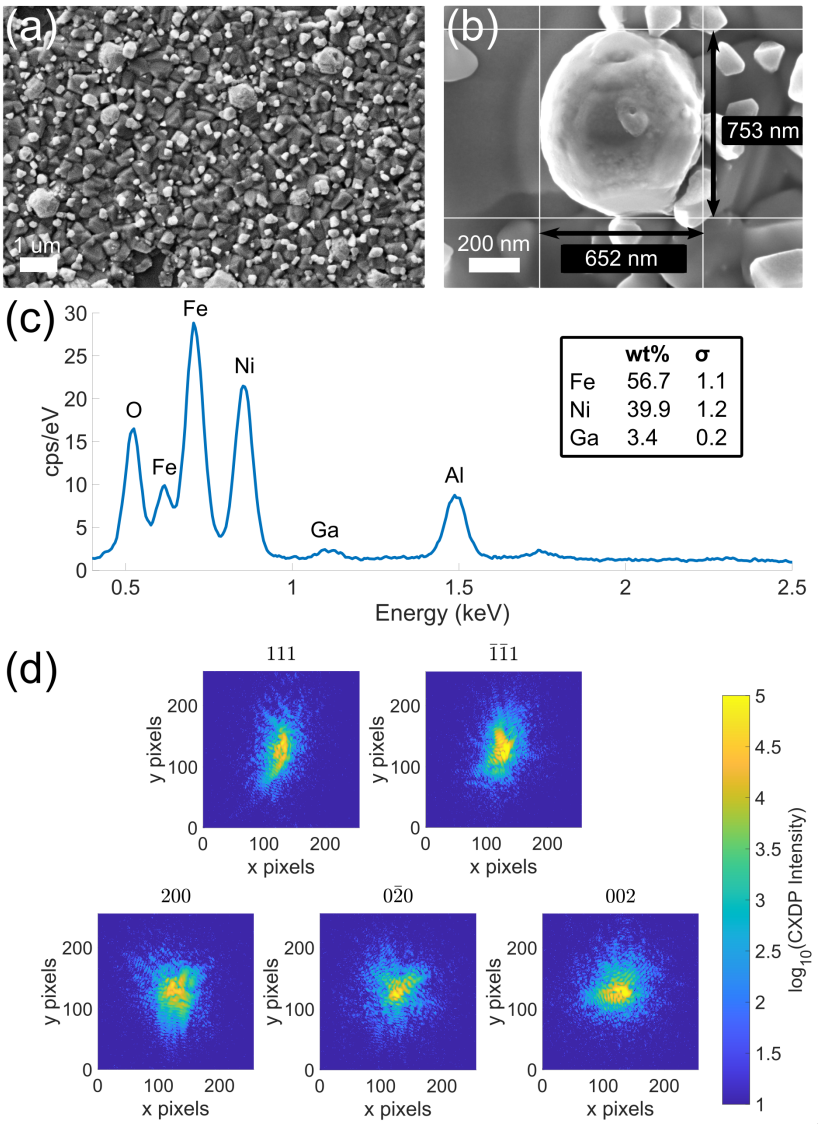

Figure 4.1: (a) Dewetted Fe-Ni alloy microcrystals on a sapphire substrate. (b) Fe-Ni microcrystal 1B is used for the computation of strain and rotation tensors. (c) EDX spectrum for crystal 2B on the substrate, which is similar across all crystals on the substrate. Only the L-lines for the most pronounced elements in the crystal are shown above. The composition excludes the Al and O substrate peaks. The Ga impurity is due to FIB milling around the crystal vicinity [47]. (d) Central slices of the CXDPs for each reflection, measured for crystal 1B.

MTEX, a MATLAB toolbox for texture analysis [181], to produce inverse pole figure (IPF) maps for all crystals, shown in Fig. 4.2.

Here we use the Bunge convention [183] to describe each crystal orientation (crystal frame) relative to the substrate (sample frame). The crystal orientation matrix, **UB**, is composed of **U**, which describes the rotation of the crystal reference frame, and **B** (Eq. 4.1), which characterises the unit cell parameters.

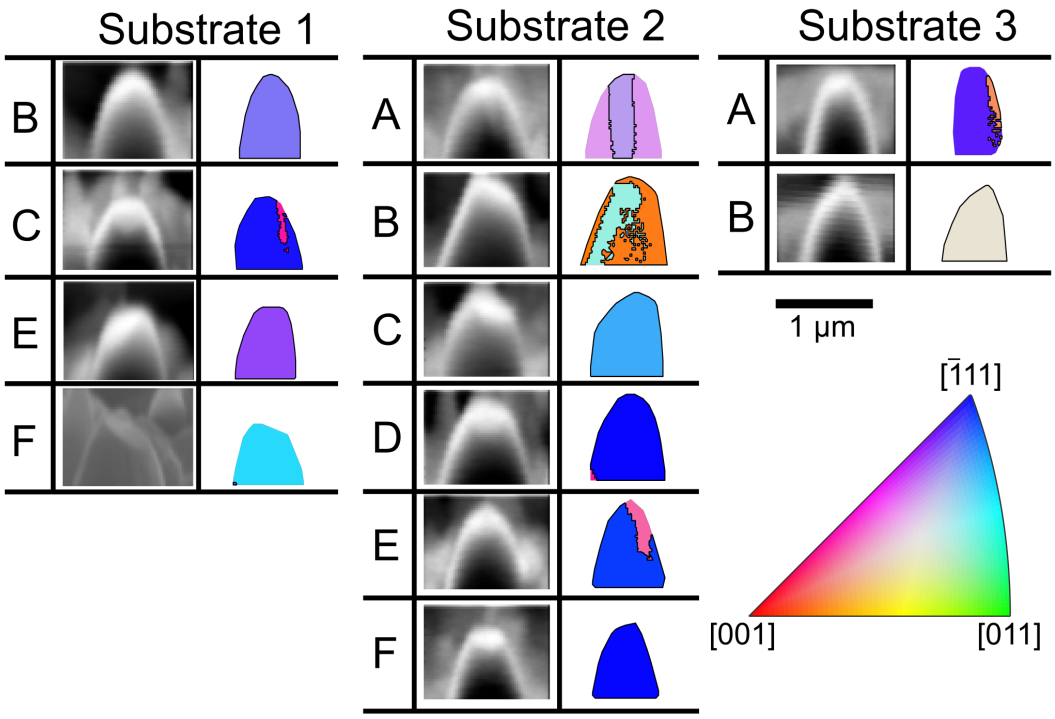

Figure 4.2: SEM image and inverse pole figure (IPF) maps for each crystal from EBSD. The colour-coding shows the out-of-plane crystal orientation. The maps allow for different grains to be identified. For each crystal, the region surrounded by thick black lines corresponds to the grain orientation used for the computation of the orientation matrix. For some samples (i.e. 1F, 3A) only a small region on the IPF map corresponded to the grain measured at the synchrotron. EBSD samples the orientation of a cylindrical volume with a height up to 40nm below the surface [182].

Using the same convention as Britton *et al.* [184], the unit cell has lattice vectors **a**, **b** and **c**, each with lengths a, b, and c, respectively. Angle α describes the angle between the **b** and **c** axes, β the angle between the **c** and **a** axes, and γ the angle between the **a** and **b** axes. **B** is used to transform the lattice base vectors to Cartesian base vectors:

$$\mathbf{B} = \begin{bmatrix} a\frac{f}{\sin(\alpha)} & 0 & 0 \\ a\frac{\cos(\gamma)-\cos(\alpha)\cos(\beta)}{\sin(\alpha)} & b\sin(\alpha) & 0 \\ a\cos(\beta) & b\cos(\alpha) & c \end{bmatrix}, \tag{4.1}$$

where

$$f = \sqrt{1-[\cos(\alpha)]^2-[\cos(\beta)]^2-[\cos(\gamma)]^2+2\cos(\alpha)\cos(\beta)\cos(\gamma)}. \tag{4.2}$$

Since all crystals in this study have a fcc structure, **B** is the 3×3 identity matrix

multiplied by the lattice constant.

UB provides the direction and radial position of specific *hkl* reflections, $\mathbf{H}_{hkl}$, in laboratory coordinates, [185]

$$\mathbf{H}_{hkl} = \mathbf{UB} \begin{bmatrix} h \\ k \\ l \end{bmatrix}. \tag{4.3}$$

Several different coordinate frames are used in EBSD that refer to different aspects of the measurement (Fig. 4.3). In this chapter, all coordinate systems and rotation matrices will be right-handed and the same notation as in Britton *et al.* [184]. For EBSD, the following subscripts describe specific coordinate systems:

- 'd' is the detector frame that describes the EBSPs.
- 's' is the EBSD sample frame that is related to the detector frame by sample. (θ_{sample}) and detector (θ_{detector}) tilts about the x-axis. The x_s and y_s axes correspond to the directions of EBSD scan points.
- 'm' is the SEM map frame. This corresponds to how the EBSPs overlay on SEM maps, and thus how the EBSD orientation is referenced.

The EBSD software returns the orientation matrix from EBSD measurements in the SEM map frame (Fig. 4.3). The corresponding orientation matrix is referred to as $\mathbf{U}_{\mathbf{EBSD,\,m}}$. It can be constructed from a series of rotations using Euler angles, where each angle describes a rotation about a coordinate axis. Here we use right-handed rotation matrices to describe vector rotations about the x-axis (Eq. 4.4),

$$\mathbf{R}_{\text{x}}(\theta) = \begin{bmatrix} 1 & 0 & 0 \\ 0 & \cos(\theta) & -\sin(\theta) \\ 0 & \sin(\theta) & \cos(\theta) \end{bmatrix}, \tag{4.4}$$

and the z-axis (Eq. 4.5),

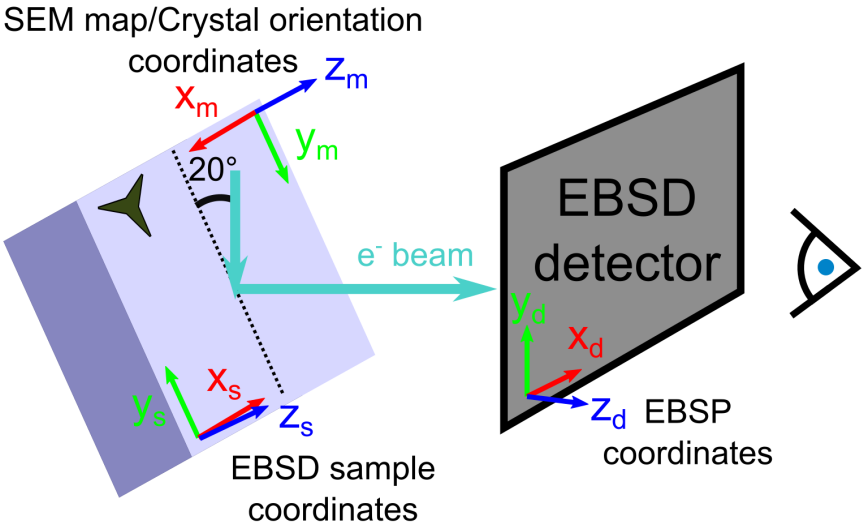

Figure 4.3: The position of the substrate in the laboratory frame for EBSD measurements is shown with relevant coordinate systems. The 3-pointed star represents the orientation of an arbitrary sample feature on the purple substrate. The EBSD detector coordinate system (x_d, y_d, z_d) describes the EBSP coordinates. The EBSD sample coordinates (x_s, y_s, z_s) correspond to the EBSD scan points. The SEM map coordinates (x_m, y_m, z_m) that show how EBSPs overlay on SEM maps. The Euler angles output by the EBSD software are with respect to the SEM map coordinates. This follows the same convention in Britton *et al.* [184].

$$\mathbf{R}_z(\theta) = \begin{bmatrix} \cos(\theta) & -\sin(\theta) & 0 \\ \sin(\theta) & \cos(\theta) & 0 \\ 0 & 0 & 1 \end{bmatrix}. \tag{4.5}$$

and Bunge convention Euler angles, ϕ_1, Φ, and ϕ_2 [184]. Equivalently, Eq. 4.4 and Eq. 4.5 correspond to left-handed rotations through angle θ for the coordinate system. To transform vectors from the crystal coordinate frame to the laboratory frame, we use Eq. 4.6 [184],

$$\mathbf{U}_{\mathbf{EBSD,\,m}}{}^{\top} = \mathbf{R}_z(-\phi_2)\mathbf{R}_x(-\Phi)\mathbf{R}_z(-\phi_1). \tag{4.6}$$

We note that the Euler angles in Eq. 4.6 are negative because the original angles as defined are for left-handed rotation matrices. First a rotation of $-\phi_1$ is applied about the original z axis, followed by a rotation of $-\Phi$ about the new x axis, and finally a rotation of $-\phi_2$ about the new z axis. For consistency with the convention here [185], we express Eq. 4.6 as

$$\mathbf{U}_{\mathbf{EBSD,\,m}} = \mathbf{R}_{\mathrm{z}}(\phi_1)\mathbf{R}_{\mathrm{x}}(\Phi)\mathbf{R}_{\mathrm{z}}(\phi_2). \tag{4.7}$$

The EBSD software already accounts for instrument tilts, θ_{sample} and θ_{detector}, and returns Euler angles in the SEM map frame (subscript m) (Fig. 4.3).

To input the orientation matrix into the *spec* orientation calculator on beamline 34-ID-C, we must define two *hkl* reflections corresponding to out-of-plane (Eq. 4.12) and in-plane reflections (Eq. 4.13) [57]. One concern is the consistency in the indexation of crystals at the 34-ID-E Laue instrument and in EBSD measurements. Due to the cubic structure of the present crystals, there are equivalent orientation matrices that differ by 90° rotations about the crystal axes. These rotations are accounted for using a $\mathbf{R}_{\text{crystal}}$ rotation matrix that captures rotations by $90(n_{x,y,z})°$, where $n_{x,y,z} \in \{-1,0,1,2\}$, about the x, y, and z axes (Eq. 4.8),

$$\mathbf{R}_{\text{crystal}} = \mathbf{R}_{\mathbf{x}}(90(n_x)°)\mathbf{R}_{\mathbf{y}}(90(n_y)°)\mathbf{R}_{\mathbf{z}}(90(n_z)°). \tag{4.8}$$

To align the EBSD map frame to the BCDI laboratory frame, a $-90°$ rotation about the x-axis is required (Fig. 4.4(a)). Combining this with Eq. 4.7 and Eq. 4.8 leads to the formation of the $\mathbf{UB}_{\mathbf{34C,\,EBSD}}$ matrix:

$$\mathbf{UB}_{\mathbf{34C,\,EBSD}} = \mathbf{R}_{\mathrm{x}}(-90°)\mathbf{U}_{\mathbf{EBSD,\,m}}\mathbf{R}_{\text{crystal}}\mathbf{B}. \tag{4.9}$$

These matrix-based orientation operators provide a generalised approach to the transformation of orientation, irrespective of the software implementation

4.3.3 Micro-beam Laue X-ray diffraction

Micro-beam Laue diffraction was used to independently verify the lattice orientation of each crystal. This was performed at beamline 34-ID-E at the APS. Further details about the instrument can be found elsewhere [57, 186]. The sample was positioned with its

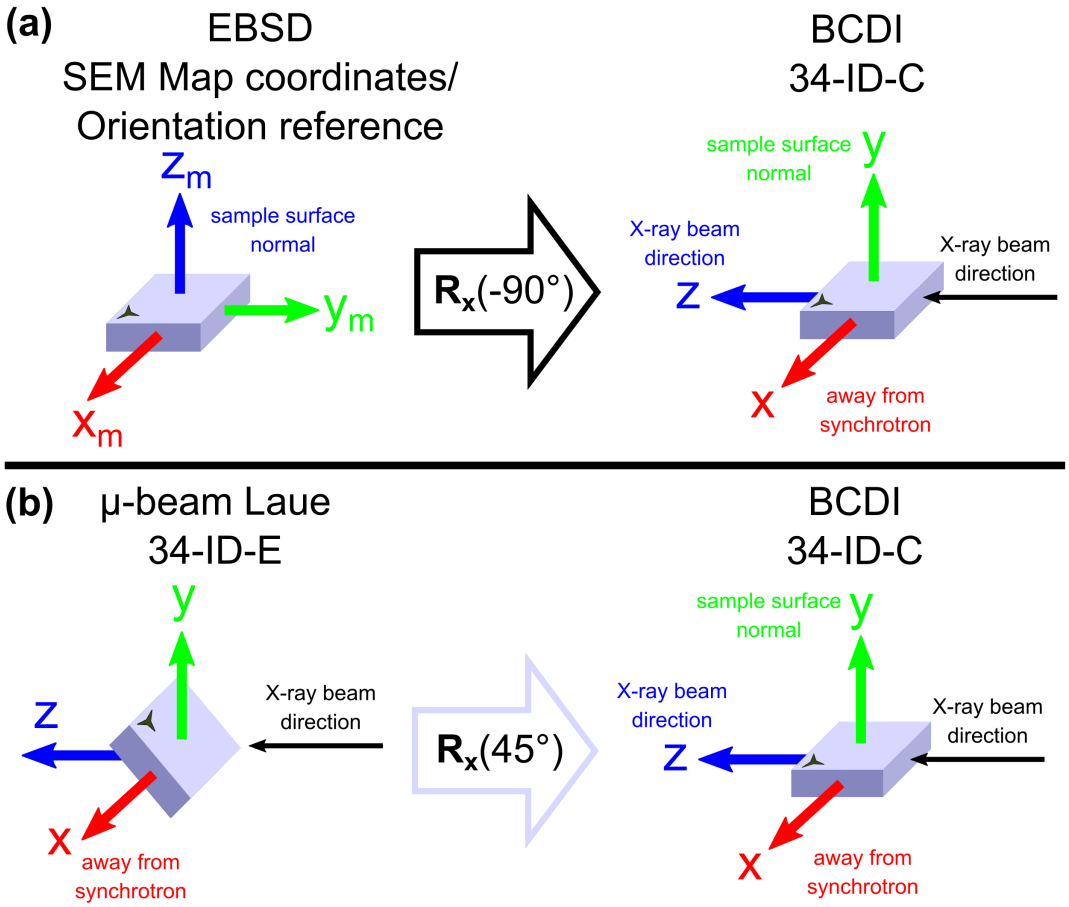

Figure 4.4: Position of the substrate in the laboratory frame for micro-beam Laue diffraction and EBSD measurements compared to the BCDI laboratory frame (x, y, z). The 3-pointed star represents the orientation of a sample feature on the purple substrate. Right-handed rotation matrices are used for the rotations. (a) shows how the EBSD laboratory coordinates, specifically the SEM map coordinates (Fig. 4.3), are related to the BCDI frame. (b) shows the transformation between the laboratory frames for Laue diffraction and BCDI, characterised by a 45° rotation about the x-axis.

surface inclined at a 45° angle to the incident beam (see Fig. 4.4(b)) and diffraction patterns were recorded using a Perkin Elmer flat-panel detector above the sample. 2D fluorescence measurements of the Fe $K\alpha_1$ peak (6.40 keV) were used to identify the spatial position of the crystals, using a monochromatic, 17 keV ($\Delta\lambda/\lambda \approx 10^{-4}$) X-ray beam focused to 0.25 μm x 0.25 μm (h × v) using Kirkpatrick–Baez (KB) mirrors.

Next, a polychromatic X-ray beam was used to collect a Laue diffraction pattern of each crystal (Fig. 4.5). The pattern shows weak Bragg reflections from the microcrystals and strong Bragg peaks from the single-crystal sapphire substrate. The two sets of peaks were indexed and fitted using the *LaueGo* software (J. Z. Tischler, tischler@aps.anl.gov). From the indexation, we could determine the **UB** matrix (Eq. 4.3). The **UB** matrix deter-

mined by Laue diffraction at the 34-ID-E instrument is referred to as $\mathbf{UB_{Laue}}$, shown here in Eq. 4.10,

$$\mathbf{UB_{Laue}} = \begin{bmatrix} | & | & | \\ \mathbf{a}^* & \mathbf{b}^* & \mathbf{c}^* \\ | & | & | \end{bmatrix}, \tag{4.10}$$

where $\mathbf{a}^*$, $\mathbf{b}^*$ and $\mathbf{c}^*$ are the column (represented by vertical lines) reciprocal space vectors returned by *LaueGo* in units of nm^{-1} in the 34-ID-E laboratory frame.

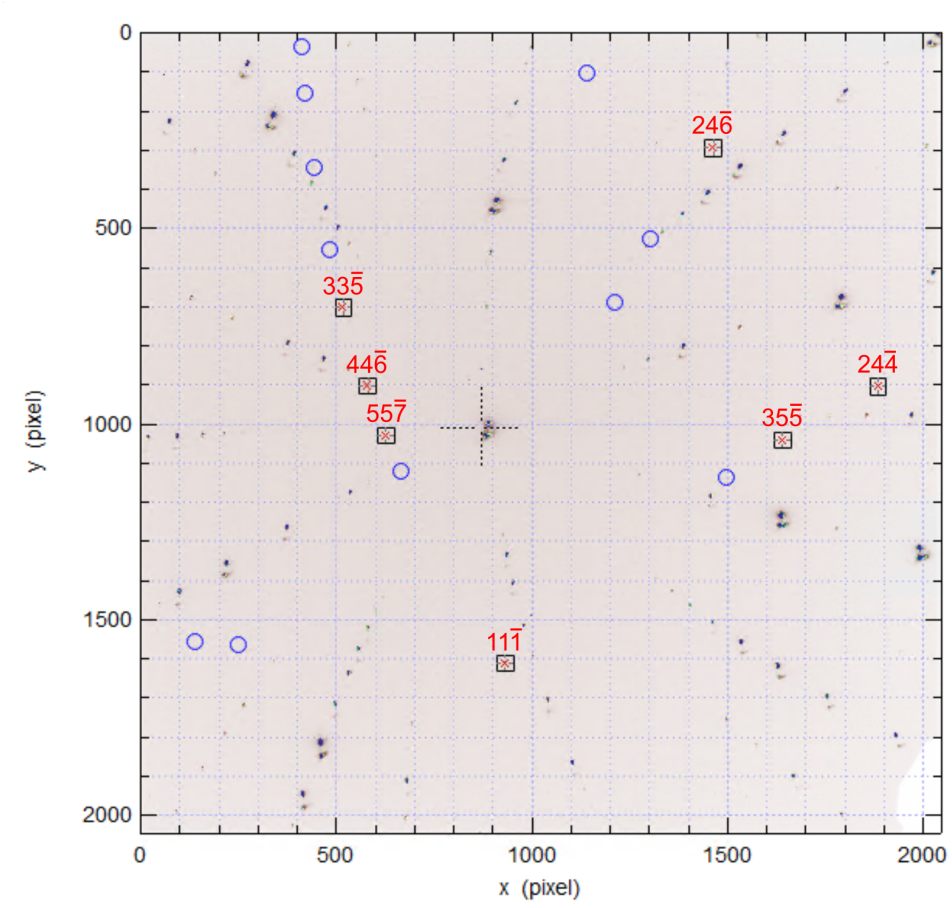

Figure 4.5: Laue diffraction pattern from microcrystal 1B. The squares show the Bragg peaks that were used for orientation determination, with their corresponding *hkl* indices shown in red. Weaker reflections from the microcrystal are expected to be inside the blue circles. Other intense peaks in the Laue diffraction pattern belong to the sapphire substrate and are not indexed here for clarity.

To convert Eq. $\mathbf{UB_{Laue}}$ into a **UB** matrix for use on the BCDI instrument 34-ID-C, $\mathbf{UB_{34C,\,Laue}}$, the 45° rotation of the sample in the Laue laboratory frame must be accounted for (Fig. 4.4(b)). To align the micro-beam Laue and BCDI laboratory frames,

a rotation of the sample by 45° about the x-axis is required [57], leading to:

$$\mathbf{UB}_{\mathbf{34C,\ Laue}} = \mathbf{R}_{\mathrm{x}}(45°)\mathbf{UB}_{\mathbf{Laue}}. \tag{4.11}$$

4.3.4 Bragg coherent X-ray diffraction imaging

BCDI was performed at beamline 34-ID-C at the APS. An *in situ* confocal microscope was used to position the microcrystal within the X-ray beam [178]. The sample was illuminated using a 9 keV (λ = 0.138 nm) coherent X-ray beam, with a bandwidth of $\Delta\lambda/\lambda \approx 10^{-4}$ from a Si(111) monochromator. The X-ray beam was focused to a size of 1.1 μm × 1.1 μm (h × v, full width at half-maximum) using KB mirrors. Beam defining slits were used to select the coherent portion of the beam at the entrance to the KB mirrors. For beamline 34-ID-C, the transverse coherence length is $\xi_h > 10\ \mu$m and the longitudinal coherence length is $\xi_w \approx 0.7\ \mu$m at a photon energy of 9 keV [71].

The sample needs to be positioned such that a specific *hkl* Bragg diffraction condition is met to produce a diffraction pattern in the far-field Fraunhofer regime. The orientation matrix determined by EBSD or Laue diffraction is communicated to the *spec* software used on 34-ID-C by defining two reflections that correspond to *hkl* values associated with laboratory x (in-plane) and y (out-of-plane) directions (note the angles referred to here are set elsewhere [57]):

1. The primary reflection (out-of-plane, *y* direction), $\mathbf{H}_{\perp}$, where the instrument angles are set to $\delta_{\mathrm{spec}} = 0°$, $\gamma_{\mathrm{spec}} = 20°$, $\theta_{\mathrm{spec}} = 0°$, $\chi_{\mathrm{spec}} = 90°$ and $\phi_{\mathrm{spec}} = -10°$. The fractional $[h\ k\ l]^{\top}$ is then:

$$\begin{bmatrix} h \\ k \\ l \end{bmatrix} = (\mathbf{UB})^{-1}\mathbf{H}_{\perp} = (\mathbf{UB})^{-1} \begin{bmatrix} 0 \\ 1 \\ 0 \end{bmatrix}. \tag{4.12}$$

2. The secondary reflection (in-plane, *x* direction), $\mathbf{H}_{\parallel}$, where the instrument angles

were set to $\delta_{\text{spec}} = 20°$, $\gamma_{\text{spec}} = 0°$, $\theta_{\text{spec}} = 10°$, $\chi_{\text{spec}} = 90°$ and $\phi_{\text{spec}} = 0°$. The fractional $[h\ k\ l]^\top$ is then:

$$\begin{bmatrix} h \\ k \\ l \end{bmatrix} = (\mathbf{UB})^{-1}\mathbf{H}_{\parallel} = (\mathbf{UB})^{-1} \begin{bmatrix} 1 \\ 0 \\ 0 \end{bmatrix}. \tag{4.13}$$

Here **UB** refers to $\mathbf{UB_{34C,\ EBSD}}$ or $\mathbf{UB_{34C,\ Laue}}$. These two fractional *hkl* vectors are then entered into *spec* as known reflections. Based on this, the expected angular positions of the $\{111\}$ and $\{200\}$ reflections from the sample were calculated. Not all $\{111\}$ and $\{200\}$ reflections could be measured as some may exceed the angular range of the sample and detector motors. Occasionally, manual motor adjustments of a few degrees were required to locate the Bragg peak. Once a Bragg peak was found, the sample tilt and positioning were refined such that the maximum intensity was on the centre of the detector positioned 0.5 m away from the sample. The angular and translational positions were saved for each Bragg peak, and were used to determine the true beamline orientation matrix, $\mathbf{UB_{34C}}$, by minimising the least-squares error associated with the measured reflections,

$$\min \sum_{hkl} \left\| \mathbf{UB_{34C}}[h\ k\ l]^\top - \mathbf{H}_{hkl} \right\|^2, \tag{4.14}$$

where $[h\ k\ l]^\top$ are Miller indices in crystal coordinates.

Differences between the true and predicted positions of the reflections using $\mathbf{UB_{34C}}$ arise from a number of different sources. The largest error is the repeatability of sample position in different coordinate systems. The use of Thorlabs 1X1 kinematic mounts, which have angular errors of less than a millidegree, helps with the precise re-mounting of samples. There is also uncertainty in the goniometer precision and alignment with the diffractometer, which can influence the angle readout. Furthermore, the centre of the detector may not be perfectly aligned to the calculated position for a given detector

distance or angle. The position of the measured Bragg peak is limited by the energy resolution of the incident X-ray as it affects the Bragg angle.

Coherent X-ray diffraction patterns (CXDPs) were collected on a 256 × 256 pixel module of a 512 × 512 pixel Timepix area detector (Amsterdam Scientific Instruments) with a GaAs sensor and pixel size of 55 μm × 55 μm positioned at 1.0 m from the sample to ensure oversampling. CXDPs were recorded by rotating the crystal through an angular range of 0.6° and recording an image every 0.005° with 0.1 s exposure time and 50 accumulations at each angle.

To optimise the signal to noise ratio and increase the dynamic range of the CXDPs, three repeated scans for each of the 111, $\bar{1}\bar{1}1$, 200, $0\bar{2}0$, and 002 reflections were performed and aligned to maximise their cross-correlation. Once aligned, the minimum acceptable Pearson cross-correlation for summation of CXDPs from a specific Bragg reflection was chosen to be 0.976, similar to previous BCDI studies [29, 30]. CXDPs were corrected for darkfield, dead-time, and whitefield (in that order) prior to cross-correlation alignment. Here, dead-time correction refers to resolving the missed photon counts due to the detector circuitry [187],

$$I_{\text{dead}} = \frac{I_0}{1 - I_0 \tau}, \tag{4.15}$$

where τ is the dead-time, I_{dead} is the dead-time corrected intensity, and I_0 is the uncorrected intensity.

Details regarding the recovery of the real space images using phase retrieval algorithms can be found in Appendix B.1 and the computation of the strain can be found in Chapter 2.4.10.

4.3.5 Sample mounting

For the SEM, EDX and EBSD analysis, samples were mounted on 12.5 mm diameter SEM specimen pin stubs using silver paint. For micro-beam Laue X-ray diffraction, they

were attached to a Thorlabs 1X1 kinematic mount. From here, a Thorlabs kinematic mount adapter between 34-ID-E and 34-ID-C was used to mount the samples for BCDI. This adapter consists of two 1X1 mounts sandwiched together to enable sample orientation to be well-preserved between the beamlines. There is no kinematic mount adapter between the SEM and BCDI instruments. Moreover, the use of magnets in the kinematic mounts inhibits their use for electron microscopy. Across the different instruments, the sample orientation was maintained throughout as shown in Fig. 4.4, which has an arbitrary sample feature to illustrate the respective orientations.

4.4 Results and Discussion

4.4.1 Orientation matrix comparison

The angular mismatch between two **UB** matrices,$\mathbf{UB_1}$ and $\mathbf{UB_2}$, can be determined by converting $\mathbf{UB_1}(\mathbf{UB_2})^{-1}$ into a rotation vector. A rotation matrix, $\mathbf{R}$, can be converted using Rodrigues' rotation formula in matrix exponential form,

$$\mathbf{R} = e^{\mathbf{w_m}}, \tag{4.16}$$

where $\mathbf{w_m}$ is an antisymmetric matrix,

$$\mathbf{w_m} = \begin{bmatrix} 0 & -w_z & w_y \\ w_z & 0 & -w_x \\ -w_y & w_x & 0 \end{bmatrix}, \tag{4.17}$$

which contains the elements of the rotation vector $\mathbf{w} = [w_x, w_y, w_z]^\top$. The rotation vector is defined by a rotation axis $\hat{\mathbf{w}}$ multiplied by a rotation, θ. If the two orientation matrices are different, $\mathbf{UB_1}(\mathbf{UB_2})^{-1}$ can be converted to a rotation vector where the angular mismatch is θ. If $\mathbf{UB_1} = \mathbf{UB_2}$, then $\mathbf{UB_1}(\mathbf{UB_2})^{-\mathbf{1}} = I_3$ and therefore $\theta = 0$.

Here we set $\mathbf{UB_1}$ and $\mathbf{UB_2}$ as $\mathbf{UB_{34C,\,EBSD}}$, $\mathbf{UB_{34C,\,Laue}}$ or $\mathbf{UB_{34C}}$. First we rearrange

Eq. 4.16 to calculate $\mathbf{w_m}$:

$$\mathbf{w_m} = \log[\mathbf{UB_1}(\mathbf{UB_2})^{-1}], \tag{4.18}$$

where log here refers to the matrix natural logarithm. Next we reconstruct the rotation vector using Eq. 4.17 and calculate its magnitude to obtain the mismatch (Eq. 4.19),

$$\theta = \|\mathbf{w}\| = \|[\mathbf{w_m}(3,2), \mathbf{w_m}(1,3), \mathbf{w_m}(2,1)]^\top\|. \tag{4.19}$$

To calculate the angular mismatch between $\mathbf{UB_{34C,\ EBSD}}$ and other orientation matrices, the permutation of $n_{x,y,z}$ that produced the smallest error was chosen. Tables 4.1 - 4.3 show the angular mismatch of $\mathbf{UB_{34C,\ Laue}}$ and $\mathbf{UB_{34C,\ EBSD}}$ compared to $\mathbf{UB_{34C}}$ for substrates 1 - 3.

The average angular mismatches for all crystals between orientation matrices: $\mathbf{UB_{34C,\ Laue}}$ and $\mathbf{UB_{34C}}$ is 4.48°, $\mathbf{UB_{34C,\ EBSD}}$ and $\mathbf{UB_{34C}}$ is 6.09°, and $\mathbf{UB_{34C,\ Laue}}$ and $\mathbf{UB_{34C,\ EBSD}}$ is 1.95°. Generally, $\mathbf{UB_{34C,\ Laue}}$ is most similar to $\mathbf{UB_{34C}}$. This is expected as there is a Thorlabs kinematic mount adapter between 34-ID-E and 34-ID-C for the precise angular alignment samples. A larger difference is observed when comparing $\mathbf{UB_{34C,\ EBSD}}$ to $\mathbf{UB_{34C}}$. This is due to the manual removal of the SEM pin stub from the electron microscope, which then needs to be re-secured to the kinematic mount. The cylindrical pin permits a greater degree of rotational freedom, thereby increasing the angular mismatch when $\mathbf{UB_{34C,\ EBSD}}$ is considered. Despite this increased angular freedom in the pin, a 2° increase in the angular uncertainty when using $\mathbf{UB_{34C,\ EBSD}}$ instead of $\mathbf{UB_{34C,\ Laue}}$ is still a very accurate result. This means only a slightly larger angular range needs to be explored in alignment.

The alignment of crystals for BCDI using EBSD remains much more time efficient because micro-beam Laue diffraction pre-alignment at 34-ID-E is no longer required. The use of EBSD for pre-alignment of BCDI samples also affords greater flexibility in experiment type. The ability to pre-characterise samples off-site should substantially increase

Table 4.1: Angular differences (°) between $\mathbf{UB_{34C}}$, $\mathbf{UB_{34C,\ Laue}}$, and $\mathbf{UB_{34C,\ EBSD}}$ for substrate 1.

1B	$\mathbf{UB_{34C}}$	$\mathbf{UB_{34C,\ Laue}}$	$\mathbf{UB_{34C,\ EBSD}}$
$\mathbf{UB_{34C}}$	-	-	-
$\mathbf{UB_{34C,\ Laue}}$	9.72	-	-
$\mathbf{UB_{34C,\ EBSD}}$	11.0	2.37	-

1C	$\mathbf{UB_{34C}}$	$\mathbf{UB_{34C,\ Laue}}$	$\mathbf{UB_{34C,\ EBSD}}$
$\mathbf{UB_{34C}}$	-	-	-
$\mathbf{UB_{34C,\ Laue}}$	2.22	-	-
$\mathbf{UB_{34C,\ EBSD}}$	5.35	3.28	-

1E	$\mathbf{UB_{34C}}$	$\mathbf{UB_{34C,\ Laue}}$	$\mathbf{UB_{34C,\ EBSD}}$
$\mathbf{UB_{34C}}$	-	-	-
$\mathbf{UB_{34C,\ Laue}}$	9.70	-	-
$\mathbf{UB_{34C,\ EBSD}}$	11.0	1.97	-

1F	$\mathbf{UB_{34C}}$	$\mathbf{UB_{34C,\ Laue}}$	$\mathbf{UB_{34C,\ EBSD}}$
$\mathbf{UB_{34C}}$	-	-	-
$\mathbf{UB_{34C,\ Laue}}$	7.14	-	-
$\mathbf{UB_{34C,\ EBSD}}$	9.56	3.05	-

Average	$\mathbf{UB_{34C}}$	$\mathbf{UB_{34C,\ Laue}}$	$\mathbf{UB_{34C,\ EBSD}}$
$\mathbf{UB_{34C}}$	-	-	-
$\mathbf{UB_{34C,\ Laue}}$	7.19	-	-
$\mathbf{UB_{34C,\ EBSD}}$	9.23	2.67	-

Table 4.2: Angular differences (°) between $\mathbf{UB_{34C}}$, $\mathbf{UB_{34C,\,Laue}}$, and $\mathbf{UB_{34C,\,EBSD}}$ for substrate 2.

2A	$\mathbf{UB_{34C}}$	$\mathbf{UB_{34C,\,Laue}}$	$\mathbf{UB_{34C,\,EBSD}}$
$\mathbf{UB_{34C}}$	-	-	-
$\mathbf{UB_{34C,\,Laue}}$	1.81	-	-
$\mathbf{UB_{34C,\,EBSD}}$	2.00	0.845	-

2B	$\mathbf{UB_{34C}}$	$\mathbf{UB_{34C,\,Laue}}$	$\mathbf{UB_{34C,\,EBSD}}$
$\mathbf{UB_{34C}}$	-	-	-
$\mathbf{UB_{34C,\,Laue}}$	0.366	-	-
$\mathbf{UB_{34C,\,EBSD}}$	3.33	3.56	-

2C	$\mathbf{UB_{34C}}$	$\mathbf{UB_{34C,\,Laue}}$	$\mathbf{UB_{34C,\,EBSD}}$
$\mathbf{UB_{34C}}$	-	-	-
$\mathbf{UB_{34C,\,Laue}}$	11.0	-	-
$\mathbf{UB_{34C,\,EBSD}}$	11.2	0.306	-

2D	$\mathbf{UB_{34C}}$	$\mathbf{UB_{34C,\,Laue}}$	$\mathbf{UB_{34C,\,EBSD}}$
$\mathbf{UB_{34C}}$	-	-	-
$\mathbf{UB_{34C,\,Laue}}$	0.392	-	-
$\mathbf{UB_{34C,\,EBSD}}$	0.659	0.269	-

2E	$\mathbf{UB_{34C}}$	$\mathbf{UB_{34C,\,Laue}}$	$\mathbf{UB_{34C,\,EBSD}}$
$\mathbf{UB_{34C}}$	-	-	-
$\mathbf{UB_{34C,\,Laue}}$	0.977	-	-
$\mathbf{UB_{34C,\,EBSD}}$	4.34	4.11	-

2F	$\mathbf{UB_{34C}}$	$\mathbf{UB_{34C,\,Laue}}$	$\mathbf{UB_{34C,\,EBSD}}$
$\mathbf{UB_{34C}}$	-	-	-
$\mathbf{UB_{34C,\,Laue}}$	0.425	-	-
$\mathbf{UB_{34C,\,EBSD}}$	1.58	1.23	-

Average	$\mathbf{UB_{34C}}$	$\mathbf{UB_{34C,\,Laue}}$	$\mathbf{UB_{34C,\,EBSD}}$
$\mathbf{UB_{34C}}$	-	-	-
$\mathbf{UB_{34C,\,Laue}}$	2.49	-	-
$\mathbf{UB_{34C,\,EBSD}}$	3.86	1.52	-

Table 4.3: Angular differences (°) between $\mathbf{UB_{34C}}$, $\mathbf{UB_{34C,\ Laue}}$, and $\mathbf{UB_{34C,\ EBSD}}$ for substrate 3.

3A	$\mathbf{UB_{34C}}$	$\mathbf{UB_{34C,\ Laue}}$	$\mathbf{UB_{34C,\ EBSD}}$
$\mathbf{UB_{34C}}$	-	-	-
$\mathbf{UB_{34C,\ Laue}}$	0.369	-	-
$\mathbf{UB_{34C,\ EBSD}}$	2.28	2.25	-
3B	$\mathbf{UB_{34C}}$	$\mathbf{UB_{34C,\ Laue}}$	$\mathbf{UB_{34C,\ EBSD}}$
$\mathbf{UB_{34C}}$	-	-	-
$\mathbf{UB_{34C,\ Laue}}$	9.69	-	-
$\mathbf{UB_{34C,\ EBSD}}$	10.7	2.09	-
Average	$\mathbf{UB_{34C}}$	$\mathbf{UB_{34C,\ Laue}}$	$\mathbf{UB_{34C,\ EBSD}}$
$\mathbf{UB_{34C}}$	-	-	-
$\mathbf{UB_{34C,\ Laue}}$	5.03	-	-
$\mathbf{UB_{34C,\ EBSD}}$	6.49	1.74	-

throughput and make MBCDI a much more widely accessible technique, especially at beamlines without pink beam capability or access to a nearby Laue instrument.

4.4.2 Determination of strain

MBCDI allows the strain and rotation tensors to be computed if at least three reflections are measured, providing more information about the crystal defects present [22,29,30,47]. Fig. 4.6 shows the strain and rotation tensors reconstructed from five measured Bragg reflections of crystal 1B. The ε_{xx}, ε_{yy}, and ε_{zz} slices show defects close to the edge that may not be resolved if analysing a single reflection alone [48] as some crystal defects, such as dislocations, are visible only when $\mathbf{Q}_{hkl}\cdot\mathbf{b} \neq 0$, where $\mathbf{b}$ is the Burgers vector [138].

These results were produced using a refined method for the computation of the strain and rotation tensor. A general approach for the computation of both these tensors is described in Chapter 2.4.10. This relies on the recovery of the phase of the CXDP. The intensity of the CXDP, which is the squared magnitude of the Fourier transform, $\mathscr{F}$, of the complex crystal electron density, f. The solution for the recovered phase is non-unique, as global phase offsets, C, can produce the same CXDP, i.e. $|\mathscr{F}[f(\psi(\mathbf{r}))]|^2 = |\mathscr{F}[f(\psi(\mathbf{r}) +$

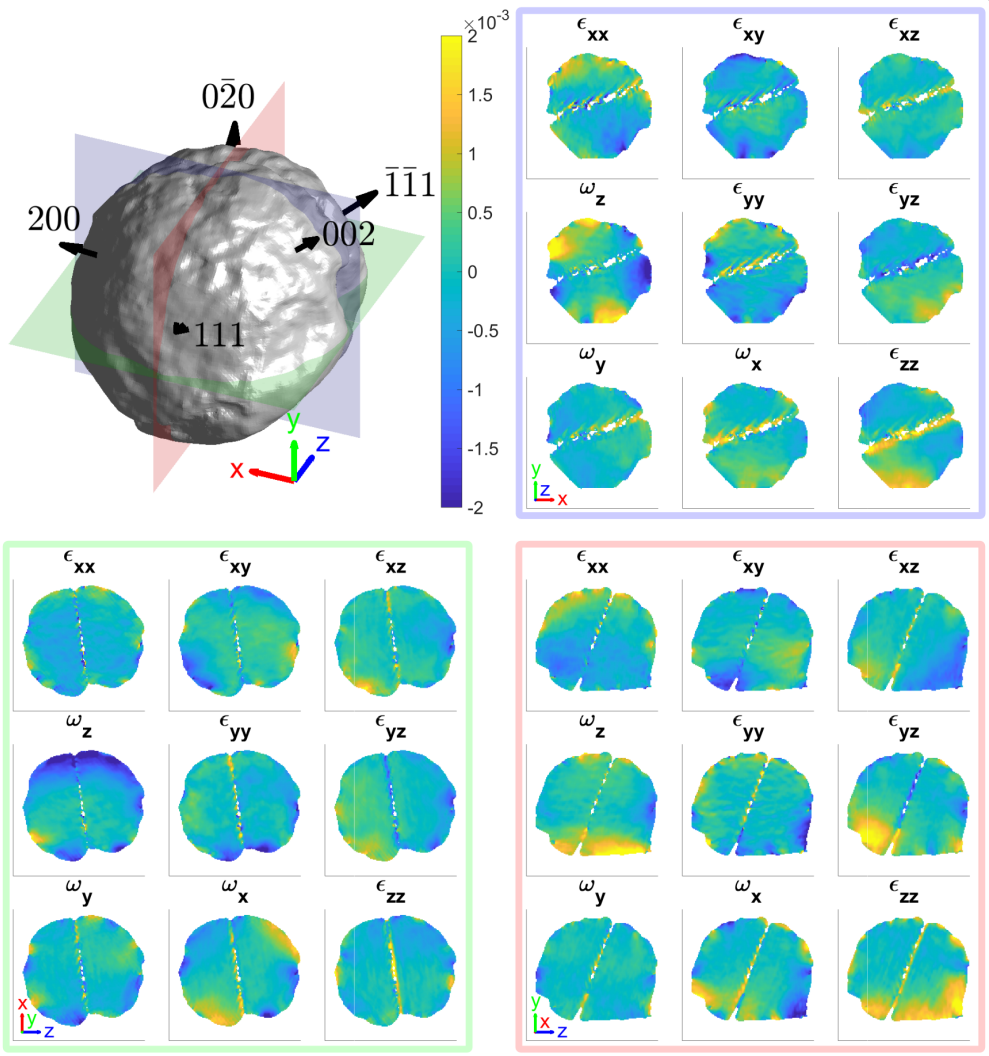

Figure 4.6: Average morphology of the 111, $\bar{1}\bar{1}1$, 200, $0\bar{2}0$, and 002 reflections for Fe-Ni crystal 1B. The average morphology taken over all five reflections is based on an amplitude threshold of 0.30. The slices through the strain and rotation tensor components are shown for the planes indicated at $x = 2.5$ nm (red), $y = 2.5$ nm (green), and $z = 2.5$ nm (blue) from the centre of mass of the microcrystal. The amplitude threshold is 0.30 and the coordinate axes are 100 nm long. Supplementary video (SV) 1-3 show the strain and rotation tensor components throughout the volume along the x, y, and z axis respectively.

$C)]|^2$. After phase retrieval, the phase values are bound between $[-\pi, \pi]$, which describes the periodic nature of the lattice structure, but not necessarily the true complex crystal electron density. For instance, if the projected displacement in the direction of $\mathbf{Q}_{hkl}$ is greater than $\pi/|\mathbf{Q}_{hkl}|$, then a phase jump, where the phase difference is 2π between two pixels, will occur. These phase jumps cause discontinuities in the derivatives of the phase, $\partial\psi_{hkl}(\mathbf{r})/\partial r$, leading to spurious, large strains. Typically, phase unwrapping algorithms can be used to remove phase jumps, but dislocations have characteristic phase vortices

[95] that end at dislocation lines, meaning that phase jumps associated with dislocations cannot be unwrapped.

To account for this, Hofmann *et al.* [30] demonstrated an approach by producing two additional copies of the phase with phase offsets of $-\frac{\pi}{2}$ and $\frac{\pi}{2}$ respectively. This shifts phase jumps to different locations, and by choosing the phase gradient with the smallest magnitude for each voxel, the correct phase derivatives can be found. Here, we employ a more efficient method used in coherent X-ray diffraction tomography from Guizar-Sicairos *et al.* [188], which has also been applied in the Bragg geometry using ptychography [152]. Rather than making multiple copies of the phase, we take the derivative of the complex exponential of the phase and determine the phase gradient using the chain rule:

$$\frac{\partial \psi_{hkl}(\mathbf{r})}{\partial j} = \mathrm{Re}\left(\frac{\partial e^{i\psi_{hkl}(\mathbf{r})}}{\partial j} \Big/ i e^{i\psi_{hkl}} \right). \tag{4.20}$$

Here $e^{i\psi_{hkl}(\mathbf{r})}$ is a circle expressed using Euler's formula, where the phase jumps disappear. Fig. 4.7 shows the difference in the two methods for computing the lattice rotation and strain tensors. We can see that the procedure based on phase offsets [30] fails to fully resolve the details in the regions with high strain, i.e. around the edges and central region of missing intensity. The new approach of computing phase gradients successfully deals with these complex regions.

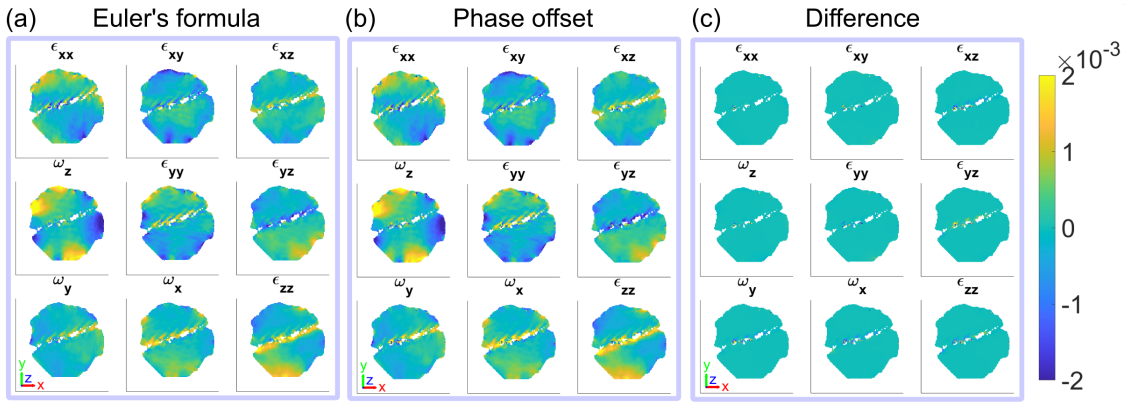

Figure 4.7: A comparison of the strain and rotation tensors at $z = 2.5$ nm computed using two different methods. (a) shows the strain and rotation tensors as computed using Eq. 4.20 [188]. (b) shows the strain and rotation tensors as computed by introducing phase offsets and choosing the phase gradient with the minimum value [30]. (c) shows the difference between the results. The amplitude threshold for the reconstructions is 0.30 and the magnitude of the coordinate axes is 100 nm.

Furthermore, we apply this to the interpolation of the phase from detector conjugated space to sample space, by interpolating the complex quantity, $e^{i\psi_{hkl}}$, instead of ψ_{hkl}. This avoids the blurring of phase jumps that occurs during direct interpolation of ψ_{hkl}, shown in Fig. 4.8.

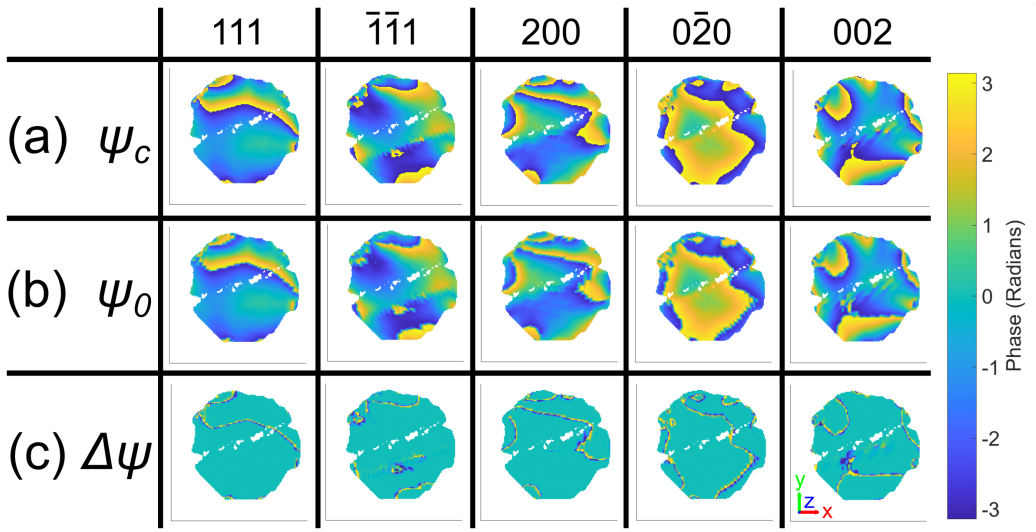

Figure 4.8: Phases for the 111, $\bar{1}\bar{1}1$, 200, $0\bar{2}0$, and 002 reflections at $z = 2.5$ nm. We compare the new method of interpolating the complex quantity of the phase, ψ_c, (a), to interpolating the phase alone, ψ_0, (b). The difference between ψ_c and ψ_0, $\Delta\psi$, highlights the information that can only be resolved around phase jumps in ψ_c (c). The amplitude threshold for the reconstructions is 0.30 and the size of the coordinate axes is 100 nm.

This refinement of strain and rotation tensor computation allows for a more accurate reconstruction of crystal defects and their associated nanoscale lattice strains. It also decreases the time required to compute the tensors since phase offsets need to be applied before and after mapping the crystal from detector conjugated space to orthogonal sample space. This will play an important role in the analysis of large MBCDI datasets, such as those obtained from *in situ* or *operando* experiments that reveal crystal defects interacting with their environment. Reconstruction accuracy in multi-Bragg peak phase retrieval algorithms that involve a shared displacement field constraint applied to all reflections would also be improved by implementing this more accurate interpolation of phase values [103, 104, 120].

4.5 Conclusion

We demonstrate that the orientation of various microcrystals on different substrates can be found using EBSD and used to align BCDI experiments. Results indicate a $\sim 2^{\circ}$ increase in angular error when using EBSD alignment compared to Laue diffraction alignment, which is still within reasonable tolerance for the search for Bragg peaks. Importantly, using EBSD to pre-align crystals allows beamtime to be more effectively utilised for BCDI dataset collection. It also removes the need for BCDI and Laue instrument coordination and enables MBCDI on BCDI instruments that do not have pink beam capability or a Laue instrument nearby. Using the orientation matrix obtained from EBSD, five reflections are located on a Fe-Ni microcrystal and full 3D strain and rotation tensors are recovered. When computing the tensors, we demonstrate a more efficient approach to resolving phase jumps, by implementing a complex phase quantity to calculate and interpolate the phase. This allows for the phase to be unwrapped and the correct strain to be resolved in the vicinity of dislocations. These refinements make BCDI a more accessible microscopy tool.

4.6 Data availability

The CXDPs, final reconstructions and data analysis scripts, including a script to compute the orientation matrix using EBSD, are publicly available at 10.5281/zenodo.6383408.

Chapter 5

Annealing of focused ion beam damage in gold microcrystals: An *in situ* Bragg coherent X-ray diffraction imaging study

Using the BCDI-related developments presented in Chapters 3 and 4, I study how lattice defects due to FIB damage, and more importantly their strain fields, are removed during annealing. Here, I explore the evolution of average lattice strain, facet sizes, lattice displacements and crystal morphologies for two FIB-milled Au crystals. It is confirmed that annealing can be used as a pathway to remove FIB-induced strain. This is an important finding for the micromechanics community which uses FIB routinely to prepare samples. This study also addresses a key limitation of using single reflection BCDI measurements, noting differences in the analysis for each reflection. The shortcomings of interpreting each reflection independently highlight the need for MBCDI measurements to determine the full lattice strain and rotation tensors. This chapter is in publication format based on the article: D. Yang, N. W. Phillips, K. Song, R. J. Harder, W. Cha, and F. Hofmann, "Annealing of focused ion beam damage in gold microcrystals: An in situ Bragg coher-

ent X-ray diffraction imaging study," *Journal of Synchrotron Radiation*, vol. 28, no. 2, pp. 550–565, 2021 [48].

N.W. Phillips and K. Song assisted with BCDI and micro-beam Laue X-ray diffraction data collection. N.W. Phillips designed the heater cell cover. BCDI experiments were performed at 34-ID-C, with help from R.J. Harder and W. Cha. The remainder of the work was carried out by the author under the supervision of F. Hofmann.

5.1 Abstract

Focused ion beam (FIB) techniques are commonly used to machine, analyse and image materials at the micro- and nanoscale. However, FIB modifies the integrity of the sample by creating defects that cause lattice distortions. Methods have been developed to reduce FIB-induced strain, however these protocols need to be evaluated for their effectiveness. Here we use non-destructive Bragg coherent X-ray diffraction imaging to study the *in situ* annealing of FIB-milled gold microcrystals. We simultaneously measure two non-collinear reflections for two different crystals during a single annealing cycle, demonstrating the ability to reliably track the location of multiple Bragg peaks during thermal annealing. The thermal lattice expansion of each crystal is used to calculate the local temperature. This is compared to thermocouple readings, which are shown to be substantially affected by thermal resistance. To evaluate the annealing process, we analyse each reflection by considering facet area evolution, cross-correlation maps of displacement field and binarised morphology, and average strain plots. The crystal's strain and morphology evolve with increasing temperature, which is likely to be caused by the diffusion of gallium in gold below ~ 280°C and the self-diffusion of gold above ~ 280°C. The majority of FIB-induced strains are removed by 380-410°C, depending on which reflection is being considered. Our observations highlight the importance of measuring multiple reflections to unambiguously interpret material behaviour.

5.2 Introduction

Focused ion beam (FIB) techniques utilise a beam of energetic ions, often gallium (Ga) extracted from liquid metal, to remove material at the micro- and nanoscale [189]. The ability to control sample features at these previously inaccessible length scales has furthered the understanding of material properties, e.g., by enabling the exploration of size-dependent material behaviour. Most notably, the "smaller-is-stronger" effect has been extensively studied using nanoindented FIB-machined specimens [8, 11]. The deformation behaviour of these samples varied significantly, depending on several competing mechanisms. One mechanism, exhibited by polycrystalline copper films [26] and Mo alloy single crystals [190], shows that FIB damage can lead to a dense population of defects, making the escape of dislocations at the surface more difficult, which causes an apparent hardening. On the contrary, softening has been reported in FIB-fabricated Mo alloy micropillars with a low initial defect density [191]. Here FIB-induced dislocation loops act as sources for glide dislocations, leading to a reduction in yield stress [191]. Additionally, FIB can cause other material changes such as amorphisation [24], local recrystallisation [25], twin nucleation [27], and intermetallic phase formation [28], to name a few.

Experiments on gold (Au) microcrystals have shown that FIB milling can cause lattice strains that extend more than 100 nm below the surface of the material [29, 47]. This can be a major concern as samples are no longer in their original state and these FIB-induced loads will act in addition to externally applied stresses. Notwithstanding, FIB remains a regularly used tool for 3D material characterisation [192], micromechanical test sample fabrication [193], and top-down preparation of transmission electron microscopy (TEM) samples [25, 189]. The severity of FIB-induced sample modification depends on specific milling conditions [194]. Methods introduced to mitigate this damage must be versatile and effective to allow FIB milling to reach its full potential as a micromachining tool.

Numerous approaches have been suggested for removing FIB damage: use of a plasma FIB [195], post-milling low energy (2 keV) ion polishing [196], sacrificial coatings [197],

chemical etching [198], and post-manufacture heat treatment [199,200]. Here we investigate the effects of annealing, a process that increases defect mobility and thereby provides a pathway for the removal of FIB-induced defects and, more importantly, the resulting strains. To evaluate the effectiveness of annealing for FIB-induced strain removal, we require a technique that allows nanoscale spatial resolution and high strain resolution. Previous *in situ* TEM studies have been performed, showing that temperatures of half the material's melting point were sufficient to remove FIB-induced dislocation loops in Al micropillars [200] and reduce defect density in FIB-made Cu samples [199]. However, TEM is limited to thin samples, where the close proximity of free surfaces can dominate behaviour. Hence, we require a technique capable of capturing high strain resolution information in 3D micron-sized volumes.

Previously, BCDI has been used to investigate annealing of 3C-SiC nanoparticles [145], diamond nanoparticles [55], magnetite crystals [170] and metallic glass [201]. Furthermore, BCDI has been extensively used to study Au subject to iron diffusion [56], copper diffusion [174] and catalytic oxidation [202]. However, these experiments only considered one reflection, and thus only the strain along the Bragg vector could be resolved. Our previous BCDI studies found that FIB-milled Au crystals had large phase features corresponding to lattice dilation and contraction [29,47,57]. These features were concentrated at the top and on the side of the milled crystals–on the surfaces exposed to the FIB beam. Defects such as stair-rod dislocations and their corresponding Burgers vectors were identified in the FIB-affected sample volume [29, 47]. This contrasts the comparatively flat, homogeneous phase observed in the as-grown crystals [29, 47, 203]. The study [29] further characterised the removal of substantial FIB damage by using a 5 keV polishing step. The ability to capture these observations throughout an entire 3D volume with high strain sensitivity and spatial resolution makes BCDI attractive for the study of FIB-damaged materials.

Here we investigate the *in situ* annealing of FIB-milled Au microcrystals using BCDI to examine how the 3D strain and crystal morphology evolve as a function of temperature.

We demonstrate the successful measurement of two unique reflections for two separate FIB-milled Au crystals during an *in situ* annealing cycle from 23°C (room/ambient temperature) to 587°C. After recovering the amplitude and phase of the crystals, we identify temperatures where structural changes occur through observations of crystal facet areas, Pearson's normalised cross-correlation coefficient, r, of $\mathbf{u}_{hkl}(\mathbf{r})$ and binary morphology masks, and average strain in different crystal volumes of interest (VOI), which are defined according to their FIB exposure. The use of two reflections for each sample highlights subtle differences in the lattice relaxation, which is observed to be dependent on the crystallographic direction and the geometry of the sample. We also consider the diffusion of Ga in Au and the self-diffusion of Au to determine which mechanism is probably responsible for specific changes. With four reflections, we faithfully identify temperatures where transitions in crystal shape, r, and average strain occur to evaluate the effectiveness of annealing in eliminating FIB-induced material damage.

5.3 Experimental methodology

5.3.1 Sample preparation

Au microcrystals were prepared on a [001]-oriented silicon substrate with a 100 nm thick thermally grown oxide layer. First, the wafer was spin-coated with ZEP resist and patterns of 2 μm wide lines were produced on the substrate using electron-beam lithography. Following the removal of the resist, the wafer was coated with a 3 nm thick Cr adhesion layer followed by 40 nm of Au. A pattern of Au lines remained on the substrate after a "lift-off" procedure was used to remove the unpatterned areas. Next, the sample was annealed at 1000°C in air for 10 h, dewetting the lines to form microcrystals ranging from 200 nm to 1 μm in diameter. Scanning electron microscopy (SEM) was used to select suitable crystals for this study.

Using a Zeiss AURIGA FIB-SEM, candidate crystals were subjected to FIB milling with Ga ion energy of 30 keV and beam current of 20 pA, as this closely mimics the

final milling cut during the manufacture of micromechanics test specimens [204–206]. Approximately one third of the crystal was removed using an incremental trench-milling mode. SEM imaging rather than low dose FIB imaging was used to position the FIB milling scan, as our previous results indicate that even a single FIB image can induce large lattice strains in the Au microcrystals [47]. Fig. 5.1(a) shows high-resolution SEM micrographs of the chosen FIB-milled microcrystals, crystal A and B, in excellent agreement with their respective morphologies recovered from BCDI at room temperature in Fig. 5.1(b-c). Crystal A and B were $\sim 10\ \mu$m apart on the substrate.

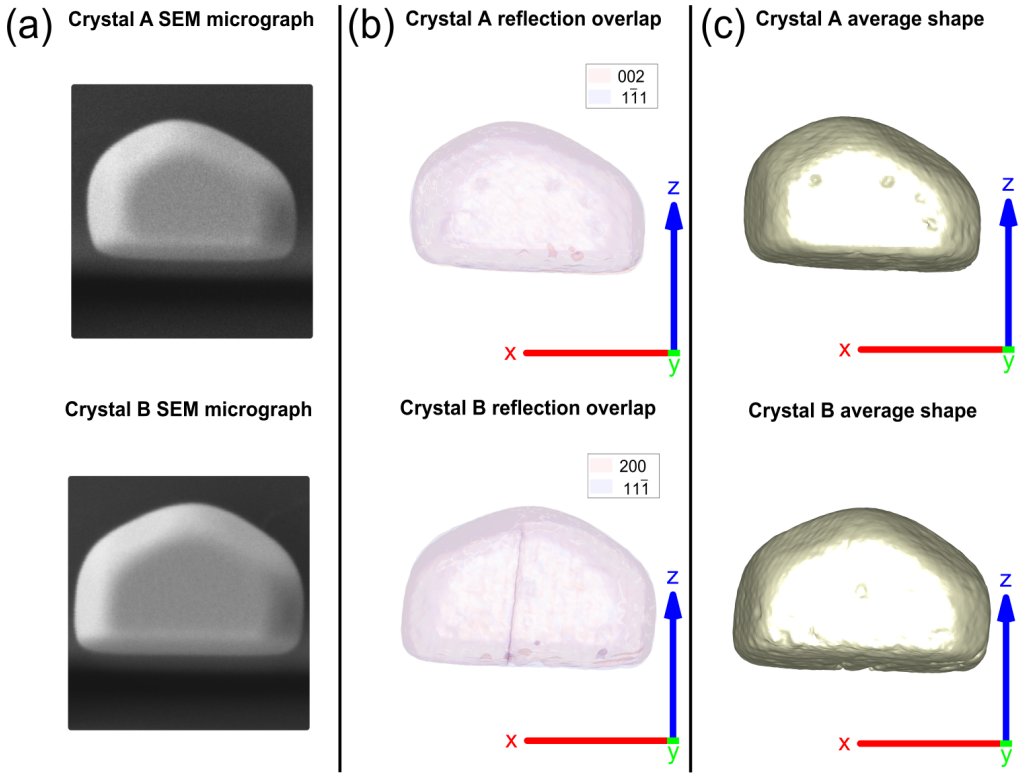

Figure 5.1: Comparison between SEM micrographs of crystals A and B and sample morphology recovered from BCDI at room temperature (23°C). (a) SEM micrographs of the FIB milled crystals. (b) Superimposed reconstructions of the two measured linearly independent reflections for each crystal. Opaque morphologies are rendered to allow examination of their agreement. The near vertical line in crystal B corresponds to a twin domain boundary on the bottom face. (c) Average morphology of the two reflections for each crystal. The amplitude threshold for (b) and (c) is 0.30. The coordinate axes are positioned in sample space and plotted with a length of 500 nm.

5.3.2 Bragg coherent X-ray diffraction

Synchrotron X-ray diffraction measurements were carried out at the APS. Before BCDI measurements, micro-beam Laue diffraction at beamline 34-ID-E was used to determine the lattice orientation of the crystals on the silicon wafer. A procedure for the alignment of BCDI measurements, based on Laue diffraction orientation measurements, is provided elsewhere [57].

BCDI measurements at beamline 34-ID-C used an X-ray beam with 9 keV photon energy ($\lambda = 0.138$ nm) and a spot size of 760 nm $\times$ 750 nm (full width at half maximum) using Kirkpatrick–Baez mirrors [64]. The Si substrate was clipped onto a heater cell available at the beamline shown in Appendix C.1. A CXDP was collected on a 256×256 pixel quadrant of a Timepix detector (Amsterdam Scientific Instruments) with a GaAs sensor and pixel size, p, of 55 μm $\times$ 55 μm positioned at a distance, D, of 1.2 m away from the sample to ensure that the diffraction pattern was oversampled [37]. The lower bound for D was determined by $D = \frac{2dp}{\lambda}$, where d is the sample size. The 002 and $1\bar{1}1$ reflections were measured for crystal A and the 200 and $11\bar{1}$ reflections for crystal B at every temperature step.

At ambient temperature, the $1\bar{1}1$ reflection for crystal A was rotated through an angular range of 0.7° while the remaining reflections occupied a range of 0.6°. For each rocking curve, a slice through the CXDP was captured every 0.004° with 0.2 s exposure time and 20 accumulations. A total of 175 increments were collected for the $1\bar{1}1$ reflection and 150 increments for the other reflections. Each CXDP measurement was repeated multiple times to optimise the signal-to-noise ratio. For crystal A, 8 scans were collected for the 002 reflection and 14 for the $1\bar{1}1$ reflection, while for crystal B, 9 scans were collected for the 200 reflection and 10 for the $11\bar{1}$ reflection at room temperature.

The angular range, number of accumulations, number of repeated scans and exposure time were adjusted at higher temperatures to sufficiently sample the temperature range as discussed in Section 5.3.2.1. From 90°C onward, an angular range of 0.7° with 0.004° steps was used, i.e. 175 increments were collected in the rocking scan for CXDPs above

room temperature, and 10 accumulations were taken instead of 20. Only 3 repeated scans were collected between 90°C and 209°C inclusive. From 213°C onward, a 0.1 s exposure time was used and only 2 scans were measured, with the exception of the $1\bar{1}1$ reflection at 213°C where 3 scans were measured. After performing flat-field and dead-time corrections (Eq. 4.15), repeated scans were aligned using a 3D version of the approach proposed by [207] to maximise their cross-correlation and only scans with r greater than 0.975 were averaged to return the CXDP used for phasing. All scans were summed and used for phase retrieval.

5.3.2.1 *In situ* annealing

The temperature was increased using the step and hold temperature profile shown in Fig. 5.2. We expect the actual temperature of the crystal, $T_{calibrated}$, to be higher than that reported by the thermocouple, $T_{measured}$. This discrepancy arises because the thermocouple is attached to the clip that fixes the substrate (Appendix C.1), whereas the microcrystals are on top of the substrate, thus the thermocouple does not measure the actual temperature of the microcrystals. There is heat loss between the microcrystals and the thermocouple due to the thermal resistance from the substrate and clip. To calculate $T_{calibrated}$ from $T_{measured}$, we use the samples as local measurement devices. In this section, we consider the thermal expansion of pure Au, $\varepsilon_{thermal} = \alpha_{Au}\Delta T$, where ΔT is the temperature change and α_{Au} is the linear thermal expansion coefficient [208], to determine $T_{calibrated}$. We assume that implanted Ga ions after FIB milling have negligible effect on the Au thermal expansion coefficient, as the ions only penetrate 20 nm below the surface [29].

Since Au has fcc crystal structure, lattice thermal expansion acts uniformly in all directions, causing the Bragg angle to decrease with increasing temperature. To track the Bragg peak, an alignment macro was run during the temperature ramp that ensured the diffractometer was positioned such that the maximum intensity was always centred in the top left quadrant of the detector immediately before the start of the rocking scans. This protocol ensured that the strain measured by BCDI was relative to the zero-strain

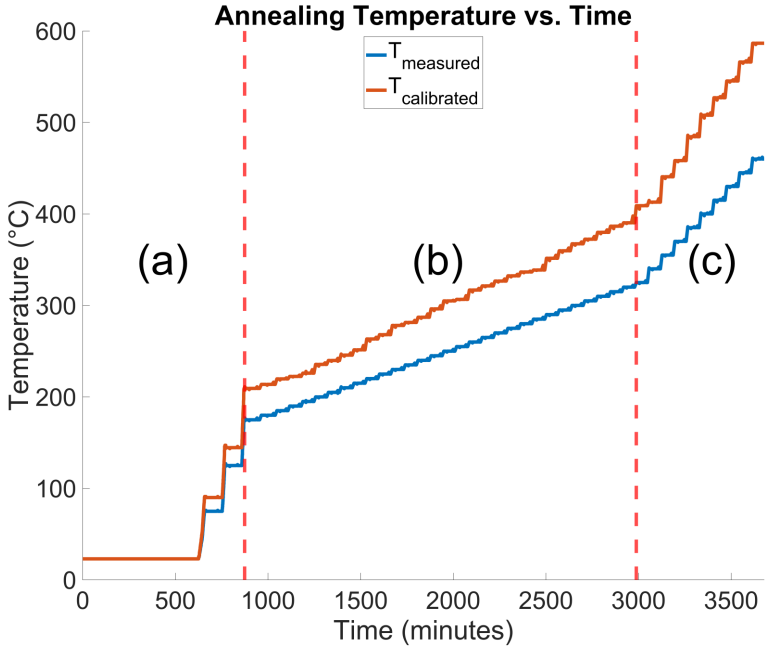

Figure 5.2: The annealing temperature profile as a function of time. Changes in the temperature step size are marked by the red dashed lines. (a) $T_{calibrated}$ was raised from room temperature to 209°C using $\sim$ 50°C steps with a ramp rate of 2°C/min. (b) From 209°C to 409°C, $\sim$ 5°C steps were used with a ramp rate of 50°C/min. Finally, from 409°C to 587°C, $\sim$ 20°C steps were used with a ramp rate of 50°C/min. The ramp rate reported here is with respect to $T_{measured}$ and was lower in (a) to ensure that the alignment macro could update the positions of the reflections for larger temperature steps.

reference region for each reflection as explained in Section 5.3.3, allowing a comparison between temperatures. By tracking the change in detector position at every temperature step, i, the lattice parameter, a_i, at each step can be calculated:

$$a_i = \frac{\lambda}{2\sin(\theta_i)}\sqrt{h^2+k^2+l^2}, \quad \text{where} \quad \theta_i = \frac{1}{2}\cos^{-1}\left(\frac{\mathbf{S}_i \cdot \mathbf{S}_0}{\mathbf{S}_0 \cdot \mathbf{S}_0}\right) \tag{5.1}$$

where θ_i is the Bragg angle, $\mathbf{S}_i$ is the outgoing wavevector (the detector position) and $\mathbf{S}_0$ is the incident wavevector. Using a_i and the literature value of α_{Au}, we calculate $T_{calibrated}$:

$$T_{\text{calibrated},i} = \frac{\varepsilon_{\text{thermal},i}}{\alpha_{Au}} + 23°\text{C}, \quad \text{where} \quad \varepsilon_{\text{thermal},i} = \frac{a_i - a_{23°\text{C}}}{a_{23°\text{C}}} \tag{5.2}$$

Fig. 5.3 shows the discrepancy between $\varepsilon_{thermal}$ plotted against $T_{calibrated}$ and $T_{measured}$. The correction for $T_{calibrated}$ was determined by averaging over the four reflections, with a mean standard deviation of $\sim$ 8°C, indicating good agreement amongst the four reflec-

tions.

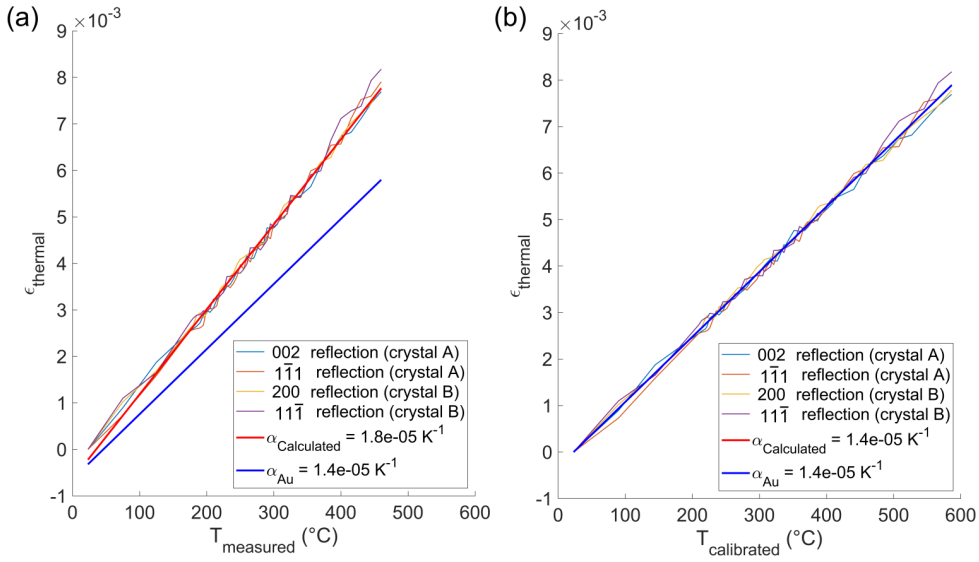

Figure 5.3: A comparison of $\varepsilon_{thermal}$ plotted against (a) $T_{measured}$ and (b) $T_{calibrated}$ for each reflection. The $\varepsilon_{thermal}$ was calculated using Eq. 5.1 and 5.2 by tracing the angular position of the detector during annealing. In (a), the measured $\varepsilon_{thermal}$ averaged over all reflections (red line) does not agree with the predicted $\varepsilon_{thermal}$ (blue line) when plotted using $T_{measured}$. In (b), the measured $\varepsilon_{thermal}$ plotted using $T_{calibrated}$ (determined by α_{Au}) overlaps with the predicted $\varepsilon_{thermal}$ as intended.

In this chapter all temperatures noted refer to $T_{calibrated}$ rather than $T_{measured}$ unless specified. The temperature profile (shown in Fig. 5.2) has three varying temperature steps so as to capture the entirety of the annealing process whilst retaining a high sampling rate between 209-409°C. At low temperatures the migration energy was believed to be too high for noticeable interstitial and vacancy movement, hence larger temperature steps of $\sim$ 50°C were used. Below $T_{Hüttig}$, the Hüttig temperature, which marks the threshold for surface atom mobility (127°C for Au) [209], no changes are expected. Indeed, in this experiment, we focus on atomic mobility over tens of nanometres below the surface, as this is the thickness of the layer in which Ga implantation causes atomic displacement damage [29]. Such solid-state diffusion is expected to occur above $T_{Tammann}$, the Tammann temperature (327°C for bulk Au recrystallisation) [209], thus from 209°C $\sim$ 5°C steps were taken to increase the temperature resolution of our data set in order to capture structural transitions. It is important to note that the Hüttig and Tammann temperatures are semi-empirical ($T_{Hüttig} = 0.3T_{melting}$) and ($T_{Tammann} = 0.5T_{melting}$) and depend on sur-

face texture, orientation, morphology and particle size [210] based on the Gibbs-Thomson equation [211]. After reaching 409°C, the temperature was increased using $\sim 20^{\circ}$ C steps. This was because much of the FIB damage was expected to already have been removed, based on a study showing the near complete recovery of nanoindented Au microcrystals annealed at ~ 0.65 times the melting temperature (596°C for Au) [212].

5.3.3 Phasing of the diffraction data

Before the real-space, complex-valued electron density of the crystals can be reconstructed, the phase of the diffracted wavefield must be recovered using an iterative phase retrieval algorithm [134]. The use of established phase revival algorithms enables the recovery of the object by iteratively applying real and reciprocal space constraints to an initial guess [89, 99, 134, 136]. Here, the starting guess for each reflection is of particular interest, as seeding with a good start guess generally results in a faster convergence. At each temperature (except the initial and final temperatures), we could seed the reconstruction with the reconstruction from the previous or succeeding temperature step (see Appendix C.2). We instead seed each reconstruction with itself through multiple rounds [30], with the initial round being seeded with a random guess (see details in Appendix C.3).

Once the phases were retrieved, the strain fields projected along the Bragg vector, $\varepsilon_{hkl}(\mathbf{r})$, were calculated using Eq. 2.78.

These strain fields are relative to the zero-strain reference of the reconstruction. The assumption of close to zero lattice strain beyond a distance of ~ 150 nm from the FIB-milled surface has previously been validated [29, 47]. Thus, we establish a $40 \times 40 \times 40$ voxel volume centred on the bulk VOI's (Fig. 5.9) centre of mass, a region relatively unaffected by FIB-induced strain, as the strain reference for every reconstruction [22]. The amplitude threshold is 0.30 for all reconstructions. Furthermore, each final object is eroded by 1 voxel in an attempt to remove a phasing surface artefact caused by steep phase gradients across the air-sample interface convolved with the resolution function [98].

We report the 3D spatial resolution to be ~ 23 nm. This was determined by differen-

tiating two amplitude line profiles drawn across the air-sample interface and fitting each of them with a Gaussian. The final spatial resolution was the average of the full width at half maximum of the two Gaussians for all reconstructions. We note that the resolution is somewhat dependent on the measurement directions in reciprocal space and the geometry of the sample. Appendix C.4 shows a plot of the spatial resolution of each line profile for each crystal reflection with respect to temperature.

5.4 Results and discussion

5.4.1 Crystal strain and morphology

Fig. 5.4 shows a comparison of the strain found along each reflection, $\mathbf{Q}_{hkl}$, of the FIB-milled crystals between the initial and final temperature. At room temperature, the reconstructed crystal morphologies are rough, especially on the surface of the milled face where complex sputtering and redeposition processes compete, which results in a pitted surface morphology. In Fig. 5.4 the four trench-like features visible on the surface of the 200 reflection for crystal B are near-surface dislocations caused by the milling process. These manifest as pipes of missing intensity in the amplitude of the reconstruction and are at the centre of a phase vortex [30, 47, 95, 153, 156]. The phase vortices of the 200 reflection are identified in Appendix C.5. Dislocations are visible only when $\mathbf{Q}_{hkl} \cdot \mathbf{b} \neq 0$ [138] and therefore are not necessarily visible for all reflections. For crystal B, the dislocations are visible only for the 200 data. From two reflections alone, it is not possible to uniquely identify the Burgers vector of these dislocations, although it is likely that it is of $(a/3) < 110 >$ type [47].

The room temperature 2D strain slices for each reflection are comparable in magnitude, with a maximum strain of $\sim 1.5 \times 10^{-3}$, to published data for glancing incidence FIB damage in Au [29]. The same publication reports a thin compressive region followed by a tensile region along the milled face, which is prominently observed here in the 200 reflection for crystal B. A previous normal incidence FIB-milling study on Au micro-

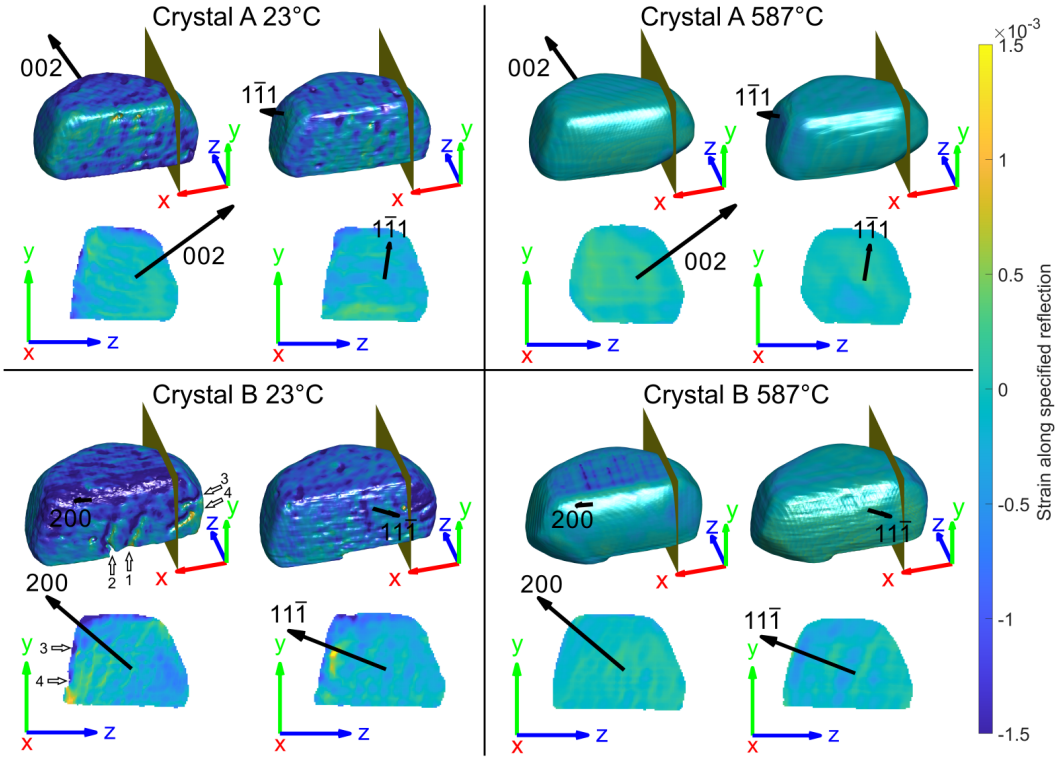

Figure 5.4: Rendering of the strain in crystal A and B for each reflection at 23°C and 587°C. In the top row of each quadrant the milled face is shown with a slice perpendicular to the x-axis. The bottom row of each quadrant is the 2D view of the corresponding slice. The small edge at the bottom of crystal B is a twin domain boundary marking a region of missing intensity. The black arrows represent the Bragg vector direction. The coordinate axes are positioned in sample space and plotted with a length of 250 nm. Numbered white arrows highlight trench-like structures that are reminiscent of dislocations. The blue hashed region at 587°C on the top face of the 200 reflection for crystal B is a reconstruction artefact (see Section 5.3.3) and does not physically represent a compressive layer.

crystals at room temperature [47] reported a compressive layer at the top of the samples, caused by normal incident angle ions impacting the top of the crystal from the tails of the FIB probe. This is seen in the 002 reflection for crystal A and both the 200 and $11\bar{1}$ reflections for crystal B.

After heating to 587°C, the strain and the crystal morphology have changed dramatically (Fig. 5.4) and presents a relatively constant strain in the 2D slices. Additionally, the surface morphology is observed to become smooth and evolution of the facets is observed. Supplementary videos (SV) SV1 and SV2 show the evolution of the surface morphology and internal strain for each crystal. In Fig. 5.4 the dislocations or pits on the milled face in the 200 reflection disappear after roughly (1) 296°C, (2) 352°C, (3) 372°C and (4) 380°C, indicated by the elimination of phase vortices, as surface restructuring is well underway.

These temperatures are mostly consistent with being above the Tammann temperature (327°C) for Au.

5.4.2 Facet area

With increasing temperature, both milled faces expanded outwards along the z-direction and became rounder at the bottom, demonstrating the formation of low-index facets, shown in Fig. 5.5, as a means to reduce the overall free surface energy. Facet areas were computed by calculating the area of the crystal whose isonormal is within a 19° angular threshold of a given facet normal unit vector. In principle a maximum angular threshold of 27.4° could be used, which is half the angle between $\{111\}$ and $\{100\}$ planes. Our chosen tolerance is below this maximum value since not all facets are fully developed, and the edges of the crystal are rounded and thus should not be classified as part of a facet.

Fig. 5.6 and supplementary video SV3 show facet area evolution as temperature increases for both crystals. Fig. 5.4 shows that the facet at the bottom right edge of crystal A that appears after 410°C (see supplementary video SV1) is $(00\bar{1})$ and the facet at the bottom left edge of crystal B that appears after 441°C (see supplementary video SV2) is $(1\bar{1}\bar{1})$. The identification of these facets is based on Fig. 5.5 and supplementary video SV3. The formation of low-index facets has been suggested to relieve strain [213], and contribute to thermodynamic equilibrium [214]. However, we do not fully reach the Winterbottom thermodynamic equilibrium shape [215] due to finite measurement time. For Au, the order of free surface energies for low index facets is $\{111\} < \{100\} < \{110\}$ based on ab initio techniques that concur with the number of nearest-neighbour broken bonds [216]. Thermodynamically, the formation of a $(1\bar{1}\bar{1})$ facet is most favourable, shown in crystal B. However, the production of the $(00\bar{1})$ facet in crystal A and the disappearance of the $(00\bar{1})$ facet in crystal B after 527°C are not improbable as normal movement of facets in dislocation-free single crystals can be restricted by the magnitude of the nucleation barriers if the crystal is larger than a few nanometres [217]. In crystal

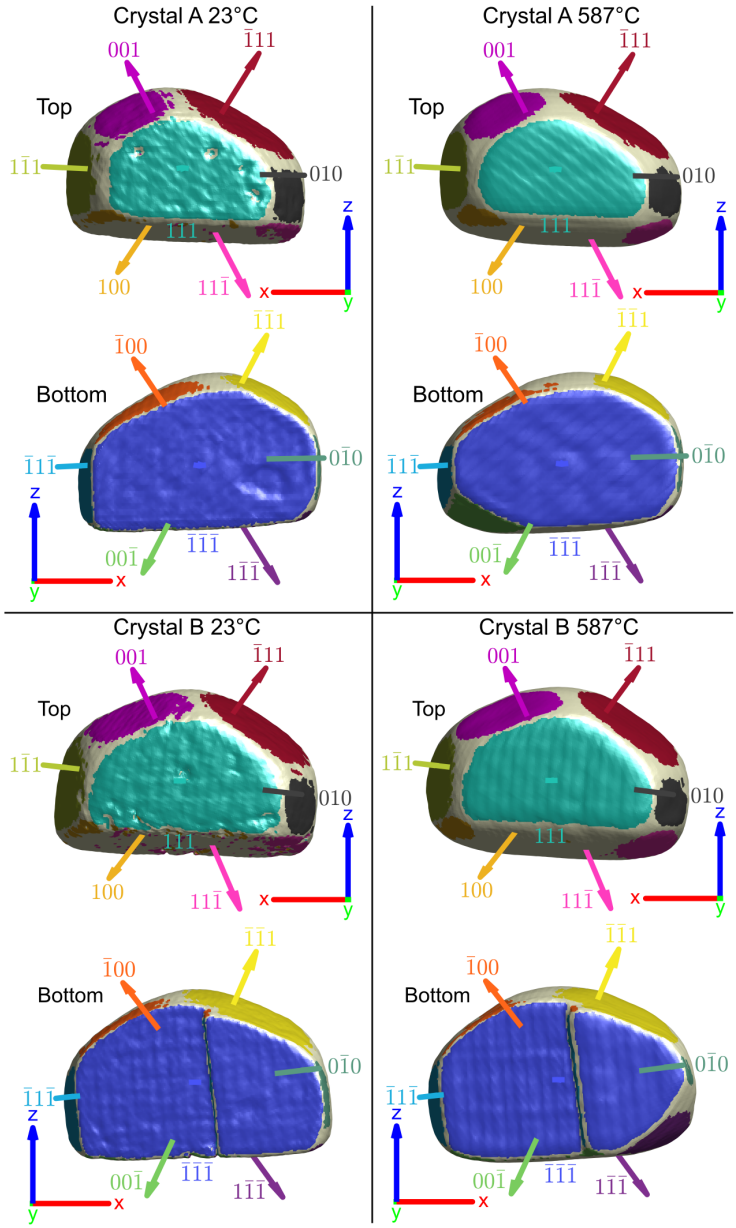

Figure 5.5: Normal vectors for each separately coloured facet are shown at 23°C and 587°C for both crystals. Note only vectors pointing out of the page in the top and bottom views are drawn for clarity. The coordinate axes are positioned in sample space and plotted with a length of 250 nm.

B, the $(00\bar{1})$ facet shrinks after 527°C but the $(1\bar{1}\bar{1})$ facet grows, suggesting that the latter is a lower energy configuration.

5.4.3 Normalised displacement field cross-correlation matrix

To pinpoint transitions in strain, we consider a Pearson r correlation matrix of the displacement fields between different temperatures for each reflection. When analysing sin-

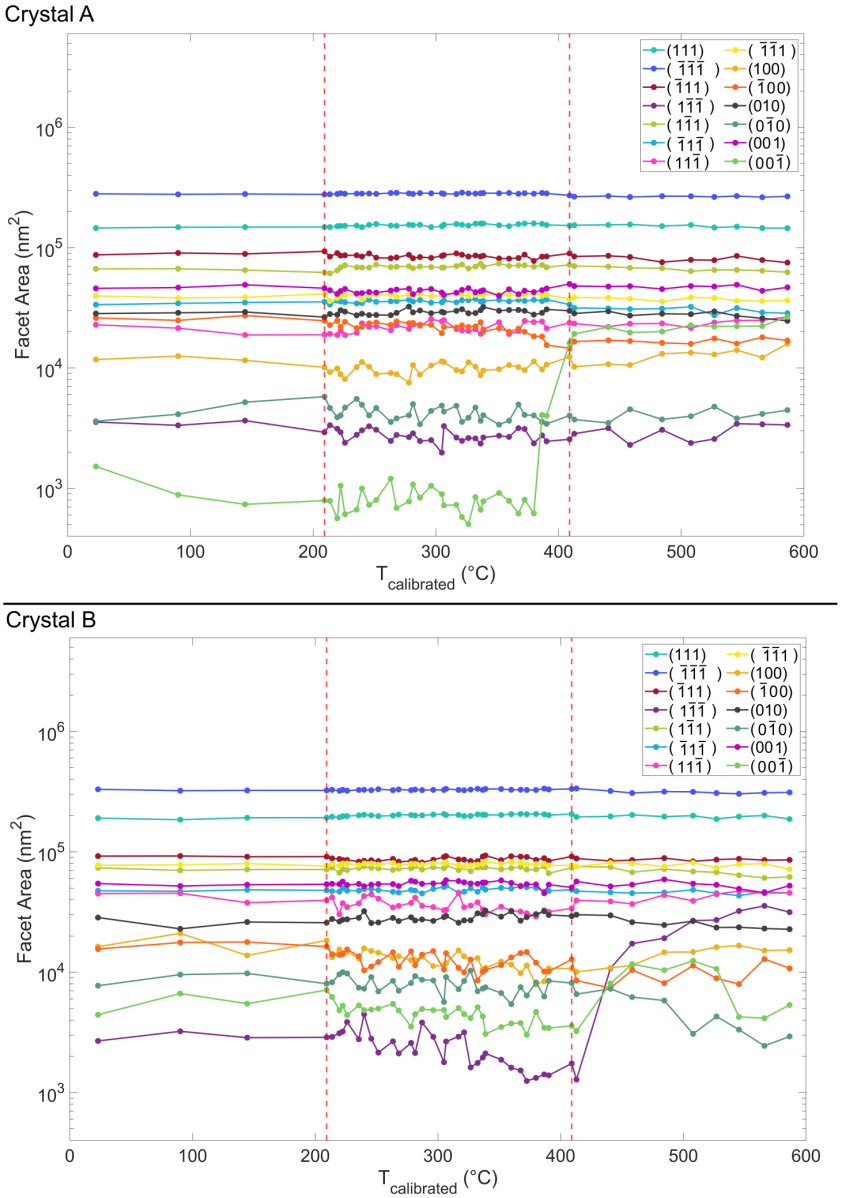

Figure 5.6: Low-index facet areas of crystal A and B as a function of temperature. See Fig. 5.5 for facet locations on the crystal.

gle reflections, this method has been used [143, 146] to infer structural transitions. The value of r between each combination of temperatures was computed using Eq. 5.3 [146]:

$$r(x,y) = \frac{\sum_n (x_n - \bar{x})(y_n - \bar{y})}{\sqrt{\sum_n (x_n - \bar{x})^2} \sqrt{\sum_n (y_n - \bar{y})^2}} \tag{5.3}$$

where x_n is the value for a given voxel and temperature, $\bar{x}$ is the mean of the entire array for that temperature, y_n is the value for the same voxel at another temperature and

$\bar{y}$ is the mean of the entire array at that temperature. The cross-correlation coefficient is calculated for each voxel in the array. By definition, $r = 1$ for the diagonal because the same array is perfectly correlated to itself. Before computing r, each crystal was shifted such that its centre of mass was in the middle of the $256 \times 256 \times 256$ voxel array, which was subsequently cropped to a $98 \times 186 \times 126$ voxel array, still fully encapsulating the crystal, to speed up r computation.

The r matrix is shown in Fig. 5.7 for $\mathbf{u}_{hkl}(\mathbf{r})$. Before using Eq. 2.44 to calculate $\mathbf{u}_{hkl}(\mathbf{r})$, phase ramps were removed by re-centring the Fourier transform of the complex electron density and a phase unwrapping algorithm [218] was used to remove phase wraps. Furthermore, we accounted for arbitrary phase offsets by establishing a $40 \times 40 \times 40$ voxel volume centred about the bulk VOI's centre of mass as the zero-phase reference for every reconstruction, similar to the procedure adopted for strain in Section 5.3.3.

Structural transitions in the sample are identified by sharp changes in r presented in Fig. 5.7. Surprisingly the two reflections from crystal A have different temperatures where the most significant changes occur: abruptly after 410°C in the 002 reflection and less abruptly at 380°C in the $1\bar{1}1$ reflection. These transitions are also reflected in the facet area plot for crystal A in Fig. 5.6. The discrepancy between transition points could be due to the $(00\bar{1})$ facet forming at 380°C but grows significantly larger after 410°C.

Some of these abrupt changes in r occur as a result of sudden relaxation events associated with the removal of a defect, such as dislocations (3), removed at 372°C, and (4), removed at 380°C, from Fig. 5.4 and supplementary video SV2. In crystal A the 002 reflection has reached a steady annealed state after 410°C, but this annealed state is less defined in the other reflections. Examining the same family of reflections can lead to different conclusions, as crystal B shows less abrupt transitions within the r matrices (especially the 200 reflection) that suggest a more gradual recovery of the lattice. In addition to these prominent transitions within the r matrix, less pronounced fluctuations are present and here are attributed to the oscillation between intermediate annealing states.

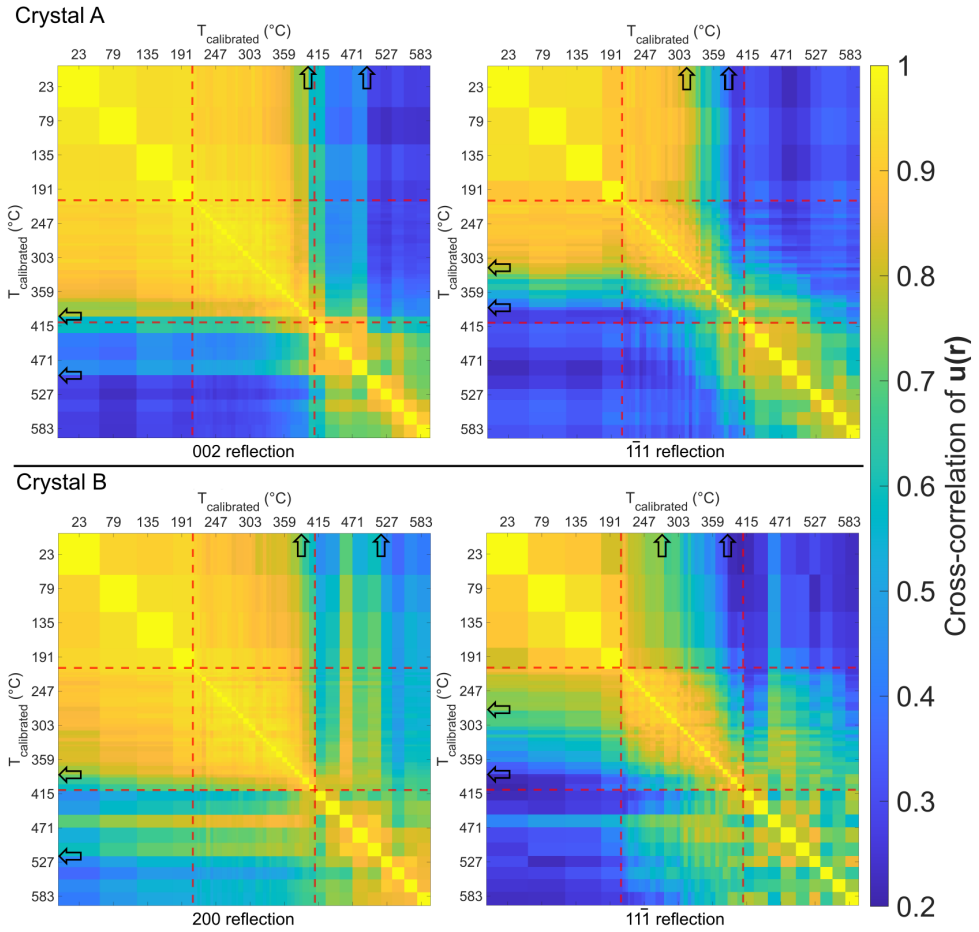

Figure 5.7: Reflection-specific r matrices between $\mathbf{u}_{hkl}(\mathbf{r})$ for different temperatures. r is calculated for each voxel in the array. The difference in r values corresponds to structural evolution. The 002 reflection for crystal A shows an abrupt r change after 410°C, suggesting the abrupt removal of most defects. This is less evident in the $11\bar{1}$ reflection for crystal B, which shows many subtle structural changes as a function of temperature. The red dashed lines indicate where the temperature sampling changed. Black arrows represent the most noticeable changes in displacement.

The differences in observations between reflections from the same crystal arise because not all defects are visible in every reflection and the projection of associated displacement fields varies for each combination of Burgers vector and scattering vector. This variance in material transformation points highlights the importance of multi-reflection analysis, as it can be misleading to derive conclusions from just a single r matrix.

5.4.4 Normalised morphology cross-correlation matrix

To separate morphology-related changes from lattice displacement changes, the r correlation matrix of the morphology is shown in Fig. 5.8. The morphology of a crystal was

created by applying a 0.30 threshold to the reconstructed amplitude.

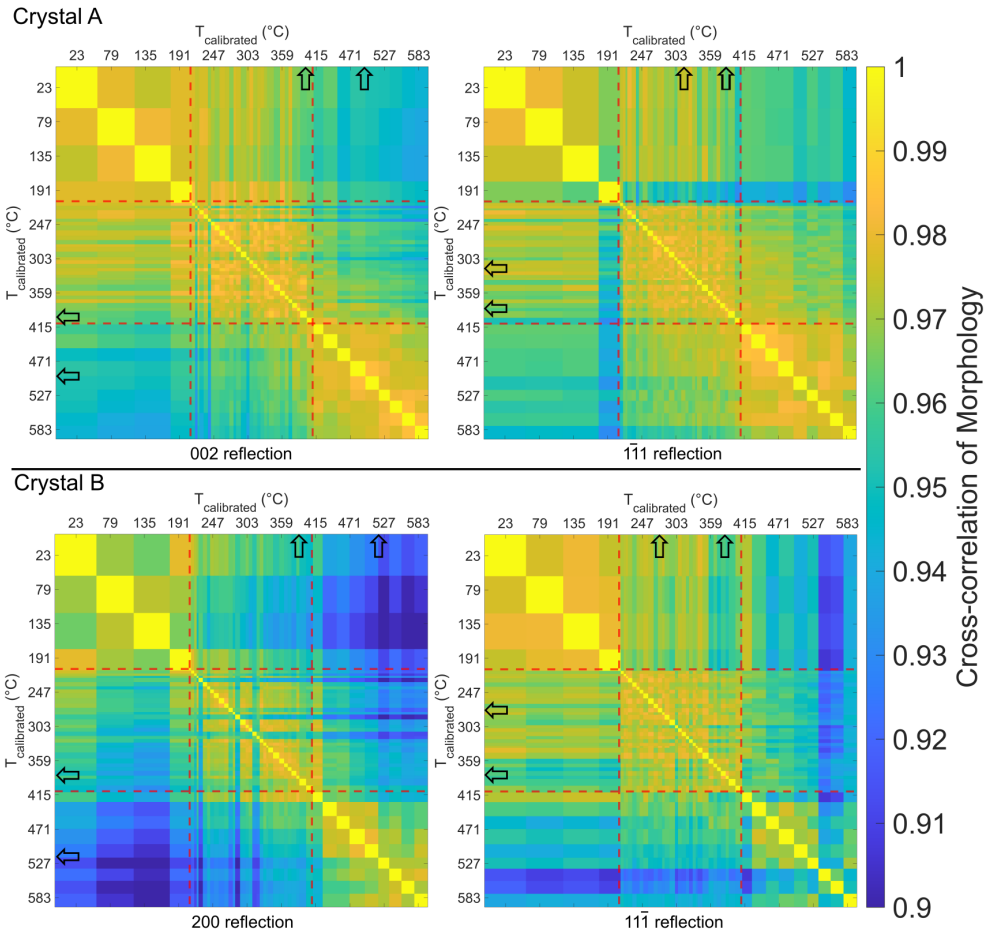

Figure 5.8: Reflection-specific r matrices for the morphology at different temperatures. r is calculated for each voxel in the array. The difference in r values corresponds to morphology evolution. There is a more gradual r transition as the temperature increases compared to Fig. 5.7. The red dashed lines indicate where the temperature sampling changed. Black arrows represent the most noticeable changes in displacement as observed in Fig. 5.7.

There is good agreement between the morphology r matrices and the facet area plots. For instance, the disappearance of the $(00\bar{1})$ facet in crystal B shown in Fig. 5.6 after 527°C can also be clearly identified in the $11\bar{1}$ reflection in Fig. 5.8. Notable changes in r for $\mathbf{u}_{hkl}(\mathbf{r})$ in Fig. 5.7, marked by hollow black arrows in Fig. 5.7 and Fig. 5.8 are different to changes in r for the morphologies shown in Fig. 5.8. There are less abrupt r changes in Fig. 5.8, suggesting that annealing causes smaller incremental changes in morphology, different from the sudden changes in $\mathbf{u}_{hkl}(\mathbf{r})$ (see Fig. 5.7). However, there are changes in $\mathbf{u}_{hkl}(\mathbf{r})$ that cannot be seen in the facet area plots in Fig. 5.6 or the morphology matrices in Fig. 5.8, namely around $\sim$ 310°C in the $1\bar{1}1$ reflection in Fig. 5.7. Changes in strain

that cannot be explained by changes in morphology can be examined directly in the next section.

5.4.5 Average lattice strain in regions of interest

We will now consider the average strain within particular regions of the crystal, illustrating key differences in the local lattice environment. The average lattice strain for a reflection was computed by calculating the strain for each voxel using Eq. 2.78, and taking the mean over all voxels with an electron density magnitude greater than 0.30. Each crystal has been divided into four VOIs, shown in Fig. 5.9, according to how the Ga-beam has interacted with the sample. The VOIs are labelled glancing, normal, corner and bulk. The glancing VOI is defined as 100 nm (20 voxels) from the surface of the milled face where the Ga beam impinged on the sample at glancing incidence. Although the FIB milling was intended to be normal to the substrate, the milled face is $\sim 80^{\circ}$ from the local sample surface normal. This is caused by the tail of the Gaussian-like FIB probe profile not being able to fully reach the bottom of the crystal. The normal VOI is 100 nm from the top of the crystal, corresponding to the region where the FIB beam arrives approximately normal to the sample surface. The corner VOI is the volume that joins the glancing and normal regions. Previously the corner was seen to have the most defects [29]. The bulk VOI is the remaining part of the crystal. The average lattice strain for the different VOIs at every temperature point is shown in Fig. 5.9.

In Fig. 5.9, the strain within the bulk VOI remained approximately zero for all reflections and temperatures because no FIB-induced strain was present prior to annealing. The room temperature data is similar to the values reported previously [29]. As the temperature increases, we see that FIB damage is removed, and the average strain converges to zero. We observe that the glancing and normal VOIs behave similarly regardless of reflection, with the normal VOI having more compressive strain than the glancing VOI. This suggests that the FIB tail imparts more damage to the top face of the crystal than does glancing incidence milling to the milled face, in agreement with previous work [29, 47].

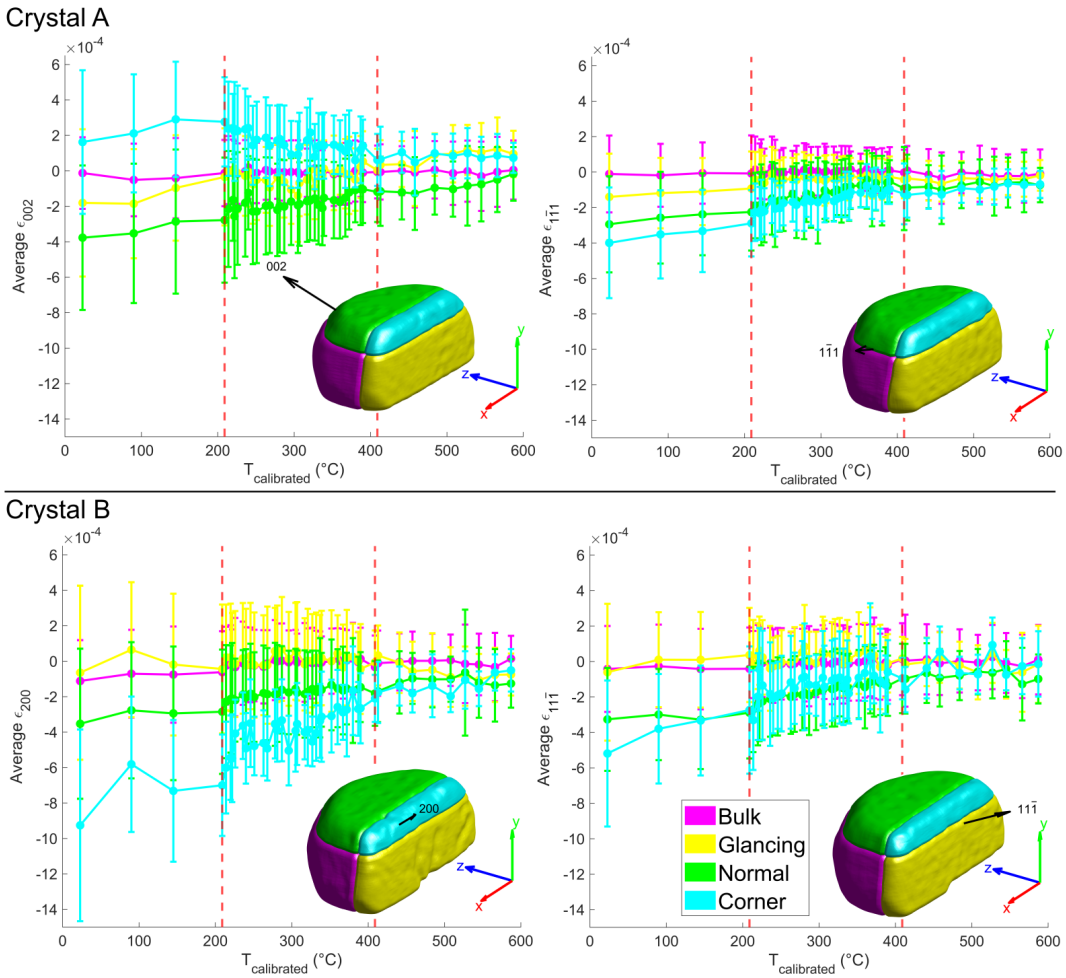

Figure 5.9: Average lattice strain in different VOIs as a function of temperature. Vertical bars correspond to the standard deviation of the strain. Over the annealing cycle, the average strain in each reflection gradually decreases and stagnates after ~ 410°C, as does the magnitude of the standard deviation. The magnitude and direction of the average strain are reflection-dependent, especially in the corner VOIs. The coordinate axes are positioned in sample space and plotted with a length of 250 nm. The red dashed lines indicate where the temperature sampling changed. The rendered crystals show the locations of the VOIs.

The most reflection-dependent VOI is the corner, where both the average magnitude and the sign of strain vary. For the corner VOI in crystal A, the 002 reflection shows tensile strain whereas the $1\bar{1}1$ reflection shows compressive strain of similar average magnitude for the same crystal. The average strain magnitude can be dependent on the reflection. This is observed in the corner VOI for crystal B at room temperature, where the 200 reflection has nearly twice the average strain magnitude of the $11\bar{1}$ reflection. These significant differences would not be evident from single reflection BCDI experiments.

The average strain curves approach zero at ~ 410°C in Fig. 5.9. This is above the

Tammann temperature (327°C) and matches the temperature where facet change is observed for crystal A in Fig. 5.6 and where structural changes occur for the 002 reflection for crystal A in Fig. 5.7. Above ~ 410°C there is little strain evolution, indicating that most of the damage in the crystal has been annealed out. Further evidence for this transition point can be seen in the standard deviation magnitudes of Fig. 5.9. Below ~ 410°C, the standard deviation magnitudes for the glancing, normal and corner VOIs (plotted in Appendix C.6) are greater than that of the bulk VOI. Above ~ 410°C, the standard deviations across all VOIs are similar, indicating that the average strain across all VOIs has become equally homogeneous. The removal of strain inside the crystals can also be seen by comparing the maximum intensity slices of the CXDPs in Appendix C.7 and noting the change in fringe sharpness before and after annealing. The evolution of these CXDP slices can be seen in supplementary videos SV4 and SV5.

We also note that the differences in the rate of average strain removal seem to depend on the severity of the initial FIB damage. It appears that having a higher initial average strain magnitude leads to a greater initial change in average strain. This is most apparent when comparing the rate of average strain change in the corner, glancing and normal VOIs for any reflection, as well as solely the corner VOIs in crystal B.

5.4.6 Analysis technique comparisons

It is interesting to compare information extracted from the facet area plots, *r* matrices and average strain plots. While we see that the facet area plots and displacement *r* matrices can highlight distinct transition points, only major changes can be confidently identified. In particular, crystal transitions can be readily identified in the facet area plots and displacement *r* matrices but remain harder to resolve when observing average strain plots and morphology *r* matrices. The primary advantage of the average strain plots over the consideration of *r* matrices is the ability to identify the magnitude and the direction of strains in various VOIs, which can confirm whether the FIB-induced strain has indeed been removed.

The seemingly abrupt structural evolution in the facet area plots and displacement r matrices contrasts the more uniform rate of strain change observed in the average strain plots and morphology r matrices. The facet area plots and displacement r matrices portray annealing as a process controlled by sudden substantial changes, implying a rapid evolution in morphology and removal of strain after a certain temperature is reached, as shown by the formation of facets in Fig 5.6 and the r for $\mathbf{u}_{hkl}(\mathbf{r})$ in Fig 5.7. For the same reflection in the morphology r matrices in Fig 5.8 and in the average strain plots in Fig. 5.9, annealing appears as a gradual process, by which the change in temperature leads to a progressive change in lattice relaxation and facet edge softening. The trench-like dislocations observed in Fig. 5.4 gradually decrease in size but also fully disappear once certain temperatures are reached, seen in supplementary video SV2, exhibiting both gradual and sudden changes in crystal structure as a result of annealing.

The accuracy of these observations is limited by our spatial resolution and sampling time. To better resolve defect dynamics, faster scans and higher photon flux are required, which the Advanced Photon Source Upgrade Project promises to deliver. Regardless, the conclusions drawn from each of the analysis techniques are complementary and reveal different aspects of the crystal behaviour, but point toward an annealing temperature of 380-410°C. These methods are suitable for the analysis of individual reflections, but can benefit from the incorporation of multiple reflections, enabling more comprehensive comparisons to be made.

5.4.7 Diffusion considerations

Scan times on the order of minutes for BCDI rocking curves limit fast structural changes from being resolved. However, we are able to capture structural evolution on the timescale of the rocking scans, such as the formation of facets, disappearance of dislocations and relative changes in $\mathbf{u}_{hkl}(\mathbf{r})$. These changes can be interpreted in terms of the diffusion of Ga in Au, the self-diffusion of Au at the surface or within the bulk of the crystal and the escape of dislocations to the free surface.

Fig. 5.10 shows the temperature and time required for diffusion of Ga over lengths from 1 nm to 20 nm, as well as self-diffusion of Au over 1 nm to 100 nm. We use diffusion coefficients for these two systems as they provide an indication of relative atomic mobility at various temperatures. The diffusion coefficient of Ga in Au was obtained from [219], while the self-diffusion of Au was obtained from [220]. We determine the time required for 1 nm of diffusion as a function of temperature, for each scenario, as shown by the exponential curves in Fig. 5.10. The penetration depth of Ga under the FIB conditions used is ~ 20 nm [29], thus we calculate the time required for a diffusion length of 20 nm as the upper limit of Ga diffusion. Diffusion lengths between 1 and 20 nm are shown as a grey region. Similarly, for the self-diffusion of Au, diffusion lengths between 1 and 200 nm are relevant, as the greatest change in facet area is about 4000 nm^2 (Fig. 5.6). Superimposed on this time-temperature plot is the temperature history of the present Au samples (dotted blue line), indicating the time spent at each temperature during the annealing process.

To Fig. 5.10 we can further add the changes in $\mathbf{u}_{hkl}(\mathbf{r})$ cross-correlation observed as a function of temperature (Fig. 5.7). From ~ 190°C until ~ 410°C, there is a gradual reduction in the cross-correlation value. Considering the diffusion lengths of Ga and Au, this change at lower temperatures up to ~ 280°C is likely to be driven by bulk Ga diffusion and Au surface diffusion. Above this temperature bulk Au self-diffusion may be responsible. At ~ 410°C Fig. 5.7 shows a rapid change in cross-correlation coefficient, suggesting major structural changes as discussed above. The diffusion curves in Fig. 5.10 suggest that this is associated with the rearrangement of Au rather than Ga atoms.

On Fig. 5.10 we have superimposed the temperatures at which removal of dislocations is observed (black lines labelled 1 to 4, consistent with dislocation numbers in Fig. 5.4), as well as the temperatures at which the $(00\bar{1})$ and $(1\bar{1}\bar{1})$ facets are formed (green and purple lines respectively, consistent with Fig. 5.5 and 5.6). Apart from the removal of dislocation 1, which is at the boundary between Ga diffusion and Au diffusion dominated areas, all other structural changes appear to be driven by Au migration.

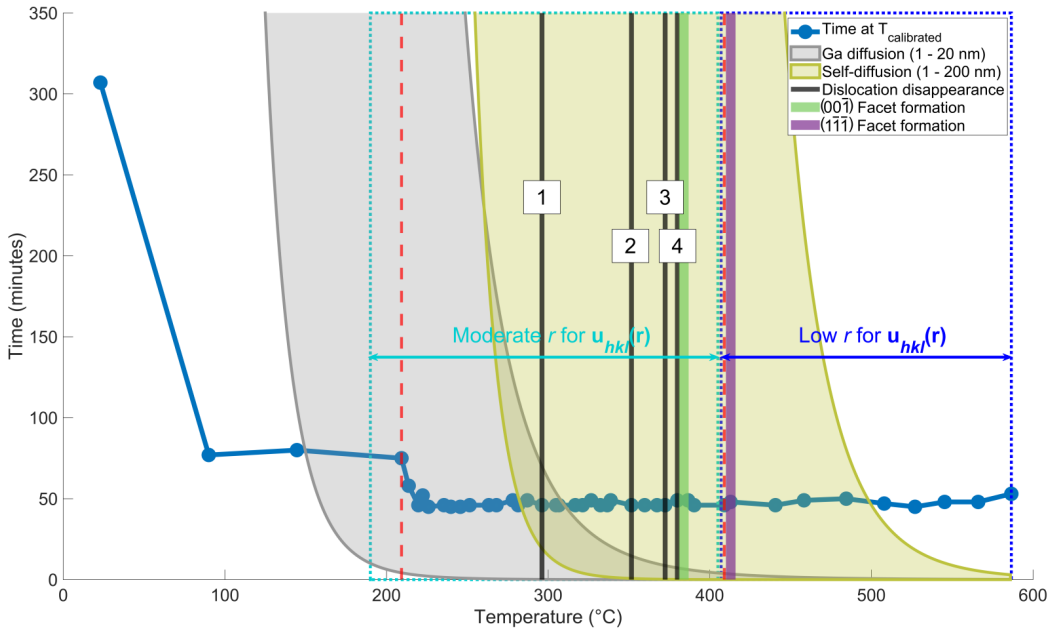

Figure 5.10: The time required for the bulk diffusion of Ga over lengths from 1 to 20 nm (light grey region) and Au diffusion over distances from 1 to 200 nm (dark yellow region) throughout the annealing. Superimposed are temperature points where dislocations in Fig. 5.4 disappeared, temperature points where facets have formed in Fig. 5.6, and temperature regions where the $\mathbf{u}_{hkl}(\mathbf{r})$ r values changed noticeably (see Fig. 5.7). The dotted blue line shows the time-temperature trajectory of the Au sample in this study, indicating the time spent at each annealing temperature. The red dashed lines indicate where the temperature sampling changed.

5.5 Conclusion

We have presented an *in situ* BCDI study of the annealing of FIB-induced damage in Au microcrystals. Two separate crystals with two reflections each were measured, confidently switching between reflections and samples, during an annealing cycle. By tracking the change in detector position, we could use the thermal strain of the microcrystals for temperature calibration. We have also presented a new approach that monitors the reduction of free surface energy by following morphology evolution through the formation of facets. The annealing process was analysed using facet areas, cross-correlation matrices and average strain plots, which provide complementary information. Surprisingly, two different reflections from the same crystal can show different behaviour. This highlights the need to measure multiple reflections in order to gain a complete picture of sample evolution. Full annealing was achieved at a temperature of 380-410°C. However, the complexity of the process becomes apparent when trying to evaluate the rate of strain re-

moval, as the facet area plots and displacement *r* matrices portray annealing as an abrupt process, while the morphology *r* matrices and average strain plots show much more gradual changes. The gentle evolution of the crystal below $\sim$ 280°C is likely the result of bulk Ga diffusion and Au surface diffusion whilst more substantial changes (i.e. removal of dislocations and formation of facets) above $\sim$ 280°C are likely dominated by the self-diffusion of Au. This experiment demonstrates that annealing is a viable option for the removal of FIB damage as evidenced by a decrease in strain heterogeneity inside the crystal, removal of defects on the crystal surface and reduction of mean strain in FIB-damaged areas. Annealing can thus be used as a method to remove FIB-induced sample damage prior to further modification of a sample e.g. nanoindentation, bending etc.

We anticipate that the techniques developed here could be used to pioneer novel *in situ* BCDI measurements in complex environments for multiple samples and reflections simultaneously.

5.6 Data availability

The processed diffraction patterns, final reconstructions and data analysis scripts are publicly available at 10.5281/zenodo.4423216.

Chapter 6

In situ Bragg coherent X-ray diffraction imaging of corrosion in a Co-Fe alloy microcrystal

Further applying the developments presented in Chapters 3 and 4, I now explore the evolution of average lattice strain and crystal morphology and how it impacts the dissolution rate of a Co-Fe microcrystal in hydrochloric acid solution. Initially, the surface of the crystal is most strained. This dissolves to leave a progressively less strained surface. Within the crystal bulk, the average strain closer to the centre of the crystal increases during corrosion. The localised corrosion rate was determined by comparing BCDI reconstructions. This revealed the preferential dissolution of facets more exposed to the acid stream, highlighting an experimental geometry effect. This chapter is in publication format based on the article: D. Yang, N. W. Phillips, K. Song, C. Barker, R. J. Harder, W. Cha, W. Liu, and F. Hofmann, "In situ Bragg coherent X-ray diffraction imaging of corrosion in a Co–Fe alloy microcrystal," *CrystEngComm*, vol. 24, no. 7, pp. 1334–1343, 2022 [49]. This article is featured on the front cover of the issue and categorised as a quarterly 'HOT' article, which is "highlighted by reviewers as being interesting and significant research for the crystal engineering community".

N.W. Phillips and K. Song assisted with BCDI diffraction data collection. C. Barker provided sputtered thin films for sample fabrication. BCDI experiments were performed remotely at 34-ID-C, with help from R.J. Harder and W. Cha. Micro-beam Laue X-ray diffraction experiments were performed remotely at 34-ID-E, with help from W. Liu. The remainder of the work was carried out by the author under the supervision of F. Hofmann.

6.1 Abstract

Corrosion is a major concern for many industries, as corrosive environments can induce structural and morphological changes that lead to material dissolution and accelerate material failure. The progression of corrosion depends on nanoscale morphology, stress, and defects present. Experimentally monitoring this complex interplay is challenging. Here, we implement *in situ* Bragg coherent X-ray diffraction imaging (BCDI) to probe the dissolution of a Co-Fe alloy microcrystal exposed to hydrochloric acid (HCl). By measuring five Bragg reflections from a single isolated microcrystal at ambient conditions, we compare the full three-dimensional (3D) strain state before corrosion and the strain along the [111] direction throughout the corrosion process. We find that the strained surface layer of the crystal dissolves to leave a progressively less strained surface. Interestingly, the average strain closer to the centre of the crystal increases during the corrosion process. We determine the localised corrosion rate from BCDI data, revealing the preferential dissolution of facets more exposed to the acid stream, highlighting an experimental geometry effect. These results bring new perspectives to understanding the interplay between crystal strain, morphology, and corrosion; a prerequisite for the design of more corrosion-resistant materials.

6.2 Introduction

Corrosion processes are important in a wide variety of fields such as geology [221], renewable energy [222], and catalysis [223]. There is a keen interest in the investigation

of reaction kinetics over different time scales to better predict how a material transforms in a corrosive environment. However, often the corrosion rates reported in the laboratory setting and in the field are inconsistent, despite well-controlled extrinsic conditions of the experiment [224–226]. Frequently, the cause for the corrosion rate discrepancy is based on intrinsic factors related to the properties of the sample [224, 225], for example, morphological features and lattice defects are not accounted for in the bulk dissolution rate determined from mineral powders. Crystals possess heterogeneous spatial reactivity on the crystal surface [221,224,225], as reaction rates tend to differ along facets, edges, and vertices [227,228]. In addition to these morphological features, dissolution rates can be influenced by internal features such as crystal defects. For example, dislocation-induced etch pits [229, 230] are a commonly reported result of the interaction between defect-induced strain fields and corrosion. This highlights the importance of studying defect-mediated corrosion and the effects of lattice strain on local nanoscale corrosion. Consolidating our understanding of these processes will aid in the design of more corrosion-resistant materials.

Corrosion mechanisms start with the interaction of the crystal surface with a corrosive medium. Techniques such as vertical scanning interferometry (VSI) [231], atomic-force-microscopy (AFM) [232], digital holographic microscopy [233], and phase-shift interferometry [234] are used to probe surface dissolution rates. However, these methods primarily focus on measuring upwards-facing sample features at the surface. Liquid cell transmission electron microscopy (LCTEM) techniques have been used to study pitting corrosion [235], but these studies focus on thin samples where surface effects are dominant and are prone to bubble formation due to radiolysis [236]. *Ab initio* molecular dynamics simulations (AIMD) have been used to predict the energy barriers of dissolution for crystal edges, corners, and kinks [237], but we note that the direct determination of dissolution rate for spatially resolved surface sites remains uncommon in the laboratory. Three-dimensional localised dissolution information has only been recently reported using transmission X-ray microscopy (TXM) [238] and three-dimensional (3D) X-ray mi-

crotomography (XMT) [226, 228]. Although TXM and XMT provide a spatial resolution on the order of 50 nm, they are limited to probing morphological features.

Crystal lattice defects beneath the crystal surface must also be considered when investigating corrosion. Defects can induce strain in the crystal lattice, which changes the activation barrier for dissolution near the defect [239]. Areas having dislocations, grain boundaries, and high surface roughness dissolve faster than defect-free regions [221]. Indeed, it was through the appearance of etch pits that dislocations were first visualised [240]. Experiments have shown that crystal lattice strain can noticeably increase the dissolution rate for calcite [239, 241] and sodium chlorate crystals [242] compared to theoretical values. A full picture of crystal corrosion mechanisms can therefore only be obtained by also studying how the evolution of defect networks, lattice strains within the crystal and local morphology modify the local corrosion characteristics.

To elucidate how both crystal strain and morphology influence localised corrosion, we use Bragg coherent X-ray diffraction imaging (BCDI) to study the evolution of a Co-Fe alloy microcrystal. A binary alloy was chosen for this study to identify how strain distributions can be affected by the presence of another element during corrosion [162, 243]. BCDI allows 3D-resolved, nanoscale strain measurements with a 3D spatial resolution of 10 - 30 nm and a strain resolution on the order of $\sim 2 \times 10^{-4}$ [47], making it well suited to probing crystal defects and morphology. Currently, at third-generation synchrotron light sources, several minutes are required to collect a BCDI dataset. At these timescales, BCDI allows the *in situ* probing of slow dynamic changes during the corrosion process. Several *in situ* BCDI experiments have been reported, for example, Pt nanocrystals during methane oxidation [244], silver-gold alloys undergoing nitric acid-induced dealloying [162, 243], and magnetite reacting with hydrochloric acid (HCl) [170].

Here, we image the spatial and temporal evolution of a Co-Fe alloy microcrystal submerged in an aqueous HCl solution (pH $= 0.65$) using *in situ* BCDI. Prior to corrosion, we measured five crystal reflections to determine the full lattice strain and rotation tensor, providing a clearer understanding of the defects initially present inside the crystal. Dur-

ing the corrosion, we measure the 111 reflection at 2.6, 4 and 6 hours after the start of acid exposure to examine how the 3D strain, crystal morphology, and local variations in dissolution rate evolve as a function of corrosion. The experiment provides a new perspective for the analysis of corrosion, by probing how both strain and morphology affect the localised dissolution of the crystal.

6.3 Methods

6.3.1 Sample manufacture

Samples were produced by sputter deposition of a thin film onto a single crystal sapphire wafer (C-plane orientation). The thickness of the film was 100 nm. The thin film was dewetted in a vacuum furnace purged with a 5% hydrogen, balance Argon, gas mixture at 1250°C for 16 hours. The resulting crystals exhibit a face-centred cubic structure, range from 100 nm to 1 μm in size, (Fig. 6.1(a)) and adhere to the substrate surface.

The samples were coated with 10 nm of amorphous carbon to assist with scanning electron microscope (SEM) imaging. The coating was applied through thermal evaporation using a Leica ACE600 Coater. SEM images were taken on a ZEISS Auriga focused ion beam (FIB)-SEM equipped with an in-lens detector with an acceleration voltage of 7 kV. To facilitate reliable measurement of multiple reflections from a specific microcrystal, Ga ion FIB was used to remove the surrounding crystals within a 20 μm radius using a current of 150 pA - 6 nA. The isolated crystal is shown in Fig. 6.1(c). Only SEM imaging was used to position the FIB milling scan, as our previous results indicate that even a single low dose FIB image can induce large lattice strains [47]. Energy-dispersive X-ray spectroscopy (EDX) analysis was used to determine the elemental composition of the crystal (Fig. 6.1(c)). All elements are homogeneous throughout the crystal (see Appendix D.3). EDX was performed on a ZEISS EVO equipped with an X-act detector (Oxford Instruments). The EDX spectrum in Fig 6.1(d) was acquired on an elliptical region encapsulating the crystal for 104 seconds using an acceleration voltage of 10 kV.

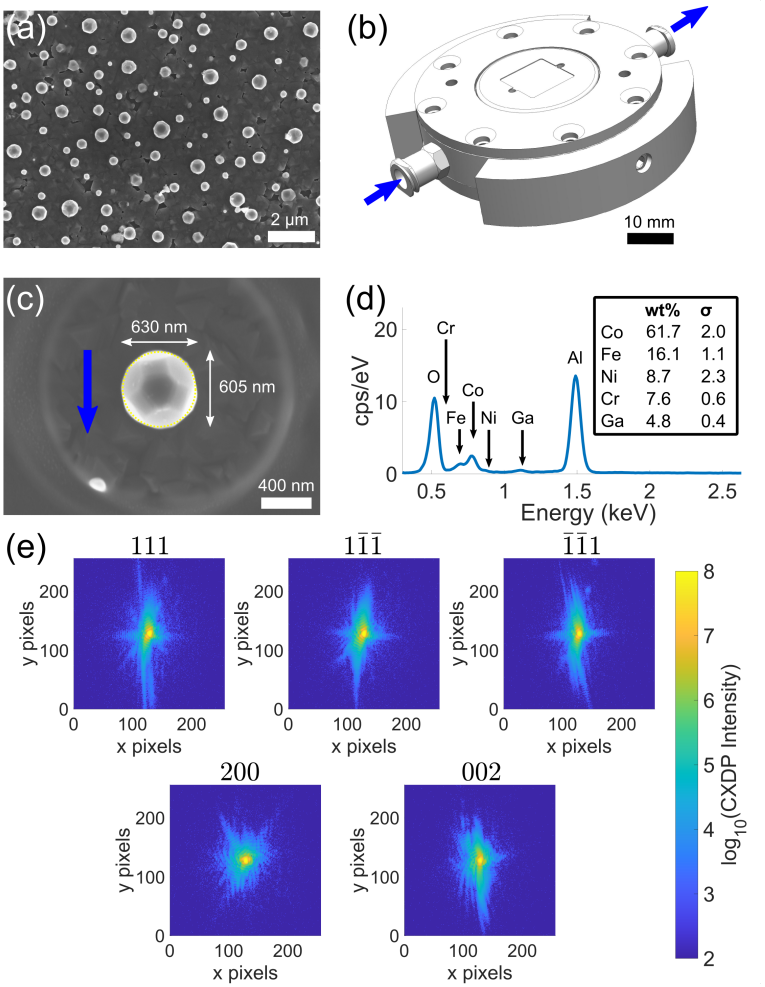

Figure 6.1: (a) Dewetted Co-Fe alloy microcrystals on a sapphire substrate. (b) A schematic of the fluid flow cell at beamline 34-ID-C (APS) used for *in situ* corrosion. The blue arrows show the direction of fluid flow. (c) The Co-Fe microcrystal measured during the experiment before corrosion. The dotted yellow line represents the region measured using energy-dispersive X-ray spectroscopy (EDX). (d) EDX data for the FIB-isolated sample. Only the L-lines for the most pronounced elements in the crystal are shown above. All elements are homogeneous throughout the crystal (see Appendix D.3). The spectrum composition excludes the Al and O substrate peaks. (e) Central slices of the CXDP for each reflection measured before corrosion.

6.3.2 Experimental measurements

Synchrotron X-ray diffraction measurements were performed at the APS. Prior to BCDI measurements, micro-beam Laue diffraction at beamline 34-ID-E was used to determine the lattice orientation of the crystal. This served to pre-align the crystal for BCDI measurements at beamline 34-ID-C, as previously described [57].

The substrate was attached to the fluid flow cell (Fig. 6.1(b)) provided at beamline 34-ID-C using dental wax. Diffraction measurements used an X-ray energy of 9 keV (λ = 0.138 nm), with a bandwidth of $\Delta\lambda/\lambda \approx 1.3 \times 10^{-4}$ from a Si(111) monochromator.

The X-ray beam was focused to a size of 740 nm × 680 nm (h × v, full width at half-maximum) using Kirkpatrick-Baez (KB) mirrors. Beam defining slits were used to select the coherent portion of the beam at the entrance to the KB mirrors. For beamline 34-ID-C, the transverse coherence is $\xi_h > 10$ μm and the longitudinal coherence is $\xi_w \approx 0.7$ μm at an energy of 9 keV [71].

CXDPs were collected on a 256 × 256 pixel Timepix area detector (Amsterdam Scientific Instruments) with a GaAs sensor and pixel size, p, of 55 μm × 55 μm positioned at 0.75 m from the sample to ensure oversampling. CXDPs were recorded by rotating the crystal through an angular range of 0.7° and recording an image every 0.005° with 0.1 s exposure time and 35 accumulations at each angle. The lower bound for the detector distance was determined by $2dp/\lambda = 0.50$ m, where d is the sample size.

To optimise the signal to noise ratio and increase the dynamic range of the CXDPs, multiple repeated scans of each reflection were performed at ambient conditions and aligned to maximise their cross-correlation. Once aligned, the minimum acceptable Pearson cross-correlation for summation of CXDPs from a specific Bragg reflection was chosen to be 0.981, similar to other BCDI studies [29, 30]. CXDPs were corrected for dark-field, dead-time (Eq. 4.15), and whitefield (in that order) prior to cross-correlation alignment. CXDPs from the following reflections were collected (the number of repeat scans that were averaged is noted in [] brackets): 111 [10], $\bar{1}\bar{1}1$ [9], $1\bar{1}\bar{1}$ [9], 200 [10], 002 [10]. Details regarding the recovery of the real space images using phase retrieval algorithms can be found in Appendix D.1 and the computation of the strain can be found in Chapter 2.4.10.

6.3.3 Corrosion

The fluid flow cell was covered with a 0.0508 mm thick mylar film. HCl solution (0.22 mol/L, pH=0.65) was injected at a flow rate of 40 mL/min during the full 6 hours. Single scans for the 111 reflection for the crystal were measured at 2.6, 4 and 6 hours after the start of acid injection. CXDPs were recorded and processed using the same procedure as

before corrosion.

6.4 Results

Fig. 6.2 shows the strain and rotation tensors reconstructed from five measured Bragg reflections. The average amplitude taken over all five reflections is based on an amplitude threshold of 0.25.

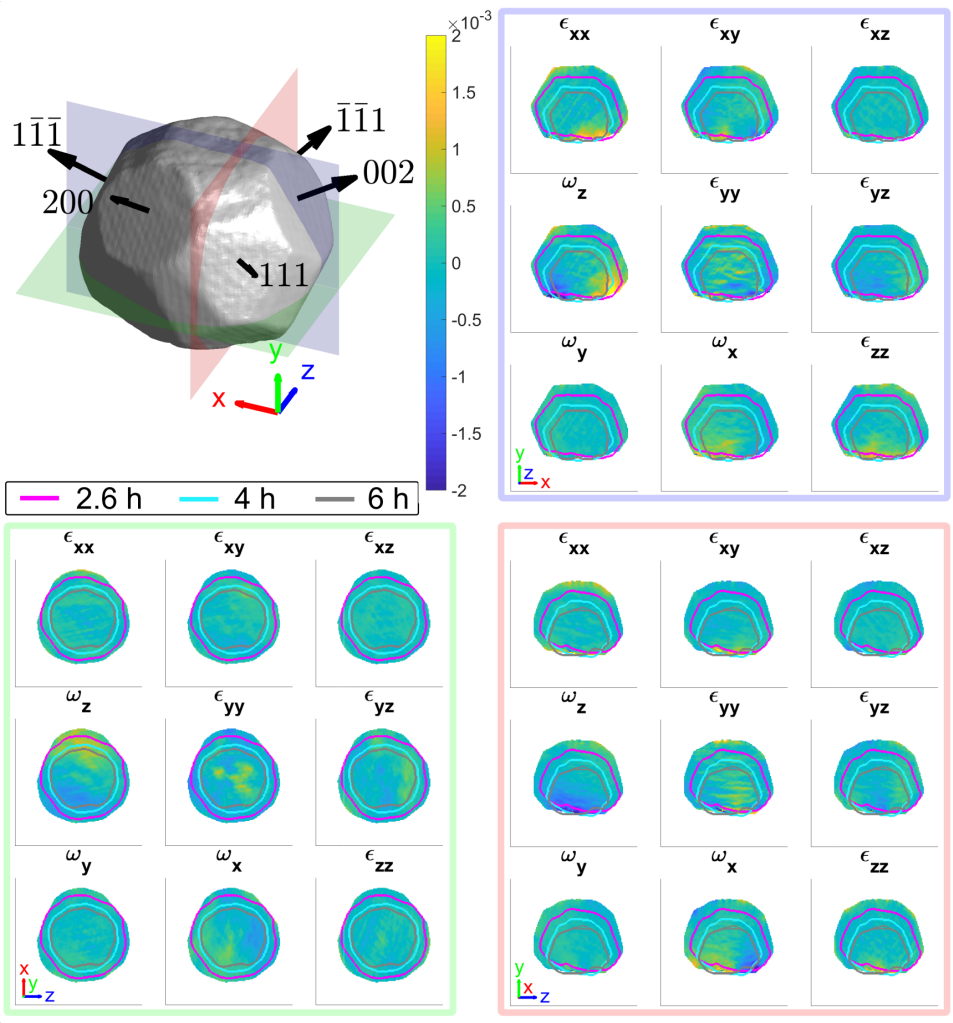

Figure 6.2: Average morphology of the 111, $1\bar{1}\bar{1}$, $\bar{1}\bar{1}1$, 200, 002 reflections at ambient conditions. The slices through the strain and rotation tensor components are shown for the planes indicated at $x = -87.5$ nm (red), $y = -67.5$ nm (green), and $z = -7.5$ nm (blue) from the centre of mass of the microcrystal. The outlines in the strain and rotation tensor figure panels corresponds to the 111 reconstruction after 2.6 h (magenta), 4 h (cyan) and 6 h (grey) after corrosion. The amplitude threshold is 0.25 and the magnitude of the coordinate axes is 100 nm. Supplementary video (SV) 1-3 show the strain and rotation tensor components throughout the volume along the x, y, and z axis respectively.

The strain and rotation tensor components are fairly homogeneous, similar to other

crystals fabricated by dewetting methods [29, 47, 134]. Numerous small surface defects are visible in the cross-sectional edges of the crystal. At the base of each cross-section, there are regions of strain that are likely due to lattice mismatch with the sapphire substrate [245].

The evolution of crystal morphology as the corrosion progresses is shown in Fig. 6.3(a) with the displayed colour corresponding to the local lattice strain along $[111]$. Prior to corrosion, there is more tensile strain on the surface, observable in the cross-sectional panels of the 3D strain tensor in Fig.6.2. As expected, the crystal decreases in size and surface features such as the facets and edges become rougher. There is a trend where the average surface strain decreases as corrosion proceeds (Fig. 6.3 (b)), along with a subtle overall reduction in surface strain variation (Fig. 6.3 (c)). Dissolution mainly occurs at the top of the crystal, which is more exposed to the HCl solution relative to the bottom. Interestingly, in Fig. 6.3(a), the strain at the base of the crystal does not change significantly. We attribute this to there being negligible corrosion at the base of the crystal due to the contact with the substrate and subsequent protection of this surface. Alignment of the crystal for subsequent time points was performed using the base of the crystal as a common reference point.

Semi-transparent morphologies of each reconstruction during corrosion are shown superimposed in Fig. 6.4. There is a pit that forms on the (100) facet and enlarges during the corrosion (red circle). Pits can nucleate from highly strained morphological features or by preferential dissolution near a dislocation core–the dissolution of strains surrounding the dislocation core would reduce the overall energy of the crystal [229, 230]. In this case there are no noticeable heterogeneities at the site of the pit and there is no noticeable dislocation at the region where the pit nucleated, shown in Fig 6.3(a), so it is unlikely that the pit was created by crystallographic features. A hypothesis for the formation and enlargement of the pit comes from the direction of fluid flow (shown by the direction of the blue arrow): the region of the pit is most exposed to the moving liquid. However, the corrosion rate here is smaller than that reported by Horng, where Co-Fe was formed from

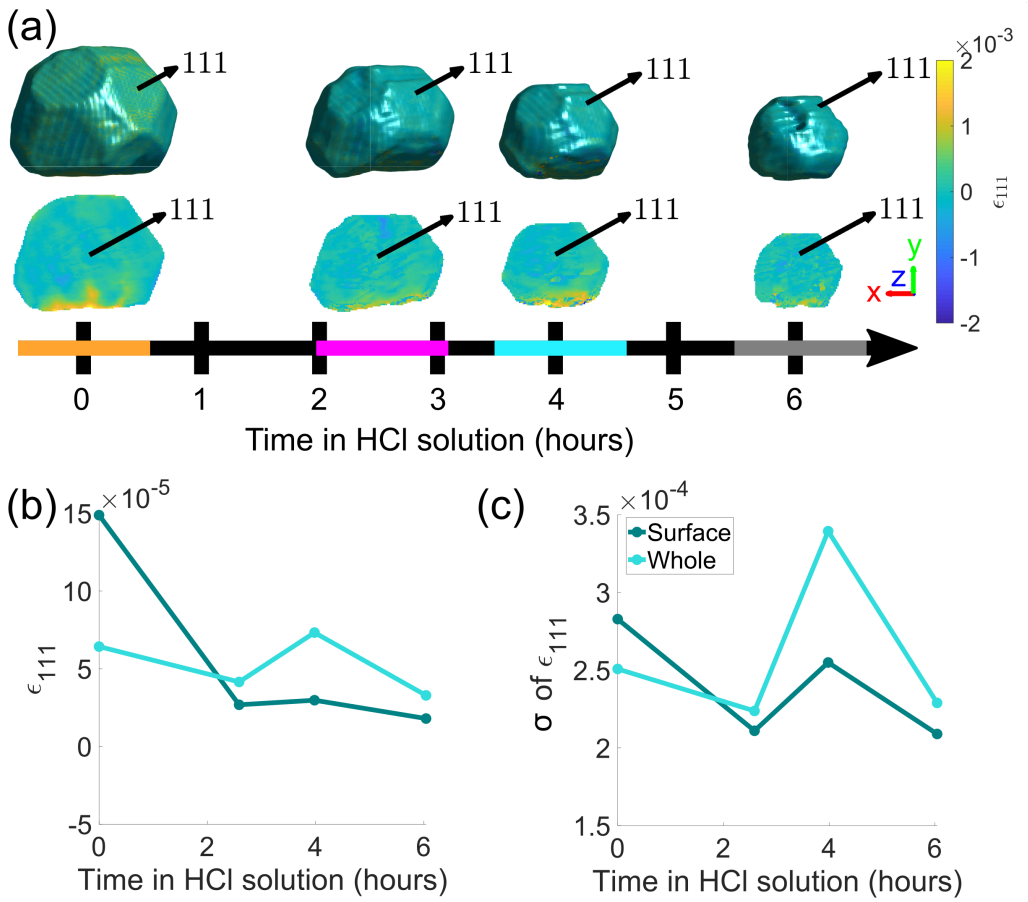

Figure 6.3: (a) Reconstructions of the 111 reflection with an isosurface in amplitude coloured according to the local lattice strain along [111] as a function of reaction time. Central slices perpendicular to the z-axis are shown in the row below. The amplitude threshold is 0.25 and the magnitude of the coordinate axes corresponds to 100 nm. The coloured bands on the time axis correspond to the reconstructions at those time points and are used throughout the article. Supplementary video SV4 rotates around the crystal during corrosion. Supplementary video SV5 shows slices through the crystal during corrosion. (b) The average surface strain compared to the average strain of the whole crystal along [111]. (c) The standard deviation of data points shown in (b).

powder metallurgy and corroded in stagnant HCl [246].

6.5 Discussion

6.5.1 Crystal morphology

The order of free surface energies for low index facets is $\{111\} < \{100\} < \{110\}$ based on ab initio techniques that account for the number of nearest-neighbour broken bonds [216]. It is expected that the facets with the highest energy will dissolve most quickly. Based

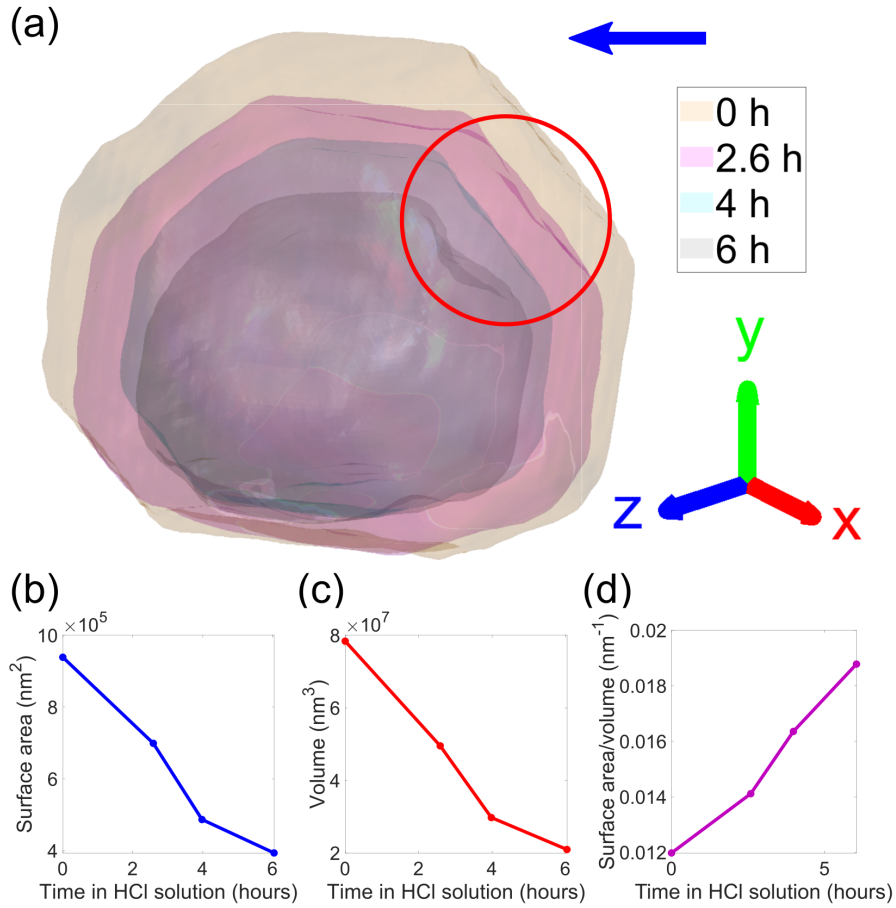

Figure 6.4: (a) Translucent morphologies of the 111 reconstructions as a function of corrosion time. The morphologies are aligned such that their bottom facets share at least one common point, which corresponds to the crystal being fixed onto the substrate. The red circle highlights the formation of a pit on the (100) facet. The blue arrow shows the direction of fluid flow. The amplitude threshold is 0.25 and the magnitude of the coordinate axes corresponds to 100 nm. (b-d) The evolution of volume, surface area, and surface area to volume ratio of the crystal as a function of corrosion time, respectively.

on the identification of facets in Appendix D.2, the area for each facet was calculated. To characterise the change in area between different families of facets, we normalise each facet by its initial facet area and plot the change over the period of corrosion, as shown in Fig. 6.5(a). Surprisingly, all facets sizes decrease, at a similar rate, with no clear dependence on crystallographic direction.

To quantify the surface normal retreat for each facet family, we calculate the facet-normal distance from the centre of mass of the facet to the centre of mass of the crystal for each time point. The change in surface normal distance is shown in Fig. 6.5(b). Consistent with the facet size change, there is negligible facet-dependent change in surface retreat.

While there is no clear difference between different families of facets when looking

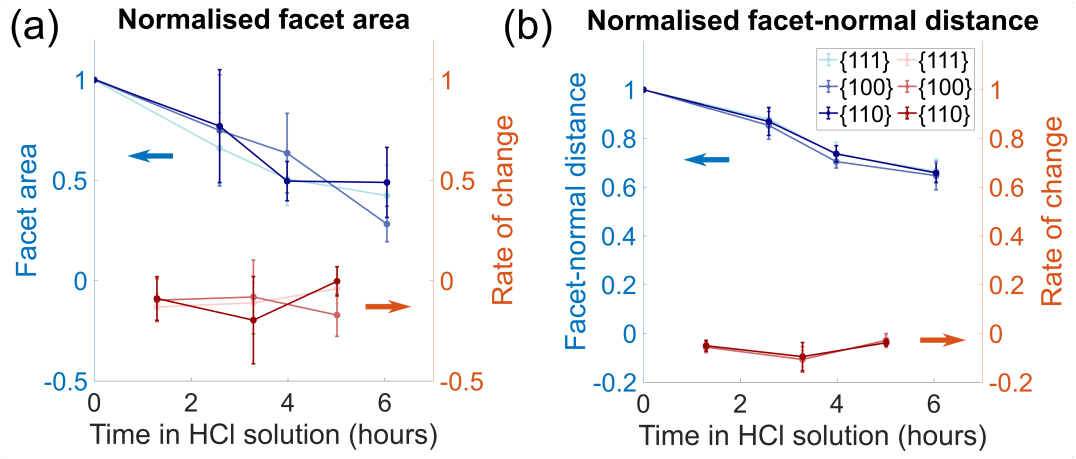

Figure 6.5: (a) The normalised average facet area for different families of facets (blue) and the change in normalised average facet area (red). (b) The normalised facet-normal distance (blue) from the centre of mass of the facet to the centre of mass of the crystal for each time point, and the change in normalised facet-normal distance (red). The blue and red arrows point to the y-axis for each set of lines.

at their average facet sizes and average facet-normal distance to the centre of mass of the crystal, the localised dissolution rate, discussed in Section 6.5.2, provides a clearer picture of how subtle geometric constraints affect corrosion.

6.5.2 Dissolution

The local dissolution rate was determined by computing a 3D Euclidean distance map from the morphology of the crystal, which represents the crystal-fluid interface at each time point during corrosion [228]. Each voxel beyond the crystal surface was labelled with the smallest normal distance to the crystal surface. To determine the local dissolution at t_i, the 3D Euclidean distance map was computed for t_{i+1} and the values were taken using the 3D coordinates of the crystal-fluid interface at t_i. For crystal edges and vertices, the local dissolution at t_i is the distance normal to the considered edge at t_{i+1}. The local dissolution rate, based on the notation from Noiriel *et al.* [228], was computed by

$$r'_{\text{diss}} = \frac{d\mathbf{I_{fc}} \cdot \mathbf{n}}{dt}, \tag{6.1}$$

where $\mathbf{I_{fc}}$ is the position vector and $\mathbf{n}$ is the normal to the crystal surface.

When determining the dissolution rate, we note that the maximum change within the

crystal during a scan of $\sim$10 minutes is 9 nm. This is significantly less than the average spatial resolution of the reconstructions (see Appendix D.1). Furthermore, since the crystal remained attached to the substrate while measurements were performed, all the reconstructions were aligned such that the bottom surface of the crystal remained in the same position.

Fig. 6.6 shows the crystal surface coloured according to the local dissolution rate. The dissolution rate is calculated based on the alignment of the bottom facets because the crystal is fixed onto the substrate. The results reveal that the dissolution of the crystal is not straightforward and evolves both spatially and temporally. From 0 - 2.6 h, the average corrosion rate is 0.0042 nm/s. From 2.6 - 4 h, the average corrosion rate approximately doubles to 0.0074 nm/s. Finally, from 4 - 6 h the corrosion rate decreases to 0.0033 nm/s.

This low-high-low corrosion rate pattern is likely a result of the carbon coating initially present on the surface of the crystal. A previous study by Larijani *et al.* shows that the corrosion of 316 stainless steel coated with 200 nm of carbon has a corrosion current density two orders of magnitude smaller and a higher corrosion potential in a prototypical fuel cell environment with a pH of 2 [247]. Thus, the lower initial localised dissolution rate from 0 - 2.6 h (Fig. 6.6) is attributed to the passivation due to the carbon coating, which is slowly removed.

To understand these changes, histograms of observed dissolution rates were plotted. Note that there is a large proportion that shows zero dissolution rate, corresponding to the bottom of the crystal. The first time interval from 0 - 2.6 h shows a wide variation of dissolution rates, with a broad peak at 0.0044 nm/s and a narrow peak at 0.0071 nm/s. The second time interval from 2.6 - 4 h shows one large peak at about 0.0083 nm/s and a much smaller one at 0.0041 nm/s. The final time interval from 4 - 6 h shows a double peak at about 0.0028 nm/s and 0.0057 nm/s.

A reason for the heterogeneous dissolution rate from 0 - 2.6 h is the dissolution of vertices and edges, which have been shown to be removed faster [238] due to the large number of step and kink atoms present [248, 249]. These step and kink atoms have lower

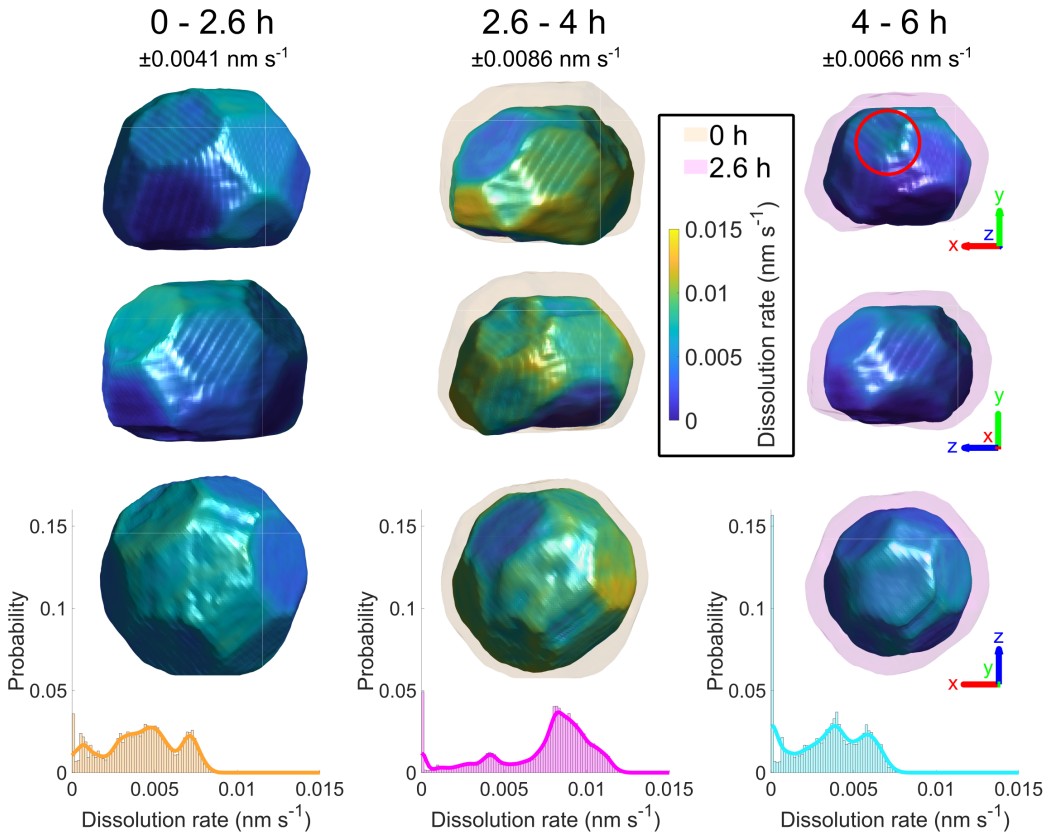

Figure 6.6: Crystal surface coloured according to local dissolution rate and histograms of dissolution rate between adjacent time points. The error is ± 0.0041, 0.0086, and 0.0066 nm/s for 0 - 2.6, 2.6 - 4, and 4 - 6 h respectively. The semi-transparent volumes represent the crystal morphology at the previous time step. The red circle highlights the localised increase in dissolution rate where the pit becomes noticeable at 6 h (Fig. 6.4(a)). The amplitude threshold is 0.25 and the magnitude of the coordinate axes corresponds to 100 nm. Supplementary video SV6 rotates around the crystal during corrosion.

coordination than facet atoms, which increases their exposure to the fluid. Furthermore, these sites can increase the reactivity by stabilising reaction intermediates and lowering energy barriers [250].

The dissolution rate decreases again after 4 h, to similar levels as between 0 h and 2.6 h, though more homogeneously distributed. This is attributed to the crystal becoming rounder, whereby solution mass transport lowers the dissolution rate relative to that of acute corners and edges [238]. The pit becomes significantly enlarged after 6 h (Fig. 6.4). This localised higher dissolution of the pit is reflected by the rightmost peak from 4 - 6 h in Fig. 6.6.

Fig. 6.7 shows that the facet dissolution is highly position-dependent. The bottom of the crystal is protected from acid exposure by the substrate and therefore experiences the

least corrosion. We observe an increase in dissolution rate from facets near the base of the crystal to the top surface, where the dissolution rate is highest. We attribute this trend to a reduction in solution mass transport near the substrate, which has also been observed in larger calcite crystals [238]. As the crystal decreases in size, the bottom facets contribute to a larger fraction of surface area and thus biases the dissolution rate histogram towards lower values.

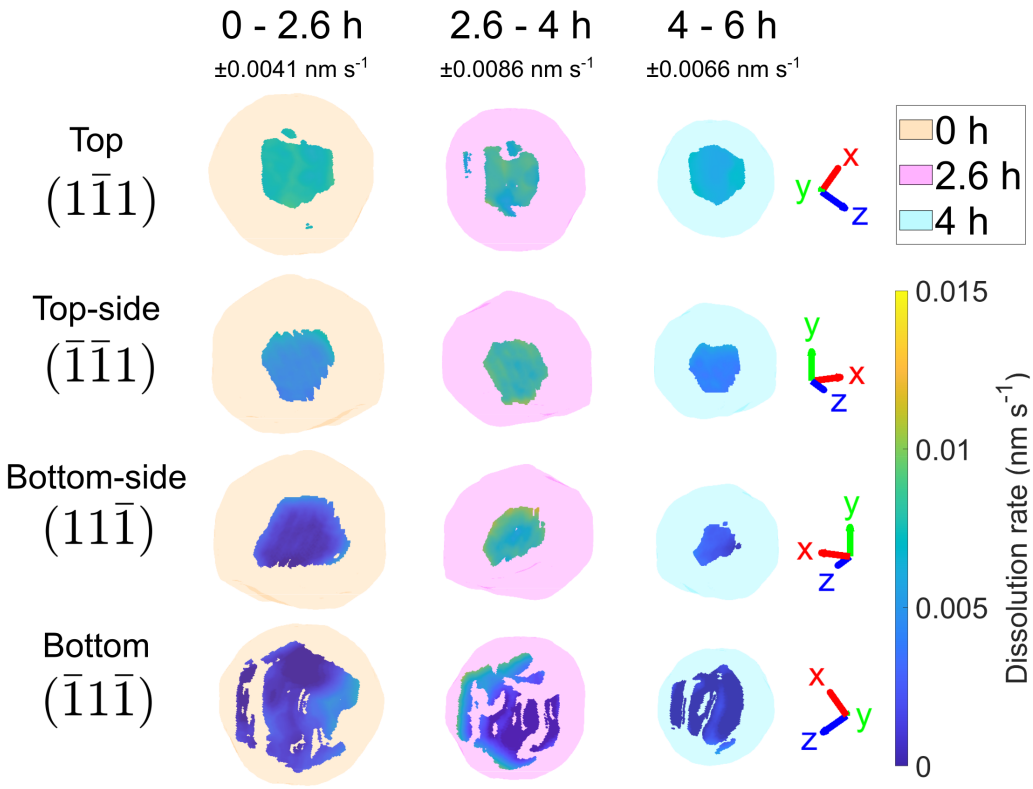

Figure 6.7: The dissolution of the top $(1\bar{1}1)$, upper-middle $(\bar{1}\bar{1}1)$, lower-middle $(11\bar{1})$, and bottom $(\bar{1}1\bar{1})$ facets. The error is ± 0.0041, 0.0086, and 0.0066 nm/s for 0 - 2.6, 2.6 - 4, and 4 - 6 h respectively. The semi-transparent volumes represent the crystal morphology at the time step. There is an increase in dissolution rate at 2.6 - 4h. The dissolution rate decreases the closer the facet is to the bottom of the crystal. The amplitude threshold is 0.25 and the magnitude of the coordinate axes corresponds to 100 nm.

6.5.3 Crystal strain

We hypothesize that the heterogeneous dissolution rate from 0 - 2.6 h is due to the higher surface strain, which progressively decreases as the reaction proceeds (Fig. 6.3(b)). Regions of higher strain have been reported to increase the dissolution rate due to increased internal energy [239, 241, 242]. The average strain inside the crystal presented in Fig.

6.3(b and c) is analysed in more detail in Fig 6.8, which shows the average strain along [111] for concentric shells within the crystal. Each shell is one voxel thick, centred about the crystal's centre of mass, and is scaled down from the surface morphology. The surface strain is clearly highest before corrosion and decreases as the reaction progresses. With increasing corrosion time, the average strain increases within the volume of the crystal (Fig. 6.8(a)) and the strain distributions inside the crystal become less homogeneous (Fig. 6.8(b)).

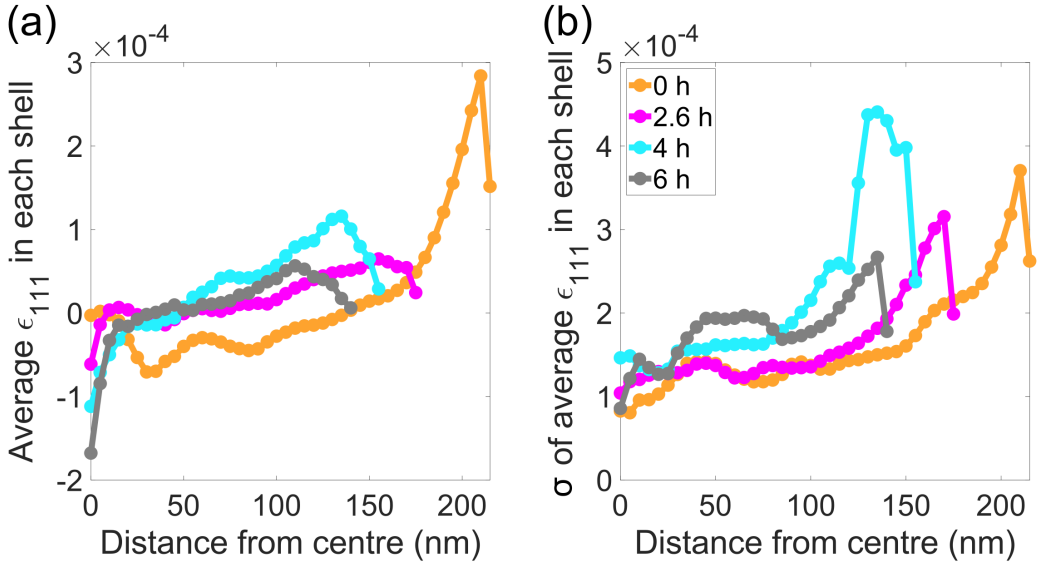

Figure 6.8: (a) The average strain along [111] as a function of distance from the centre of mass of the crystal at each time point. (b) The standard deviation of the average strain in (a).

After the edges, vertices, and most strained regions of the crystal dissolve in the first 4 hours, the dissolution rate decreases. This could be due to the core being more stable after more highly strained outer layers of the crystal have been removed, which agrees with the observations of Clark *et al.* [95]. Interestingly, the standard deviation of the strain in each shell becomes smaller closer to the centre (Fig. 6.8(b)). However, the standard deviation at a given distance from the centre increases with advancing corrosion. This suggests that the strain within the crystal becomes more heterogeneous as the crystal dissolves.

Based on post-corrosion EDX analysis, there is no significant dealloying of Fe, the less noble element, from the present crystals. However, a change in Cr and Ni impurities after corrosion suggests that there may have been preferential leaching (see Appendix

D.3).

Here, the BCDI rocking scans required just under 10 minutes to collect. For *ex situ* measurements, repeated scans are typically aligned and summed to improve reconstruction quality. However, due to the constant evolution of the crystal, only slow changes in corrosion can be probed. Pre-corrosion measurements showed no evidence of beam-induced sample damage based on the high cross-correlation of repeated scans. We therefore attribute subsequent changes of the sample during *in situ* corrosion entirely to the corrosion of the sample itself. X-ray radiation can cause excess heat and the ionisation of water [251], both of which can accelerate the corrosion rate. This must be considered when using *in situ* BCDI to study wet chemistry processes.

6.6 Conclusion

This prototypical study demonstrates the feasibility of using BCDI to understand how strain and morphology contribute to nanoscale corrosion rate. We note that analysing localised dissolution is critical to understanding how defects affect the nature of corrosion. Here, we observe that localised corrosion rates can be up to two times higher than the average corrosion rate of the crystal. Regions such as vertices and edges are shown to corrode faster than facets, leading to a progressively rounder crystal morphology. Furthermore, corrosion leads to a relaxation of surface strain. These findings would not be apparent when analysing changes in average facet size and average facet-normal distance. Finally, we demonstrate that corrosion at the sub-micron level appears to be heavily dependent on environmental conditions, as the top facets that are more exposed to the flowing fluid corrode more quickly than the bottom facets.

BCDI uniquely allows the *in situ* study of how corrosion progresses and interacts with the crystal morphology, defects and strain distribution. This insight into transient structures is not accessible via any other technique and can be crucial in understanding the driving mechanisms of corrosion. In turn, this may enable the design of better corrosion-

resistant materials in the future, e.g. by enabling the selection of corrosion-resistant textures in polycrystalline samples.

6.7 Data availability

The processed diffraction patterns, final reconstructions, and data analysis scripts are publicly available at 10.5281/zenodo.5548084.

Chapter 7

Conclusions

This thesis presents several advances in the study of crystal defect behaviour in response to external environments using *in situ* BCDI methods. BCDI provides high spatial and strain resolution in sample dimensions up to 1 μm, to an extent that makes BCDI unparalleled to any other strain microscopy technique. However, BCDI is still a relatively new tool, and currently has a relatively high barrier to entry. With the development of fourth-generation synchrotron sources, there will be greater potential for BCDI to be applied to study different systems. By publishing computer scripts to orthonormalise sheared reconstructions and introducing a reliable method to pre-align microcrystals without the need for synchrotron radiation, BCDI will hopefully become a more user-friendly and widespread tool to study lattice strains. The large datasets in *in situ* BCDI in this thesis have motivated the development of more efficient and accurate approaches to compute lattice strains. These tools have enabled several insights on how defect-induced strain fields evolve as a function of time when exposed to high temperatures or corrosive solutions. This contributes to a better understanding of defect evolution pathways in response to harsh environments. It will allow for more accurate predictive models and ultimately the design of engineering alloys with tailored properties for specific applications. Below I summarise the research questions outlined in Chapter 1. These developments aid in reducing the barrier to entry for new users of BCDI. It is foreseen that BCDI will be made

available at more facilities as part of planned synchrotron upgrade projects.

1. *How can BCDI become an everyday microscopy tool?*

   BCDI is currently a specialised microscopy tool. It requires detailed knowledge of X-rays and crystallography to obtain the desired information. The user will need to know the crystal structure and preferably the crystal orientation. Furthermore, CXDPs can be hard to reconstruct if the sample is too heavily deformed, and requires a coordinate transformation to interpret the reconstruction properly. To lower the barrier to entry, in Chapter 3, I outline the correct coordinate transformations following phase retrieval and published BCDI simulation and space mapping scripts for those unfamiliar with BCDI. Additionally, in Chapter 4, I present how a crystal can be pre-aligned for BCDI by using EBSD, a non-X-ray based method. This alternative method should allow users to more easily find Bragg peaks from their sample. I also highlight a more efficient and accurate method to calculate the strain fields for a measured BCDI reflection, which can improve the reliability of reconstructions.

2. *How are strain fields and their corresponding defects removed during a dynamic process?*

   I use *in situ* BCDI to measure the annealing of FIB-damaged Au microcrystals in Chapter 5. The FIB damage is removed around 380-410°C, indicating that annealing can be used as a pathway to remove FIB-induced strain. The gentle evolution of the crystal below $\sim$280°C is likely the result of bulk Ga diffusion and Au surface diffusion whilst more substantial changes (i.e. removal of dislocations and formation of facets) above $\sim$280°C are likely dominated by the self-diffusion of Au. Interestingly, annealing can be perceived as an abrupt process when interpreting the facet area plots and displacement r matrices, but it can also be perceived as a gradual process when analysing the morphology r matrices and average strain plots.

3. *How do localised strain fields and different morphological features interact with the sample environment?*

   The corrosion of a Co-Fe microcrystal is monitored using *in situ* BCDI in Chapter 6. Here, corrosion leads to a relaxation of average surface strain. Regions such as vertices and edges are shown to corrode faster than facets, with localised corrosion rates up to two times higher than the average corrosion rate of the crystal. Within the crystal, slight increase in average strain as corrosion progresses is observed. Corrosion at the sub-micron level appears to be heavily dependent on environmental conditions, as the top facets that are more exposed to the flowing fluid corrode more quickly than the bottom facets.

4. *To what extent can in situ BCDI be used as a tool to probe defect evolution?*

   BCDI provides a unique combination of high spatial and strain resolution without the need for a vacuum, making it highly suitable for *in situ* or *in operando* measurements. Chapters 5 and 6 demonstrate that *in situ* BCDI can provide temporal resolution up to ~ 10 minutes for a single reflection. This can potentially be reduced by 50% using chrono CDI [94] or 30% using continuous scanning [163]. This makes BCDI suitable for probing slow changes. However, in Chapter 5, I find that interpreting a single reflection alone can be misleading. Ideally, one should perform MBCDI to obtain the most unambiguous information, but *in situ* MBCDI would come at the expense of temporal resolution, which would be ~ 1 hour without further optimisation. With a recent focus on ML [128–131] and simultaneous phase retrieval [103, 104, 120], the future feasibility of MBCDI experiments is promising, which will provide a richer interpretation of crystal defects.

   One particular concern in Chapter 6 is the influence of X-ray induced radiolysis on the experimental system. X-rays can cause the radiolysis of water, producing $OH^{\bullet}$, OH^{-}, H_2O_2, H_3O^{+}, $H^{\bullet}$, $HO_2^{\bullet}$, and H_2 [252]. This can have unintended consequences on the experiment being performed, for example resulting in expedited corrosion of the sample. The intrinsic radiolysis of water does have implications for mimicking

corrosion of water cooling components of nuclear reactions, where the water is exposed to neutron irradiation. However, wet BCDI experiments concerning fuel cells [58, 161], dissolution [49, 162, 243], and hydration [171] may be subject to unwanted radiolysis effects. The effect of radiolysis on wet *in situ* or *in operando* BCDI experiments should be examined further.

The work from this thesis will contribute to the development of BCDI as a mainstream tool for probing nanoscale strain evolution. The number of dedicated BCDI beamlines across the world has increased during the past decade, and the development of more brilliant, fourth-generation synchrotron X-ray sources increases the possibility of obtaining new information using BCDI. Samples have greatly diversified from traditional "noble metals" towards "real materials," e.g., alloys [161, 162], battery components [155–157], geological compounds [95, 170, 171], nanowires [50, 107, 172], multiferroics [117, 147], and techniques such as ptychography [74, 150–152] have been applied to BCDI, enabling the study of samples that extend beyond the coherent dimensions of the X-ray beam. More sophisticated reconstruction algorithms are being developed with machine learning [128–131], enabling more complicated crystals to be reconstructed. The popularity of MBCDI has increased with recent crystal pre-orientation procedures [57, 139], enabling more strain information to be extracted from a single crystal. This has also provided motivation for simultaneous phase retrieval using multiple Bragg peaks, which generally leads to more converged reconstructions [103, 104, 120]. These developments can better enable the investigation of complex samples in realistic environments to elucidate the structure-to-function relationship of crystalline materials.

Appendix A

Chapter 3 Appendix

A.1 34-ID-C beamline to right-handed conversion

The motor angles from beamline 34-ID-C are converted to right-handed angles in Table A.1, and the accessible motor ranges are noted. In Table A.1, angle_{bl} refers to the angle recorded in *spec* at 34-ID-C.

A.2 Laboratory example additional images

An MBCDI experiment was performed at 34-ID-C. The sample was a tungsten ($a_0 =$ 3.17 Å) microcrystal prepared by a focused ion beam (FIB) liftout procedure [30] with $\lambda = 0.124$ nm. The recovered amplitudes for two reflections, $\bar{1}\bar{1}0$ and $\bar{1}10$, are shown in

Table A.1: Converting from 34-ID-C (APS) beamline angles to right-handed angles

Right-handed sample motor angles	Sample motor limits
$\theta = \theta_{\text{bl}}$	$-180° < \theta_{\text{bl}} < 180°$
$\chi = 90 - \chi_{\text{bl}}$	$-15° < \chi_{\text{bl}} < 15°$
$\phi = \phi_{\text{bl}}$	$-17° < \phi_{\text{bl}} < 17°$
Right-handed detector motor angles	Setector motor limits
$\delta = \delta_{\text{bl}}$	$-1° < \delta_{\text{bl}} < 45°$
$\gamma = 90 - \gamma_{\text{bl}}$	$-1° < \gamma_{\text{bl}} < 90°$

Table A.2: Laboratory-based MBCDI experiment right-handed angles

$\bar{1}\bar{1}0$ reflection	$\bar{1}10$ reflection
$\theta_{\bar{1}\bar{1}0} = 96.70°$	$\theta_{\bar{1}10} = -174.2°$
$\chi_{\bar{1}\bar{1}0} = -0.9938°$	$\chi_{\bar{1}10} = 0.9590°$
$\phi_{\bar{1}\bar{1}0} = 0.1112°$	$\phi_{\bar{1}10} = 9.954°$
$\delta_{\bar{1}\bar{1}0} = 32.26°$	$\delta_{\bar{1}10} = 29.58°$
$\gamma_{\bar{1}\bar{1}0} = -2.132°$	$\gamma_{\bar{1}10} = -13.39°$

this section. The right-handed detector angles for the reflections are listed in below.

A.2.1 Electron micrograph comparison

The SS shape calculated from the $\bar{1}10$ DCS shape using `DCS_to_SS`, and a comparison with an SEM image of the sample is shown in Fig. A.1.

A.2.2 Laboratory SS shape comparison

The SS shapes from two laboratory-based reflections, $\bar{1}10$ and $\bar{1}\bar{1}0$, are calculated using `DCS_to_SS`. The two SS objects are overlapped and viewed in the x-y, x-z and y-z planes in Fig. A.2, showing a 99.84% overlap, indicating a high accuracy of the experiment and the script, mentioned in Section 3.6.1.

A.2.3 DCS shape reconstruction

For the cylinder, the reconstructed DCS shape for 111 was transformed to the DCS shape for $\bar{1}20$ using `DCS_to_DCS` and compared to the reconstructed DCS shape for $\bar{1}20$ in Fig. A.3(a). For the laboratory sample, the reconstructed DCS shape for $\bar{1}10$ was transformed to the DCS shape for $\bar{1}\bar{1}0$ using `DCS_to_DCS` and compared with the reconstructed DCS shape for $\bar{1}\bar{1}0$ in Fig. A.3(b). They show a 97.7% and 99.9% overlap respectively, indicating a high accuracy of the experiment and the script, mentioned in Section 3.6.2.

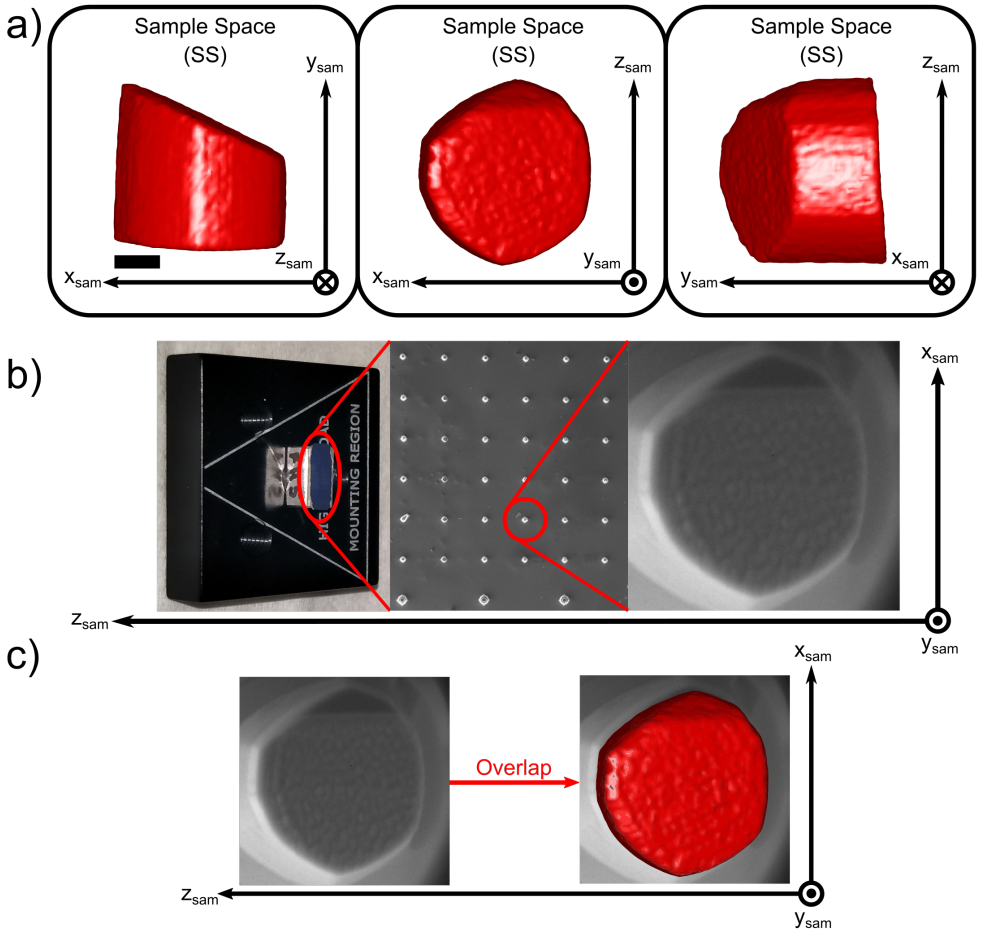

Figure A.1: Comparison between (a) the calculated SS shape from the $\bar{1}10$ reflection and (b) an electron micrograph of the sample. Excellent overlap between the calculated SS shape and the SEM micrograph is shown in (c). The unique shape of this object inspires confidence in the orientation of the object and thus in the faithfulness of the rotations applied to recover the SS object. The scale bar in SS corresponds to 200 nm.

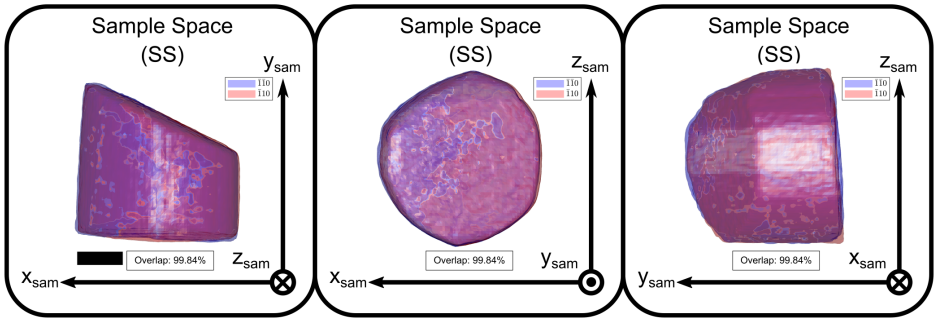

Figure A.2: Comparison between calculated SS shapes from two different reflections, $\bar{1}\bar{1}0$ and $\bar{1}10$, displayed for the x-y, x-z and y-z planes from left to right for a tungsten strain-microscopy sample. The 99.8% amplitude agreement overlap highlights the accuracy of the scripts in a laboratory-based experiment. The scale bar in SS corresponds to 200 nm.

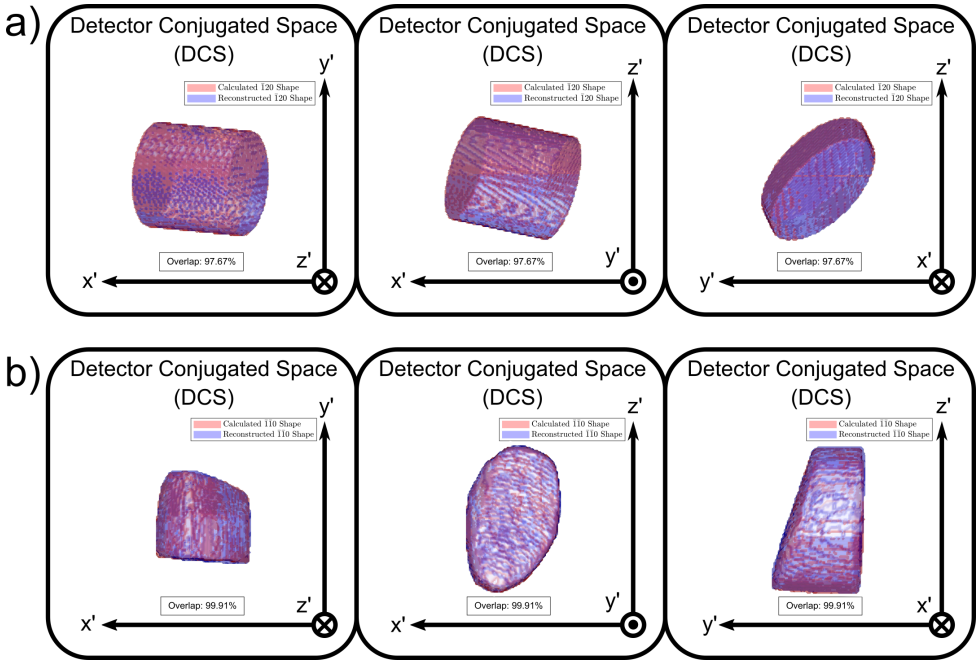

Figure A.3: Comparison between calculated DCS shape and reconstructed DCS shape for (a) simulated cylinder and (b) laboratory sample, displayed for the x-y, x-z and y-z planes from left to right. It shows a 97.7% and a 99.9% amplitude agreement overlap respectively, highlighting the accuracy of the scripts relative to a reconstructed shape.

Appendix B

Chapter 4 Appendix

B.1 Phase retrieval

The reconstruction process of CXDPs was executed in two stages, using the output from the previous stage to seed the next phasing stage (listed below). The CXDPs have a size of $256 \times 256 \times 128$ voxels.

1. Each reconstruction was seeded with a random guess. A guided phasing approach [93] with 40 individuals and four generations was used with a geometric average breeding mode. For each generation and population, a block of 20 error reduction (ER) and 180 hybrid input-output (HIO) iterations, with $\beta = 0.9$, was repeated three times. This was followed by 20 ER iterations to return the final object. The shrinkwrap algorithm [89] with a threshold of 0.1 was used to update the real-space support every iteration. The σ for the Gaussian kernel shrinkwrap smoothing for each generation was $\sigma = 2.0, 1.5, 1.0, 1.0$ respectively. The best reconstruction was determined using a sharpness criterion, as it is the most appropriate metric for crystals containing defects [92]. The two worst reconstructions were removed after each generation.

2. The reconstruction was seeded with the output from stage 1. This stage was identical to stage 1, except now for each generation and population, a block of 20 error

reduction (ER) and 180 hybrid input-output (HIO) iterations, with $\beta = 0.9$, was repeated 15 times, followed by 1000 ER iterations. Here the final 50 iterates were averaged to produce the final image.

The overall average 3D spatial resolution was 35 nm. This was determined by differentiating the electron density amplitude across the crystal/air interface for the five reflection directions and fitting a Gaussian to each of the profiles. The reported spatial resolution is the averaged full width at half maximum of the Gaussian profiles. The average 3D spatial resolution was 30, 38, 39, 31 and 39 nm at for the 111, $\bar{1}\bar{1}1$, 200, $0\bar{2}0$, and 002 reconstructions respectively.

B.2 EDX results

Fig. B.1 shows homogeneous elemental distribution of crystal 2B corresponding to the SEM spectrum in Fig. 4.1(c).

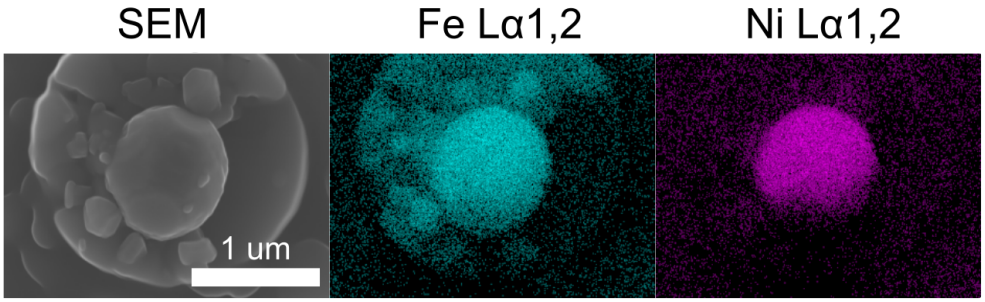

Figure B.1: EDX elemental analysis maps of a Fe-Ni crystal. Shown are 2D signals for the primary Fe-Ni emission lines.

B.3 Supplementary video descriptions

A brief description of each supplementary video is listed below.

- SV1 shows x-y plane slices through the lattice strain and rotation tensors in Fig. 4.6.

- SV2 shows y-z plane slices through the lattice strain and rotation tensors in Fig. 4.6.
- SV3 shows z-x plane slices through the lattice strain and rotation tensors in Fig. 4.6.

Appendix C

Chapter 5 Appendix

C.1 34-ID-C heater cell

Fig. C.1(a) shows the heater within a furnace enclosure. Fig. C.1(b) shows a rendering of the enclosure cover, consisting of a stainless-steel cover plate attached to a base using stainless-steel threaded rods and nuts. Only two rods were used to minimise the obstruction of the incident and reflected X-rays. The circular hole in the plate was covered with a quartz window to allow observation of the sample with a confocal microscope with a 5$\times$ objective lens during the annealing experiment. The sides of the furnace enclosure cover were covered with metalized Kapton (not shown) to allow for the transmission of X-rays and favourable thermal transport for cooling of the film.

C.2 Effect of seeding on the retrieved electron density

This section addresses how the seeding of the phase retrieval algorithm influences the final object's amplitude and strain. For a CXDP at an arbitrary temperature, we consider the following options:

1. Seeding with the reconstruction from the temperature step immediately below the current temperature, except if the current temperature is 23°C, in which case a ran-

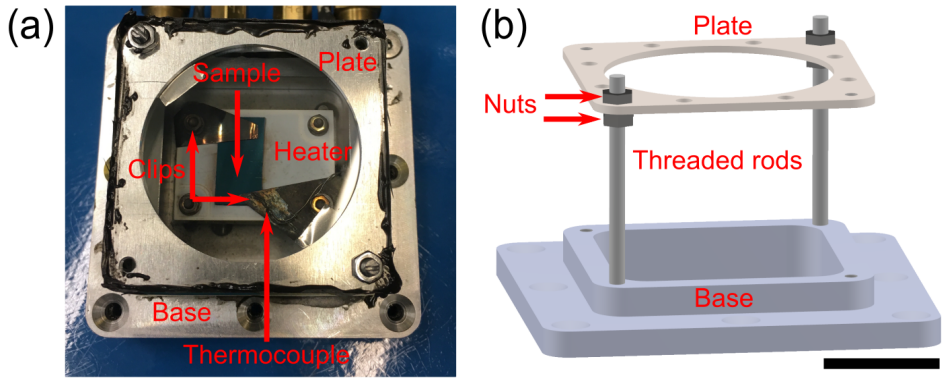

Figure C.1: (a) The sample clipped in the heater cell as seen through the heater enclosure window. Note the thermocouple is attached to the clip, which contacts the silicon substrate. This results in thermal resistance between the Au crystals and the thermocouple, causing the discrepancy between the measured and actual temperature of the sample. (b) A rendering of the furnace enclosure cover. The scale bar corresponds to 20 mm.

dom guess is used.

2. Seeding with the reconstruction from the temperature step immediately above the current temperature, except if the current temperature is 587°C, in which case a random guess is used.

3. Seeding with a random guess regardless of the current temperature.

fa A simpler phase retrieval algorithm compared to the one listed in Appendix C.3 was implemented to exaggerate the differences in the final reconstructions. A pattern of 20 error reduction (ER) and 180 hybrid input-output (HIO) iterations was repeated three times followed by 20 ER iterations, for a total of 620 iterations. This algorithm was applied to each CXDP padded to a size of $256 \times 256 \times 176$ voxels. After phase retrieval, each object was mapped into orthogonal sample space and the strain was calculated using Eq. 2.78 and the procedure found at the end of Appendix C.3.

To compute the error between two reconstructions generated using two different seeding approaches, we sum the difference between the two reconstructions for each voxel, n, and normalise it over the union of the morphologies (created using an amplitude threshold of 0.30) for that particular reflection and temperature, This yields Eq. C.1 and Eq. C.2 for the strain error and amplitude error respectively:

$$\mathrm{E}_{\varepsilon} = \frac{\sum_{n} |\varepsilon_{\text{seed a}} - \varepsilon_{\text{seed b}}|}{\sum_{n} \text{Mask}}, \text{ and} \tag{C.1}$$

$$\mathrm{E}_{\omega} = \frac{\sum_{n} |\omega_{\text{seed a}} - \omega_{\text{seed b}}|}{\sum_{n} \text{Mask}}, \tag{C.2}$$

where seed a and b are any two of the three seeding scenarios listed previously. Fig. C.2 shows how the strain and amplitude for reconstructions generated using each seeding variable compare.

In Fig. C.2 we observe that no two seeds generate reconstructions that are exactly the same, which would otherwise be represented by a line with negligible differences. Spikes on the plots point out that at least one reconstruction did not converge as well as the others. At temperatures where all error comparison lines overlap, the reconstructions are equally different from each other. The average strain error is $\sim 2 \times 10^{-4}$, which agrees well with the uncertainty seen in previous studies [29, 30, 47]. The red lines in Fig. C.2 represent the error between the two non-random seeds, and are in general lower than the error between either seed and the random guess. This shows that phasing with a seed generates reconstructions that converge more rapidly, compared to phasing with a random guess. However, we cannot conclude whether phasing with a reconstruction from the next or previous temperature step yields a more accurate result. Thus, we decided for each reconstruction to be seeded with itself at the same temperature from the previous phasing round (except for the first round, where a random guess was used for all temperatures), instead of seeding with a reconstruction at a different temperature in the same round as explained in Section 5.3.3.

C.3 Phase retrieval

The reconstruction process for every CXDP was executed in four stages, similar to the approach used by [30], using the output from the previous stage to seed the next phasing stage (listed below). Note the 002 reflection for crystal A and 200 and $11\bar{1}$ reflections for crystal B at room temperature were padded to a size of $256 \times 256 \times 176$ voxels to make them consistent with the other CXDPs in the study.

1. Each CXDP was seeded with a random guess. A guided phasing approach with 40 individuals and four generations was used [93]. The first and second generations used low resolution data while the remaining generations used full resolution data. For each generation, a block of 20 ER and 180 HIO iterations, with $\beta = 0.9$, was repeated three times. This was followed by 20 ER iterations, which were averaged to return the final object. The best reconstruction was determined using a sharpness criterion, as it is the most appropriate metric for crystals containing defects [92]. The shrinkwrap algorithm [89] was used to periodically update the real-space support.

2. The reconstruction was seeded with the output from stage 1. This stage was identical to the previous except now we account for the longitudinal and transverse partial coherence [99] using the Richardson-Lucy deconvolution algorithm.

3. The reconstruction was seeded with the output from stage 2. A block of 20 ER and 180 HIO iterations was repeated 15 times, followed by 1000 iterations of ER. The final 50 ER iterations were averaged to produce the final output. The same partial coherence settings in stage 2 were included, but guided phasing was omitted.

4. Stage 3 was repeated, using the output from stage 3 as the seed.

Next, phase offsets of 0, $-\frac{\pi}{2}$, and $\frac{\pi}{2}$ were applied to the electron density for each reconstruction and the resulting phases outside $-\pi$ to π were returned to this range by adding or subtracting 2π. The resulting reconstructions for each of the three offsets were

transformed from detector conjugated space to orthogonal sample space with a voxel size of $5 \times 5 \times 5$ nm^3. Phase ramps were eliminated by centring the Fourier transform of the complex electron density. This set of phase offset data was differentiated and the minimum gradient for each voxel was used to calculate the strain, preserving its sign, to avoid discontinuities which otherwise arise at dislocation cores [30].

C.4 Spatial resolution

We note that the spatial resolution is dependent on the measurement directions in reciprocal space and the geometry of the sample. The spatial resolution was calculated by considering two line profiles that cross the air-sample interface for each reflection: one normal to the top face and the other normal to the milled face. The spatial resolution was determined by differentiating the profiles and fitting the resulting peak with a Gaussian. The average 2σ of the fitted Gaussian at each temperature step is reported as the spatial resolution. A plot of the spatial resolution vs. temperature is shown in Fig. C.3.

C.5 Dislocations in crystal B, (200) reflection

The phase for crystal B's 200 reflection at room temperature is shown in Fig. C.4. Vortex-like phase features that resemble dislocations are highlighted. These features are present in the trench-like regions shown in Fig. 5.4.

C.6 Standard deviation of average strain

The standard deviation of the strain for a particular VOI provides information about strain heterogeneity within the VOI. This can be used to evaluate the extent of annealing, whereby a lowered standard deviation corresponds to a more relaxed crystal lattice. The strain standard deviation vs. temperature for all VOIs is plotted in Fig. C.5.

C.7 CXDP comparison

Differences in the collected CXDPs at different temperatures show evidence of structural change. The asymmetry in the Bragg peak is indicative of strain within the crystal lattice. A comparison of the CXDPs at 23°C and 587°C is shown in Fig. C.6.

C.8 Supplementary video descriptions

Below is a list of brief descriptions for supplementary videos.

- SV1 shows the evolution of the surface morphology and internal strain for crystal A based on Fig. 5.4.
- SV2 shows the evolution of the surface morphology and internal strain for crystal B based on Fig. 5.4.
- SV3 shows facet area evolution as temperature increases for both crystals based on Fig. 5.5 and Fig. 5.6.
- SV4 shows the evolution of the CXDP slices for crystal A based on Fig. C.6.
- SV5 shows the evolution of the CXDP slices for crystal B based on Fig. C.6.

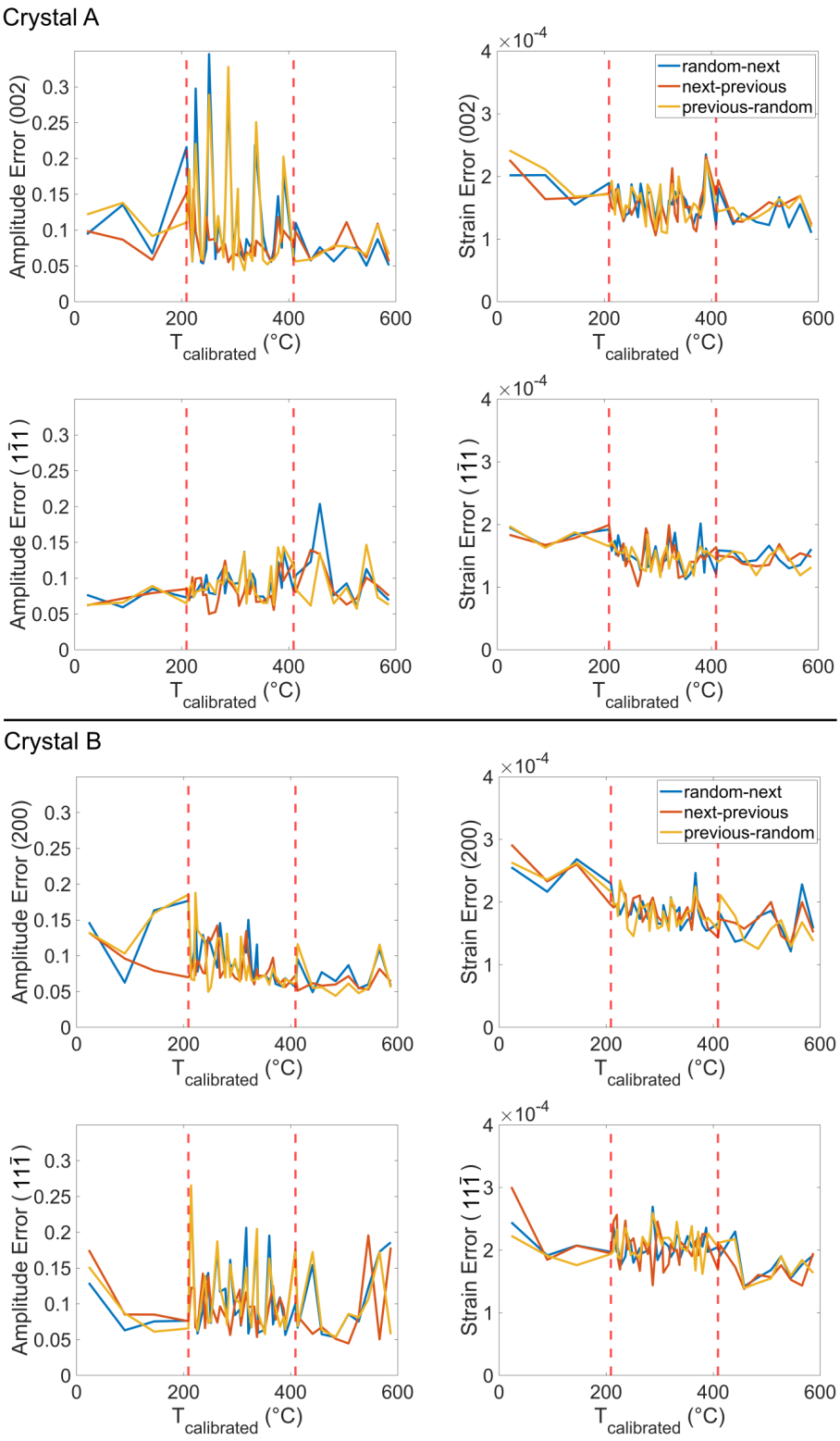

Figure C.2: The amplitude and strain error, computed using Eq. C.1 and C.2 respectively, between reconstructions obtained using different seeding approaches. Each line represents the error between any two of the three seeding variables. The red error line has the lowest error on average. The large error spikes are the result of poorly converged solutions. The red dashed lines indicate where the temperature sampling changed.

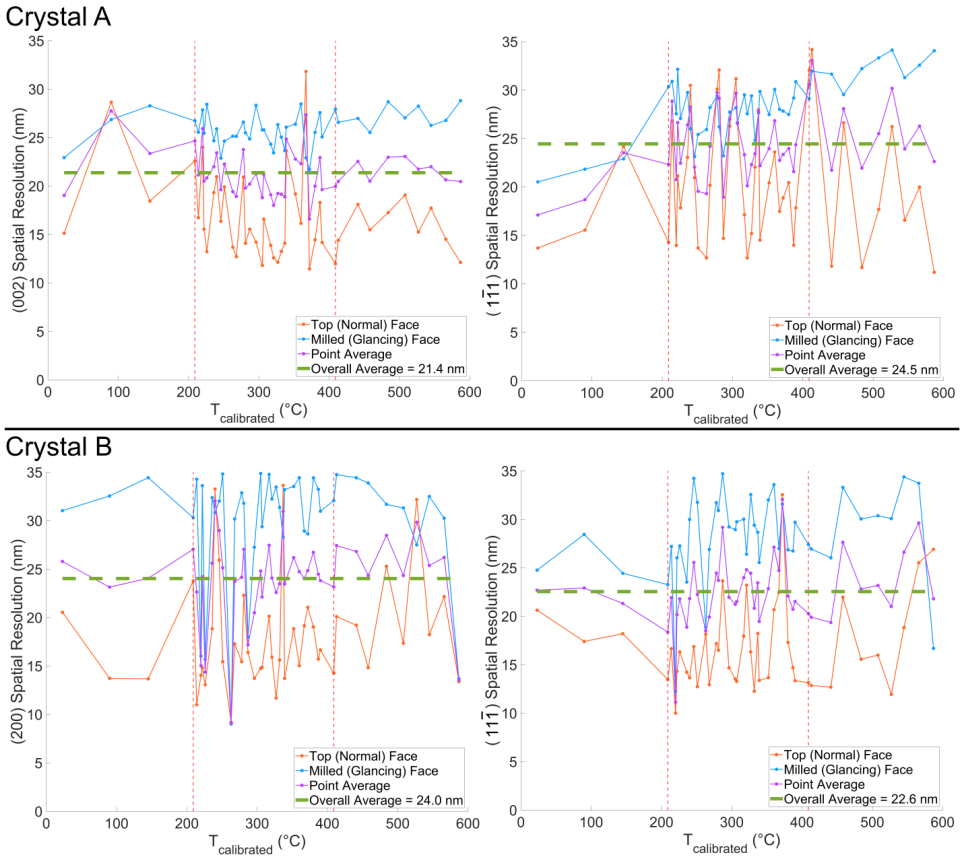

Figure C.3: Spatial resolutions with respect to temperature for each reflection. The overall average for each crystal is the mean of the point averages across all temperatures. The spatial resolution for this experiment, 23 nm, is the overall average for all reflections. The red dashed lines indicate where the temperature sampling changed.

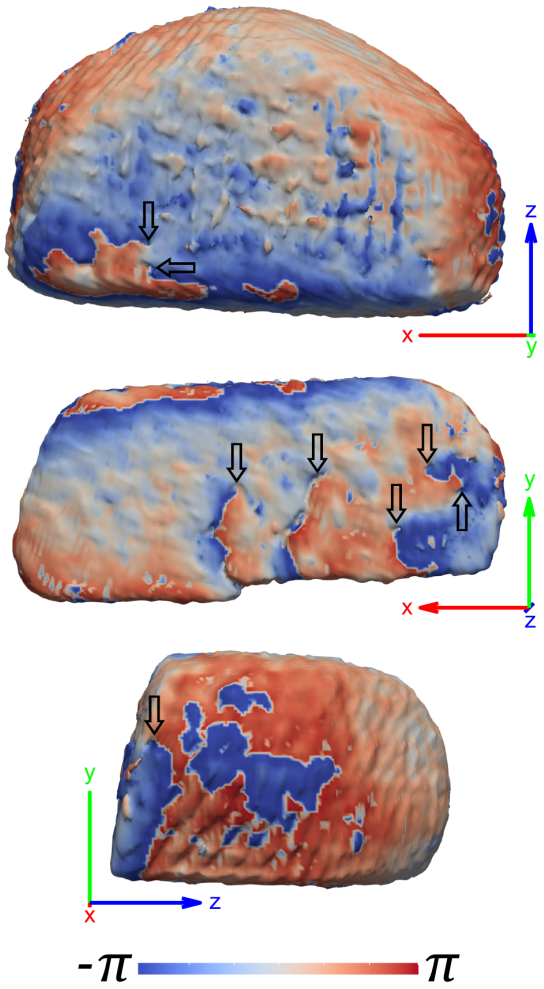

Figure C.4: A phase isosurface rendering of crystal B's 200 reflection at room temperature, showing phase vortices reminiscent of dislocations marked by black arrows. The coordinate axes are positioned in sample space and plotted with a length of 200 nm. Here the amplitude threshold is 0.04 and no phase unwrapping was performed.

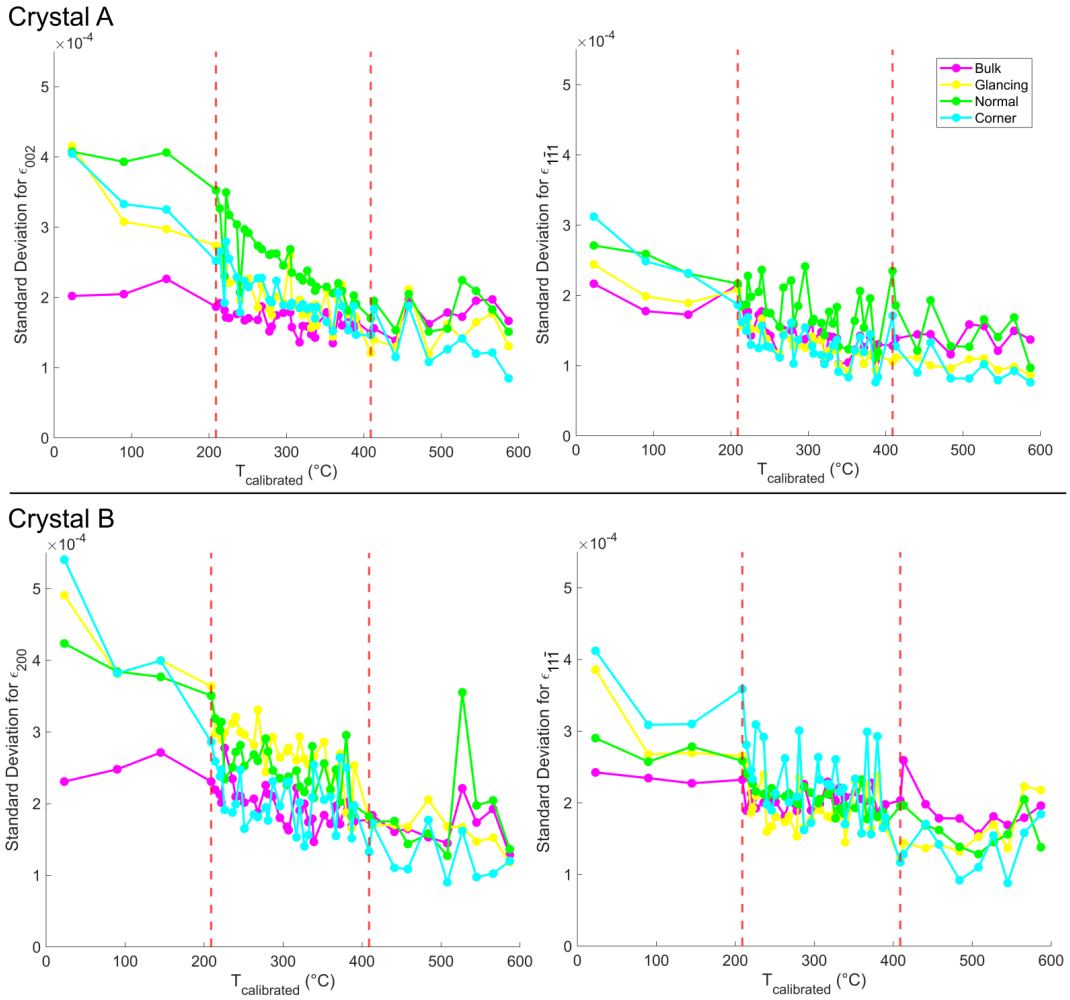

Figure C.5: Standard deviation of strain for different VOIs at each temperature point. As annealing proceeds, the standard deviation follows a decreasing trend in all VOIs, which shows a reduction in strain heterogeneity across all reflections. After ~ 410°C, all standard deviation values are fairly constant, suggesting that FIB-induced strain has been removed.

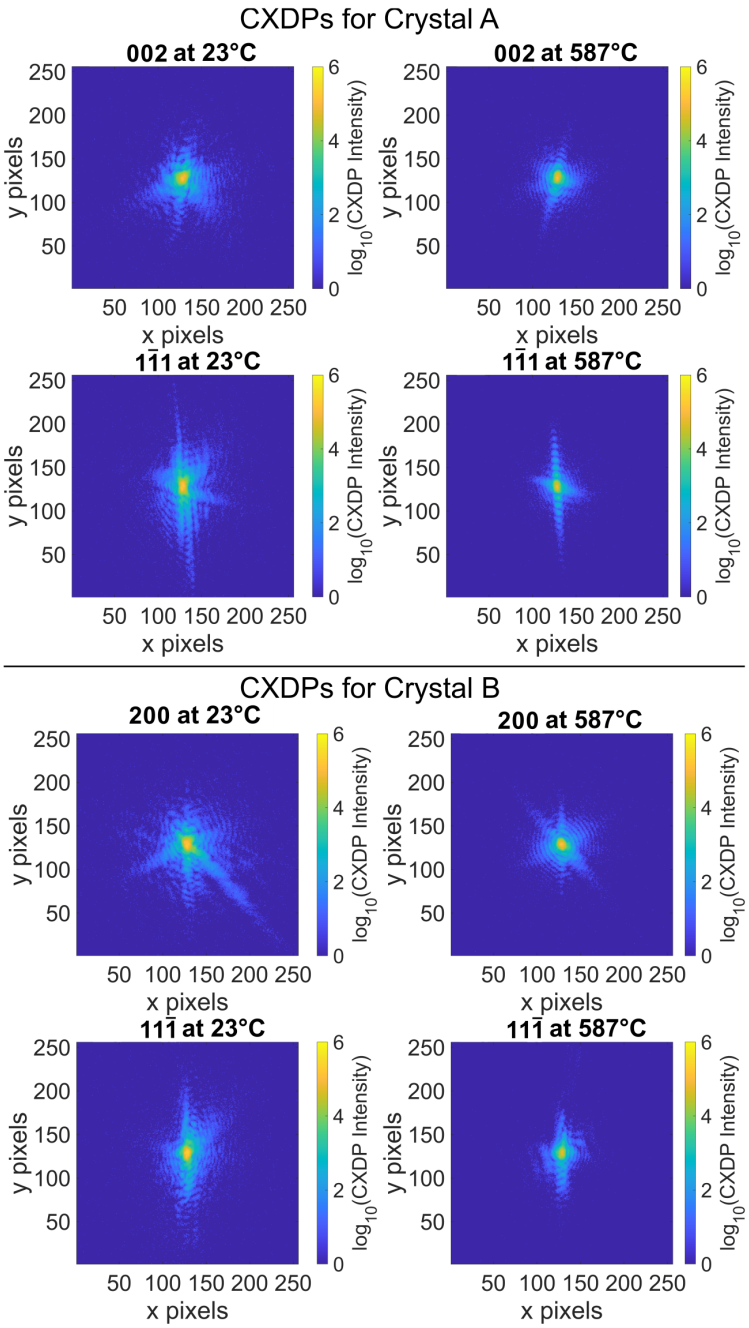

Figure C.6: Central slice of the unprocessed CXDPs at the lowest and highest temperatures for each reflection. The asymmetry in the CXDP slices before annealing indicates a high degree of strain. This strain is alleviated after heat treatment, which is demonstrated by the centrosymmetric fringes at 587°C. The evolution of the raw CXDPs for each reflection during heat treatment can be seen in supplementary videos SV4 and SV5.

Appendix D

Chapter 6 Appendix

D.1 Phase retrieval

The reconstruction process of CXDPs was executed in stages, using the output from the previous stage to seed the next phasing stage (listed below). Initially, CXDPs were padded to a size of $256 \times 256 \times 144$ voxels.

1. Each reconstruction was seeded with a random guess. A guided phasing approach [93] with 40 individuals and four generations was used with a geometric average breeding mode. For each generation and population, a block of 20 error reduction (ER) and 180 hybrid input-output (HIO) iterations, with $\beta = 0.9$, was repeated three times. This was followed by 20 ER iterations to return the final object. The shrinkwrap algorithm [89] with a threshold of 0.1 was used to update the real-space support for every iteration. The σ for the Gaussian kernel shrinkwrap smoothing for each generation was $\sigma = 2.0, 1.5, 1.0, 1.0$ respectively. The best reconstruction was determined using a sharpness criterion, as it is the most appropriate metric for crystals containing defects [92]. The two worst reconstructions were removed after each generation.

2. The reconstruction was seeded with the output from stage 1. This stage was identical to stage 1, except now we account for the longitudinal and transverse par-

tial coherence using a mutual coherence function (MCF) [99]. Starting from the 50th iteration, the MCF was updated every 50 iterations using 20 iterations of the Richardson–Lucy deconvolution algorithm [119].

3. The reconstruction was seeded with the output from stage 2. This stage was identical to stage 2, except now we use a guided phasing approach with 10 individuals and four generations. For each generation and population, a block of 20 error reduction (ER) and 180 hybrid input-output (HIO) iterations, with $\beta = 0.9$, was repeated 15 times, followed by 1000 ER iterations. The final 50 iterates were averaged to produce the final image.

The average 3D spatial resolution was 30 nm. This was determined by differentiating the electron density amplitude across the crystal/acid interface for the five reflection directions and fitting a Gaussian to each of the profiles. The reported spatial resolution is the averaged full width at half maximum of the Gaussian profiles. The average 3D spatial resolution for each reconstruction during corrosion was 23, 31, 30 and 38 nm at 0, 2.6, 4 and 6 h respectively.

D.2 Facet evolution

Fig. D.1 highlights the evolution of facets. Facet areas are identified by selecting the surface elements that have an isonormal within a 19° angular threshold of a given facet normal unit vector. The facet normal vectors were calculated from the orientation matrix obtained by minimising the error between the five known reflections in sample space. In principle, a maximum angular threshold of 27.4° could be used, which is half the angle between $\{111\}$ and $\{100\}$ planes. Our chosen tolerance is below this maximum since not all facets are fully developed, and the edges and vertices of the crystal appear rounded and thus should not be classified as part of a facet. The facet areas were calculated by summing the areas of all surface elements that fall within the angular threshold for facet identification.

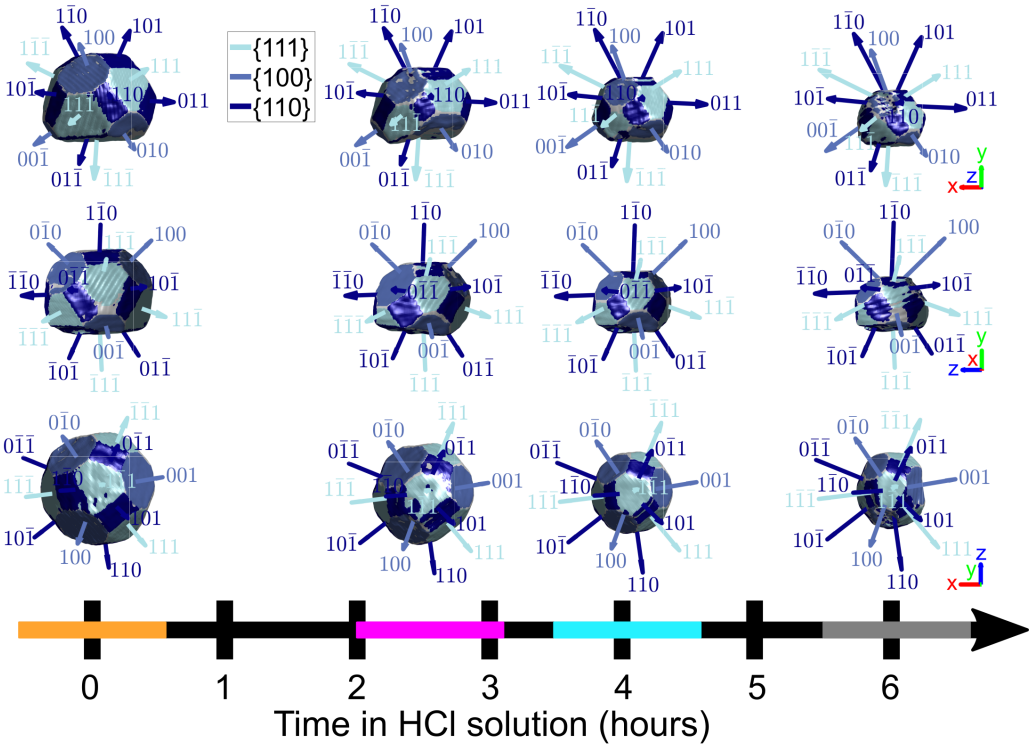

Figure D.1: The identification of facets on the crystal surface as a function of corrosion time. Shown are the x-y, x-z, and y-z planes. The coloured bands on the time axis correspond to the reconstructions at those time points and are used throughout the article. For the crystals, the amplitude threshold is 0.25 and the magnitude of the coordinate axes corresponds to 100 nm. Supplementary video SV7 rotates around the crystal with facets identified at each time point during corrosion.

D.3 EDX results

Fig. D.2 compares two other crystals (B and C) on the substrate before and after corrosion using SEM images and EDX spectra. There is no obvious indication of dealloying, as the ratio of Co and Fe does not show significant change. Preferential leaching of Cr or Ni may occur, but is not considered further since the concentrations within the samples are low. The concentration of Ga decreased, suggesting the dissolution of most of the FIB-contaminated parts of the crystal.

Fig. D.3 shows homogeneous elemental distribution of the two crystals shown in Fig. D.2 after corrosion.

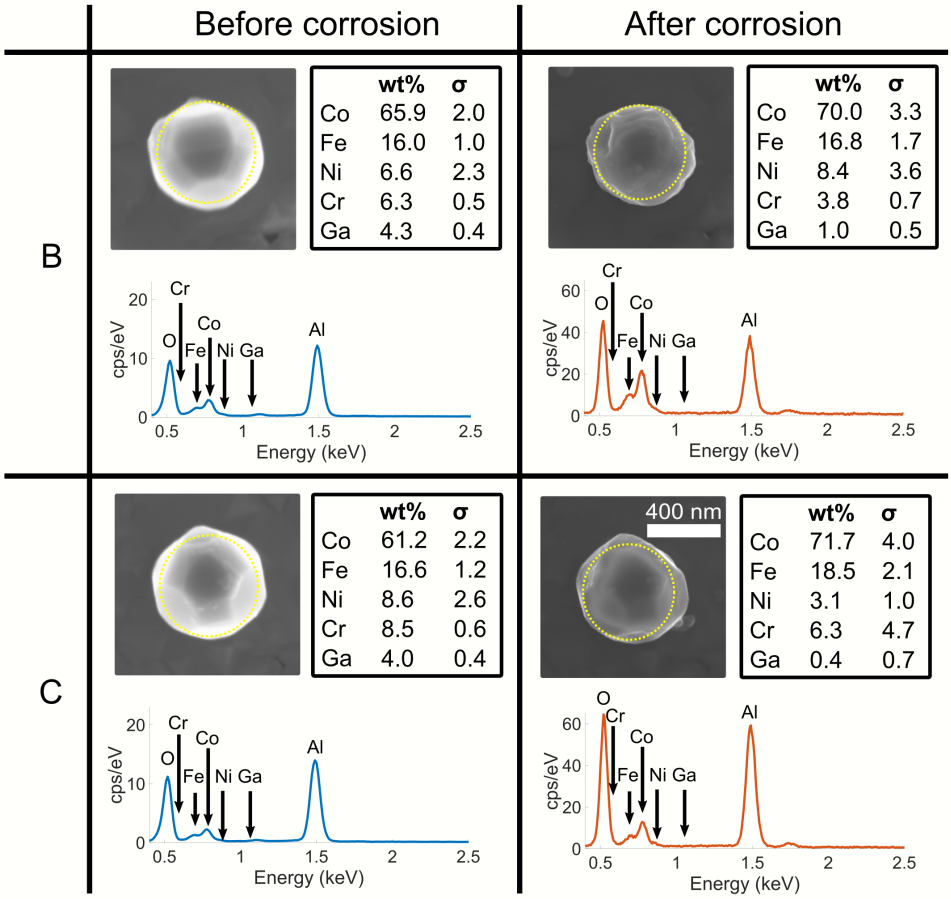

Figure D.2: A comparison between two other crystals (B and C) on the substrate before and after corrosion using SEM and EDX. The EDX spectra before corrosion (blue) were collected on a ZEISS EVO with an acceleration voltage of 10 kV, consistent with the spectrum shown in Fig. 6.1(d). EDX spectra after corrosion (orange) were collected on a ZEISS Merlin analytical SEM with an acceleration voltage of 10 kV. The dotted yellow line represents the region measured using EDX.

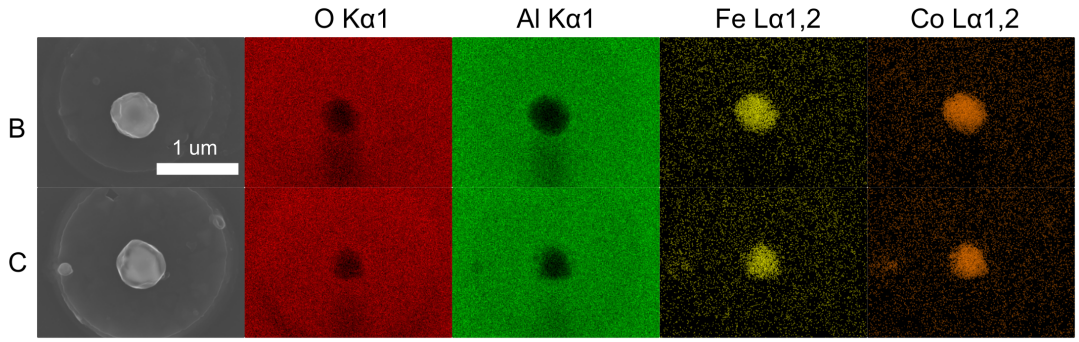

Figure D.3: EDX elemental analysis maps of the two crystals (B and C) shown in Fig. D.2. Shown are 2D signals for the substrate, Al_2O_3, and primary Co-Fe emission lines. The maps were collected using a ZEISS Merlin analytical SEM equipped with a Xmax 150 detector (Oxford Instruments) with an acceleration voltage of 10 kV.

D.4 Supplementary video descriptions

A brief description of each supplementary video is listed below.

- SV1 shows x-y plane slices through the lattice strain and rotation tensors in Fig. 6.2.
- SV2 shows y-z plane slices through the lattice strain and rotation tensors in Fig. 6.2.
- SV3 shows z-x plane slices through the lattice strain and rotation tensors in Fig. 6.2.
- SV4 shows the rotation of the crystal coloured by strain at various time points during corrosion, based on Fig. 6.3(a).
- SV5 shows x-y plane slices through the crystal at various time points during corrosion, based on Fig. 6.3(a).
- SV6 shows the rotation of the crystal coloured by strain at various time points during corrosion, based on Fig. 6.6.
- SV7 shows the rotation of the crystal coloured by facets at various time points during corrosion, based on Fig. D.1.

Appendix E

List of abbreviations

3D	three-dimension
AIMD	*Ab initio* molecular dynamics
AFM	atomic-force-microscopy
ANL	Argonne National Laboratory
APS	Advanced Photon Source
ARC	Advanced research computing
BCDI	Bragg coherent X-ray diffraction imaging
BP	Bragg ptychography
CDI	coherent X-ray diffraction imaging
CXDP	coherent X-ray diffraction pattern
CNN	convolutional neural network
DCS	detector conjugated space
DRS	detector reciprocal space
DLS	Diamond Light Source
DM	difference map
DNN	deep deconvolutional network
EBSD	electron backscatter diffraction
EBSP	electron backscatter pattern

EDX	energy-dispersive X-ray spectroscopy
ED-XAS	energy-dispersive X-ray absorption spectroscopy
EM	electron microscopy
ePIE	extended ptychographical iterative engine
ER	error reduction
ESRF	European Synchrotron Radiation Facility
FCC	face-centred cubic
FIB	focused ion beam
FWHM	full width at half maximum
FSC	Fourier shell correlation
GS	Gerchberg-Saxton
HCl	hydrochloric acid
HIO	hybrid input-output
HRTEM	high-resolution transmission electron microscopy
ID	insertion device
KB	Kirkpatrick-Baez
LCTEM	liquid cell transmission electron microscopy
LS	laboratory space
MBCDI	multi-reflection Bragg coherent X-ray diffraction imaging
MCF	mutual coherence function
ML	machine learning
OPLD	optical path length difference
NN	neural network
PIE	ptychographic iterative engine
PRTF	phase retrieval transfer function
RAAR	relaxed averaged alternating reflections
RL	Richardson—Lucy
RLS	reciprocal laboratory space

ROI	region of interest
SEM	scanning electron microscopy
SS	sample space
STEM	scanning transmission electron microscopy
SV	supplementary video
TEM	transmission electron microscopy
TXM	transmission X-ray microscopy
VSI	vertical scanning interferometry
vwBCDI	variable-wavelength BCDI
XAFS	X-ray absorption fine structure
XANES	X-ray absorption near-edge spectroscopy
XFEL	X-ray free electron laser
XMT	X-ray microtomography

References

[1] Y. Sun, S. E. Thompson, and T. Nishida, "Physics of strain effects in semiconductors and metal-oxide-semiconductor field-effect transistors," *Journal of Applied Physics*, vol. 101, no. 10, p. 104503, 2007.

[2] A. Khorshidi, J. Violet, J. Hashemi, and A. A. Peterson, "How strain can break the scaling relations of catalysis," *Nature Catalysis*, vol. 1, no. 4, pp. 263–268, 2018.

[3] I. Aharonovich, D. Englund, and M. Toth, "Solid-state single-photon emitters," *Nature Photonics*, vol. 10, no. 10, pp. 631–641, 2016.

[4] J. P. Pender, G. Jha, D. H. Youn, J. M. Ziegler, I. Andoni, E. J. Choi, A. Heller, B. S. Dunn, P. S. Weiss, R. M. Penner, and C. B. Mullins, "Electrode Degradation in Lithium-Ion Batteries," *ACS Nano*, vol. 14, no. 2, pp. 1243–1295, 2020.

[5] H. Clemens and S. Mayer, "Design, processing, microstructure, properties, and applications of advanced intermetallic TiAl alloys," *Advanced Engineering Materials*, vol. 15, no. 4, pp. 191–215, 2013.

[6] S. J. Zinkle and G. S. Was, "Materials challenges in nuclear energy," *Acta Materialia*, vol. 61, no. 3, pp. 735–758, 2013.

[7] O. Barrera, D. Bombac, Y. Chen, T. D. Daff, E. Galindo-Nava, P. Gong, D. Haley, R. Horton, I. Katzarov, J. R. Kermode, C. Liverani, M. Stopher, and F. Sweeney, "Understanding and mitigating hydrogen embrittlement of steels: a review of ex-

perimental, modelling and design progress from atomistic to continuum," *Journal of Materials Science*, vol. 53, no. 9, pp. 6251–6290, 2018.

[8] J. R. Greer and J. T. M. De Hosson, "Plasticity in small-sized metallic systems: Intrinsic versus extrinsic size effect," *Progress in Materials Science*, vol. 56, no. 6, pp. 654–724, 2011.

[9] S. Cao, F. F. Tao, Y. Tang, Y. Li, and J. Yu, "Size- and shape-dependent catalytic performances of oxidation and reduction reactions on nanocatalysts," *Chemical Society Reviews*, vol. 45, no. 17, pp. 4747–4765, 2016.

[10] W. H. Qi and M. P. Wang, "Size and shape dependent melting temperature of metallic nanoparticles," *Materials Chemistry and Physics*, vol. 88, no. 2-3, pp. 280–284, 2004.

[11] J. N. F. Michael D. Uchic, Dennis M. Dimiduk and W. D. Nix, "Sample Dimensions Influence Strength and Crystal Plasticity," *Science*, vol. 305, no. 5686, pp. 986–989, 2004.

[12] Z. Song and Z. H. Xie, "A literature review of in situ transmission electron microscopy technique in corrosion studies," *Micron*, vol. 112, pp. 69–83, 2018.

[13] Y. Peng, K. Miao, W. Sun, C. Liu, H. Wu, L. Geng, and G. Fan, "Recent Progress of Synchrotron X-Ray Imaging and Diffraction on the Solidification and Deformation Behavior of Metallic Materials," *Acta Metallurgica Sinica (English Letters)*, vol. 35, no. 1, pp. 3–24, 2022.

[14] D. Karpov and E. Fohtung, "Bragg coherent diffractive imaging of strain at the nanoscale," *Journal of Applied Physics*, vol. 125, no. 12, p. 121101, 2019.

[15] M. J. Hÿtch, J.-L. Putaux, and J.-M. Pénisson, "Measurement of the displacement field of dislocations to 0.03 Å by electron microscopy," *Nature*, vol. 423, no. 6937, pp. 270–273, 2003.

[16] Y. Yuan, K. Amine, J. Lu, and R. Shahbazian-Yassar, "Understanding materials challenges for rechargeable ion batteries with in situ transmission electron microscopy," *Nature Communications*, vol. 8, no. 1, p. 15806, 2017.

[17] Q. Yu, M. Legros, and A. M. Minor, "In situ TEM nanomechanics," *MRS Bulletin*, vol. 40, no. 1, pp. 62–70, 2015.

[18] M. L. Taheri, E. A. Stach, I. Arslan, P. A. Crozier, B. C. Kabius, T. LaGrange, A. M. Minor, S. Takeda, M. Tanase, J. B. Wagner, and R. Sharma, "Current status and future directions for in situ transmission electron microscopy," *Ultramicroscopy*, vol. 170, pp. 86–95, 2016.

[19] K. Arakawa and M. P. Short, *Experimental Validation of Models: In Situ TEM for Radiation Damage*, pp. 2503–2516. Springer International Publishing, 2020.

[20] D. Hull and D. Bacon, *Introduction to Dislocations*. Oxford: Butterworth-Heinemann, 5 ed., 2011.

[21] D. R. Mason, X. Yi, M. A. Kirk, and S. L. Dudarev, "Elastic trapping of dislocation loops in cascades in ion-irradiated tungsten foils," *Journal of Physics Condensed Matter*, vol. 26, no. 37, p. 375701, 2014.

[22] N. W. Phillips, H. Yu, S. Das, D. Yang, K. Mizohata, W. Liu, R. Xu, R. J. Harder, and F. Hofmann, "Nanoscale lattice strains in self-ion implanted tungsten," *Acta Materialia*, vol. 195, pp. 219–228, 2020.

[23] H. Yu, X. Yi, and F. Hofmann, "3D reconstruction of the spatial distribution of dislocation loops using an automated stereo-imaging approach," *Ultramicroscopy*, vol. 195, pp. 58–68, 2018.

[24] B. Basnar, A. Lugstein, H. Wanzenboeck, H. Langfischer, E. Bertagnolli, and E. Gornik, "Focused ion beam induced surface amorphization and sputter pro-

cesses," *Journal of Vacuum Science & Technology B: Microelectronics and Nanometer Structures*, vol. 21, no. 3, p. 927, 2003.

[25] S. Rubanov and P. R. Munroe, "FIB-induced damage in silicon," *Journal of Microscopy*, vol. 214, no. 3, pp. 213–221, 2004.

[26] D. Kiener, C. Motz, M. Rester, M. Jenko, and G. Dehm, "FIB damage of Cu and possible consequences for miniaturized mechanical tests," *Materials Science and Engineering A*, vol. 459, no. 1-2, pp. 262–272, 2007.

[27] C. Lou, J. Yu, L. Liu, Y. Ren, and X. Zhang, "{1 0 -1 2} twin nucleation induced by FIB micro-stress in magnesium single crystal," *Materials Letters*, vol. 210, pp. 139–142, 2018.

[28] R. P. Babu, S. Irukuvarghula, A. Harte, and M. Preuss, "Nature of gallium focused ion beam induced phase transformation in 316L austenitic stainless steel," *Acta Materialia*, vol. 120, pp. 391–402, 2016.

[29] F. Hofmann, R. J. Harder, W. Liu, Y. Liu, I. K. Robinson, and Y. Zayachuk, "Glancing-incidence focussed ion beam milling: A coherent X-ray diffraction study of 3D nano-scale lattice strains and crystal defects," *Acta Materialia*, vol. 154, pp. 113–123, 2018.

[30] F. Hofmann, N. W. Phillips, S. Das, P. Karamched, G. M. Hughes, J. O. Douglas, W. Cha, and W. Liu, "Nanoscale imaging of the full strain tensor of specific dislocations extracted from a bulk sample," *Physical Review Materials*, vol. 4, no. 1, p. 013801, 2020.

[31] J. Miao, T. Ishikawa, I. K. Robinson, and M. M. Murnane, "Beyond crystallography: Diffractive imaging using coherent X-ray light sources," *Science*, vol. 348, no. 6234, pp. 530–535, 2015.

[32] G. A. Chahine, M. I. Richard, R. A. Homs-Regojo, T. N. Tran-Caliste, D. Carbone, V. L. R. Jaques, R. Grifone, P. Boesecke, J. Katzer, I. Costina, H. Djazouli, T. Schroeder, and T. U. Schülli, "Imaging of strain and lattice orientation by quick scanning X-ray microscopy combined with three-dimensional reciprocal space mapping," *Journal of Applied Crystallography*, vol. 47, no. 2, pp. 762–769, 2014.

[33] H. Simons, A. King, W. Ludwig, C. Detlefs, W. Pantleon, S. Schmidt, F. Stöhr, I. Snigireva, A. Snigirev, and H. F. Poulsen, "Dark-field X-ray microscopy for multiscale structural characterization," *Nature Communications*, vol. 6, no. 1, p. 6098, 2015.

[34] B. C. Larson, W. Yang, G. E. Ice, J. D. Budai, and J. Z. Tischler, "Three-dimensional X-ray structural microscopy with submicrometre resolution," *Nature*, vol. 415, no. 6874, pp. 887–890, 2002.

[35] Y. H. Lo, L. Zhao, M. Gallagher-Jones, A. Rana, J. Lodico, W. Xiao, B. C. Regan, and J. Miao, "In situ coherent diffractive imaging," *Nature Communications*, vol. 9, no. 1, p. 1826, 2018.

[36] X. Huang, H. Miao, J. Steinbrener, J. Nelson, D. Shapiro, A. Stewart, J. Turner, and C. Jacobsen, "Signal-to-noise and radiation exposure considerations in conventional and diffraction x-ray microscopy," *Optics Express*, vol. 17, no. 16, p. 13541, 2009.

[37] D. Sayre, "Some implications of a theorem due to Shannon," *Acta Crystallographica*, vol. 5, p. 843, 1952.

[38] R. W. Gerchberg and W. O. Saxton, "A Practical Algorithm for the Determination of Phase from Image and Diffraction Plane Pictures," *Optik*, vol. 35, no. 2, pp. 237–246, 1972.

[39] J. R. Fienup, “Reconstruction of an object from the modulus of its Fourier transform,” *Optics Letters*, vol. 3, no. 1, pp. 27–29, 1978.

[40] J. R. Fienup, “Phase retrieval algorithms: a comparison,” *Applied Optics*, vol. 21, no. 15, pp. 2758–2769, 1982.

[41] J. Miao, P. Charalambous, J. Kirz, and D. Sayre, “Extending themethodology of X-ray crystallography to allow imaging of micrometre-sized non-crystalline specimens,” *Nature*, vol. 400, no. July, pp. 342–344, 1999.

[42] S. Maddali, I. Calvo-Almazan, J. Almer, P. Kenesei, J. S. Park, R. Harder, Y. Nashed, and S. O. Hruszkewycz, “Sparse recovery of undersampled intensity patterns for coherent diffraction imaging at high X-ray energies,” *Scientific Reports*, vol. 8, no. 1, p. 4959, 2018.

[43] D. Yang, N. W. Phillips, and F. Hofmann, “Mapping data between sample and detector conjugated spaces in Bragg coherent diffraction imaging,” *Journal of Synchrotron Radiation*, vol. 26, no. 6, pp. 2055–2063, 2019.

[44] S. Maddali, P. Li, A. Pateras, D. Timbie, N. Delegan, A. L. Crook, H. Lee, I. Calvo-Almazan, D. Sheyfer, W. Cha, F. J. Heremans, D. D. Awschalom, V. Chamard, M. Allain, and S. O. Hruszkewycz, “General approaches for shear-correcting coordinate transformations in Bragg coherent diffraction imaging. Part I,” *Journal of Applied Crystallography*, vol. 53, no. 2, pp. 393–403, 2020.

[45] P. Li, S. Maddali, A. Pateras, I. Calvo-Almazan, S. O. Hruszkewycz, V. Chamard, and M. Allain, “General approaches for shear-correcting coordinate transformations in Bragg coherent diffraction imaging. Part II,” *Journal of Applied Crystallography*, vol. 53, no. 2, pp. 404–418, 2020.

[46] Y. Takahashi, A. Suzuki, S. Furutaku, K. Yamauchi, Y. Kohmura, and T. Ishikawa, “Bragg x-ray ptychography of a silicon crystal: Visualization of the dislocation

strain field and the production of a vortex beam," *Physical Review B - Condensed Matter and Materials Physics*, vol. 87, no. 12, p. 121201, 2013.

[47] F. Hofmann, E. Tarleton, R. J. Harder, N. W. Phillips, P.-W. Ma, J. N. Clark, I. K. Robinson, B. Abbey, W. Liu, and C. E. Beck, "3D lattice distortions and defect structures in ion-implanted nano-crystals," *Scientific Reports*, vol. 7, no. 1, p. 45993, 2017.

[48] D. Yang, N. W. Phillips, K. Song, R. J. Harder, W. Cha, and F. Hofmann, "Annealing of focused ion beam damage in gold microcrystals: An in situ Bragg coherent X-ray diffraction imaging study," *Journal of Synchrotron Radiation*, vol. 28, no. 2, pp. 550–565, 2021.

[49] D. Yang, N. W. Phillips, K. Song, C. Barker, R. J. Harder, W. Cha, W. Liu, and F. Hofmann, "In situ Bragg coherent X-ray diffraction imaging of corrosion in a Co–Fe alloy microcrystal," *CrystEngComm*, vol. 24, no. 7, pp. 1334–1343, 2022.

[50] M. C. Newton, S. J. Leake, R. Harder, and I. K. Robinson, "Three-dimensional imaging of strain in a single ZnO nanorod," *Nature Materials*, vol. 9, no. 2, pp. 120–124, 2010.

[51] I. Robinson and R. Harder, "Coherent X-ray diffraction imaging of strain at the nanoscale," *Nature Materials*, vol. 8, no. 4, pp. 291–298, 2009.

[52] R. A. Vicente, I. T. Neckel, S. K. R. S. Sankaranarayanan, J. Solla-Gullón, and P. S. Fernández, "Bragg Coherent Diffraction Imaging for in Situ Studies in Electrocatalysis," *ACS Nano*, vol. 15, no. 4, pp. 6129–6146, 2021.

[53] T. W. Cornelius and O. Thomas, "Progress of in situ synchrotron X-ray diffraction studies on the mechanical behavior of materials at small scales," *Progress in Materials Science*, vol. 94, pp. 384–434, 2018.

[54] A. Ulvestad, K. Sasikumar, J. W. Kim, R. Harder, E. Maxey, J. N. Clark, B. Narayanan, S. A. Deshmukh, N. Ferrier, P. Mulvaney, S. K. Sankaranarayanan, and O. G. Shpyrko, "In Situ 3D Imaging of Catalysis Induced Strain in Gold Nanoparticles," *Journal of Physical Chemistry Letters*, vol. 7, no. 15, pp. 3008–3013, 2016.

[55] S. O. Hruszkewycz, W. Cha, P. Andrich, C. P. Anderson, A. Ulvestad, R. Harder, P. H. Fuoss, D. D. Awschalom, and F. J. Heremans, "In situ study of annealing-induced strain relaxation in diamond nanoparticles using Bragg coherent diffraction imaging," *APL Materials*, vol. 5, no. 2, p. 026105, 2017.

[56] A. K. C. Estandarte, C. M. Lynch, M. Monteforte, J. Rawle, C. Nicklin, and I. Robinson, "Bragg coherent diffraction imaging of iron diffusion into gold nanocrystals," *New Journal of Physics*, vol. 20, no. 11, p. 113026, 2018.

[57] F. Hofmann, N. W. Phillips, R. J. Harder, W. Liu, J. N. Clark, I. K. Robinson, and B. Abbey, "Micro-beam Laue alignment of multi-reflection Bragg coherent diffraction imaging measurements," *Journal of Synchrotron Radiation*, vol. 24, no. 5, pp. 1048–1055, 2017.

[58] S. Choi, M. Chung, D. Kim, S. Kim, K. Yun, W. Cha, R. Harder, T. Kawaguchi, Y. Liu, A. Ulvestad, H. You, M. K. Song, and H. Kim, "In Situ Strain Evolution on Pt Nanoparticles during Hydrogen Peroxide Decomposition," *Nano Letters*, vol. 20, no. 12, pp. 8541–8548, 2020.

[59] T. A. Assefa, A. F. Suzana, L. Wu, R. J. Koch, L. Li, W. Cha, R. J. Harder, E. S. Bozin, F. Wang, and I. K. Robinson, "Imaging the Phase Transformation in Single Particles of the Lithium Titanate Anode for Lithium-Ion Batteries," *ACS Applied Energy Materials*, vol. 2021, pp. 111–118, 2021.

[60] D. Yang, M. T. Lapington, G. He, K. Song, M. Zhang, C. Barker, R. J. Harder, W. Cha, W. Liu, N. W. Phillips, and F. Hofmann, "Refinements for Bragg coherent

X-ray diffraction imaging: Electron backscatter diffraction alignment and strain field computation," *Journal of Applied Crystallography*, vol. 55, pp. 1184–1195, 2022.

[61] W. K. Röntgen, "A New Form of Radiation," *Science*, vol. 3, no. 72, pp. 726–729, 1896.

[62] J. Als-Nielsen and D. McMorrow, *Elements of modern X-ray physics*. Oxford: Wiley-Blackwell, 2nd ed. ed., 2011.

[63] L. Li, Y. Xie, E. Maxey, and R. Harder, "Methods for operando coherent X-ray diffraction of battery materials at the Advanced Photon Source," *Journal of Synchrotron Radiation*, vol. 26, no. 1, pp. 220–229, 2019.

[64] P. Kirkpatrick and A. V. Baez, "Formation of optical images by X-rays," *Journal of the Optical Society of America*, vol. 38, no. 9, pp. 766–774, 1948.

[65] A. Authier, *Dynamical Theory of X-Ray Diffraction*. Oxford: Oxford University Press, 2003.

[66] M. Born, E. Wolf, A. B. Bhatia, P. C. Clemmow, D. Gabor, A. R. Stokes, A. M. Taylor, P. A. Wayman, and W. L. Wilcock, *Principles of Optics*. Cambridge: Cambridge University Press, 1999.

[67] W. Friedrich, P. Knipping, and M. Laue, "Interferenzerscheinungen bei Röntgenstrahlen," *Annalen der Physik*, vol. 346, no. 10, pp. 971–988, 1913.

[68] W. H. Bragg and W. L. Bragg, "The reflection of X-rays by crystals," *Proceedings of the Royal Society of London. Series A, Containing Papers of a Mathematical and Physical Character*, vol. 88, pp. 428–438, 1913.

[69] W. L. Bragg, "The structure of some crystals as indicated by their diffraction of X-rays," *Proceedings of the Royal Society of London. Series A, Containing Papers of a Mathematical and Physical Character*, vol. 89, no. 610, pp. 248–277, 1913.

[70] I. A. Vartanyants and O. M. Yefanov, "Coherent X-ray Diffraction Imaging of Nanostructures," *arXiv*, pp. 1–51, 2013.

[71] S. J. Leake, M. C. Newton, R. Harder, and I. K. Robinson, "Longitudinal coherence function in X-ray imaging of crystals," *Optics Express*, vol. 17, no. 18, p. 15853, 2009.

[72] G. J. Williams, H. M. Quiney, A. G. Peele, and K. A. Nugent, "Coherent diffractive imaging and partial coherence," *Physical Review B - Condensed Matter and Materials Physics*, vol. 75, no. 10, p. 104102, 2007.

[73] I. A. Vartanyants and A. Singer, "Coherence properties of hard x-ray synchrotron sources and x-ray free-electron lasers," *New Journal of Physics*, vol. 12, p. 35004, 2010.

[74] X. Huang, R. Harder, S. Leake, J. Clark, and I. Robinson, "Three-dimensional Bragg coherent diffraction imaging of an extended ZnO crystal," *Journal of Applied Crystallography*, vol. 45, no. 4, pp. 778–784, 2012.

[75] K. A. Nugent, "Coherent methods in the X-ray sciences," *Advances in Physics*, vol. 59, no. 1, pp. 1–99, 2010.

[76] A. Schell, "A technique for the determination of the radiation pattern of a partially coherent aperture," *IEEE Transactions on Antennas and Propagation*, vol. 15, no. 1, pp. 187–188, 1967.

[77] I. A. Vartanyants and I. K. Robinson, "Partial coherence effects on the imaging of small crystals using coherent x-ray diffraction," *Journal of Physics Condensed Matter*, vol. 13, no. 47, pp. 10593–10611, 2001.

[78] E. Wolf, "A macroscopic theory of interference and diffraction of light from finite sources II. Fields with a spectral range of arbitrary width," *Proceedings of the*

Royal Society of London. Series A, Mathematical and Physical Sciences, vol. 230, no. 1181, pp. 246–265, 1955.

[79] L. Mandel and E. Wolf, *Optical coherence and quantum optics*. Cambridge: Cambridge University Press, 1995.

[80] P. P. Ewald, "Introduction to the dynamical theory of X-ray diffraction," *Acta Crystallographica Section A*, vol. 25, no. 1, pp. 103–108, 1969.

[81] W. Cha, A. Ulvestad, M. Allain, V. Chamard, R. Harder, S. J. Leake, J. Maser, P. H. Fuoss, and S. O. Hruszkewycz, "Three Dimensional Variable-Wavelength X-Ray Bragg Coherent Diffraction Imaging," *Physical Review Letters*, vol. 117, no. 22, p. 225501, 2016.

[82] S. Marchesini, "Phase retrieval and saddle-point optimization," *J. Opt. Soc. Am. A*, vol. 24, no. 10, pp. 3289–3296, 2007.

[83] C. E. Shannon, "Communication in the Presence of Noise," *Proceedings of the IRE*, vol. 37, no. 1, pp. 10–21, 1949.

[84] J. Miao and D. Sayre, "On possible extensions of X-ray crystallography through diffraction-pattern oversampling," *Acta Crystallographica Section A: Foundations of Crystallography*, vol. 56, no. 6, pp. 596–605, 2000.

[85] J. Miao, D. Sayre, and H. N. Chapman, "Phase retrieval from the magnitude of the Fourier transforms of nonperiodic objects," *Journal of the Optical Society of America A*, vol. 15, no. 6, pp. 1662–1669, 1998.

[86] G. J. Williams, H. M. Quiney, B. B. Dhal, C. Q. Tran, K. A. Nugent, A. G. Peele, D. Paterson, and M. D. de Jonge, "Fresnel coherent diffractive imaging," *Physical Review Letters*, vol. 97, no. 2, p. 025506, 2006.

[87] B. Abbey, K. A. Nugent, G. J. Williams, J. N. Clark, A. G. Peele, M. A. Pfeifer, M. de Jonge, and I. McNulty, "Keyhole coherent diffractive imaging," *Nature Physics*, vol. 4, no. 5, pp. 394–398, 2008.

[88] J. M. Rodenburg, A. C. Hurst, A. G. Cullis, B. R. Dobson, F. Pfeiffer, O. Bunk, C. David, K. Jefimovs, and I. Johnson, "Hard-X-ray lensless imaging of extended objects," *Physical Review Letters*, vol. 98, no. 3, p. 034801, 2007.

[89] S. Marchesini, H. He, N. Chapman, P. Hau-Riege, A. Noy, R. Howells, U. Weierstall, and H. Spence, "X-ray image reconstruction from a diffraction pattern alone," *Physical Review B - Condensed Matter and Materials Physics*, vol. 68, no. 14, p. 140101, 2003.

[90] J. R. Fienup and C. C. Wackerman, "Phase-retrieval stagnation problems and solutions," *Journal of the Optical Society of America A*, vol. 3, no. 11, pp. 1897–1907, 1986.

[91] X. Huang, J. Nelson, J. Steinbrener, J. Kirz, J. J. Turner, and C. Jacobsen, "Incorrect support and missing center tolerances of phasing algorithms," *Optics Express*, vol. 18, no. 25, pp. 26441–26449, 2010.

[92] A. Ulvestad, Y. Nashed, G. Beutier, M. Verdier, S. O. Hruszkewycz, and M. Dupraz, "Identifying Defects with Guided Algorithms in Bragg Coherent Diffractive Imaging," *Scientific Reports*, vol. 7, no. 1, p. 9920, 2017.

[93] C. C. Chen, J. Miao, C. W. Wang, and T. K. Lee, "Application of optimization technique to noncrystalline x-ray diffraction microscopy: Guided hybrid input-output method," *Physical Review B - Condensed Matter and Materials Physics*, vol. 76, no. 6, p. 064113, 2007.

[94] A. Ulvestad, A. Tripathi, S. O. Hruszkewycz, W. Cha, S. M. Wild, G. B. Stephenson, and P. H. Fuoss, "Coherent diffractive imaging of time-evolving samples with

improved temporal resolution," *Physical Review B*, vol. 93, no. 18, p. 184105, 2016.

[95] J. N. Clark, J. Ihli, A. S. Schenk, Y. Y. Kim, A. N. Kulak, J. M. Campbell, G. Nisbet, F. C. Meldrum, and I. K. Robinson, "Three-dimensional imaging of dislocation propagation during crystal growth and dissolution," *Nature Materials*, vol. 14, no. 8, pp. 780–784, 2015.

[96] G. K. Williamson and W. H. Hall, "X-ray line broadening from filed aluminium and wolfram," *Acta Metallurgica*, vol. 1, no. 1, pp. 22–31, 1953.

[97] G. Xiong, O. Moutanabbir, M. Reiche, R. Harder, and I. Robinson, "Coherent X-ray diffraction imaging and characterization of strain in silicon-on-insulator nanostructures," *Advanced Materials*, vol. 26, no. 46, pp. 7747–7763, 2014.

[98] J. Carnis, L. Gao, S. Labat, Y. Y. Kim, J. P. Hofmann, S. J. Leake, T. U. Schülli, E. J. M. Hensen, O. Thomas, and M.-I. Richard, "Towards a quantitative determination of strain in Bragg Coherent X-ray Diffraction Imaging: artefacts and sign convention in reconstructions," *Scientific Reports*, vol. 9, no. 1, p. 17357, 2019.

[99] J. Clark, X. Huang, R. Harder, and I. Robinson, "High-resolution three-dimensional partially coherent diffraction imaging," *Nature Communications*, vol. 3, no. 1, p. 993, 2012.

[100] A. Tripathi, O. Shpyrko, and I. McNulty, "Influence of noise and missing data on reconstruction quality in coherent X-ray diffractive imaging," *AIP Conference Proceedings*, vol. 1365, pp. 305–308, 2011.

[101] V. Favre-Nicolin, S. Leake, and Y. Chushkin, "Free log-likelihood as an unbiased metric for coherent diffraction imaging," *Scientific Reports*, vol. 10, no. 1, p. 2664, 2020.

[102] P. Thibault and M. Guizar-Sicairos, "Maximum-likelihood refinement for coherent diffractive imaging," *New Journal of Physics*, vol. 14, no. 6, p. 063004, 2012.

[103] M. J. Wilkin, S. Maddali, S. O. Hruszkewycz, A. Pateras, R. L. Sandberg, R. Harder, W. Cha, R. M. Suter, and A. D. Rollett, "Experimental demonstration of coupled multi-peak Bragg coherent diffraction imaging with genetic algorithms," *Physical Review B*, vol. 103, no. 21, p. 214103, 2021.

[104] Y. Gao, X. Huang, H. Yan, and G. J. Williams, "Bragg coherent diffraction imaging by simultaneous reconstruction of multiple diffraction peaks," *Physical Review B*, vol. 103, no. 1, p. 14102, 2021.

[105] M. J. Cherukara, W. Cha, and R. J. Harder, "Anisotropic nano-scale resolution in 3D Bragg coherent diffraction imaging," *Applied Physics Letters*, vol. 113, no. 20, p. 203101, 2018.

[106] H. N. Chapman, A. Barty, S. Marchesini, A. Noy, S. P. Hau-Riege, C. Cui, M. R. Howells, R. Rosen, H. He, J. C. H. Spence, U. Weierstall, T. Beetz, C. Jacobsen, and D. Shapiro, "High-resolution ab initio three-dimensional x-ray diffraction microscopy," *Journal of the Optical Society of America A*, vol. 23, no. 5, pp. 1179–1200, 2006.

[107] D. Dzhigaev, A. Shabalin, T. Stankevič, U. Lorenz, R. P. Kurta, F. Seiboth, J. Wallentin, A. Singer, S. Lazarev, O. M. Yefanov, M. Borgström, M. N. Strikhanov, L. Samuelson, G. Falkenberg, C. G. Schroer, A. Mikkelsen, R. Feidenhans'L, and I. A. Vartanyants, "Bragg coherent x-ray diffractive imaging of a single indium phosphide nanowire," *Journal of Optics*, vol. 18, no. 6, p. 064007, 2016.

[108] M. van Heel and G. Harauz, "Exact filters for general geometry three dimensional reconstruction," *Optik*, vol. 78, no. 4, pp. 146–156, 1986.

[109] M. Van Heel and M. Schatz, "Fourier shell correlation threshold criteria," *Journal of Structural Biology*, vol. 151, no. 3, pp. 250–262, 2005.

[110] V. Elser, "Phase retrieval by iterated projections," *Journal of the Optical Society of America A*, vol. 20, no. 1, pp. 40–55, 2003.

[111] E. J. Candès, Y. C. Eldar, T. Strohmer, and V. Voroninski, "Phase Retrieval via Matrix Completion," *SIAM Review*, vol. 57, no. 2, pp. 225–251, 2015.

[112] G. Oszlányi and A. Sütó, "The charge flipping algorithm," *Acta Crystallographica Section A: Foundations of Crystallography*, vol. 64, no. 1, pp. 123–134, 2008.

[113] D. R. Luke, "Relaxed averaged alternating reflections for diffraction imaging," *Inverse Problems*, vol. 21, no. 1, pp. 37–50, 2005.

[114] Y. Shechtman, Y. C. Eldar, O. Cohen, H. N. Chapman, J. Miao, and M. Segev, "Phase Retrieval with Application to Optical Imaging: A contemporary overview," *IEEE Signal Processing Magazine*, vol. 32, no. 3, pp. 87–109, 2015.

[115] M. C. Newton, R. Harder, X. Huang, G. Xiong, and I. K. Robinson, "Phase retrieval of diffraction from highly strained crystals," *Physical Review B*, vol. 82, no. 16, p. 165436, 2010.

[116] X. Huang, R. Harder, G. Xiong, X. Shi, and I. Robinson, "Propagation uniqueness in three-dimensional coherent diffractive imaging," *Physical Review B*, vol. 83, no. 22, p. 224109, 2011.

[117] D. Dzhigaev, Z. Zhang, L. A. Mar al, S. Sala, A. Björling, A. Mikkelsen, and J. Wallentin, "Three-dimensional coherent x-ray diffraction imaging of ferroelastic domains in single $CsPbBr_3$ perovskite nanoparticles," *New Journal of Physics*, vol. 23, no. 6, p. 063035, 2021.

[118] L. B. Lucy, "An iterative technique for the rectification of observed distributions," *The Astronomical Journal*, vol. 79, no. 6, p. 745, 1974.

[119] W. H. Richardson, "Bayesian-Based Iterative Method of Image Restoration," *Journal of the Optical Society of America*, vol. 62, no. 1, pp. 55–59, 1972.

[120] M. C. Newton, "Concurrent Phase Retrieval for Imaging Strain in Nanocrystals," *Physical Review B*, vol. 102, no. 1, p. 14104, 2020.

[121] Z. Wang, O. Gorobtsov, and A. Singer, "An algorithm for Bragg coherent x-ray diffractive imaging of highly strained nanocrystals," *New Journal of Physics*, vol. 22, no. 1, p. 013021, 2020.

[122] P. Godard, M. Allain, V. Chamard, and J. Rodenburg, "Noise models for low counting rate coherent diffraction imaging," *Optics Express*, vol. 20, no. 23, p. 25914, 2012.

[123] S. Maddali, M. Allain, W. Cha, R. Harder, J. S. Park, P. Kenesei, J. Almer, Y. Nashed, and S. O. Hruszkewycz, "Phase retrieval for Bragg coherent diffraction imaging at high x-ray energies," *Physical Review A*, vol. 99, no. 5, p. 53838, 2019.

[124] S. Maddali, J. S. Park, H. Sharma, S. Shastri, P. Kenesei, J. Almer, R. Harder, M. J. Highland, Y. Nashed, and S. O. Hruszkewycz, "High-energy coherent x-ray diffraction microscopy of polycrystal grains: Steps toward a multiscale approach," *Physical Review Applied*, vol. 14, no. 2, p. 24085, 2020.

[125] S. J. Leake, V. Favre-Nicolin, E. Zatterin, M. I. Richard, S. Fernandez, G. Chahine, T. Zhou, P. Boesecke, H. Djazouli, and T. U. Schülli, "Coherent nanoscale X-ray probe for crystal interrogation at ID01, ESRF – The European Synchrotron," *Materials and Design*, vol. 119, pp. 470–471, 2017.

[126] M. J. Cherukara, Y. S. Nashed, and R. J. Harder, "Real-time coherent diffraction inversion using deep generative networks," *Scientific Reports*, vol. 8, no. 1, p. 16520, 2018.

[127] L. Wu, P. Juhas, S. Yoo, and I. Robinson, "Complex imaging of phase domains by deep neural networks," *IUCrJ*, vol. 8, no. 1, pp. 12–21, 2021.

[128] L. Wu, S. Yoo, A. F. Suzana, T. A. Assefa, J. Diao, R. J. Harder, W. Cha, and I. K. Robinson, "Three-dimensional coherent X-ray diffraction imaging via deep convolutional neural networks," *npj Computational Materials*, vol. 7, no. 1, p. 175, 2021.

[129] A. Scheinker and R. Pokharel, "Adaptive 3D convolutional neural network-based reconstruction method for 3D coherent diffraction imaging," *Journal of Applied Physics*, vol. 128, p. 184901, 2020.

[130] B. Lim, E. Bellec, M. Dupraz, S. Leake, A. Resta, A. Coati, M. Sprung, E. Almog, E. Rabkin, T. Schulli, and M. I. Richard, "A convolutional neural network for defect classification in Bragg coherent X-ray diffraction," *npj Computational Materials*, vol. 7, no. 1, p. 115, 2021.

[131] H. Chan, Y. S. Nashed, S. Kandel, S. O. Hruszkewycz, S. K. Sankaranarayanan, R. J. Harder, and M. J. Cherukara, "Rapid 3D nanoscale coherent imaging via physics-aware deep learning," *Applied Physics Reviews*, vol. 8, no. 2, p. 21407, 2021.

[132] A. Constantinescu and A. Korsunsky, *Elasticity with MATHEMATICA®: An introduction to continuum mechanics and linear elasticity*, vol. 9780521842. Cambridge: Cambridge University Press, 2007.

[133] J. Miao, T. Ishikawa, B. Johnson, E. H. Anderson, B. Lai, and K. O. Hodgson, "High resolution 3D X-ray diffraction microscopy," *Physical Review Letters*, vol. 89, no. 8, p. 88303, 2002.

[134] I. K. Robinson, I. A. Vartanyants, G. J. Williams, M. A. Pfeifer, and J. A. Pitney, "Reconstruction of the shapes of gold nanocrystals using coherent x-ray diffraction," *Physical Review Letters*, vol. 87, no. 19, p. 195505, 2001.

[135] D. Gentili, G. Foschi, F. Valle, M. Cavallini, and F. Biscarini, "Applications of dewetting in micro and nanotechnology," *Chemical Society Reviews*, vol. 41, no. 12, pp. 4430–4443, 2012.

[136] G. J. Williams, M. A. Pfeifer, I. A. Vartanyants, and I. K. Robinson, "Three-Dimensional Imaging of Microstructure in Au Nanocrystals," *Physical Review Letters*, vol. 90, no. 17, p. 175501, 2003.

[137] M. A. Pfeifer, G. J. Williams, I. A. Vartanyants, R. Harder, and I. K. Robinson, "Three-dimensional mapping of a deformation field inside a nanocrystal," *Nature*, vol. 442, no. 7098, pp. 63–66, 2006.

[138] D. B. Williams and B. C. Carter, *Transmission Electron Microscopy: A Textbook for Materials Science*. New York: Springer, 2 ed., 2009.

[139] M. I. Richard, S. Fernández, J. Eymery, J. P. Hofmann, L. Gao, J. Carnis, S. Labat, V. Favre-Nicolin, E. J. Hensen, O. Thomas, T. U. Schülli, and S. J. Leake, "Crystallographic orientation of facets and planar defects in functional nanostructures elucidated by nano-focused coherent diffractive X-ray imaging," *Nanoscale*, vol. 10, no. 10, pp. 4833–4840, 2018.

[140] P. Ehrhart, H. Trinkaus, and B. C. Larson, "Diffuse scattering from dislocation loops," *Phys. Rev. B*, vol. 25, no. 2, pp. 834–848, 1982.

[141] A. Pateras, R. Harder, W. Cha, J. G. Gigax, J. K. Baldwin, J. Tischler, R. Xu, W. Liu, M. J. Erdmann, R. Kalt, R. L. Sandberg, S. Fensin, and R. Pokharel, "Combining Laue diffraction with Bragg coherent diffraction imaging at 34-ID-C," *Journal of Synchrotron Radiation*, vol. 27, no. 5, pp. 1430–1437, 2020.

[142] A. Yau, R. J. Harder, M. W. Kanan, and A. Ulvestad, "Imaging the Hydrogen Absorption Dynamics of Individual Grains in Polycrystalline Palladium Thin Films in 3D," *ACS Nano*, vol. 11, no. 11, pp. 10945–10954, 2017.

[143] A. Yau, W. Cha, M. W. Kanan, G. B. Stephenson, and A. Ulvestad, "Bragg coherent diffractive imaging of single-grain defect dynamics in polycrystalline films," *Science*, vol. 356, no. 6339, pp. 739–742, 2017.

[144] N. Vaxelaire, S. Labat, T. W. Cornelius, C. Kirchlechner, J. Keckes, T. Schulli, and O. Thomas, "New insights into single-grain mechanical behavior from temperature-dependent 3-D coherent X-ray diffraction," *Acta Materialia*, vol. 78, pp. 46–55, 2014.

[145] S. O. Hruszkewycz, S. Maddali, C. P. Anderson, W. Cha, K. C. Miao, M. J. Highland, A. Ulvestad, D. D. Awschalom, and F. J. Heremans, "Strain annealing of SiC nanoparticles revealed through Bragg coherent diffraction imaging for quantum technologies," *Physical Review Materials*, vol. 2, no. 8, p. 86001, 2018.

[146] A. Ulvestad, M. J. Welland, S. S. Collins, R. Harder, E. Maxey, J. Wingert, A. Singer, S. Hy, P. Mulvaney, P. Zapol, and O. G. Shpyrko, "Avalanching strain dynamics during the hydriding phase transformation in individual palladium nanoparticles," *Nature Communications*, vol. 6, no. 1, p. 10092, 2015.

[147] D. Karpov, Z. Liu, T. D. S. Rolo, R. Harder, P. V. Balachandran, D. Xue, T. Lookman, and E. Fohtung, "Three-dimensional imaging of vortex structure in a ferroelectric nanoparticle driven by an electric field," *Nature Communications*, vol. 8, no. 1, p. 280, 2017.

[148] J. M. Rodenburg and H. M. Faulkner, "A phase retrieval algorithm for shifting illumination," *Applied Physics Letters*, vol. 85, no. 20, pp. 4795–4797, 2004.

[149] A. M. Maiden and J. M. Rodenburg, "An improved ptychographical phase retrieval algorithm for diffractive imaging," *Ultramicroscopy*, vol. 109, no. 10, pp. 1256–1262, 2009.

[150] P. Godard, G. Carbone, M. Allain, F. Mastropietro, G. Chen, L. Capello, A. Diaz, T. H. Metzger, J. Stangl, and V. Chamard, "Three-dimensional high-resolution

quantitative microscopy of extended crystals," *Nature Communications*, vol. 2, no. 1, p. 568, 2011.

[151] A. I. Pateras, M. Allain, P. Godard, L. Largeau, G. Patriarche, A. Talneau, K. Pantzas, M. Burghammer, A. A. Minkevich, and V. Chamard, "Nondestructive three-dimensional imaging of crystal strain and rotations in an extended bonded semiconductor heterostructure," *Physical Review B - Condensed Matter and Materials Physics*, vol. 92, no. 20, p. 205305, 2015.

[152] P. Li, N. W. Phillips, S. Leake, M. Allain, F. Hofmann, and V. Chamard, "Revealing nano-scale lattice distortions in implanted material with 3D Bragg ptychography," *Nature Communications*, vol. 12, no. 1, p. 7059, 2021.

[153] M. Dupraz, G. Beutier, T. W. Cornelius, G. Parry, Z. Ren, S. Labat, M. I. Richard, G. A. Chahine, O. Kovalenko, M. De Boissieu, E. Rabkin, M. Verdier, and O. Thomas, "3D Imaging of a Dislocation Loop at the Onset of Plasticity in an Indented Nanocrystal," *Nano Letters*, vol. 17, no. 11, pp. 6696–6701, 2017.

[154] W. Yang, X. Huang, R. Harder, J. N. Clark, I. K. Robinson, and H. K. Mao, "Coherent diffraction imaging of nanoscale strain evolution in a single crystal under high pressure," *Nature Communications*, vol. 4, no. 1, p. 1680, 2013.

[155] A. Singer, M. Zhang, S. Hy, D. Cela, C. Fang, T. A. Wynn, B. Qiu, Y. Xia, Z. Liu, A. Ulvestad, N. Hua, J. Wingert, H. Liu, M. Sprung, A. V. Zozulya, E. Maxey, R. Harder, Y. S. Meng, and O. G. Shpyrko, "Nucleation of dislocations and their dynamics in layered oxide cathode materials during battery charging," *Nature Energy*, vol. 3, no. 8, pp. 641–647, 2018.

[156] A. Ulvestad, A. Singer, J. N. Clark, H. M. Cho, J. W. Kim, R. Harder, J. Maser, Y. S. Meng, and O. G. Shpyrko, "Topological defect dynamics in operando battery nanoparticles," *Science*, vol. 348, no. 6241, pp. 1344–1347, 2015.

[157] A. Ulvestad, A. Singer, H. M. Cho, J. N. Clark, R. Harder, J. Maser, Y. S. Meng, and O. G. Shpyrko, "Single particle nanomechanics in operando batteries via lensless strain mapping," *Nano Letters*, vol. 14, no. 9, pp. 5123–5127, 2014.

[158] A. Ulvestad, J. N. Clark, A. Singer, D. Vine, H. M. Cho, R. Harder, Y. S. Meng, and O. G. Shpyrko, "In situ strain evolution during a disconnection event in a battery nanoparticle," *Physical Chemistry Chemical Physics*, vol. 17, no. 16, pp. 10551–10555, 2015.

[159] J. Diao, X. Shi, T. A. Assefa, L. Wu, A. F. Suzana, D. S. Nunes, D. Batey, S. Cipiccia, C. Rau, R. J. Harder, W. Cha, and I. K. Robinson, "Evolution of ferroelastic domain walls during phase transitions in barium titanate nanoparticles," *Physical Review Materials*, vol. 4, no. 10, p. 106001, 2020.

[160] D. Kim, M. Chung, S. Kim, K. Yun, W. Cha, R. Harder, and H. Kim, "Defect Dynamics at a Single Pt Nanoparticle during Catalytic Oxidation," *Nano Letters*, vol. 19, no. 8, pp. 5044–5052, 2019.

[161] T. Kawaguchi, V. Komanicky, V. Latyshev, W. Cha, E. R. Maxey, R. Harder, T. Ichitsubo, and H. You, "Electrochemically Induced Strain Evolution in Pt-Ni Alloy Nanoparticles Observed by Bragg Coherent Diffraction Imaging," *Nano Letters*, vol. 21, no. 14, pp. 5945–5951, 2021.

[162] W. Cha, Y. Liu, H. You, G. B. Stephenson, and A. Ulvestad, "Dealloying in Individual Nanoparticles and Thin Film Grains: A Bragg Coherent Diffractive Imaging Study," *Advanced Functional Materials*, vol. 27, no. 25, p. 1700331, 2017.

[163] N. Li, M. Dupraz, L. Wu, S. J. Leake, A. Resta, J. Carnis, S. Labat, E. Almog, E. Rabkin, V. Favre-Nicolin, F. E. Picca, F. Berenguer, R. van de Poll, J. P. Hofmann, A. Vlad, O. Thomas, Y. Garreau, A. Coati, and M. I. Richard, "Continuous scanning for Bragg coherent X-ray imaging," *Scientific Reports*, vol. 10, no. 1, p. 12760, 2020.

[164] P. Emma, R. Akre, J. Arthur, R. Bionta, C. Bostedt, J. Bozek, A. Brachmann, P. Bucksbaum, R. Coffee, F. J. Decker, Y. Ding, D. Dowell, S. Edstrom, A. Fisher, J. Frisch, S. Gilevich, J. Hastings, G. Hays, P. Hering, Z. Huang, R. Iverson, H. Loos, M. Messerschmidt, A. Miahnahri, S. Moeller, H. D. Nuhn, G. Pile, D. Ratner, J. Rzepiela, D. Schultz, T. Smith, P. Stefan, H. Tompkins, J. Turner, J. Welch, W. White, J. Wu, G. Yocky, and J. Galayda, "First lasing and operation of an ångstrom-wavelength free-electron laser," *Nature Photonics*, vol. 4, no. 9, pp. 641–647, 2010.

[165] J. N. Clark, L. Beitra, G. Xiong, A. Higginbotham, D. M. Fritz, H. T. Lemke, D. Zhu, M. Chollet, G. J. Williams, M. Messerschmidt, B. Abbey, R. J. Harder, A. M. Korsunsky, J. S. Wark, and I. K. Robinson, "Ultrafast three-dimensional imaging of lattice dynamics in individual gold nanocrystals," *Science*, vol. 341, no. 6141, pp. 56–59, 2013.

[166] A. Ulvestad, M. J. Cherukara, R. Harder, W. Cha, I. K. Robinson, S. Soog, S. Nelson, D. Zhu, G. B. Stephenson, O. Heinonen, and A. Jokisaari, "Bragg Coherent Diffractive Imaging of Zinc Oxide Acoustic Phonons at Picosecond Timescales," *Scientific reports*, vol. 7, no. 1, p. 9823, 2017.

[167] J. N. Clark, L. Beitra, G. Xiong, D. M. Fritz, H. T. Lemke, D. Zhu, M. Chollet, G. J. Williams, M. M. Messerschmidt, B. Abbey, R. J. Harder, A. M. Korsunsky, J. S. Wark, D. A. Reis, and I. K. Robinson, "Imaging transient melting of a nanocrystal using an X-ray laser," *Proceedings of the National Academy of Sciences of the United States of America*, vol. 112, no. 24, pp. 7444–7448, 2015.

[168] R. H. Bates, "Fourier phase problems are uniquely solvable in more than one dimension. I: Underlying theory," *Optik*, vol. 61, no. 3, pp. 247–262, 1982.

[169] J. Carnis, A. R. Kshirsagar, L. Wu, M. Dupraz, S. Labat, M. Texier, L. Favre, L. Gao, F. E. Oropeza, N. Gazit, E. Almog, A. Campos, J.-S. Micha, E. J. M.

Hensen, S. J. Leake, T. U. Schülli, E. Rabkin, O. Thomas, R. Poloni, J. P. Hofmann, and M.-I. Richard, "Twin boundary migration in an individual platinum nanocrystal during catalytic CO oxidation," *Nature Communications*, vol. 12, no. 1, p. 5385, 2021.

[170] K. Yuan, S. S. Lee, W. Cha, A. Ulvestad, H. Kim, B. Abdilla, N. C. Sturchio, and P. Fenter, "Oxidation induced strain and defects in magnetite crystals," *Nature Communications*, vol. 10, no. 1, p. 703, 2019.

[171] X. Liu, M. A. Aranda, B. Chen, P. Wang, R. Harder, and I. Robinson, "In Situ Bragg Coherent Diffraction Imaging Study of a Cement Phase Microcrystal during Hydration," *Crystal Growth and Design*, vol. 15, no. 7, pp. 3087–3091, 2015.

[172] S. Lazarev, D. Dzhigaev, Z. Bi, A. Nowzari, Y. Y. Kim, M. Rose, I. A. Zaluzhnyy, O. Y. Gorobtsov, A. V. Zozulya, F. Lenrick, A. Gustafsson, A. Mikkelsen, M. Sprung, L. Samuelson, and I. A. Vartanyants, "Structural Changes in a Single GaN Nanowire under Applied Voltage Bias," *Nano Letters*, vol. 18, no. 9, pp. 5446–5452, 2018.

[173] F. Berenguer, P. Godard, M. Allain, J. M. Belloir, A. Talneau, S. Ravy, and V. Chamard, "X-ray lensless microscopy from undersampled diffraction intensities," *Physical Review B - Condensed Matter and Materials Physics*, vol. 88, no. 14, p. 144101, 2013.

[174] G. Xiong, J. N. Clark, C. Nicklin, J. Rawle, and I. K. Robinson, "Atomic diffusion within individual gold nanocrystal," *Scientific Reports*, vol. 4, no. 1, p. 6765, 2014.

[175] R. Harder, "Deep neural networks in real-time coherent diffraction imaging," *IUCrJ*, vol. 8, no. 1, pp. 1–3, 2021.

[176] A. Richards, "University of Oxford Advanced Research Computing," aug 2015.

[177] M. A. Pfeifer, *Structural studies of lead nanocrystals using coherent X-ray diffraction*. PhD thesis, University of Illinois Urbana-Champaign, 2005.

[178] L. Beitra, M. Watari, T. Matsuura, N. Shimamoto, R. Harder, and I. Robinson, "Confocal microscope alignment of nanocrystals for coherent diffraction imaging," in *AIP Conference Proceedings*, vol. 1234, pp. 57–60, 2010.

[179] A. Ulvestad, J. N. Clark, R. Harder, I. K. Robinson, and O. G. Shpyrko, "3D Imaging of Twin Domain Defects in Gold Nanoparticles," *Nano Letters*, vol. 15, no. 6, pp. 4066–4070, 2015.

[180] B. L. Adams, S. I. Wright, and K. Kunze, "Orientation imaging: The emergence of a new microscopy," *Metallurgical Transactions A*, vol. 24, no. 4, pp. 819–831, 1993.

[181] F. Bachmann, R. Hielscher, and H. Schaeben, "Grain detection from 2d and 3d EBSD data-Specification of the MTEX algorithm," *Ultramicroscopy*, vol. 111, no. 12, pp. 1720–1733, 2011.

[182] D. J. Dingley, "Progressive steps in the development of electron backscatter," *Journal of Microscopy*, vol. 213, no. 3, pp. 214–224, 2004.

[183] H. J. Bunge, *Texture Analysis in Materials Science*. Butterworths, 1 ed., 1982.

[184] T. B. Britton, J. Jiang, Y. Guo, A. Vilalta-Clemente, D. Wallis, L. N. Hansen, A. Winkelmann, and A. J. Wilkinson, "Tutorial: Crystal orientations and EBSD - Or which way is up?," *Materials Characterization*, vol. 117, pp. 113–126, 2016.

[185] W. R. Busing and H. A. Levy, "Angle calculations for 3- and 4-circle X-ray and neutron diffractometers," *Acta Crystallographica*, vol. 22, no. 4, pp. 457–464, 1967.

[186] W. Liu, G. E. Ice, B. C. Larson, W. Yang, J. Z. Tischler, and J. D. Budai, "The Three-Dimensional X-ray Crystal Microscope: A New Tool for Materials Charac-

terization," *Metallurgical and Materials Transactions A*, vol. 35, no. 7, pp. 1963–1967, 2004.

[187] R. D. Evans, *The atomic nucleus*. International series in pure and applied physics, New York ; London: McGraw-Hill, 1955.

[188] M. Guizar-Sicairos, A. Diaz, M. Holler, M. S. Lucas, A. Menzel, R. A. Wepf, and O. Bunk, "Phase tomography from x-ray coherent diffractive imaging projections," *Optics Express*, vol. 19, no. 22, p. 21345, 2011.

[189] N. S. Rajput and X. Luo, "FIB Micro-/Nano-fabrication," in *Micromanufacturing Engineering and Technology: Second Edition*, pp. 61–80, Elsevier Inc., 2015.

[190] H. Bei, S. Shim, M. K. Miller, G. M. Pharr, and E. P. George, "Effects of focused ion beam milling on the nanomechanical behavior of a molybdenum-alloy single crystal," *Applied Physics Letters*, vol. 91, no. 11, p. 111915, 2007.

[191] S. Shim, H. Bei, M. K. Miller, G. M. Pharr, and E. P. George, "Effects of focused ion beam milling on the compressive behavior of directionally solidified micropillars and the nanoindentation response of an electropolished surface," *Acta Materialia*, vol. 57, no. 2, pp. 503–510, 2009.

[192] N. Nan, J. Wang, and A. A. Eckstein, "FIB-SEM Three-Dimensional Tomography for Characterization of Carbon-Based Materials," *Advances in Materials Science and Engineering*, vol. 2019, p. 8680715, 2019.

[193] E. B. Brousseau, S. S. Dimov, and D. T. Pham, "Some recent advances in multi-material micro- and nano-manufacturing," *International Journal of Advanced Manufacturing Technology*, vol. 47, no. 1-4, pp. 161–180, 2010.

[194] J. Hütsch and E. T. Lilleodden, "The influence of focused-ion beam preparation technique on microcompression investigations: Lathe vs. annular milling," *Scripta Materialia*, vol. 77, pp. 49–51, 2014.

[195] A. Ernst, M. Wei, and M. Aindow, "A Comparison of Ga FIB and Xe-Plasma FIB of Complex Al Alloys," *Microscopy and Microanalysis*, vol. 23, no. S1, pp. 288–289, 2017.

[196] L. A. Giannuzzi, R. Geurts, and J. Ringnalda, "2 keV Ga^+ FIB Milling for Reducing Amorphous Damage in Silicon," *Microscopy and Microanalysis*, vol. 11, no. S02, p. 828, 2005.

[197] S. Rubanov and P. R. Munroe, "Investigation of the structure of damage layers in TEM samples prepared using a focused ion beam," *Journal of Materials Science Letters*, vol. 20, no. 13, pp. 1181–1183, 2001.

[198] P. Roediger, H. D. Wanzenboeck, S. Waid, G. Hochleitner, and E. Bertagnolli, "Focused-ion-beam-inflicted surface amorphization and gallium implantation-new insights and removal by focused-electron-beam-induced etching," *Nanotechnology*, vol. 22, no. 23, p. 235302, 2011.

[199] D. Kiener, Z. Zhang, S. Šturm, S. Cazottes, P. J. Imrich, C. Kirchlechner, and G. Dehm, "Advanced nanomechanics in the TEM: Effects of thermal annealing on FIB prepared Cu samples," *Philosophical Magazine*, vol. 92, no. 25-27, pp. 3269–3289, 2012.

[200] S. Lee, J. Jeong, Y. Kim, S. M. Han, D. Kiener, and S. H. Oh, "FIB-induced dislocations in Al submicron pillars: Annihilation by thermal annealing and effects on deformation behavior," *Acta Materialia*, vol. 110, pp. 283–294, 2016.

[201] B. Chen, J. Diao, Q. Luo, J. Rawle, X. Liu, C. Nicklin, J. Shen, and I. Robinson, "In-situ investigation of crystallization and structural evolution of a metallic glass in three dimensions at nano-scale," *Materials and Design*, vol. 190, p. 108551, 2020.

[202] A. F. Suzana, A. Rochet, A. R. Passos, J. P. Castro Zerba, C. C. Polo, C. V. Santilli, S. H. Pulcinelli, F. Berenguer, R. Harder, E. Maxey, and F. Meneau, "In situ

three-dimensional imaging of strain in gold nanocrystals during catalytic oxidation," *Nanoscale Advances*, vol. 1, no. 8, pp. 3009–3014, 2019.

[203] R. Harder and I. K. Robinson, "Coherent X-Ray Diffraction Imaging of Morphology and Strain in Nanomaterials," *JOM*, vol. 65, no. 9, pp. 1202–1207, 2013.

[204] D. Kiener, W. Grosinger, G. Dehm, and R. Pippan, "A further step towards an understanding of size-dependent crystal plasticity: In situ tension experiments of miniaturized single-crystal copper samples," *Acta Materialia*, vol. 56, no. 3, pp. 580–592, 2008.

[205] L. L. Li, Z. J. Zhang, J. Tan, C. B. Jiang, R. T. Qu, P. Zhang, J. B. Yang, and Z. F. Zhang, "Stepwise work hardening induced by individual grain boundary in Cu bicrystal micropillars," *Scientific Reports*, vol. 5, no. 1, p. 15631, 2015.

[206] J. Gong, T. Benjamin Britton, M. A. Cuddihy, F. P. Dunne, and A. J. Wilkinson, "⟨a⟩ Prismatic, ⟨a⟩ basal, and ⟨c+a⟩ slip strengths of commercially pure Zr by micro-cantilever tests," *Acta Materialia*, vol. 96, pp. 249–257, 2015.

[207] M. Guizar-Sicairos, S. T. Thurman, and J. R. Fienup, "Efficient subpixel image registration algorithms," *Optics Letters*, vol. 33, no. 2, pp. 156–158, 2008.

[208] A. M. Howatson, P. G. Lund, and J. D. Todd, *Engineering Tables and Data*. Oxford : Department of Engineering Science, University of Oxford, 2009.

[209] Y. Odarchenko, D. J. Martin, T. Arnold, and A. M. Beale, "CO oxidation over supported gold nanoparticles as revealed by: Operando grazing incidence X-ray scattering analysis," *Faraday Discussions*, vol. 208, no. 0, pp. 243–254, 2018.

[210] J. A. Moulijn, A. E. van Diepen, and F. Kapteijn, "Catalyst deactivation: is it predictable? What to do?," *Applied Catalysis A General*, vol. 212, no. 1-2, pp. 3–16, 2001.

[211] W. Thomson, "LX. On the equilibrium of vapour at a curved surface of liquid," *The London, Edinburgh, and Dublin Philosophical Magazine and Journal of Science*, vol. 42, no. 282, pp. 448–452, 1871.

[212] O. Kovalenko, C. Brandl, L. Klinger, and E. Rabkin, "Self-Healing and Shape Memory Effects in Gold Microparticles through the Defects-Mediated Diffusion," *Advanced Science*, vol. 4, no. 8, p. 1700159, 2017.

[213] J. W. Kim, S. Manna, R. Harder, J. Wingert, E. E. Fullerton, and O. G. Shpyrko, "Bragg coherent diffractive imaging of ferromagnetic nickel nanoparticles," *Journal of Applied Physics*, vol. 123, no. 20, p. 204302, 2018.

[214] O. Kovalenko and E. Rabkin, "Mechano-stimulated equilibration of gold nanoparticles on sapphire," *Scripta Materialia*, vol. 107, pp. 149–152, 2015.

[215] W. L. Winterbottom, "Equilibrium shape of a small particle in contact with a foreign substrate," *Acta Metallurgica*, vol. 15, no. 2, pp. 303–310, 1967.

[216] I. Galanakis, N. Papanikolaou, and P. H. Dederichs, "Applicability of the broken-bond rule to the surface energy of the fcc metals," *Surface Science*, vol. 511, no. 1, pp. 1–12, 2002.

[217] W. W. Mullins and G. S. Rohrer, "Nucleation Barrier for Volume-Conserving Shape Changes of Faceted Crystals," *Journal of the American Ceramic Society*, vol. 83, no. 1, pp. 214–16, 2000.

[218] R. Cusack and N. Papadakis, "New robust 3-D phase unwrapping algorithms: Application to magnetic field mapping and undistorting echoplanar images," *NeuroImage*, vol. 16, no. 3 I, pp. 754–764, 2002.

[219] R. P. Gupta, W. S. Khokle, J. Wuerfl, and H. L. Hartnagel, "Diffusion of gallium in thin gold films on GaAs," *Thin Solid Films*, vol. 151, no. 3, pp. L121–L125, 1987.

[220] S. M. Makin, A. H. Rowe, and A. D. Leclaire, "Self-Diffusion in Gold," *Proceedings of the Physical Society. Section B*, vol. 70, no. 6, pp. 545–552, 1957.

[221] A. C. Lasaga, *Kinetic theory in the earth sciences*. Princeton Series in Geochemistry, Princeton, N.J.: Princeton University Press, 1998.

[222] S. Sahin and M. Übeyli, "A review on the potential use of austenitic stainless steels in nuclear fusion reactors," *Journal of Fusion Energy*, vol. 27, no. 4, pp. 271–277, 2008.

[223] P. Strasser, S. Koh, T. Anniyev, J. Greeley, K. More, C. Yu, Z. Liu, S. Kaya, D. Nordlund, H. Ogasawara, M. F. Toney, and A. Nilsson, "Lattice-strain control of the activity in dealloyed core-shell fuel cell catalysts," *Nature Chemistry*, vol. 2, no. 6, pp. 454–460, 2010.

[224] C. Fischer, R. S. Arvidson, and A. Lüttge, "How predictable are dissolution rates of crystalline material?," *Geochimica et Cosmochimica Acta*, vol. 98, pp. 177–185, 2012.

[225] C. Fischer, I. Kurganskaya, T. Schäfer, and A. Lüttge, "Variability of crystal surface reactivity: What do we know?," *Applied Geochemistry*, vol. 43, pp. 132–157, 2014.

[226] C. Noiriel, M. Oursin, and D. Daval, "Examination of crystal dissolution in 3D: A way to reconcile dissolution rates in the laboratory?," *Geochimica et Cosmochimica Acta*, vol. 273, pp. 1–25, 2020.

[227] G. D. Saldi, M. Voltolini, and K. G. Knauss, "Effects of surface orientation, fluid chemistry and mechanical polishing on the variability of dolomite dissolution rates," *Geochimica et Cosmochimica Acta*, vol. 206, pp. 94–111, 2017.

[228] C. Noiriel, M. Oursin, G. Saldi, and D. Haberthür, "Direct Determination of Dissolution Rates at Crystal Surfaces Using 3D X-ray Microtomography," *ACS Earth and Space Chemistry*, vol. 3, no. 1, pp. 100–108, 2019.

[229] N. Cabrera, M. M. Levine, and J. S. Plaskett, "Hollow Dislocations and Etch Pits," *Phys. Rev.*, vol. 96, no. 4, p. 1153, 1954.

[230] A. C. Lasaga and A. E. Blum, "Surface chemistry, etch pits and mineral-water reactions," *Geochimica et Cosmochimica Acta*, vol. 50, no. 10, pp. 2363–2379, 1986.

[231] C. Fischer and A. Lüttge, "Converged surface roughness parameters - A new tool to quantify rock surface morphology and reactivity alteration," *American Journal of Science*, vol. 307, no. 7, pp. 955–973, 2007.

[232] P. E. Hillner, S. Manne, A. J. Gratz, and P. K. Hansma, "AFM images of dissolution and growth on a calcite crystal," *Ultramicroscopy*, vol. 42-44, pp. 1387–1393, 1992.

[233] A. S. Brand, P. Feng, and J. W. Bullard, "Calcite dissolution rate spectra measured by in situ digital holographic microscopy," *Geochimica et Cosmochimica Acta*, vol. 213, pp. 317–329, 2017.

[234] S. Ueta, H. Satoh, Y. Nishimura, A. Ueda, and K. Tsukamoto, "Dynamic and topographic observation of calcite dissolution using enhanced in-situ phase-shift interferometry," *Journal of Crystal Growth*, vol. 363, pp. 294–299, 2013.

[235] S. W. Chee, S. H. Pratt, K. Hattar, D. Duquette, F. M. Ross, and R. Hull, "Studying localized corrosion using liquid cell transmission electron microscopy," *Chemical Communications*, vol. 51, no. 1, pp. 168–171, 2015.

[236] J. M. Grogan, N. M. Schneider, F. M. Ross, and H. H. Bau, "Bubble and pattern formation in liquid induced by an electron beam," *Nano Letters*, vol. 14, no. 1, pp. 359–364, 2014.

[237] J.-C. Chen, B. Reischl, P. Spijker, N. Holmberg, K. Laasonen, and A. S. Foster, "Ab initio Kinetic Monte Carlo simulations of dissolution at the NaCl-water interface," *Physical Chemistry Chemical Physics*, vol. 16, no. 41, pp. 22545–22554, 2014.

[238] K. Yuan, V. Starchenko, S. S. Lee, V. De Andrade, D. Gursoy, N. C. Sturchio, and P. Fenter, "Mapping Three-dimensional Dissolution Rates of Calcite Microcrystals: Effects of Surface Curvature and Dissolved Metal Ions," *ACS Earth and Space Chemistry*, vol. 3, no. 5, pp. 833–843, 2019.

[239] J. Schott, S. Brantley, D. Crerar, C. Guy, M. Borcsik, and C. Willaime, "Dissolution kinetics of strained calcite," *Geochimica et Cosmochimica Acta*, vol. 53, no. 2, pp. 373–382, 1989.

[240] F. L. Vogel and L. C. Lovell, "Dislocation etch pits in silicon crystals," *Journal of Applied Physics*, vol. 27, no. 12, pp. 1413–1415, 1956.

[241] E. M. Gutman, *Mechanochemistry of Solid Surfaces*. World Scientific, 1994.

[242] J. Morel and S. W. Den Brok, "Increase in dissolution rate of sodium chlorate induced by elastic strain," *Journal of Crystal Growth*, vol. 222, no. 3, pp. 637–644, 2001.

[243] Y.-c. K. Chen-Wiegart, R. Harder, D. C. Dunand, and I. McNulty, "Evolution of dealloying induced strain in nanoporous gold crystals," *Nanoscale*, vol. 9, no. 17, pp. 5686–5693, 2017.

[244] D. Kim, M. Chung, J. Carnis, S. Kim, K. Yun, J. Kang, W. Cha, M. J. Cherukara, E. Maxey, R. Harder, K. Sasikumar, S. K. R. S. Sankaranarayanan, A. Zozulya, M. Sprung, D. Riu, and H. Kim, "Active site localization of methane oxidation on Pt nanocrystals," *Nature Communications*, vol. 9, no. 1, p. 3422, 2018.

[245] G. Beutier, M. Verdier, G. Parry, B. Gilles, S. Labat, M. I. Richard, T. Cornelius, P. F. Lory, S. Vu Hoang, F. Livet, O. Thomas, and M. De Boissieu, "Strain inhomo-

geneity in copper islands probed by coherent X-ray diffraction," *Thin Solid Films*, vol. 530, pp. 120–124, 2013.

[246] C. T. Horng, "Corrosion rates and electrokinetics of cobalt and cobalt-rich cobalt-iron alloys in sulfuric and hydrochloric acids," Master's thesis, Missouri University of Science and Technology, 1968.

[247] M. M. Larijani, M. Yari, A. Afshar, M. Jafarian, and M. Eshghabadi, "A comparison of carbon coated and uncoated 316L stainless steel for using as bipolar plates in PEMFCs," *Journal of Alloys and Compounds*, vol. 509, no. 27, pp. 7400–7404, 2011.

[248] A. Lüttge, R. S. Arvidson, and C. Fischer, "A stochastic treatment of crystal dissolution kinetics," *Elements*, vol. 9, no. 3, pp. 183–188, 2013.

[249] L. Briese, R. S. Arvidson, and A. Luttge, "The effect of crystal size variation on the rate of dissolution – A kinetic Monte Carlo study," *Geochimica et Cosmochimica Acta*, vol. 212, pp. 167–175, 2017.

[250] F. Viñes, Y. Lykhach, T. Staudt, M. P. Lorenz, C. Papp, H. P. Steinrück, J. Libuda, K. M. Neyman, and A. Görling, "Methane activation by platinum: Critical role of edge and corner sites of metal nanoparticles," *Chemistry - A European Journal*, vol. 16, no. 22, pp. 6530–6539, 2010.

[251] J. G. Mesu, A. M. Beale, F. M. De Groot, and B. M. Weckhuysen, "Probing the influence of X-rays on aqueous copper solutions using time-resolved in situ combined video/X-ray absorption near-edge/ultraviolet-visible spectroscopy," *Journal of Physical Chemistry B*, vol. 110, no. 35, pp. 17671–17677, 2006.

[252] S. L. Caër, "Water radiolysis: Influence of oxide surfaces on H_2 production under ionizing radiation," *Water*, vol. 3, no. 1, pp. 235–253, 2011.